Fluorescence Properties of Colloidal Semiconducting Nanoplatelets. From Single Emitters to Self-Assemblies

Jiawen Liu

Sorbonne Université

Ecole doctorale Physique en Ile de France

Institut des NanoSciences de Paris

Fluorescence Properties of Colloidal Semiconducting Nanoplatelets

From Single Emitters to Self-Assemblies

Par Jiawen Liu

Thèse de doctorat de physique, de la particule à la matière condensée

Dirigée par Laurent Coolen

Soutenue le 28 Septembre 2020

Devant le jury composé de :

Mme.	Sophie Brasselet	Rapportrice
M.	Stephane Berciaud	Rapporteur
M.	Julien Laurat	Examinateur
M.	Louis Biadala	Examinateur
M.	Benjamin Abecassis	Examinateur
M.	Laurent Coolen	Directeur de thèse

Acknowledgements

This PhD work has been carried out in INSP (Institut des NanoSciences de Paris) at Sorbonne Université. Taking this chance, I would like to thank all the people who have helped me during my PhD. I will never be able to complete this PhD thesis without the help and support from them.

First of all, I would like to sincerely thank my supervisor Laurent Coolen, who kindly accepted my application and helped me to get the funding from EDPIF. During the past three years, Laurent gave me generous support, constant availability for scientific discussion and any type of advice. He is a great teacher, with the patience to explain all the questions in detail and the kindness to share his knowledge anytime. He is also a great role model, from whom I learned to think and behave like a decent scientific researcher. I'm really grateful for having him as my supervisor.

I would like to thank Agnès Maître for hosting me in the group "Nanostructures and optics". She is always very happy for questions and discussions, and she loves to share her solid knowledge and insightful ideas with others. I also greatly appreciate the help from all the friendly colleagues in the group: I would like to thank Mathieu Mivelle (for sharing his knowledge on FDTD simulation, magnetic transition dipoles etc.), Bruno Gallas (for the help on ellipsometry measurements etc.), Catherine Schwob and Jean-Marc Frigerio (for the interesting discussion, valuable advice during my work), Willy Daney de Marcillac (for the valuable assistance in the lab, especially during my cryogenic measurements) and Yoan Prado (for the work in the chemistry room). It is a great pleasure to work with all of them. I am grateful for all the stimulating scientific discussions and precious advice.

I will never forget my friends, the PhD students and postdocs in the group. A special thank goes to Arnaud Choux, my officemate; we had a lot of interesting discussions and I would like to thank him for the help both in my work and in daily life. I am also glad to have met Juan Uriel Esparza and Amit Raj Dhawan, who enriched my knowledge of optics and inspired me during my research. I would like to thank Ali Mcheik, Jonathan Pairraire, Cyrine Ernandes and Mathieu Nicolas for the interesting scientific discussion and the spare time we spend together. I would also like to thank Fu Feng, a former PhD student in the group, who initially installed the homebuilt optical microscope before I came to the group. Then I would like to thank the

interns that I have worked with: Jian Cao, Chenxi Ma and particularly Zakarya Ouzit, who is now a PhD candidate in the group. Hope they are all doing well at their current work and wish them the best future.

I will also never forget the precious technical support from the engineers in the lab: Loïc Becerra, Dominique Demaille, Erwan Dandeu, Stéphan Suffit for the help in the cleanroom, and Francis Breton for the handy software interface that I have been using every day.

Besides the tight collaboration in INSP, during my PhD I had the opportunities to collaborate with several groups from other labs and there are many people that I would like to acknowledge. First, a very special thank goes to Benjamin Abécassis and his PhD student Lilian Guillemeney (Laboratoire de Chimie, ENS Lyon), for the fruitful collaboration on the fantastic CdSe assembly samples with great quality and interesting properties. Without these essential samples, I will never have such a good chance to observe collective photo-physical effects and obtain so many interesting scientific results. Second, I would like to thank Jean-Pascal Sutter and Virginie Bereau (Laboratoire de Chimie de Coordination, Toulouse) for the interesting collaboration on rare-earth-doped chiral crystals, which gave me a great chance to expand my experimental skills to circularly polarized emission analysis at cryogenic temperature. I also profited a lot from the collaboration with Thierry Pauporté and his students, Maria Ulfa, Pengjiu Wang, Tao Zhu and Daming Zheng, which led to many interesting publications about perovskite solar cells.

Next, I sincerely thank Sophie Brasselet and Stéphane Berciaud for reviewing my PhD thesis and for the advice they gave to this manuscript. I also would like to thank Julien Laurat, Louis Biadala, Benjamin Abécassis for being the jury member of my defense. I deeply appreciate their time spent on my thesis and defense, and their kind recognition of my PhD work.

Last but certainly not least, I would like to thank my dad, my mom and my fiancé Zhang Shuo. Nothing could happen without their unconditional support and endless love. This thesis is dedicated to them.

Sincerely,
Jiawen Liu

Contents

Chapter 1. Introduction of samples, theories and experimental setup

Introduction

Since the first report of nanocrystals with quantum confinement effects in the early 1980s [1], semiconducting nanoparticles have been massively studied because of the increasing importance to understand the physics in nanoscale objects in the past decades. Colloidal nanocrystals, as one of the most important classes of semiconductor quantum dots, have been studied intensively for more than 30 years. Nowadays, the family of colloidal nanoparticles is not limited to the 0-dimensional quantum dots [2], but also expands to various structures, including 1-dimensional nano rods [3] and 2-dimensional nanoplatelets [4].

2-dimensional semiconducting nanoplatelets (NPLs), or to say colloidal quantum wells, have attracted considerable attention since the initial report by Ithurria and Dubertret in 2008 [4]. Nanoplatelets have a well-controlled ultra-thin thickness consisted by a certain number of monolayers of atoms and have a controllable lateral expansion, resulting in unique optical characteristics, such as extraordinary narrow emission peak, low Stokes shift, large oscillator strength [5], and deterministic in-plane radiating dipoles [6].

Colloidal nanoplatelets present a strong natural tendency to aggregate because of their higher surface-to-volume ratio. By a choice of appropriate ligands and solvents, platelet stacking can be induced and one can obtain highly ordered complex structures. The first linear assembly of nanoplatelets was reported by Tessier et al. in 2013 [7]. After that, Benjamin Abécassis from Laboratoire de Chimie de l'ENS de Lyon has been the pioneer for linear platelet self-assembly. He demonstrated a robust procedure to synthesize stable co-facially stacked platelet chains with controllable length as long as 4 micrometers [8].

Many efforts have been devoted to investigations of photo-physical properties of isolated nano-emitters, either as single emitters or ensembles, while the research on highly-ordered self-assembly of emitters, which constitutes attractive systems for studying interactions and couplings between neighbour emitters, is still lacking. The knowledge of collective photo-physical properties is crucial to improve the efficiency of optoelectronics employing a dense-packed layer of particles. Other

potential applications may also be achieved once the collective behaviour of assembled particles is understood.

With this in mind, we collaborated during this thesis with Benjamin Abécassis and his PhD student Lilian Guillemeney, to investigate novel photo-physics on high-quality self-assembled chains of NPLs. As our expertise in the "Nanostructures et optique" group in Institut des NanoSciences de Paris, we used various optical analysis techniques, including micro-photoluminescence, time-correlated single photon counting, polarimetry, Fourier plane imaging and cryogenic photoluminescence, to analyse the fluorescence properties of different CdSe samples, from isolated single platelets, clusters of few platelets to self-assembled long chains. Our study involved various aspects of decay dynamics, blinking behaviours, dimensionality and directionality of transition dipoles, dipole-dipole interactions etc. The general goal was to reveal emerging collective effects in self-assembled samples, and to demonstrate that the properties of isolated single emitters will be drastically modified by the self-assembly.

Around the world, self-assembled chains of platelets have been achieved by very few other groups [9,10,11], while other assembly configurations have also been demonstrated, such as "face-down" or "edge-up" solid platelet films [12,13,14]. The previous research on assembled platelets involved non-radiative inter-NPL energy transitions [15], decay dynamics [16], and applications like light-emitting diodes [17] and lasing [18].

This thesis consists of 5 chapters.

In the first chapter, we will start with a general introduction of colloidal nanocrystals, nanoplatelets as well as self-assembled platelet chains. We will introduce a bit of history of the colloidal nanocrystals, their attractive optical properties and synthesis methods. We will also introduce the theoretical backgrounds involved in the studies in this thesis. Our homebuilt micro-photoluminescence setup will be briefly presented in the last section of this chapter.

In the 2nd chapter, we will report on excitonic energy transfer in self-assembled NPLs. Excitonic energy transfer has been intensively studied in solid films of emitters, which is however limited by the insufficient control of the order of the building blocks. In this chapter, we will combine the highly-ordered linear assembly of NPL chains with the micro-photoluminescence to study inter-NPL excitonic energy diffusions. We will estimate the energy diffusion length by imaging analysis, from which we will then estimate the inter-NPL energy transfer rate by the development of a diffusion equation model, which relates the transfer rate to the diffusion length in the image. This knowledge

is important for the fundamental study of collective photo-physics and also for the application significance, such as to improve the efficiency of light-emitting diode, photovoltaic solar cells, etc.

In the 3rd chapter, we will investigate the fluorescent behaviours of single NPLs, clusters and chains, including their blinking behaviours, decay dynamics and single photon emissions. Different techniques are involved: a time-correlated single-photon counting (TCSPC) module is employed to record the blinking time traces and decay curves, and a Hanbury-Brown and Twiss (HBT) configuration is used to obtain the second order photon correlation function. We will study how assembly modifies the fluorescent behaviour, and will conclude respectively on the typical behaviours of non-assembled and assembled emitters. This is not only important for the study of self-assembly effects, but also a powerful tool to distinguish the cases between single NPLs and clusters, which cannot be resolved by optical microscope.

In chapter 4, we will investigate the dimensionality and directionality of dipoles in NPLs emitters, from single isolated NPLs to assembled NPL chains. For single NPLs, it has been both theoretically estimated by optical selection rules and experimentally demonstrated that they are supposed to have two in-plane dipoles contributing to the emission. However, the dipole's dimensionality and orientation in co-facial assembly of NPL chains have never been fully investigated. Particularly, in assembled chains, all the NPLs are supposed to stand vertically on their edge, allowing for the deterministic vertical dipoles when deposited on a substrate, which is then of major interest for efficient surface plasmon couplings and emission optimization.

To study these questions, in our group, a polarimetric protocol for dipole orientation analysis of single emitters has been established, as well as the Fourier plane imaging, by which one can analytically probe the dipole components and orientations. In chapter 4, we will use a combination of polarimetry and Fourier plane imaging to probe the proportions of dipole components in both single and assembled emitters, with a record precision of ±3% thanks to the careful design of experimental configurations. By comparing the results of single NPLs and NPLs chains, we can study how stacked dielectric shape and other effects modify the transition dipoles, which will improve our understanding on collective photo-physics in self-assembled nanostructures.

In the last chapter, we will give conclusions of the works in this thesis and propose perspectives for future studies.

1.1 Introduction of colloidal nanoplatelets (NPLs)

With the development of nanoscience and nanotechnology, it has been of increasing importance to understand the physics in semiconducting materials with size reduced to the nanometer scale. This is motivated not only by its fundamental importance, but also by the practical significance as the size of electronics and optoelectronics has been reduced following Moore's law in the past decades. To study this topic, semiconducting nanocrystals (NCs) with sizes less than 100 nm, which are sometimes referred to as artificial atoms, have been great research objects.

In this section, we will first introduce the basics of colloidal nanocrystals, including a bit of history, their optical properties and the methods for synthesis. Then we will introduce the more recent 2-dimensional nanoplatelets (NPLs), including their novel optical properties in comparison with spherical nanocrystals (quantum dots) and the engineering of their geometry. In the last section, we will review the self-assembly of NPLs and introduce our samples.

1.1.1 Colloidal nanocrystals

Semiconducting nanocrystals with quantum confinement effects were reported for the first time in the 1980s [1], opening a new area of fundamental studies in semiconductor nanomaterials and attracting considerable attention in the fabrications and applications of modern optoelectronics. In 1993, C. Murray, D. Norris and M. Bawendi synthesized and characterized monodisperse cadmium chalcogenide nanocrystals (quantum dots) [2], making the colloidal nanocrystals a subject of intense study in the past decades. At the same time, another class of nanocrystals, i.e. epitaxial quantum dots, was fabricated by L. Goldstein et al. in 1985 [19], which requires more complex fabrication techniques but can provide, at low temperature, coherent states of light and rich quantum-optical effects.

Nowadays, the family of colloidal nanoparticles is not limited to the 0-dimensional quantum dots (with 3 dimensional quantum confinement), but also expands to various structures, including nano rods (i.e. 1D nanocrystals with 2D confinement) [3] and 2D nanoplatelets (with 1D confinement) [4]. In addition, there are other complex samples that have been synthesized and characterized with engineered dimensions and structures, such as tetrapods [20], nanowires [21], or nanoribbons [22].

Nanocrystals and quantum confinement effects

Nanocrystals are generally synthesized by II-VI or III-V materials, such as CdSe, CdS, InP, InAs, etc. High-quality nanocrystals should possess high luminescence quantum yields, good stabilities of luminescent properties, and compatibilities with desired solvents. All these properties rely on the proper passivation of dangling bonds present on the nanocrystal surface [23], which can be achieved by growing additional layers of appropriate materials outside of the emitting nanocrystal to form a "shell". Thus, in addition to "core-only" nanocrystals, "core-shell" structure attracts considerable attention as well. By engineering sizes and materials of the shell, the optical performance of nanocrystals will be modified, as will be introduced later in the section on heterostructures.

Unlike bulk semiconductor materials, nanocrystals possess optical properties determined not only by the intrinsic property of the materials, but also by the size of the nanocrystal due to quantum confinements. Briefly, this effect can be observed when the size of the crystal is much smaller than the wavelength of the wavefunction of the electron and the hole, so that the motion of the electron and the hole are "confined" in the crystal, leading to a transition from continuous to discrete energy levels. Basics of semiconductor physics and more theoretical backgrounds will be introduced later in section 1.2.

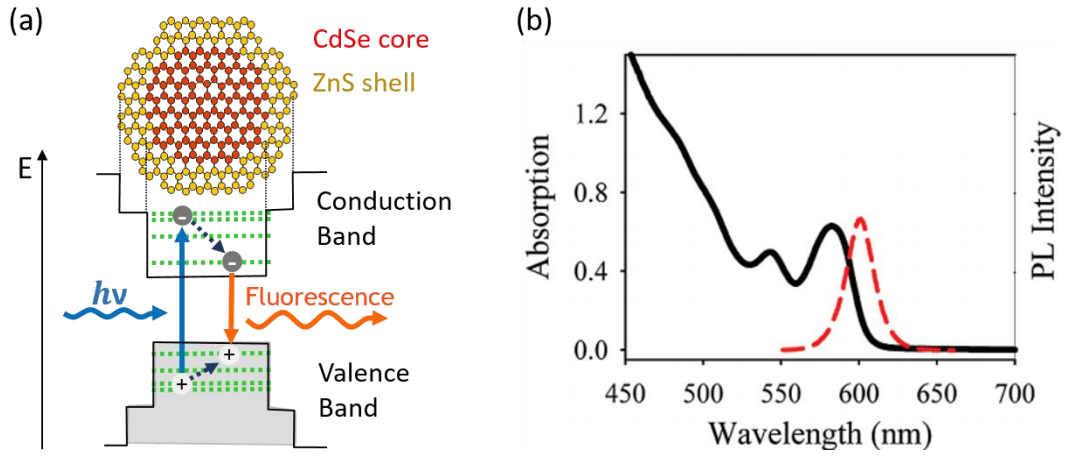

Figure 1-1. (a) Potential profile of a CdSe/ZnS core-shell nanocrystal. The energy levels of the excited carriers (electrons and holes) become quantized because of the quantum confinement effect originating from the limited size of the semiconductor nanocrystal. (b) UV-vis absorption (black solid line) and fluorescence (red dashed line) spectra of CdSe/ZnS QDs in solution, adapted from ref. [24].

To intuitively show the fluorescence mechanism and the quantum confinement effect, as an example, we consider a nanocrystal with a CdSe core and a ZnS shell (figure 1-1 (a)), which is one of the most successful nanocrystal systems having been synthesized in high quality and extensively studied. The pumping energy hv is absorbed by the nanocrystal, promoting an electron to the

conduction band and leaving a hole in the valence band. Then the electron-hole pair will relax to the lowest energy levels and recombine either radiatively by emitting a fluorescence photon or non-radiatively if defects are present. Due to the limited volume of the nanocrystal, the wavefunction of the electron and the hole are strongly confined. Thus, as shown in figure 1-1 (b), the absorption spectrum of the nanocrystal is close to a continuum at higher energies but at lower energies shows peaks indicative of quantum confinement, while the emission spectrum displays a single peak which can shift as a function of the NC size.

Colloidal synthesis method

The favorable and promising optical properties of nanocrystals are affected by their size, as depicted in figure 1-2, which then can be controlled precisely during the fabrication procedure. Various synthetic methods (one can refer to ref. [25]) have been developed for the growth of nanostructures and here we will briefly introduce the colloidal synthesis method related to the samples that will be studied in this thesis.

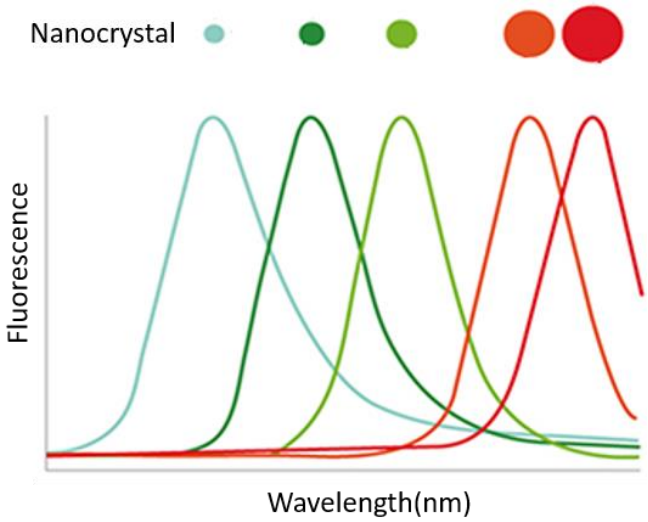

Figure 1-2. Tuning the mission wavelength of nanocrystals by modifying their size.

Colloidal synthesis has two main types, i.e. hot-injection and one-pot method. Here we take the hot-injection method as an example to briefly present the preparation processes in figure 1-3. First, a surfactant (e.g. oleic acid) solution and the precursor (e.g. cadmium precursor) are mixed in a three-neck flask equipped with a heater. Then, the reactive reactant is injected into the flask at a specific moment. By careful control of the temperature and the reaction atmosphere (e.g. inert gas), the desired nanocrystals will be obtained in the mixed solutions at a certain time. Most importantly, by modifying the temperature and the reaction time, the colloidal synthesis method allows for controlled synthesis

of colloidal hybrid nanostructures with excellent monodispersity, uniform size and shape, and high purity.

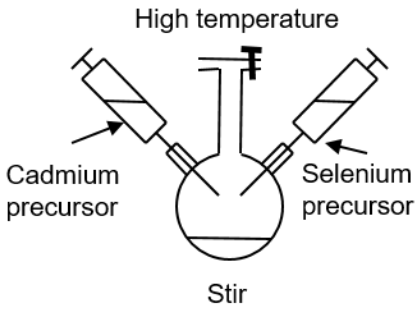

Figure 1-3. Hot-injection sythesis of colloidal CdSe nanocrystals.

Compared to the epitaxial quantum dots obtained by vacuum deposition, which are particularly good for making high-quality (low-defect, highly stable) semiconductor crystals from a compound or from a number of different elements, the colloidal nanocrystal has its own advantages: low cost, high yield, solution processability, precise control in shapes and sizes, good compatibility with versatile substrates, etc.

1.1.2 Colloidal nanoplatelets (NPLs)

NPLs and their optical characteristics

The nanoplatelets (NPLs) of II-VI semiconducting materials have attracted considerable attention since the pathbreaking report by S. Ithurria and B. Dubertret in 2008 [4]. A colloidal NPL is a 2-dimensional nanocrystal, or to say a colloidal quantum well, with a strong 1D quantum confinement in the direction vertical to the NPL's flat plane. Thanks to the atomic layer precision in colloidal synthesis, NPLs are essentially monodisperse in thickness, while the lateral dimension can be extended on an order of tens of nanometers or even larger with a shape control over the aspect ratio [26].

NPLs have attractive optical properties as compared to spherical nanocrystals:

1) Their photoluminescence peak is extraordinary narrow (typically of 12 nm) (yellow dotted line in figure 1-4) and tunable according to their thickness;

2) NPL ensembles have negligible inhomogeneous broadening in their emission spectra (green dashed line in figure 1-4), indicating the perfect uniformity in their thickness;

3) Their transition dipoles present large oscillator strength resulting from increased exciton center-of-mass extension [5,27], which will then significantly enhance the absorption cross-section [28] and accelerate the decay of excitons;

4) They have two in-plane emitting dipoles parallel to the platelet plane and can be deterministically deposited on a substrate with a horizontal orientation [6,29].

In addition to unique optical properties, NPLs have a large and flat surface, which makes them promising building blocks in self-assembly (as will be presented later in this section). When stacked co-facially, the center-to-center separation distance between adjacent NPLs is short, with very well controlled orientation and thus the orientation of their transition dipoles is matched, resulting in an efficient dipole-dipole interaction. Thanks to the perfect thickness monodispersity in stacked NPLs, their inhomogeneous line width is negligible with a very low Stokes shift [30]. Therefore, their emission and absorption spectra overlap, allowing a picosecond scale exciton diffusion (FRET) between neighbour NPLs in an assembly [31].

Thus, colloidal NPLs inherit the advantages of colloidal nanocrystals while possessing many emerging superior properties as compared to quantum dots, which make NPLs excellent candidates for versatile applications, such as lasing [32,33,34,35,36], light-emitting diodes [37,38,39], photovoltaics [15], single photon sources [40] and field-effect transistors [41].

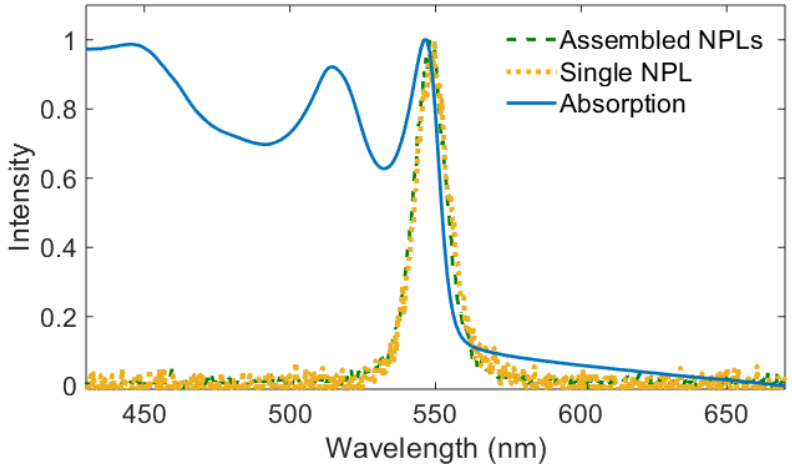

Figure 1-4. Absorption spectrum (blue) of single NPLs in solution, and emission spectra of a single NPL (yellow) or an assembled NPL chain (green).

Besides, NPLs can serve as a good platform of 2D materials for many fundamental studies, such as magnetic circular dichroism (MCD) [42], exciton mobility [43], dark exciton emission [44], etc.

Core-only NPLs

Commonly, CdSe NPLs with respectively 3, 4, 5, 6 monolayers in thickness have corresponding emission wavelengths at around 462, 513, 553, and 585 nm [45]. S. Delikanli et al. demonstrated the synthesis of ultrathin 2-monolayer CdSe NPLs [46] and found on them a lower luminescence quality similar to the spherical QDs with diameter less than 2 nm [47]: the optical properties start to be dominated by surface-induced effects, which yield a broad Stokes-shifted emission with lower quantum efficiency. As a summary, structural and spectroscopic characteristics of zinc-blende CdSe NPLs are presented in table 1-1. Note that there is a dispersion in the meaning of the "n-ML" denomination in early papers, here in this thesis we are using the now-common denomination.

Table 1-1. Structural and spectroscopic characteristics of zinc-blende CdSe NPLs

Structure	Designation	Wavelength	Thickness
3Cd-2Se	2 ML	394 nm	0.6 nm
4Cd-3Se	3 ML	462 nm	0.9 nm
5Cd-4Se	4 ML	513 nm	1.2 nm
6Cd-5Se	5 ML	553 nm	1.5 nm
7Cd-6Se	6 ML	585 nm	1.9 nm

In addition to CdSe NPLs, other II-VI semiconductor core-only NPLs were also reported, such as CdS and CdTe [5], PbS [48] or PbSe NPL [49], etc.

In terms of crystalline structures, both wurtzite and zinc-blende NPL can be synthesized depending on the fabrication conditions (ligand, reaction temperature etc.) [4,50]. Generally, zinc blende NPLs are obtained using carboxylic acid ligands with temperatures in the range of 150-240 °C, while amines and lower temperatures yield NPLs in the wurtzite structure. In this thesis, all the considered NPLs have a zinc-blende structure.

Heterostructured NPLs

Heterostructured nanocrystals can provide an additional degree of freedom and therefore improve the performance of the hybrid system. One can modify the optoelectronic properties by using nanocrystals with heterostructure, such as the core-shell nanocrystals shown in figure 1-1 (a). Depending on the materials used in the heterostructure, different electron-hole localization regimes can be obtained in excited emitters:

1) Type-I structure (figure 1-5 (a)): a narrow band gap material is used as the core, covered by a wide band gap material as the shell; the wide band gap shell works as a passivator of surface states, increasing the efficiency and stability of photoluminescence. In the type-I regime, the electron and the hole are confined within the narrow band-gap core material and form a direct exciton. The opposite situation, i.e. the "inverted type- I structure", is also possible, in which a wide band gap material is used in the core and a narrow band gap material forms the shell.

2) Type-II regime (figure 1-5 (c)): the materials of the core and the shell have their band gaps misaligned so that the core has the lowest electron band edge but the highest hole band edge or vice versa, so that the electron and hole are separated in different parts of the heterostructure, resulting in an indirect exciton.

3) Quasi type-II structure (figure 1-5 (b)): in some cases, the narrow band gap in the core material is displaced and reach a similar level as a band edge of the wide band gap shell. For quasi type-II case, one of the carriers (i.e. the hole) is confined in the core while the wavefunction of the other carrier can spread over a large area of the heterostructure.

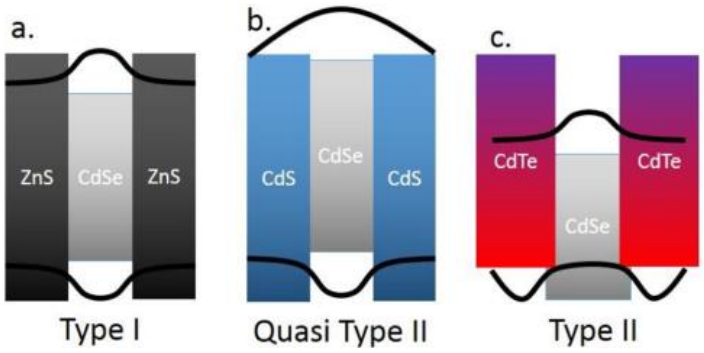

Figure 1-5. Scheme of hetero band structures with type I (a), quasi-type II (b), or type II (c) band aligment. Adapted from ref. [51].

In NPLs, heterostructures can be formed by sandwiching a core by shells ("core-shell" structure), or by growing a "crown" laterally around the core and forming a so-called "core-crown structure" as shown in figure 1-6. Various heterostructured NPLs have been reported in the literature, such as:

1) Core-crown NPLs, including type-I CdSe/CdS NPLs [52,53], inverted type-I NPLs [54], type-II CdSe/CdTe NPLs [55,56], type-II CdTe–CdSe NPLs [57], Type-II CdS/ZnSe NPLs [58] and composition tuneable CdSe/$CdSe_{1-x}Te_x$ core/crown NPLs [59];

2) Core-shell NPLs: CdSe/CdS and CdSe/CdZnS heterostructures [60], CdSe/ZnS NPLs [61], CdSe/CdS/ZnS NPLs [62], etc.

3) More complicated structures, such as the CdSe/CdS core/crown@shell samples [63].

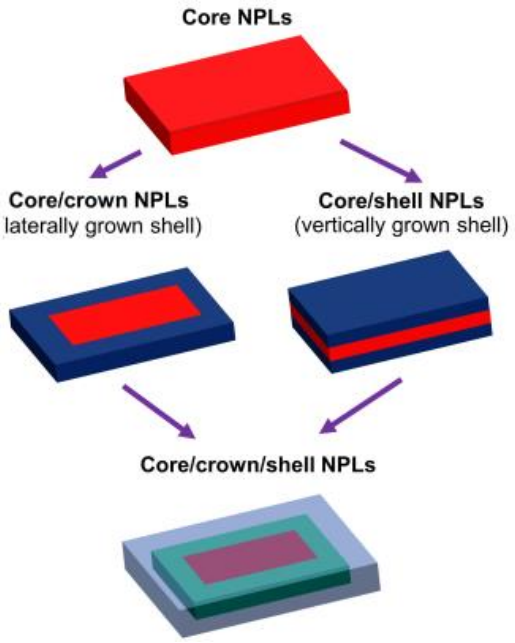

Figure 1-6. Schematics of core-only, core/crown, core/shell, and core/crown@shell NPLs. Adapted from ref. [64].

Strategies for tuning the emission color

NPL's emission peak can be tuned by different strategies. The most straightforward method is to change the thickness of NPLs as shown in table 1-1, which will directly modify the quantum confinement and consequently change the corresponding emission wavelength. However, controlling the emission of NPLs by thickness is limited by the discrete wavelengths corresponding to the number of monolayers. In the meantime, other methods have been proposed to fabricate NPLs with different wavelengths. One approach is to engineer the heterostructures by growing quasi type-II band structure, in which the change in emission color can be attributed to reduced confinement by exciton delocalization into the shell [61]. In addition to changing the thickness or structure of the NPLs, Y. Kelestemur et al. synthesised CdSe/$CdSe_{1-x}Te_x$ core/crown hetero-nanoplatelets and demonstrated that by changing the composition the emission color can vary from green to red [59]. Besides, S. Delikanli et al. prepared CdS/CdSe core/crown NPLs with inverted type-I band alignment and their emitting wavelength range covers all visible range by growing the CdSe crown around the CdS core with different thickness [54].

Apart from emission colors, other optical properties, such as emission rates and blinking, are also drastically influenced by the structure of NPLs. Generally, compared to core-only NPLs, heterostructured NPLs have 1) slower recombination lifetime, which is commonly attributed to the

decreasing electron and hole exciton wave function overlap; and 2) fewer blinking events, because of better passivation of nonradiative surface defects by the shell. More properties of blinking and decay dynamics will be discussed in chapter 3.

To modify the optical properties of NPLs, doping is another strategy that has been commonly used in nanocrystals. By doping metal ions in semiconductor materials, new energy levels can be created and result in different fluorescent behaviours. Various types of metal-ion doping in NPLs have been reported, such as Mn^{2+} doping in CdSe NPLs nanoribbons [65] or CdSe/CdS core shell NPLs [66], Cu^{2+} doping in CdSe NPLs [67] and Ag^{2+} doping in CdSe NPLs [68].

Synthesis of our CdSe NPL samples

The colloidal CdSe NPL samples used in this thesis were synthesized by Lilian Guillemeney under the supervision of Benjamin Abécassis from Laboratoire de Chimie de l'ENS de Lyon. Briefly, the first step was to prepare cadmium oleate from a mixture of dissolved sodium oleate and cadmium nitrate tetrahydrate through a careful washing and drying process. Then the cadmium oleate was introduced with selenium powder and ODE in a three-neck flask equipped with a septum, a temperature controller and an air condenser. The temperature and the reaction atmosphere were carefully controlled and cadmium acetate dihydrate and oleic acid were successively added. After cooling the flask, a mixture containing 5-ML CdSe NPL, 3ML-CdSe NPL and quantum dots were obtained in solution, from which the 5-ML CdSe NPLs were separated by centrifugation. More details about the synthesis and assembly protocol can be found in ref. [31].

CdSe nanoplatelets with a 1.5-nm thickness (6 layers of Cd and 5 layers of Se) were synthesized corresponding to a fluorescence wavelength of 550 nm. The lateral dimensions were 7 x 20 nm² (with 2-nm width dispersion and 4-nm length dispersion) as measured using transmission electron microscopy (TEM) in figure 1-7.

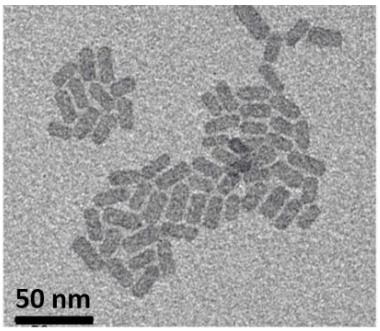

Figure 1-7. TEM images of single CdSe nanoplatelets.

Colloidal NPLs present a strong natural tendency to aggregate because of their higher surface-to-volume ratio. In order to avoid stacking, proper ligands and solvents can be used to dissolve the NPLs. On the other hand, NPL clusters can be obtained by reducing the dilution concentration when depositing the dispersion solution of single NPLs on the substrate. As shown in figure 1-8, we can obtain horizontal or vertical clusters consisted of various number of NPLs.

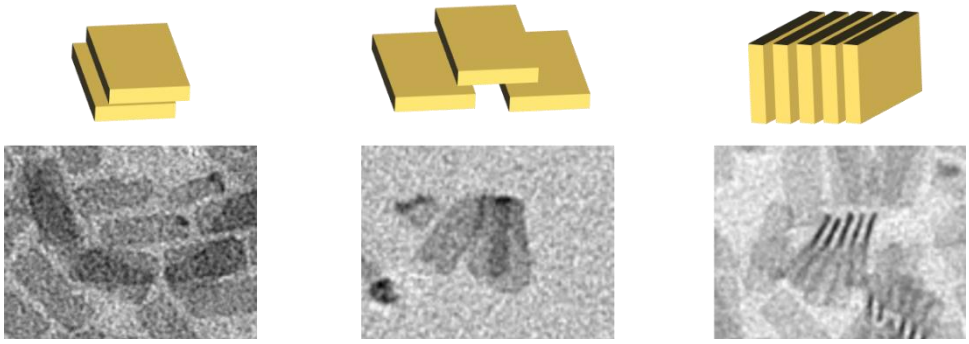

Figure 1-8. schematics and TEM images of 3 representative clusters, either lying face down or standing on their edge, with number of NPLs $N = 2$, 3 and 5, respectively.

1.1.3 Self-assembled chains of CdSe nanoplatelets

The state of the art on self-assembled NPLs

NPL stacking can be induced by a choice of appropriate ligands and solvents, from which one can obtain highly ordered complex structures that can then be promising functional materials for future applications.

The first linear assembly of NPLs was reported by Tessier et al. in 2013 [7]. Since then, Benjamin Abécassis has been the pioneer for linear NPL self-assembly: in 2014, Abécassis and coworkers reported on self-assembled bundles of NPL chains ("giant needles") with lengths in micrometer scale, and demonstrated that the ordered stacking of the NPLs leads to strongly polarized fluorescence [69]; in 2015, Jana et al obtained stable stacks of NPL chains by a method of ligand exchange [70], and then proposed a simple and robust procedure to synthesize long NPLs threads with controllable lengths in 2016 [8]; they also showed helicoidal twists in the NPL chains and single NPLs, which are due to surface strain caused by the ligand [71].

Linear self-assembly of NPLs has also been achieved by very few other groups, from Belarus [9], Turkey [16], Germany [10] and Korea [11]. In addition, NPLs also have been reported to form solid films with controllable face-down or edge-up configurations [12,13,14].

Self-assembly of NPLs has served as platforms for various studies. As examples, on the stacked chains, B. Guzelturk et al. demonstrated that photoluminescence quantum yield and lifetime are decreased by an order of magnitude, resulting from strong energy-transfer-assisted quenching [16]. M. Tessier et al. showed an additional emission line appearing in the photoluminescence spectrum at low temperatures and attributed it to the longitudinal optical (LO) phonon replica of the band-edge exciton [7]. Besides, many investigations were also focused on self-assembled NPLs solid films: C. Rowland et al. reported on the non-radiative energy transfer in CdSe NPLs solid films consisted of 4 or 5 mono-layer emitters and estimated an energy transfer rate of ~10 ps between neighbor emitters [15]; B. Diroll et al. analysed the low-temperature second peak in films of NPLs and attributed it to excimer states [18], while other groups proposed different mechanisms such as surface states [72] and most recently negatively-charged trions [73]. Several groups managed to control the orientation of CdSe NPLs layer, either face-down or edge-up, and showed that these different assembly configurations can be promising for applications like light-emitting diodes [17] and lasing [74].

Methods of self-assembly of NPLs

Many strategies for the self-assembly of NPLs have been proposed in the literature, including ligand exchange [9], addition of polar solvents [16,69], inducing depletion attraction forces [8], and Langmuir protocols [12,14]. Recently, R. Momper et al. reported on a new planar stacking method without using nonvolatile insulating additives so that the charge carrier transportation can be improved and lead to the development of novel optoelectronic devices [13].

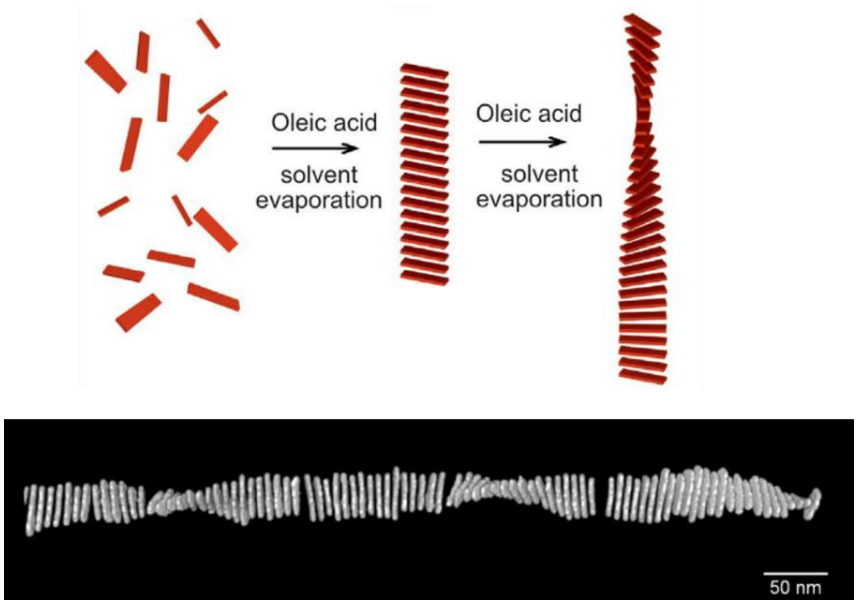

Figure 1-9. Top: scheme of the twisted ribbon formation mechanism. Bottom: 3D model from the tomographic reconstruction of a twisted chain. Adapted from ref. [71].

In the case of our sample, the assembly takes place in solution during the drying of dispersion of NPL in the presence of oleic acid: an appropriate amount of 5-monolayer CdSe NPL solution was diluted in hexane and oleic acid was then added, the amount of which is crucial to the length of assembled NPLs chains. The sample was sonicated for 10 minutes and the solvent was slowly evaporated. At this point, highly-ordered NPLs chains can be obtained. More details about the synthesis and assembly protocol of our samples can be found in ref. [31].

Twisted long chains and non-twisted short chains

By changing the amount of oleic acid added in the NPL dispersion solution (figure 1-9), Lilian Guillemeney and Benjamin Abécassis obtained two batches of samples: 1) short chains with lengths typically between 100-500 nm (figure 1-10 (a)), or 2) long chains with lengths longer than 1000 nm (figure 1-10 (b)). They found in longer chains twisted portions, which do not trend to appear on short chains. It is because the different amount of oleic acid added during the assembly helps to assemble NPLs but also induces inter-platelet strain, as reported by S. Jana et al. [71]. Additionally, it was also reported for the twisted chains that the twist angle of the stacked NPL is only ~10° and the twist occurs in limited portions (roughly 20 %) of the chains, while most of NPLs form straight stacks, as observed by high-angle annular dark-field scanning transmission electron microscopy (HAADF-STEM) in figure 1-9.

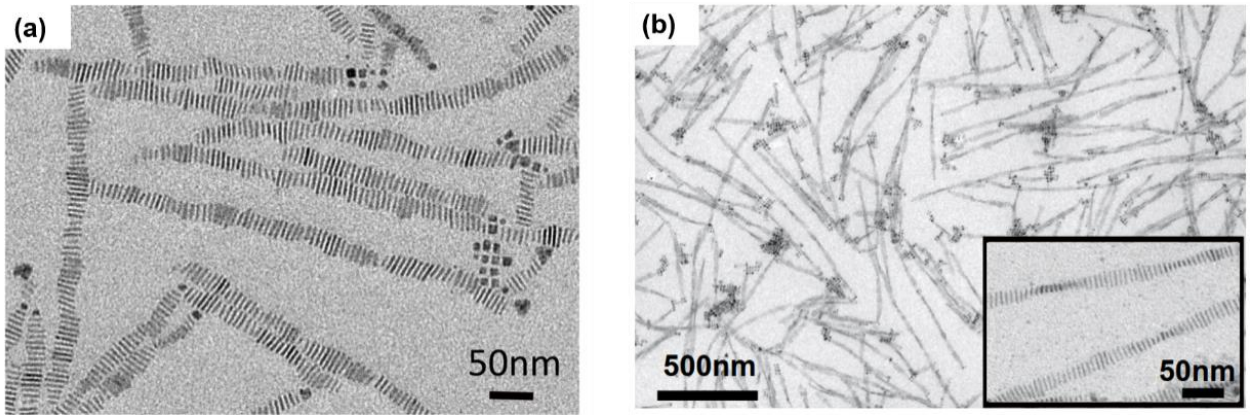

Figure 1-10. TEM images of non-twisted short chains (a) and twisted long chains (b).

Inter-platelet separation distance in chains

The NPL center-to-center separation distance δ of a given chain was obtained from TEM images by averaging over around 50 platelets. This was repeated for 6 chains and an average value of $\delta = 5.69$ nm was measured with 0.02 nm standard deviation. Another method to estimate the separation distance is to use small-angle X-ray scattering [71], by which a distance of $\delta = 5.84$ nm

is found. Benjamin Abécassis also performed similar measurements on high resolution STEM images acquired in HAADF mode (figure 1-11). In this case, he found $\delta = 4.75$ nm.

We believe the differences between these values is due to the environmental conditions in which the measurements are performed: in the case of SAXS, the measurement is performed in solution and solvent molecules can be present between the NPL thus increasing the distance between them. In the TEM, the measurements are performed in vacuum. This can have two effects: expand the organic molecules but also evaporate all the solvent molecules between the NPL and thus decrease the distance. The level of vacuum being different between the STEM and TEM measurements (higher vacuum in the case of STEM) it is not surprising to observe differences in the distances between the two measurements.

During our optical measurements we are in an intermediate case since we performed the measurements under ambient pressure but after the evaporation of the solvent. We will then take the intermediate value of 5.7 nm as an estimate of the inter-platelet separation distance in chains.

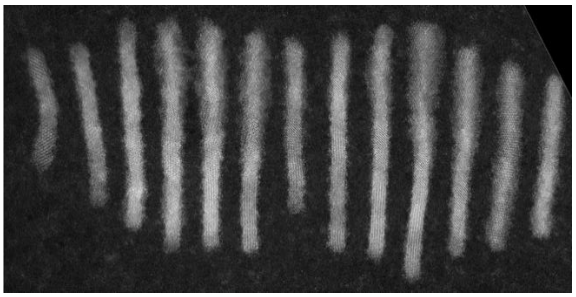

Figure 1-11. High-resolution HAADF image of a CdSe NPL stack.

Besides, the twisting of the NPL is not expected to impact the center to center distance since we observe on the STEM images (figure 1-11) that the twisting is correlated between two neighbour NPL. This is also confirmed by SAXS experiments where the position of the peak did not vary with time during the different steps of the assembly process (one can refer to fig. S2 in ref. [71]).

1.2 Theoretical backgrounds

Bloch's theorem and envelope function approximation in nanocrystals

The states of electrons and holes on different energy levels can be described by their wavefunctions. According to Bloch's theorem, the electronic wavefunctions in a bulk crystal can be written as

$$\Psi_{nk}(\vec{r}) = u_{nk}(\vec{r}) \cdot e^{i\vec{k}\vec{r}} \tag{1.1}$$

in which u_{nk} is the periodic function in the lattice of the crystal, $\vec{k}$ is the wavevector, and n is the band index, representing the conduction band or valence band for the electron or hole, respectively.

If we assume that the nanocrystal diameter (e.g. on an order of nanometers or tens of nanometers) is much larger than the lattice constant (typically ~0.4 nm) of the semiconductor material, the wavefunction of electron or hole (denoted by subscripts e/h) can be expressed in a linear combination of Bloch functions:

$$\Psi_{e/h}(\vec{r}) = \sum_k C_{nk} \cdot u_{nk}(\vec{r}) \cdot e^{i\vec{k}\vec{r}} \tag{1.2}$$

where C_{nk} is an expansion coefficient ensuring that the sum of Bloch functions still satisfy the boundary conditons of the confinements and the values of k necessary to expand the wavefunction are much smaller than the Brillouin lattice cell.

Close to the Γ-point (k=0), we can assume the Bloch functions u_{nk} have a weak $\vec{k}$ dependence, then the wavefunction can be approximated as:

$$\Psi_{e/h}(\vec{r}) = u_{n0}(\vec{r}) \cdot \sum_k C_{nk} \cdot e^{i\vec{k}\vec{r}} = u_{n0}(\vec{r}) \cdot f_{e/h}(\vec{r}) \tag{1.3}$$

in which $f_{e/h}(\vec{r}) = \sum_k C_{nk} \cdot e^{i\vec{k}\vec{r}}$ is defined as the envelope function. The envelope function approximation allows the description of quantum-confined states of electrons and holes, as will be presented below. Other possible methods include more bottom-up numerical calculations of electron states by combination of the Cd and Se orbitals. They are useful for smaller (1-2 nm diameter) nanocrystals where the envelope function approximation fails, but provide less physical qualitative understanding.

Bohr radius and quantum confinement regimes

Previously, we compared nanocrystals to bulk semiconductors and we stated that we have quantum confinement effect when the size of crystals becomes very small. Bohr radius can be used as a convenient length scale to precise the regimes of quantum confinement (strong or weak confinement), which is defined as:

$$r_B = \varepsilon_r \frac{m_0}{m^*} a_0 \tag{1.4}$$

in which ε_r is the dielectric constant of the material, m_0 stands for the mass of a free electron, $m^* = \frac{m_e^* m_h^*}{m_e^* + m_h^*}$ is the reduced mass of the exciton and a_0 means the Bohr radius of a hydrogen atom.

Strong or weak confinement regimes are defined by comparing the confinement size a with the exciton's Bohr radiu r_B: when $r_B > a$, we are in the strong confinement regime, in which the Coulomb interaction is weaker than the confinement effect and is treated as a perturbation; while in the case of $r_B < a$, we are in the weak confinement regime, where the confinement is weak and the Coulomb interaction is fully taken into account.

For CdSe nanocrystals, the Bohr radius is reported to be around 4.9 nm [75]. Thus, for CdSe nanocrystals, we can have strong quantum confinement in 3 dimensions while for CdSe NPLs, we expect a strong quantum confinement along the thickness axis but weak confinements in the lateral directions.

The energy of electrons or holes in quantum wells

II-VI semiconductors have a direct band gap, with the minimum of the conduction band and the maximum of the valence band located at the origin ($k = 0$) in the k space (i.e. Γ point in the Brillouin zone).

For sufficiently low values of k, the band structures can be approximated as parabols:

$$E_c = \frac{\hbar^2 k^2}{2m_e} + E_g \tag{1.5}$$

$$E_v = -\frac{\hbar^2 k^2}{2m_h} \tag{1.6}$$

where m_e and m_h are introduced as respectively the effective masses of electrons in the conduction band and holes in the valence band, and E_g is the energy gap between conduction band and valence band. Let us develop a quantum confinement calculation in a 1D case in order to illustrate the most basic properties. In the strong confinement regime, assuming a quantum well with potential barrier $V\left(|x| < \frac{a}{2}\right) = 0$ and $V\left(|x| > \frac{a}{2}\right) = \infty$, we can solve the Schrödinger equation in region $-\frac{a}{2} < x < \frac{a}{2}$ for confined carriers and find that:

$$k = \frac{n\pi}{a} \tag{1.7}$$

where n is a positive integer (1, 2, 3, etc). Then we obtain the quantized energy level:

$$E_c = \frac{\hbar^2\pi^2 n^2}{2m_e a^2} + E_g \tag{1.8}$$

$$E_v = -\frac{\hbar^2\pi^2 n^2}{2m_h a^2} \tag{1.9}$$

Similar calculations, now involving Bessel functions, can be developed in a spherical quantum well. We then have discrete energy levels of electrons and holes due to quantum confinement, as depicted in figure 1-12.

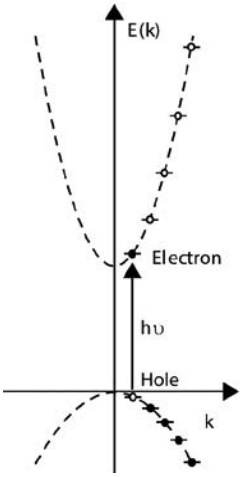

Figure 1-12. Discrete energy levels due to confinement effects. Adapted from ref. [76].

Note that here we use the effective mass approximation, which attempts to incorporate the complicated periodic potential felt by the carrier in the lattice and graphically assumes that the bands have simple parabolic forms.

According to the above calculations, the confinement energy of electrons and holes scale as $\frac{1}{a^2}$. Since the Coulomb interaction scales as $\frac{1}{a}$, in the strong confinement regime, the quadratic confinement term dominates. Thus when we write the energy of electron hole pair (exciton) states E_{ehp}, the Coulomb energy term E_c is added as a first-order energy correction:

$$E_{ehp} = E_g + \frac{\hbar^2\pi^2}{2a^2}\left(\frac{{n_e}^2}{m_e} + \frac{{n_h}^2}{m_h}\right) - E_c \tag{1.10}$$

The lowest exciton state is obtained when $n_e = n_h = 1$, thus we can write it as:

$$E_{ehp} = E_g + \frac{\hbar^2\pi^2}{2m_{eh}a^2} - E_c \tag{1.11}$$

with $m_{eh} = \frac{m_e m_h}{m_e + m_h}$ being the effective mass of the electron hole pair.

Fine structures of electrons and holes states in CdSe NCs and NPLs

In figure 1-12 we describe only two bands, the valence band and the conduction band. However, the actual structures are more complicated. The valence band and the conduction band of nanocrystals will be further split into subbands, with distinct curvatures depending on the different effective mass, resulting from orbital-spin interactions and an asymmetry in the shape.

In CdSe nanocrystals, the valence band is formed by the 4p orbit of the selenium and the conduction band corresponds to the 5s orbit of cadmium. Thus, holes on valence band have a p-like symmetry with orbital momentum quantum number $l = 1$, and electrons on conduction band have a s-like symmetry and its orbital momentum number $l = 0$. The coupling between the spin angular momentum s of a charge and its orbital angular momentum l leads to a new quantum number, i.e. total angular momentum: $J = s + l$. For the holes (as denoted by 'h' in the subscript), $J_h = l_h + s_h$, so we have J_h equals to 1/2 or 3/2, corresponding to different distinct bands: 1) $J_h = \frac{1}{2}$ (with z-component $J_{hz} = \pm\frac{1}{2}$), which is known as split-off (SO) band; 2) $J_h = \frac{3}{2}$, which is further split into two sub-bands with $J_{hz} = \pm\frac{1}{2}$ and $\pm\frac{3}{2}$ corresponding to the light hole (lh) band and the heavy hole (hh) band, respectively. For electrons, we have $J_e = \frac{1}{2}$ and its projection $J_{ez} = \pm\frac{1}{2}$.

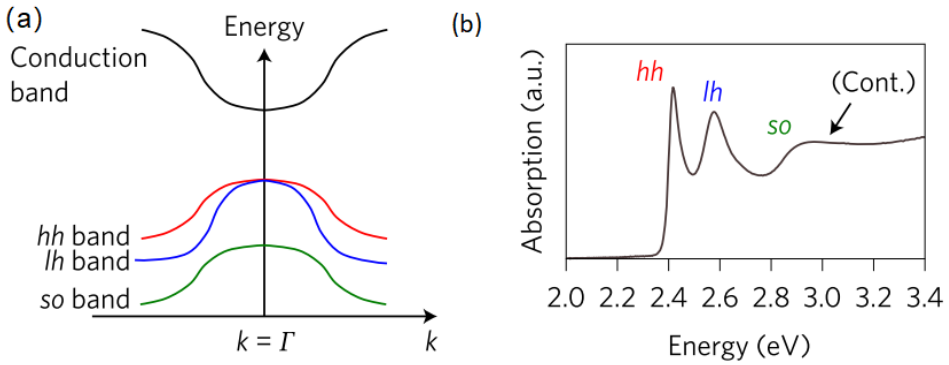

Figure 1-13. (a) Degenerate hh, lh and so sub-bands in CdSe nanoplatelets. (b) Absorption spectrum of CdSe nanoplatelets with the corresponding transitions of hh, lh and so being indicated. Adapted from ref. [77].

In bulk zinc-blende CdSe semiconductors, the hh and lh states are degenerate at $k = 0$ but the effective masses of the heavy holes are larger than that of the light holes. However, in the case of NPLs, the quantum confinement is very strong in the vertical direction because the NPLs are very thin. Since the confinement energy scales as (1/m), the degeneracy between the light and heavy holes

is lifted and the confined light-hole energy is much higher (figure 1-13 (b)). As a result, the band edge emission originates mostly from the hh state. Besides, for wurtzite nanocrystals, the intrinsic asymmetry in the wurtzite structure will also split the hh sub-bands and lh sub-bands.

Fine structures in CdSe nanocrystals

For the valence band involving six degenerate states, the actual sub bands result from a mixture of these different states, instead of being directly produced by them (following the introduction in ref. [75], the hole wave functions are expressed as combinations from different valence-band states and have mixed s-d type symmetry, which is referred to as "S-D" mixing).

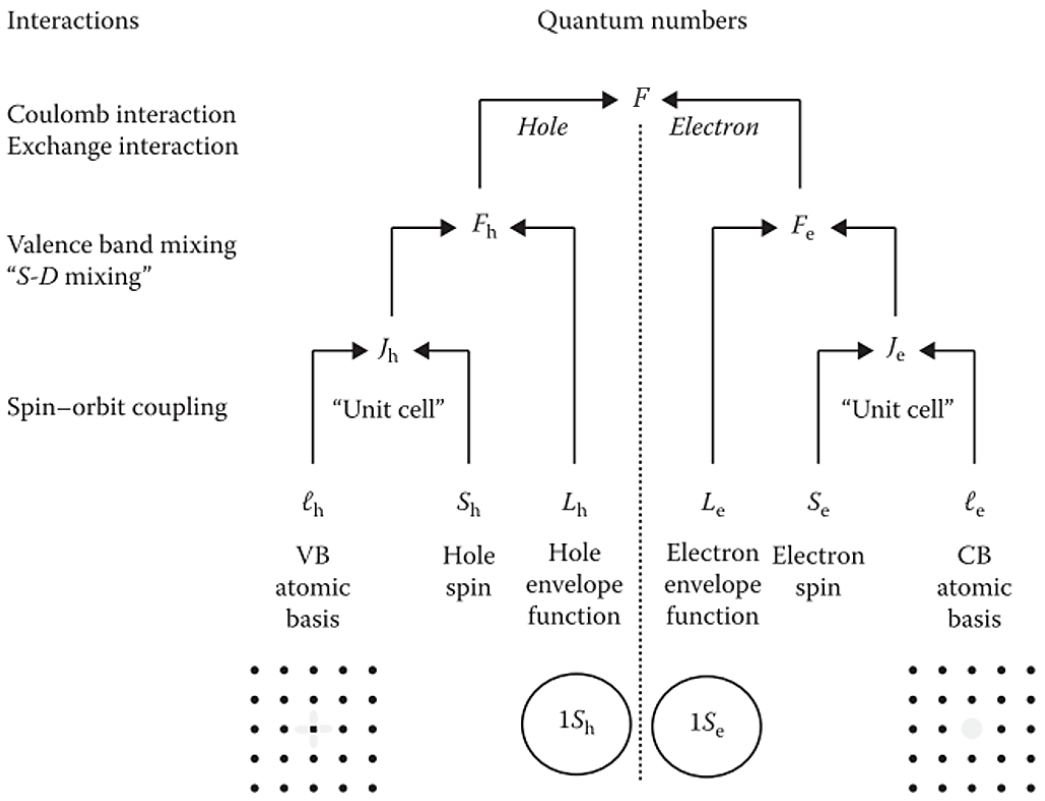

Figure 1-14. Summary of quantum numbers and important interactions in semiconductor nanocrystals. Adapted from ref. [76].

Now we use a new quantum number $F_{h,e} = L_{h,e} + J_{h,e}$, which corresponds to the total angular momentum, containing z-projection F_z from $-F$ to $+F$, to characterize the electron or hole's state. Here L is the orbital angular momentum of the envelope function obtained from the confinement problem, and J is the total angular momentum, as introduced previously. The subscripts h, e respectively correspond to the case of electrons and holes. Therefore, for an electron-hole pair (or an exciton), its total angular momentum quantum number can be calculated by $F = F_h + F_e$, which yields either 1 or 2 as the electron and hole's quantum number are 1/2 and 3/2 respectively. The

quantum numbers and the important interactions in semiconductor nanocrystals are summarized in figure 1-14 [76].

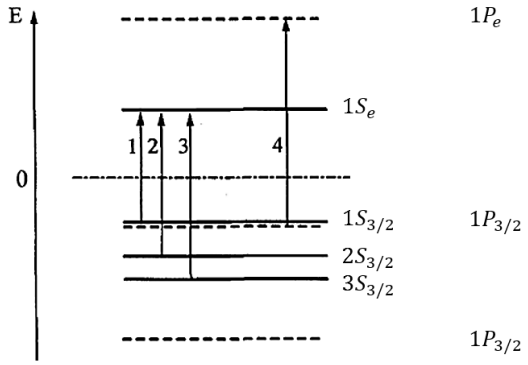

Figure 1-15. Optical transitions of a nanocrystal taking into account the mixing of the valence band states. Solid lines corresponds to S states and dashed lines are P states. Adapted from ref. [75].

To classify the energy levels and optical transitions we use a new notation written as nL_F with n being the counter for the ground and the excited states and L being the envelope function component. The first hole state in CdSe nanocrystals is $1S_{3/2}$ and the first electron state is $1S_e$. The transition between these two states is thus written as $1S_{3/2}1S_e$ (which is referred to as the band-edge exciton), as depicted in figure 1-15. This exciton state is eight-fold degenerate, because the $1S_e$ level is two-fold degenerate due to the electron-spin interaction, and the $1S_{3/2}$ state is four-fold degenerate consisted of hh ($\pm\frac{3}{2}$) and lh ($\pm\frac{1}{2}$) sub-bands.

As we mentioned above, the band-edge exciton ($1S_{3/2}1S_e$) has eight-fold degeneracy. These degeneracies will be lifted if we consider some second-order effect as introduced in ref. [76], including: a uniaxial crystal lattice (e.g. the wurtzite structure), a shape anisotropy and electron–hole exchange interactions. In the bulk regime (left side in figure 1-16), the effects of the anisotropy of the crystal lattice or the asymmetric shape of the crystallite dominates, where the exchange interaction is negligible. As the size reduces, the electron–hole exchange interactions become increasingly significant because the charges are confined together in a small volume. In the case of small nanocrystals, the confinement of the charges is very strong and thus the electron-hole exchange interaction dominates. As a result, the original eight-fold states are split into five sub energy levels dominated by exchange interactions, which can be properly described by quantum number F: for the case of $F = 2$, we have its projections $F_z = 0, \pm1, \pm2$; or when $F = 1, F_z = 0, \pm1$. In the literature, these five levels are also labelled by number $|F|$ with superscripts to distinguish upper (U) and lower (L) energy levels, as shown in figure 1-16.

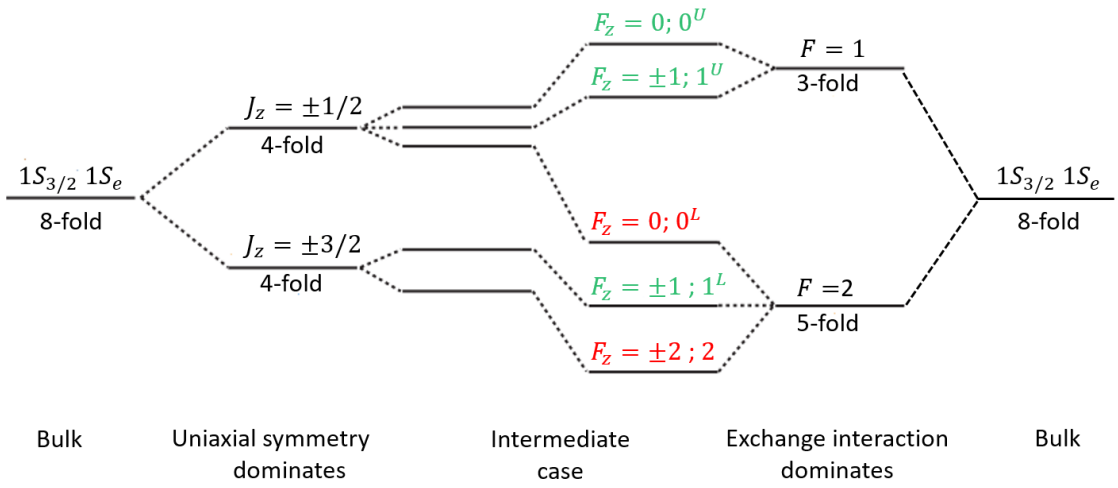

Figure 1-16. Fine structure of the exciton's energy levels, resulting from non-spherical shape of the nanocrystals, their hexagonal (wurtzite) lattice, and the exchange interaction. The levels in green are optically allowed transitions, while the red levels are passive. Adapted from ref. [76].

Fine structures have been observed in many experiments. As an interesting example, H. Htoon et al. demonstrated the fine structures of the bright exciton in CdSe quantum dots by high-resolution spectroscopy at low temperature [78].

Bright and dark excitons

In nanocrystals, not all the split energy levels are optically allowed for radiative recombination. First, the $F_z = \pm 2$ state is forbidden because the angular momentum of a photon is only 1, which cannot have an angular momentum projection of ±2. Then, the 0^U state is also forbidden due to the destructive interference of the wave functions of the two exciton states $\left|\uparrow, -\frac{1}{2}\right\rangle$ and $\left|\downarrow, \frac{1}{2}\right\rangle$, as elaborated by A. L. Efros et al. [79]. The other states (0^U, 1^U and 1^L) are optically allowed. We call the electron-hole pairs located on allowed (respectively forbidden) transition states the bright (respectively dark) excitons.

Figure 1-17 shows an example of the calculated energies sublevels in a quantum dots, including the effects of the crystal field, the non-spherical shape, and the exchange interaction in perturbation theory [80]. At room temperature, the emission is exclusively from the $\pm 1^L$ transition (the lowest optically allowed transition) with emission rate Γ_A. This state is thermally populated from ± 2 state (with thermal relaxation rate γ_{th}), which is lower in energy but optically forbidden. However, for typical spherical nanocrystals [81], at cryogenic temperatures (e.g. ~2K), the energy separation (ΔE in figure 1-17) between the dark state ± 2 and the lowest bright state $\pm 1^L$ is much larger than kT. Therefore, the excitons have to return to the ground state $|G\rangle$ through dark transition channel with

rate Γ_F being much slower than Γ_A. As we have introduced, the recombination rate of a dark exciton should be 0 because the photon cannot change the angular momentum of the system by ±2. However, experiments show that the dark exciton transition indeed happens in CdSe nanocrystals [82] and NPLs [44], in assistance of phonons or by a nonlinear process. Besides, in the presence of a strong external magnetic field, the dark transition state will become partially allowed by mixing with the optically allowed states [44]. As a result, the decay rate is generally much slower at cryogenic temperature.

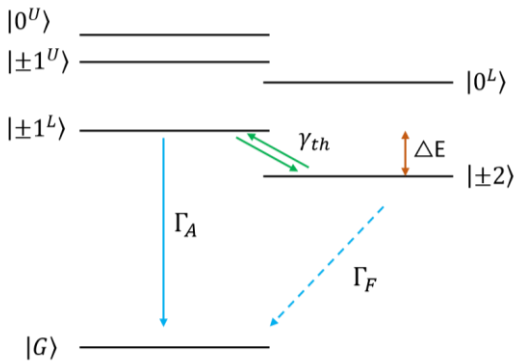

Figure 1-17. Transitions of the bright and the dark exciton (including LO-phonon coupling) in a spherical nanocrystal. Adapted from ref. [80].

Transition matrix elements

Optical dipole transitions can be characterized in terms of their dipole matrix elements (or in terms of their momentum matrix elements). If we assume that an electron transits from a valence band state $|\Psi_v\rangle$ to a conduction band state $|\Psi_c\rangle$ with a wavefunction:

$$\left|\Psi_{c,v}\right\rangle = \left|u_{c,v}(\vec{r})\right\rangle \left|f_{c,v}(\vec{r})\right\rangle \tag{1.12}$$

where $u_{c,v}$ is the periodic Bloch function and $f_{c,v}$ is the envelope function of electrons in the conduction band or holes in the valence band (with subscript c or v), then the momentum matrix element can be written as:

$$P_{v\to c} = \left\langle \Psi_c \middle| \vec{e}\hat{P} \middle| \Psi_v \right\rangle \tag{1.13}$$

in which $\hat{P} = -i\hbar\vec{\nabla}$ is the momentum operator and $\vec{e}$ is the polarization vector of the emitted or absorbed light. Considering the envelope function approximation, the matrix element can be expanded as:

$$P_{v\to c} = \langle f_c | \left\langle u_c \middle| \vec{e}\hat{P} \middle| u_v \right\rangle | f_v \rangle = \langle f_c | f_v \rangle \left\langle u_c \middle| \vec{e}\hat{P} \middle| u_v \right\rangle + \left\langle f_c \middle| \vec{e}\hat{P} \middle| f_v \right\rangle \langle u_c | u_v \rangle \tag{1.14}$$

where the second term will be equal to 0 as the Bloch functions are orthogonal ($\langle u_c|u_v\rangle = 0$). Therefore, we can simplify the momentum matrix element as:

$$P_{v\to c} = \langle f_c|f_v\rangle\langle u_c|\widehat{\vec{e}P}|u_v\rangle \tag{1.15}$$

which is also known to be proportional to the dipole matrix element [83]:

$$P_{v\to c} \propto \langle f_c|f_v\rangle\langle u_c|\hat{\mu}|u_v\rangle \tag{1.16}$$

where $\hat{\mu} = q\vec{r}$ is the dipole moment of the electromagnetic radiation.

The oscillator strength of a transition is proportional to $|\langle f_c|f_v\rangle\langle u_c|\hat{\mu}|u_v\rangle|^2$, where the integral of the Bloch functions determines the polarization of the transition and the integral of envelope functions provides selection rules.

Bloch functions of electrons and holes in split states

Following the previous introduction of the split states in the conduction band and the valence band in CdSe NPLs, the periodic Bloch functions of electrons and holes in these split states can be represented as below [79]:

1) For the electrons in the conduction band:

$$\left|u^{e}_{\frac{1}{2},-\frac{1}{2}}\right\rangle = |S\rangle|\uparrow\rangle; \qquad \left|u^{e}_{\frac{1}{2},\frac{1}{2}}\right\rangle = |S\rangle|\downarrow\rangle \tag{1.17}$$

2) For the heavy hole:

$$\left|u^{hh}_{\frac{3}{2},\frac{3}{2}}\right\rangle = \frac{1}{\sqrt{2}}|X+iY\rangle|\uparrow\rangle; \qquad \left|u^{hh}_{\frac{3}{2},-\frac{3}{2}}\right\rangle = \frac{1}{\sqrt{2}}|X-iY\rangle|\downarrow\rangle \tag{1.18}$$

3) For the light hole:

$$\left|u^{lh}_{\frac{3}{2},\frac{1}{2}}\right\rangle = -\sqrt{\frac{2}{3}}|Z\rangle|\uparrow\rangle + \frac{1}{\sqrt{6}}|X+iY\rangle|\downarrow\rangle; \quad \left|u^{lh}_{\frac{3}{2},-\frac{1}{2}}\right\rangle = \sqrt{\frac{2}{3}}|Z\rangle|\downarrow\rangle + \frac{1}{\sqrt{6}}|X-iY\rangle|\uparrow\rangle \tag{1.19}$$

4) For the split-off subband:

$$\left|u^{so}_{\frac{1}{2},\frac{1}{2}}\right\rangle = \frac{1}{\sqrt{3}}|Z\rangle|\uparrow\rangle + \frac{1}{\sqrt{3}}|X+iY\rangle|\downarrow\rangle; \qquad \left|u^{so}_{\frac{1}{2},-\frac{1}{2}}\right\rangle = \frac{1}{\sqrt{3}}|Z\rangle|\downarrow\rangle - \frac{1}{\sqrt{3}}|X-iY\rangle|\uparrow\rangle \tag{1.20}$$

Polarization of transitions dipoles

To simply derive the polarization of transitions between a conduction band and split hh, lh and so sub-bands, R. Scott et al. calculated their oscillator strength [77], omitting the mixing and interaction between them.

Given that the cubic symmetry of zinc-blende nanocrystals leads to $\langle S|x|X\rangle = \langle S|y|Y\rangle = \langle S|z|Z\rangle = K$ being a nonzero value while all other integrals are equal to zero, for the transition involving hh states, their oscillator strength can be estimated as:

$$\left|\left\langle u^{e}_{\frac{1}{2},\frac{1}{2}}\middle|\hat{\mu}\middle|u^{hh}_{\frac{3}{2},\frac{3}{2}}\right\rangle\right|^2 = \left|\left\langle u^{e}_{\frac{1}{2},-\frac{1}{2}}\middle|\hat{\mu}\middle|u^{hh}_{\frac{3}{2},-\frac{3}{2}}\right\rangle\right|^2 = 0 \tag{1.21}$$

$$\left|\left\langle u^{e}_{\frac{1}{2},\frac{1}{2}}\middle|\hat{\mu}\middle|u^{hh}_{\frac{3}{2},-\frac{3}{2}}\right\rangle\right|^2 = \left|\left\langle u^{e}_{\frac{1}{2},-\frac{1}{2}}\middle|\hat{\mu}\middle|u^{hh}_{\frac{3}{2},\frac{3}{2}}\right\rangle\right|^2 = q^2K^2\begin{pmatrix}1/2\\1/2\\0\end{pmatrix} \tag{1.22}$$

For the lh state transitions, we can write:

$$\left|\left\langle u^{e}_{\frac{1}{2},\frac{1}{2}}\middle|\hat{\mu}\middle|u^{lh}_{\frac{3}{2},\frac{1}{2}}\right\rangle\right|^2 = \left|\left\langle u^{e}_{\frac{1}{2},-\frac{1}{2}}\middle|\hat{\mu}\middle|u^{lh}_{\frac{3}{2},-\frac{1}{2}}\right\rangle\right|^2 = q^2K^2\begin{pmatrix}0\\0\\2/3\end{pmatrix} \tag{1.23}$$

$$\left|\left\langle u^{e}_{\frac{1}{2},\frac{1}{2}}\middle|\hat{\mu}\middle|u^{lh}_{\frac{3}{2},-\frac{1}{2}}\right\rangle\right|^2 = \left|\left\langle u^{e}_{\frac{1}{2},-\frac{1}{2}}\middle|\hat{\mu}\middle|u^{lh}_{\frac{3}{2},\frac{1}{2}}\right\rangle\right|^2 = q^2K^2\begin{pmatrix}1/6\\1/6\\0\end{pmatrix} \tag{1.24}$$

For transitions involving so states, similarly, we obtain:

$$\left|\left\langle u^{e}_{\frac{1}{2},\frac{1}{2}}\middle|\hat{\mu}\middle|u^{so}_{\frac{1}{2},\frac{1}{2}}\right\rangle\right|^2 = \left|\left\langle u^{e}_{\frac{1}{2},-\frac{1}{2}}\middle|\hat{\mu}\middle|u^{so}_{\frac{1}{2},-\frac{1}{2}}\right\rangle\right|^2 = q^2K^2\begin{pmatrix}1/3\\1/3\\0\end{pmatrix} \tag{1.25}$$

$$\left|\left\langle u^{e}_{\frac{1}{2},\frac{1}{2}}\middle|\hat{\mu}\middle|u^{so}_{\frac{1}{2},-\frac{1}{2}}\right\rangle\right|^2 = \left|\left\langle u^{e}_{\frac{1}{2},-\frac{1}{2}}\middle|\hat{\mu}\middle|u^{so}_{\frac{1}{2},\frac{1}{2}}\right\rangle\right|^2 = q^2K^2\begin{pmatrix}0\\0\\1/3\end{pmatrix} \tag{1.26}$$

Since CdSe NPLs have very strong confinement in the z-direction normal to the platelet plane, and because the confinement energy scales as $1/m$ and the hh sub-bands have the highest effective mass, hh sub-bands are lifted to be the highest (closest to the band edge) valence band and thus the emission is exclusively originated from $e-hh$ transition. **As a result, we expect that the emission of CdSe NPLs is an incoherent sum of two orthogonal in-plane dipoles along x and y axis,**

horizontal to the platelet plane. Besides, for the absorption at energies much higher than the band gap, hh, lh and so transitions participate almost equally in NPLs, so their absorption dipoles are isotropic [77,84].

Following the theoretical work by A.L. Efros et al. [79], now we briefly discuss transitions in consideration of exchange interactions between split band structures. Here the optically forbidden ± 2 state is omitted. For the fine states $0^{U,L}$ and $\pm 1^{U,L}$, we can write:

$$|0^{U,L}\rangle = \frac{\mp i}{\sqrt{2}}\Psi_{\uparrow,-1/2} + \frac{1}{\sqrt{2}}\Psi_{\downarrow,+1/2} \tag{1.27}$$

$$|+1^{U,L}\rangle = C^{-}\Psi_{\downarrow,+3/2} + \mp iC^{+}\Psi_{\uparrow,+1/2} \tag{1.28}$$

$$|-1^{U,L}\rangle = \mp iC^{-}\Psi_{\uparrow,-3/2} + C^{+}\Psi_{\downarrow,-1/2} \tag{1.29}$$

where the $C^{\pm}$ is a term relating to the exchange interaction. Without going into details here, one can refer to reference [79] for the definition of $C^{\pm}$ and the solution for the matrix element $P_F = \langle 0|\vec{e}\hat{P}|\Psi_F\rangle$ of the fine state transitions.

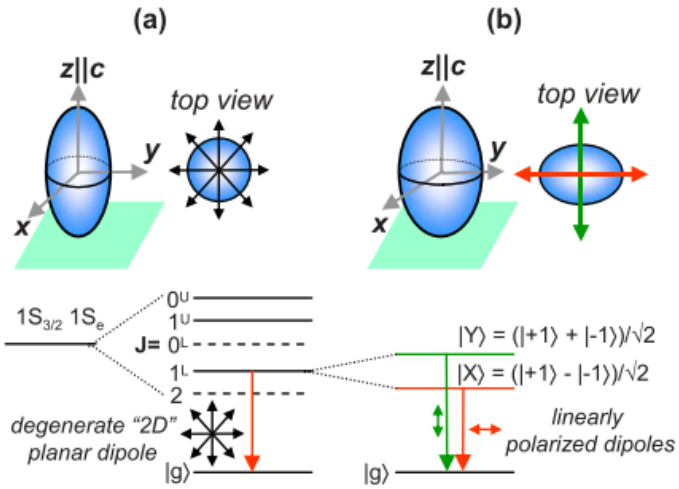

Figure 1-18. Polarization of $\pm 1^{L}$ transition in fine structures. Adapted from ref. [78]. The main elongation axis z is parallel to the c-axis of the crystalline lattice. In case (a), the nanocrystal cross-section is circular, while in case (b) an additional elongation occurs along axis y.

The states -1^{L} and -1^{U} emit polarized photons σ^{-}, while the states $+1^{L}$ and $+1^{U}$ emit polarized photons σ^{+}. As a result, each $\pm 1^{L}$ and $\pm 1^{U}$ state emits both σ^{+} and σ^{-} photons incoherently. When the structure of the nanocrystals have cylindrical symmetry, the emission results from a degenerate dipole ("2D dipole" in figure 1-18 (a)) oriented isotropically in the plane normal to the crystal axis. Alternatively, in the case of broken symmetry (figure 1-18 (b)), anisotropic

exchange will mix the ± 1 state, leading to two incoherent orthogonal dipoles ($|X\rangle$ and $|Y\rangle$ transitons) with linear polarization. In addition, for the other allowed transition 0^U, we will obtain π photon, which corresponds to a linear dipole polarized along the c-axis of the crystalline lattice.

Dielectric Effects

Since CdSe NPLs have a much larger refractive index compared to the surrounding environment, the electrical field inside the NPLs will be attenuated with respect to the external field in the outside. As a consequence, the absorption and emission will be modified, and the electric field along the nanoparticle elongation axes will be enhanced with respect to the shorter axes. This effect can be calculated analytically for an ellipsoid: a and b are the lengths along the long (x) and short (y) in-plane axis of NPLs and c is the length along z direction normal to the NPL plane. In this model the projection of inside electric field E_α^{in} and outside field E_α^{out} of the NPL can be expressed as [85]:

$$E_\alpha^{in} = \frac{E_\alpha^{out}}{1+n^\alpha(k-1)} \tag{1.30}$$

where $k = \frac{\epsilon_{in}}{\epsilon_{out}}$ is the ratio between the dielectric constants of the NPL (ϵ_{in}) and the surrounding medium (ϵ_{out}), and n^α is so called the depolarization factor along the direction $\alpha = x, y$ or z, which can be obtained by [86]:

$$n^\alpha = \frac{abc}{2}\int_0^\infty \frac{ds}{(s+\beta^2)\sqrt{(s+a^2)(s+b^2)(s+c^2)}} \tag{1.31}$$

with $\beta = a, b$ or c and $n^x + n^y + n^z = 1$. Different n^α results in anisotropic local fields in x, y and z direction of NPLs depending on the asymmetry of the dielectric shape. To compare the reduction of electric field, we can estimate the electric field screening factor, D^α, which is defined as [87]:

$$D^\alpha = \frac{E_\alpha^{in^2}}{E_\alpha^{out^2}} \tag{1.32}$$

Thus, the anisotropy in a dielectric structure can be directly related to the polarization of optical transitions. If we take our single NPL samples ($a = 20$ nm, $b = 7$ nm and $c = 1.5$ nm) as an example and numerically calculate the integral, we find $n^x = 0.165$, $n^y = 0.285$ and $n^z = 0.55$, from which we obtain $D^x = 0.50$, $D^y = 0.34$ and $D^z = 0.18$. This indicates that the dipole is more suppressed in the direction vertical to the NPL plane ($D^z/D^x = 0.36$), as compared to the effect in

the lateral dimension ($D^y/D^x = 0.68$). Then we can do the same calculation for a NPL chain ($a =$ 20 nm, $b = 7$ nm, $c = 1000$ nm and ϵ_{in} is the average of NPLs and ligand layers) and we end up with $n^x = 0.39$, $n^y = 0.55$, $n^z = 0.06$ and $D^x = 0.89$, $D^y = 0.85$ and $D^z = 0.98$, which suggests that the dipole strength will be slightly enhanced ($D^z/D^x = 1.1$) by the stacking of the dielectric structure. A more elaborate discussion of this effect will be performed in chapter 4 by numerical electromagnetic simulation.

Auger recombination

Auger recombination is a non-radiative recombination mechanism that plays an important role in all the excitonic processes, including blinking, decay and antibunching in semiconducting nanocrystals. It is a Colombian interaction mechanism between more than 2 charges, where an electron-hole pair recombines by yielding its energy to the other charge(s). Alternative to radiative recombination mechanisms, in Auger recombination process, the lost excitonic energy will not result in emission of the affiliated energy as a photon, but will be transferred to the extra electrons or holes in the emitter, promoting them into higher energy states from which they then thermalize back to the ground excitation state, losing this energy to phonons (figure 1-19). Auger effect is significantly more efficient in nanocrystals as compared to bulk semiconductors, because of the general volume law [88]: the efficiency of Auger effect is enhanced in smaller volume.

In optoelectronics, Auger effect is often detrimental: for nanocrystal lasers, non-radiative Auger recombination will reduce optical gains [89,90]; for solar cells, it will quench the carriers before they are transferred to electrons/holes extraction layers [91]; for LEDs, Auger effect will reduce the emission efficiency [92]. In addition, Auger effect can also be profitable in some other applications such as single photon source [93], as it favors anti-bunched emission (as will be explained in chapter 3), which is critical for quantum computing and quantum information technologies.

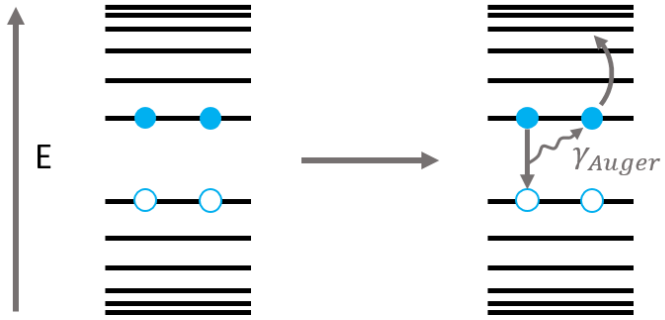

Figure 1-19. Schematic of Auger effect.

1.3 Micro-photoluminescence

Micro-photoluminescence setup

We use a homebuilt inverted fluorescence microscope, combined with different detection components, to conduct the optical measurements on single NPLs or single assembled NPL chains.

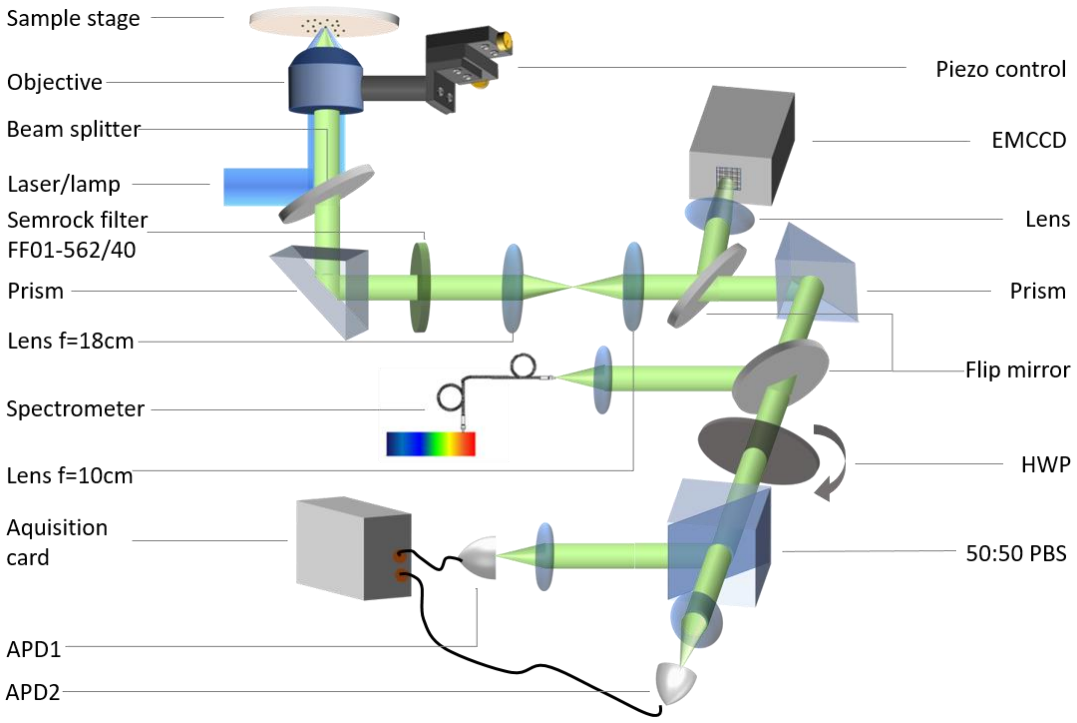

Figure 1-20. Micro-photoluminescence setup. EMCCD: electron multiplying charge coupled detector. HWP: half wave plate. PBS: polarizing beam splitter. APD: Avalanche photodiode.

This setup was initiated in 2013 by Feng Fu during his thesis directed by Laurent Coolen. It uses a diode laser and a mercury lamp as excitation sources, and a same objective to focus the excitation beam on the sample and collect its emission. The objective is mounted on a piezo-electronic stage, which can be controlled by software to scan the laser on the demanded area of the sample. As for the detectors, a monochromator (Triax 190 @Horiba) can work either in image plane mode or Fourier plane mode in cooperation with a flip Fourier lens. A time-correlated single photon counting (TCSPC) system (which will be introduced in chapter 3) of two avalanche photodiodes combined with a PicoHarp acquisition card, is also established for decay curve measurements with 500 ps characteristic time of the total system response function.

During this thesis, this setup was further improved:

1) Polarization microscopy: the polarization effects induced by the optical elements in the setup were characterized and corrected, in order to maintain the intrinsic polarization property of the emission from samples. We found that the dominant sources of diattenuation (different attenuation along the x and y axes) and dephasing (phase difference between the x and y axes) are respectively the beam splitter and the prisms, and we managed to correct these effects by adding proper compensation elements (note that here we use prisms instead of mirrors because practically we find it is easier to achieve satisfactory compensation). This development draws on the PhD work of Nguyen Thu Loan (advisor Agnès Maître) in our group on polarization corrections on a similar setup [94]. More details of setup characterization will be given in appendix A.

To evaluate the performance of the polarization-effect-corrected setup, fluorescent polymer spheres (Thermo Fisher, 200nm, 580-605 nm emission) were used as a reference emitter, the emission of which is non-polarized. As a result, a degree of linear polarization of 0.03 was measured for the microsphere emission, while an average degree of circular polarization of 0 was measured, with fluctuation in the range of ±0.02. Besides, when introducing a polarizer below the objective to fully polarize the emission, a 0.99 degree of linear polarization was obtained. We thus conclude that the emission polarization was preserved by the setup with 1-3 % precision.

In this thesis, the degree of linear polarization of NPL's emission will be analysed in chapter 4. Linear and circular polarization analyses can be performed by introducing a polarizer before the detector (spectrometer or EMCCD) and respectively rotating a half-wave plate or comparing the +45° and -45° positions of a quarter-wave plate before the polarizer.

2) Fourier plane imaging: to investigate the radiating transition dipole, Fourier plane imaging is a powerful tool, which allows access to angular resolved information (radiation diagrams) of the emitter. In addition to the Fourier imaging mode of the spectrometer established by Feng Fu, here we also implemented a Fourier imaging system by conjugating the back focal plane of the objective onto an EMCCD to record the Fourier plane image with better resolution and better efficiency, so that the precise analysis can be achieved on single nano emitters. More technical details and analytical calculations will be elaborated in chapter 4.

3) The imaging system was also improved to achieve a larger magnification on the CCD camera by modifying the lens system on the setup. Larger imaging magnification provides better resolution in imaging-based studies of energy transfer (exciton diffusion) in self-assembled chains of NPLs, which will be demonstrated in chapter 2.

Cryogenic setup

Apart from the room temperature measurements, we can also combine our micro-photoluminescence setup with a helium-flux cryostat (Oxford, HiRes II) to perform low temperature analysis (figure 1-21). Samples are glued on the cold finger of the cryostat by silver lacquers. We pump helium flux into the cryostat and, in case of a perfect thermal conductivity between the cold finger and the emitters, the lowest temperature that can be reached is ~4.5 K. The flux of helium is monitored by a flux meter and the temperature of the cold finger can be tuned by a heating controller.

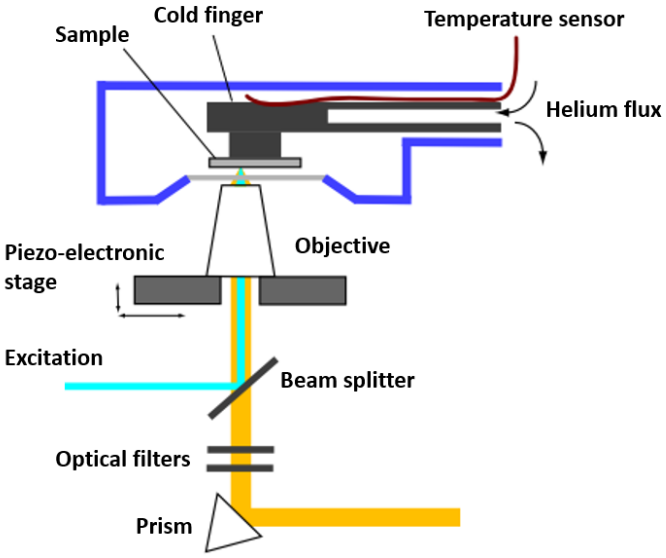

Figure 1-21. Illustration of the cryogenic setup consisting of a cryostat and a fluorescence microscope. Adapted from ref. [95].

General processes of microscopic study of single emitters

To conduct a microscopic study of single nano emitters, we first use the mercury lamp to achieve a wide field excitation and use the CCD camera (QImaging Retiga EXi, pixel size 6.45 µm correspondent to 72nm on the image) for detection. A same objective, mounted on a piezo-electric stage, is used to focus the excitation light on the sample plane and to collect its emission as well. We can also change the excitation source for a 470-nm diode laser beam (PDL 800-D PicoQuant, 70-ps pulses, 2.5-MHz rate) to either scan the area of interest to locate the single emitters or to achieve a localized excitation on a single nano emitter, with the help of the piezo-electric stage control. The back-scattered excitation light is cut by a set of filters and only the fluorescence light can reach the detectors, which can be 1) the CCD camera for image analysis, 2) the EMCCD for angular resolved Fourier plane imaging, 3) the Avalanche photodiode (APD) for time correlated single photon analysis or 4) the monochromator for angular resolved or regular spectroscopy.

Chapter 2. Long range energy transfer in self-assembled nanoplatelets

Introduction

In this chapter, our study will focus on Förster resonance energy transfer (FRET), an important physical effect that is of great importance for both fundamental research and applications. By micro-photoluminescence and imaging analysis, we will demonstrate a long-range excitonic energy transfer in self-assembled chains of CdSe nanoplatelets, of which the diffusion length is 500 nm (corresponding to energy hopping over ~90 platelets), 20 times longer than other reported results in semiconducting nanoparticle systems. In order to estimate the time of FRET transfer between neighbour nanoplatelets, we will develop a diffusion model to relate the migration length to the transfer rate, from which we obtain a result of $(1.5\ ps)^{-1}$. This rate is faster than any other excitonic mechanisms known to occur in fluorescent semiconductor nanoparticles, such as radiative recombination, Auger recombination and non-radiative quenching. Consequently, the behaviour of collectively assembled emitters is expected to present new photophysical behaviours mediated by FRET, other than simple averaging effects.

In the first section of this chapter, we will give a general introduction of the fundamentals of FRET, the relevant notions and calculations. We will also review the literature and introduce briefly the state of the art of the FRET in assembled semiconductors or in other systems. Then we will introduce our analysis protocol combining the linear self-assembly of CdSe nanoplatelet chains and micro-photoluminescence.

In the second section, we will first show the imaging result, i.e. elongated fluorescence from platelet chains under localized excitation. Then we will characterize the imaging system to analyse the excitation distribution and the point spread function, in order to obtain the system-response-corrected fluorescence pattern of single nanoplatelet chains by deconvolution. After that, we will calculate the energy migration length and also check the possibility of non-linear effects.

In the third section, we will demonstrate numerically and experimentally that the waveguiding effect is very weak on our chains. Then, we can attribute our observations of the elongated fluorescence to FRET.

In section four, a diffusion model will be developed, which can relate the FRET rate to the energy migration length. We will then deduce the FRET rate and compare it to other excitonic mechanisms known to occur in fluorescent semiconductor nanoparticles, and we expect a strong FRET mediated photo-physics in assembled emitters as compared to non-assembled individual ones.

Finally, in section five, we will finish this chapter by conclusion and perspectives.

2.1 Introduction of FRET

2.1.1 FRET effects

Förster resonance energy transfer (FRET) was first described by Theodor Förster in 1946 [96]. It has now become an important phenomenon attracting considerable interest for not only fundamental research in many aspects such as biochemistry and molecular cell biology, but also for applications including artificial light harvesting devices, biomedical sensing and optoelectronic technologies.

Basics of FRET

FRET concerns very fast short-range interaction between nano-emitters. As shown in figure 2-1, FRET process involves an excited donor emitter which could transfer its energy non-radiatively to a neighbouring acceptor emitter generating a new exciton (instead of recombining by either radiative or nonradiative ways on itself). In Förster's theory, donor and acceptor are assumed as oscillating electrical dipoles and the energy is transferred by dipole-dipole Coulombic interaction [97].

FRET is an effect with distance-dependent efficiency. We can define this efficiency η, which represents the probability of an excited donor to de-excite by transferring its energy to a neighbour acceptor, as [98]:

$$\eta = \frac{\gamma_{tr}}{\gamma_{tr}+\gamma_0} \tag{2.1}$$

in which γ_{tr} is the rate of energy transfer between the donor and the acceptor and γ_0 is the overall decay rate in the donor alone, including radiative or non-radiative paths.

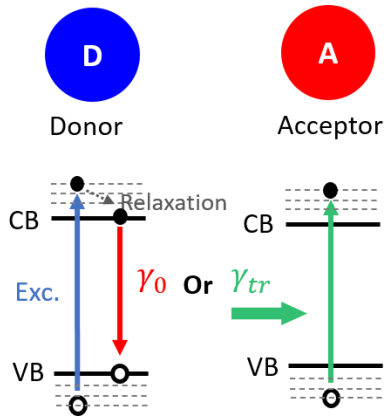

Figure 2-1. Diagram of FRET.

To analyse the efficiency as a function of the distance between the donor and the acceptor, Förster gave the following equation:

$$\eta = \frac{1}{1+(R/R_F)^6} \tag{2.2}$$

in which R is the distance between donor and acceptor and R_F is called 'Förster radius' referring to the separation distance at which the energy transfer efficiency is 50%. The Förster radius can be calculated by:

$$R_F{}^6 = \frac{9c^4\kappa^2}{8\pi}\int_{\omega=0}^{\infty}\frac{f_D(\omega)\sigma_A(\omega)}{n^4(\omega)\omega^4}d\omega \tag{2.3}$$

where n is the refractive index of homogeneous surrounding medium; $f_D(\omega)$ is the emission spectrum of the donor normalized by integral $\int f_D(\omega)d\omega = 1$; $\sigma_A(\omega)$ is the absorption cross section of the acceptor and $\int_{\omega=0}^{\infty}\frac{f_D(\omega)\sigma_A(\omega)}{n^4(\omega)\omega^4}d\omega$ is defined as the spectral overlap integral J. The orientation factor, κ^2, is calculated by:

$$\kappa^2 = \left(\overrightarrow{n_A}.\overrightarrow{n_D} - 3(\overrightarrow{n_R}.\overrightarrow{n_D})(\overrightarrow{n_R}.\overrightarrow{n_A})\right)^2 \tag{2.4}$$

with $\overrightarrow{n_R}$ the unit vector from the donor to the acceptor, and $\overrightarrow{n_A}$ (resp. $\overrightarrow{n_D}$) the dipole orientation of the donor (resp. the acceptor). Depending on the orientation and the location of the donor and the acceptor, one can obtain κ^2 ranging from 0 to 4, as shown in figure 2-2.

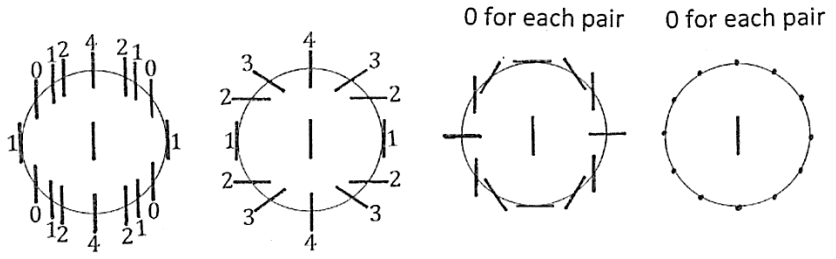

Figure 2-2. Examples of κ^2 values corresponding to different cases in which the donor dipoles locate in the center of the circle and the acceptors are along the circumference. Adapted from ref. [99].

Then, we can calculate the FRET rate from the donor to the acceptor by:

$$\gamma_{tr} = \gamma_0 \left(\frac{R_F}{R}\right)^6 \tag{2.5}$$

in which γ_0 is the overall recombination rate of the donor in the absence of the acceptor.

From the above formulas, we can know that FRET could be efficient when the following conditions are met:

1) Donor and acceptor emitters are located close from each other (less than R_F);

2) The emission spectrum of the donor overlaps the absorption spectrum of the acceptor.

3) The orientations of the donor and the acceptor are such that κ^2 is not zero.

Hetero-FRET and homo-FRET.

Hetero-FRET, as has been shown in the above-presented schematic, is the case in which the acceptor and the donor belong to two distinct populations of emitters. The donor's emission spectrum must overlap with the acceptor's absorption spectrum so that energy can be transferred from the donor to the acceptor (but not the reverse). Hetero-FRET has been investigated more widely than homo-FRET, because the former case is straightforward and convenient to be verified and analysed in assistance of optical filters, thanks to the different emission wavelengths of the donor and the acceptor.

There are many ways to evidence hetero-FRET. One of the simple methods is to analyse the sensitized emission (SE) spectrum, in which the donors are pumped and the emission of both the donors and the acceptors are detected. As a result, the emission intensity of the donor (resp. acceptor) will decrease (resp. increase) in the donor-acceptor mixture comparing to the case without the presence of acceptors (resp. donors). Similarly, one can achieve the same purpose by swiping the

excitation wavelength at the range in which the donor has a strong absorption. It is expected that the PLE spectrum of the acceptor emission is similar to the donor's absorption spectrum. Another widely employed technique to analyse hetero-FRET effect is time-resolved fluorescence emission measurements: the decay rate of the donor will be accelerated in donor-acceptor mixture, because the presence of the acceptor opens an additional decay channel.

Unlike hetero-FRET, homo-FRET involves the donor and the acceptor which belong to the same emitter population with their absorption spectrum overlapping with their own emission spectrum thanks to a small Stokes shift. Thus, when these emitters are located very closely or get assembled, it is possible to have energy transfer between them, similar to hetero-FRET but the energy transfer is reversible. Figure 2-3 presents the homo-FRET process in a simple model of 1-dimensional chain of particles, with an energy transfer rate of γ_{tr} and a diffusion length (i.e. the excitonic energy migration length) l_{FRET}.

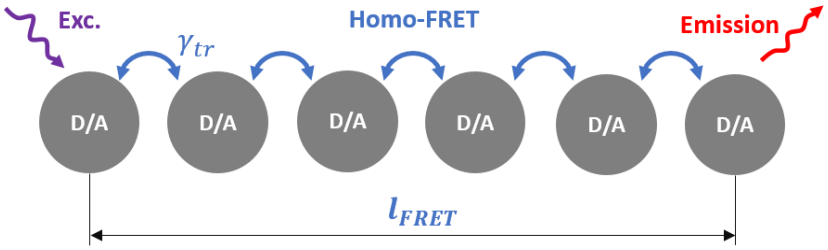

Figure 2-3. Schematic of homo-FRET diffusion in a 1-dimensional chain of particles.

Compared to hetero-FRET, analysing homo-FRET is more complicated. The aforementioned methods to detect hetero-FRET are not very applicable for homo-FRET: the spectra of the donor and the acceptor are not distinguishable and their decay dynamics are not affected by homo-FRET because the general emitter population does not decay through FRET (although some very indirect effect of FRET can affect the decay, as will be elaborated later in chapter 3).

However, there are still few ways to probe homo-FRET effect. One example is that, for the case of closely packed colloidal quantum dots film, the downhill funnelling of the excitons within the inhomogeneous broadened density of states in the QDs will result in a redshift in the emission spectra, which is commonly observed as a signature of homo-FRET [16].

Nevertheless, in our case of assembly of nanoplatelets, we cannot expect this redshift signature, because there is a negligible inhomogeneous broadening of the emission spectrum: the emission wavelength is determined solely by the vertical confinement with very little contribution from the

lateral confinement, because of their highly anisotropic shape; NPL's thickness is controlled with atomic layer precision so that the dispersion of single-platelet emission wavelength is less than 2 nm (figure 2-4). As a result, homo-FRET is difficult to evidence between nanoplatelets. In fact, the current study of FRET rate and diffusion length for nanoplatelets as well as other kinds of nano emitters are not well explored yet: mostly the FRET rate and length are theoretically calculated based on the result of lifetime estimation, with less direct support from the experimental demonstration.

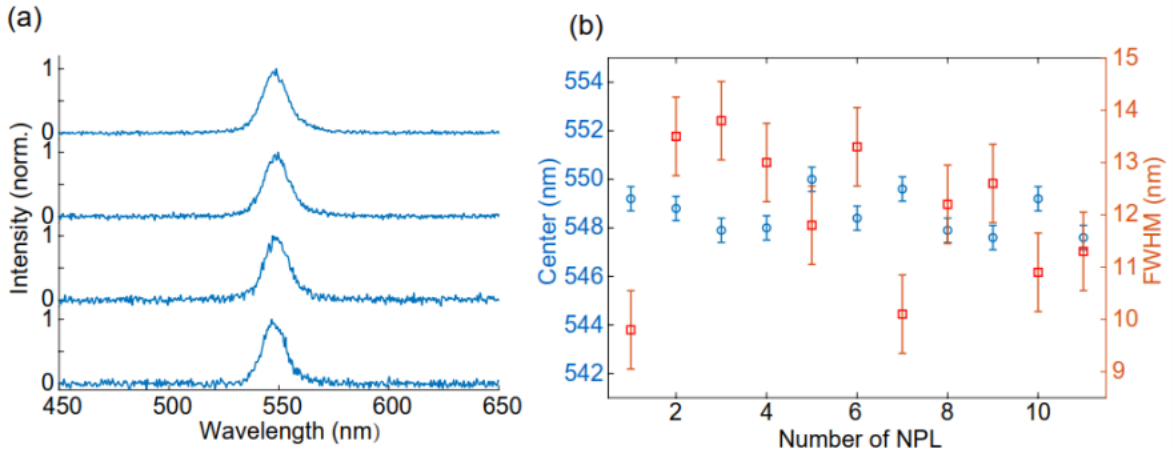

Figure 2-4. (a) spectra of 4 single nanoplatelets. (b) Emission wavelength and peak FWHM of 11 single nanoplatelets.

In the next subsection, we will give an overview of the literature about studies of FRET rate and FRET diffusion length and show the state of the art of FRET effect study on CdSe nanoplatelets.

2.1.2 State of the arts: FRET and other transfer mechanisms

In the literature, various methods were developed for the delicate characterization of FRET exciton migration [100] and the migration length has been reported to 20-30 nm for dense films [101,102] as well as clusters [103] of nanocrystals. Theoretical calculation of FRET length based on lifetime analysis is reported to be 133 nm [16] for nanoplatelets.

In other systems like in molecular or polymer, migration by FRET hopping was generally demonstrated over a few tens of nanometers [104,105,106]. Longer energy transfers distances of hundreds of nanometers or several microns have been reported by many groups under different mechanisms other than FRET, such as 1) Dexter hopping and coherent exciton motion [104,107,108]; 2) by a combination of coherent and incoherent exciton motion in the case of J- and H-aggregates [109,110]; 3) plasmon-mediated transfer along metal nanowires [111,112].

Many researchers have studied FRET rate both experimentally and theoretically in systems of semiconducting nanocrystals and yielded hopping rates ranged from tens of picosecond scale [113,114] to nanosecond scale [100]. The fastest observation of FRET rate is reported by Rowland et al., who demonstrated hetero-FRET times of 6−23 ps [15] in binary (i.e. mixture of 4-monolayer and 5-monolayer) nanoplatelet films. Guzelturk et al. developed a model of stacked NPLs with the presence of trapping sites and estimated theoretically that the FRET rate is in the range of $(23.8\ \text{ps})^{-1}$ and $(3.0\ \text{ps})^{-1}$ [115], in good agreement with Rowland's observation.

Energy transfer between nanoplatelets and other materials have also been studied. As an example, in ref. [116], it is shown the energy transfer rate from CdSe/CdS nanoplatelets to MoS_2 could be as fast as ~ $(4\ \text{ps})^{-1}$. In ref. [117], Hernández et al. showed theoretically that the distance dependence of the FRET rate depends on the geometry and dimensionality of the acceptor and on the effective dielectric constant of the donor. For NPLs, the distance dependence is calculated to be $1/d^4$ instead of $1/d^6$ for point-like quantum dots.

Besides, temperature dependent FRET behaviour has also been studied in the literature [118]: FRET efficiency is reported to linearly increase as temperature is decreased which is attributed to the increasing photoluminescence and quantum yield of the donor QDs at low temperatures.

2.1.3 Motivations

It is crucial to fundamentally understand the exciton coupling and collective behaviour in nanocrystals, which is of great importance in the optoelectronic applications involving density packed semiconductor nanoparticles such as quantum dot laser [35,119], light-emitting diodes (LED) [38,39] and quantum dot sensitized solar cells [98]: FRET may be detrimental by transferring excitonic energy to quenching sites, but it can also favour efficient charge collection and lead to new FRET-enabled excitonic devices.

However, as introduced, the collective photo-physical behaviours of packed quantum dots, dominated by FRET effect, are not yet clear. There is a general difficulty in the characterization of FRET, especially for homo-FRET in case of a film of similar nanoplatelets, because optical methods like decay curves analysis provide only ambiguous indirect information [16]. FRET rate cannot be directly extracted from this, which is why the previous study in the literature working on the decay of particle assemblies reported mostly only a theoretical estimate of the FRET rate based on the decay

curve of emitters. Besides, a clear demonstration of longer-range FRET is desired, which is currently limited in literature by a lack of highly controlled order of assembly [120].

To demonstrate longer range FRET and properly deduce the FRET rate, we use a combination of the self-assembly of CdSe nanoplatelets and micro-photoluminescence to directly image FRET energy migration, from which we can deduce the exciton transfer rate.

Nanoplatelets constitute a very interesting system for homo FRET study. As has been discussed in chapter 1, they have many optical characteristics that make them prone to FRET as compared to spherical QDs: their oscillator strength is large [5]; their Stokes shift is very low and their emission and absorption spectra overlap; their flat surface permit close stacking with very well controlled orientation; they have 2 orthogonal in-plane transition dipoles [29, 121] and when stacked co-facially, their transition dipoles are parallel, guaranteeing efficient dipole-dipole interactions.

Although there are many reports by other groups focusing on energy transfer in either clusters or a solid film of NPLs as aforementioned, the NPLs are usually assembled disorderly or with only a very short order range below 100 nm. Because of the random orders of donor and acceptor in these samples, the FRET efficiency is dramatically limited [120]. Thanks to B. Abécassis' pioneering work on linear NPL self-assembly, we possess well aligned co-facially stacking samples with good quality (bright emission revealing high quantum yield and less defects). In these co-facially stacked NPLs chains, homo FRET efficiency is expected to be exceptionally high because the center-to-center separation distance between neighbour NPLs (here labelled as δ) is short and the orientation of stacked NPLs are parallel to each other [8,70,71] while this well-ordered assembly can be as long as over micrometre scale.

Therefore, in this chapter, we will take advantage of both our expertise of single emitter analysis and the high-quality samples of CdSe NPLs self-assembly to perform analysis on single NPLs chains, in order to obtain FRET length and then to extract the FRET rate. To the best of our knowledge, this kind of imaging experiments will be the first report on the luminescence of single NPL chains (although B. Abécassis has briefly imaged bundles of chains in ref. [69]), which will give us interesting information to deepen our understanding of the photo-physics mediated by the FRET effect.

2.2. Imaging studies of energy migrations in NPLs chain

In this section, we will present the result of imaging of self-assembled chains of nanoplatelets under localized excitation by a focused laser beam. We will characterize the imaging system to analyse the excitation distribution and the point spread function, in order to reveal the system-response-corrected fluorescence pattern of single nanoplatelet chains.

2.2.1 Demonstrations of elongated fluorescence in CCD images

Experiments are performed on a homebuilt inverted fluorescence microscope, equipped with a laser scanning system (as shown in figure 1-20 in chapter 1). The excitation source could be either a mercury lamp (with bandpass filter at 330-480 nm) for wide field excitation, or a 470 nm diode laser (PDL 800-D @PicoQuant) for localized excitation, which provides 70-ps pulses at variable repetition rate. Combined with a piezo controlled stage, the laser spot can scan on samples or excite specifically the site of interest, which enables the study of individual emitters.

In the image measurement, the laser provides excitation with power of about 5 nW, which ensures the linear excitation regime (details will be given in the later section). A same objective (Olympus super-corrected apochromat 100X 1.4 N.A.) is used to focus the excitation beam on the sample and to collect the fluorescence. A set of Semrock filters (488 nm long-pass and 562/40 nm bandpass filters) are employed to remove the excitation in the collected beam. The detection is conducted by a QImaging Retiga EXi CCD camera, with a pixel size of 6.45×6.45 μm^2. The imaging magnification was about 90X so that the size of each pixel on the camera image corresponds to 72 nm on the actual sample plane.

In figure 2-5, upper and lower panels show the CCD images for three different NPL chains excited by mercury lamp (wide field excitation) and laser spot (localized excitation), respectively. Under wide field excitation, the fluorescence pattern from these different chains are about 1.5-2 μm in length, in agreement with the electron microscopy image figure 1-10 (b) in chapter 1, showing that the spin coating deposition preserved the chain structure. In the laser excitation images, the laser spot is positioned in the middle of the chains and the size of the laser spot, which will be carefully characterized later, is represented by the white circles. Thus, if no energy migration occurs within the NPL stacks, only a limited area of laser-spot-size would be luminescent. However, we detected, for all the chains considered, fluorescence from an elongated 1-μm to 1.5-μm portion that extended far beyond the spot of the excitation laser.

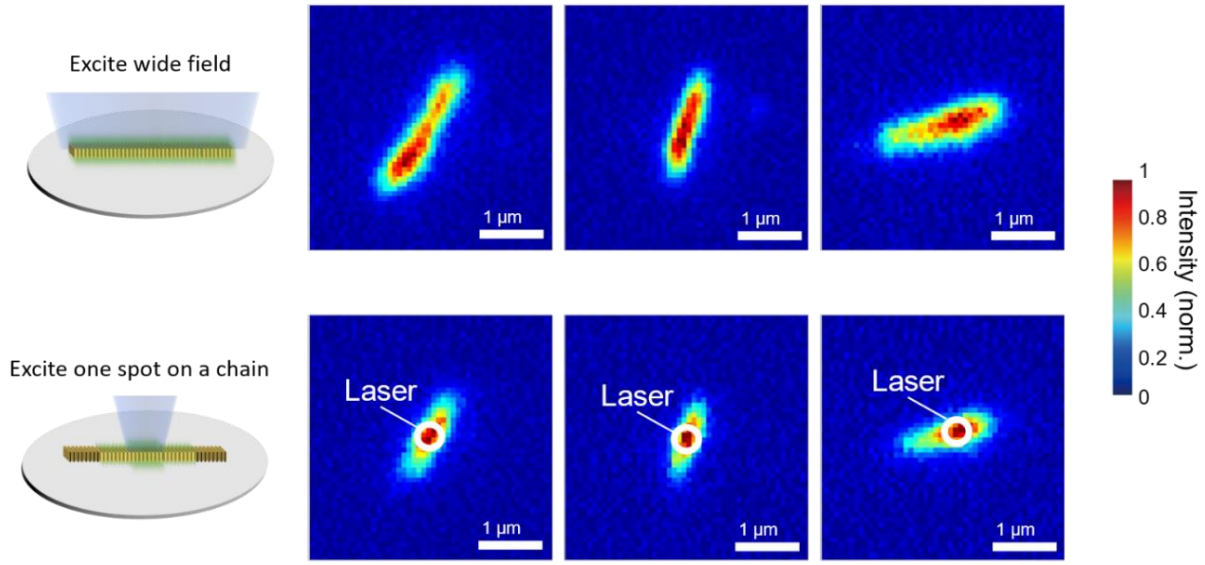

Figure 2-5. Images of three platelets chains under wide field excitation (upper panels) and excited locally by a laser spot (lower panels).

Part of this elongation can be attributed to the system's response function l_{RF}, which is a convolution of the excitation laser spot size l_{laser} and the point spread function of our imaging system l_{PSF}. In the next subsection, we will characterize these two constituents of the resolution error and deduce the resolution-corrected energy migration length.

2.2.2 Characterization of the imaging system

Point spread function (PSF) of the imaging system

To study the point spread function of the system, single non-stacked NPLs are employed as a reference since they can be considered as point-like emitters with negligible dimension (20×7 nm²) and with emission wavelength at 550 nm, same as that of the stacked NPLs samples. We use the mercury lamp to excite single NPLs and record their fluorescence images. Since the nanoplatelet's size is negligible, the corresponding image is a probe of the point spread function (PSF).

An example of PSF image is shown in figure 2-6 (a). In the up and right panels aside the CCD image, we plot the cross-section profiles along two cutting lines, which are fitted by Gaussian functions $I \propto e^{-(x/l_{PSF})^2}$ in which l_{PSF} is the $1/e$ Gaussian half-width. The fitting results give a distribution of PSF with an average value of half-widths of about 190 nm and with a dispersion of 20 nm, as shown in the histogram in figure 2-6 (b). Herein, we find the point spread function of the imaging system to be a Gaussian function with $l_{PSF} =$ 190 nm.

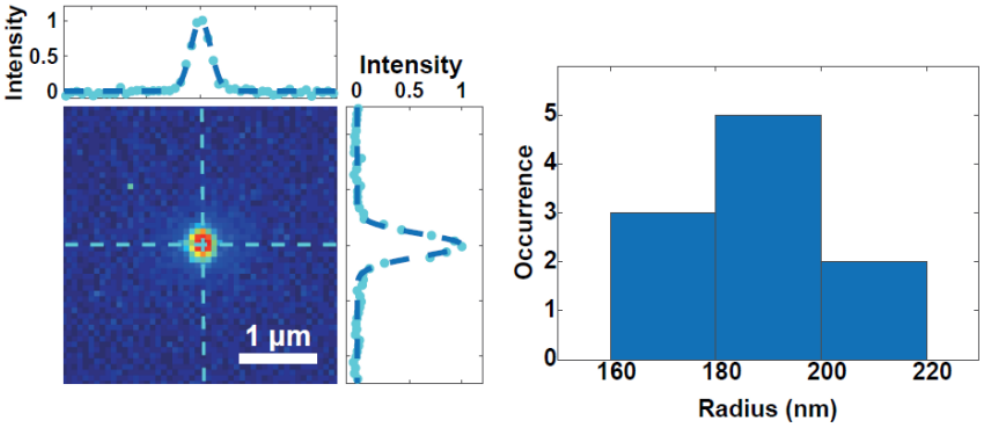

Figure 2-6. Left: image of a single NPL under wide field illumination on the camera. Profiles of longitudinal and lateral cutting lines are plotted in upper and right panels in which the bright light dots are raw data and the dashed blue lines are Gaussian fitting. Right: histogram of point spread function radii l_{PSF}.

Analysis of excitation laser spot sizes

In addition to the PSF of the imaging system, the size of the laser spot will directly affect the analysis of the FRET length as well, because, in the absence of energy migration, the fluorescence of an emitter chain will still show an elongation related to the area of laser excitation, especially if the laser spot is much larger than the transversal width of the NPLs chain. In order to know the laser excitation distribution, we can reconstitute the original laser spot size from laser scanning images of single NPLs, which are again assumed to be a point-like emitter with negligible dimension.

Figure 2-7 presents the result of laser scanning image analysis. Same as for PSF analysis, we use Gaussian functions to fit the lateral and the vertical cutting-line profiles and the statistical results show that our laser spot is l_{laser} =157 nm in radius.

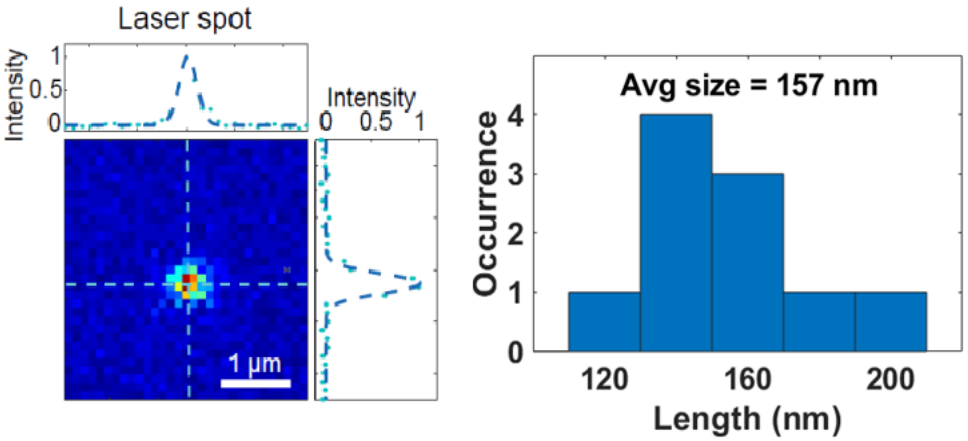

Figure 2-7. Left: confocal microscopy scan of a single nanoplatelet (scanning step 100 nm); Right: histogram of laser spot radii l_{laser} obtained by this method.

Now we can calculate the response function of the excitation and detection systems in the imaging analysis. If we consider the NPLs chain as a one-dimensional line with a long-enough longitudinal length along x-axis and zero transversal width along y-axis, the excited nanoplatelet emitters (within the linear excitation regime) along the chain will give emissions with intensity proportional to the distribution of laser excitation intensity. In the absence of the energy migration, the original emission distribution I should scale as $I \propto e^{-(x/l_{lasr})^2}$ with all NPL emitters along x axis, within a typical range l_{laser} from the center of the laser spot. The image of these emitters is convolved by the system's point spread function in both x and y directions so that the final image scales as:

$$I \propto e^{-(y/l_{PSF})^2} e^{-x^2/({l_{laser}}^2+{l_{PSF}}^2)} \tag{2.6}$$

Eventually, we expect that the transversal profile of the NPLs chain has a width equivalent to l_{PSF} = 190 nm. For longitudinal profile, if there is no energy migration within the chain, the profile along the chain has a length caused by the overall response function that is a combination of the laser spot size and the imaging PSF:

$$l_{RF} = \sqrt{{l_{laser}}^2 + {l_{PSF}}^2} = 246 \text{ nm} \tag{2.7}$$

We can confirm this deduction of total response function by characterizing the laser beam reflection profile: we remove the filter for the excitation beam so that the laser beam at 470 nm can be imaged directly by the CCD camera and the results are as shown in figure 2-8. The histogram presents an average radius of laser spot of 214 nm, which is in fact the total system response function of the laser beam with wavelength at 470 nm (l_{RF_470}= 214 nm). Considering Rayleigh's theory $R_1 : R_2 = \lambda_1 : \lambda_2$, we can calculate that the total system response function of the light at 550 nm l_{RF_550} is:

$$l_{RF\_550} = l_{RF\_470} \times \frac{550\,nm}{470\,nm} = 250 \text{ nm} \tag{2.8}$$

which is in great agreement with the convolution of result ($l_{RF} =$ 246 nm).

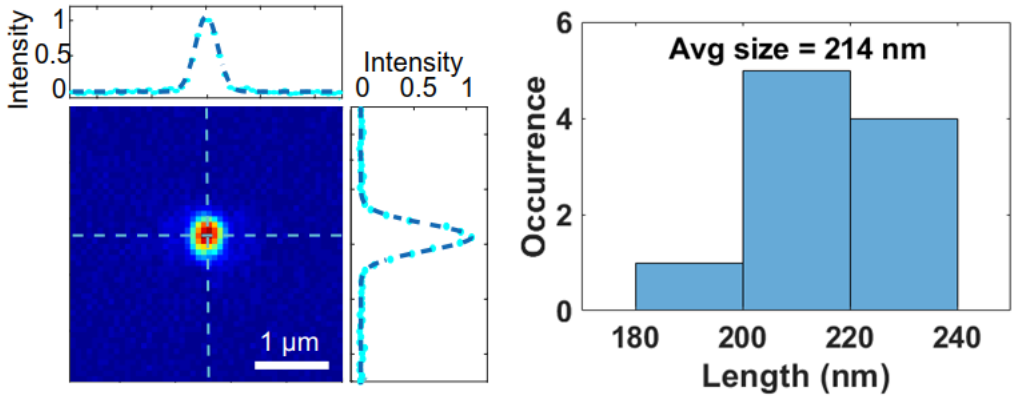

Figure 2-8. Left: Reflection image of the laser spot profile on the camera (pixel size 72 nm on the sample); Right: histogram of laser spot radii.

Since the previously observed elongated fluorescence length on the nanoplatelet chain (figure 2-5) is much larger than the characteristic size of system's response function l_{RF} (256 nm), we demonstrated that there is indeed an energy migration along the chain. In the following subsection, we will analyse the elongated fluorescence images in details and deduce the resolution-corrected energy migration length with consideration of the system's response function.

2.2.3 Studies of the energy migration length

Figure 2-9 (b) describes the fluorescence of a single chain of stacked NPLs under localized excitation (figure 2-9 (a)). We take the cross-section profiles along longitudinal axis (green dashed cutting line) and transversal axis (orange dashed cutting line) and plot them in up and right panels aside the image, respectively. Like before, the raw data (yellow and bright green dots in the panels) are fitted by Gaussian functions (orange and dark green dashed lines) and the 1/e Gaussian half-widths are extracted as shown in the histograms.

From the orange histogram, it can be seen that the average transversal width ($l_y =$ 196 nm) of the stacked NPLs thread is in great accordance with the PSF of the imaging system ($l_{PSF} =$ 190 nm). Then we analyse the radius of the longitudinal profile and we find an average length $l_x =$ 564 nm while the minimum and maximum widths are 470 nm and 720 nm respectively. This relatively large range of variation can be attributed to the different quality of NPLs assembly including the random existence of defected and twisted NPLs. The standard deviations of the measured l_x and l_y values are 86 nm and 12 nm, respectively.

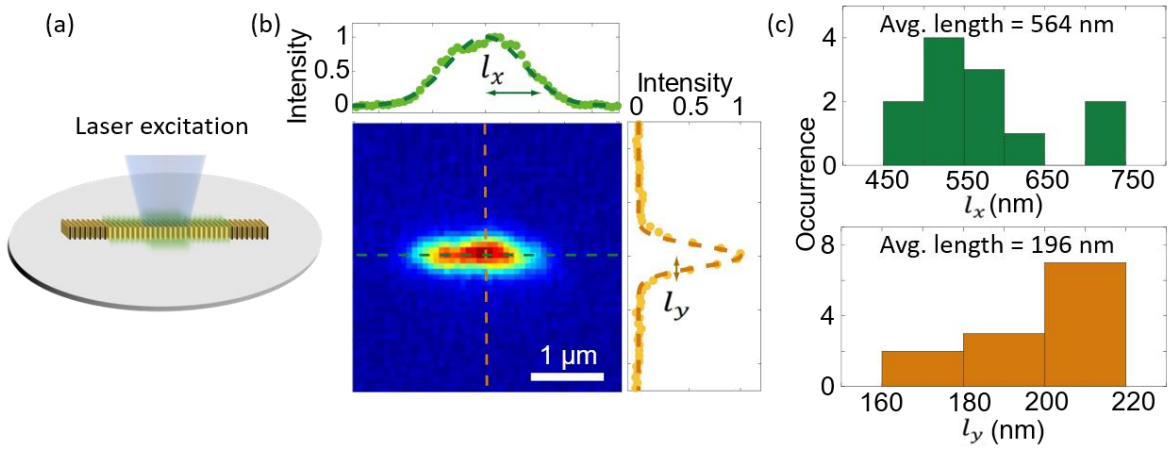

Figure 2-9. (a) Schematic of localized excitation. (b) fluorescence image of a typical NPLs chain under 5 nW excitation (dots: experimental profiles; dotted lines: Gaussian fits). (c) Histograms of the fitted l_x and l_y longitudinal and transverse widths for 12 chains.

The longitudinal length l_x in the image is in fact the convolution of energy migration length l_{FRET} and the total system response function l_{RF}. Therefore, to extract the energy migration length, we extract the deconvolution as:

$$l_{FRET} = \sqrt{{l_x}^2 - {l_{RF}}^2} \tag{2.9}$$

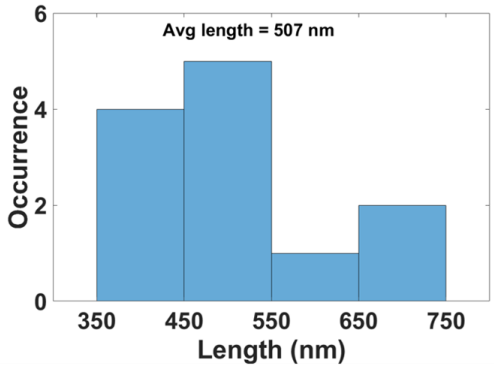

Figure 2-10. Histogram of the resolution-corrected migration length values l_{FRET}.

We end up with a histogram representing the distribution of energy migration lengths in figure 2-10: the average length is 507 nm, with the minimum and maximum values of 396 nm and 677 nm, respectively. In chapter 1, we analysed that the center-to-center separation distance between neighbour nanoplatelets is 5.7 nm. Thus, here the 500 nm migration length correspond to an energy hopping over ~ 90 nanoplatelets.

Additionally, figure 2-11 shows the luminescence images of three different NPL chains measured under the same conditions as in figure 2-9, except that the laser excitation spot was

positioned at the end of the NPL chain instead of the center. For the first 2 chains, the left portion of the profile curve (blue solid line) was fitted by a Gaussian (yellow dashed line) of respective widths 223 and 194 nm, which matches the imaging response function l_{PSF} = 190 nm. The right side of the curve was fitted with a Gaussian (red dashed line) of width respectively 543 and 504 nm, similar to the lengths l_x reported in figure 2-9 (c), so that an energy migration length of 484 and 440 nm can be extracted. For the 3rd chain, the left portion extended slightly longer (252 nm Gaussian width), possibly because the laser spot was not exactly at the end of the chain, but the estimated FRET length was 496 nm, in the same range as the first two chains and figure 2-9 (c).

Thus, the profile along the longitudinal cutting line became asymmetric with no diffusion on one side and with around 500 nm diffusion on the other side, in agreement with our observations in the case of center-localized excitation:

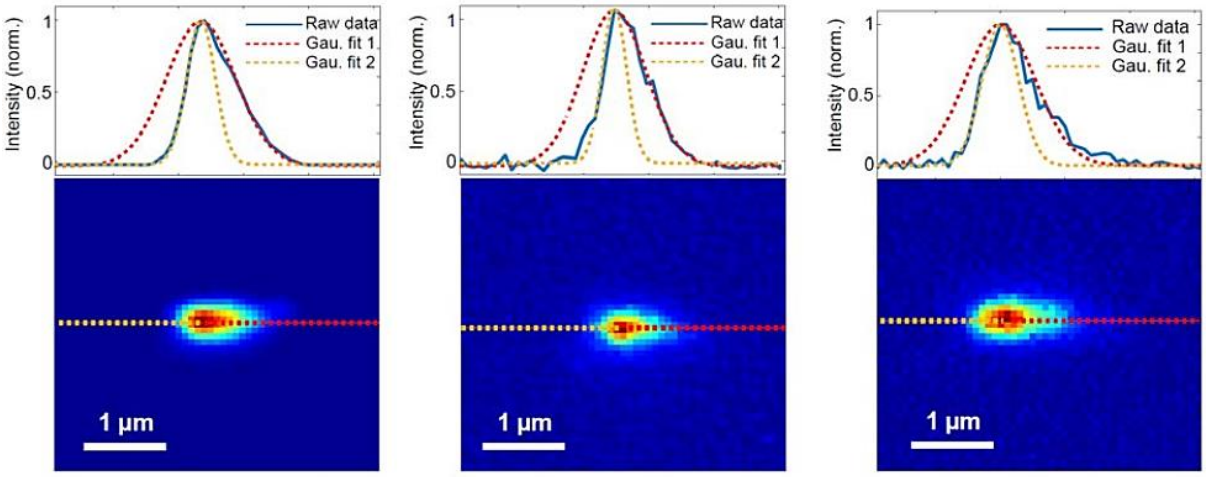

Figure 2-11. Profiles of 3 representative NPLs chains with excitation on their edge. The blue solid line is the experimental profile. The red and yellow dotted lines correspond to Gaussian fits of respectively the right and left portions of the experimental curve.

2.2.4 Exclusion of non-linear effects

Although we observed a very long energy migration distance of about 500 nm (~ 90 PLs) in the NPLs chains, this length may be attributed to nonlinearities that flatten the luminescence distribution, because exciton-exciton annihilation or photobleaching may suppress the emission intensity in the middle of the excitation beam while enhancing the signal on the external part of the beam. To exclude this possibility, we first characterize the linear excitation regime of the NPL emitter to make sure we were using appropriate excitation power during our experiments to avoid multi-excitonic effects within a given platelet.

We excited the same individual platelet with various input powers and recorded its power-dependent intensity curves (figure 2-12(a)) and decay curves (figure 2-12 (b)). Note here that, for all the measurements, we select only the on-states emission in order to exclude blinking effects from the power-dependence analysis (as will be shown in chapter 3). The power dependent intensity curve shows that the emission intensity will increase linearly with the pump power within the range from 1.5 to 10 nW, which covers the typical power (~7.5 nW) that was used in the measurements. When the excitation power varies between 1.5 and 10 nW, the decay dynamics of the selected on-state emission of the platelet also remain unchanged, confirming the absence of multi-excitonic contribution and nonlinear effects.

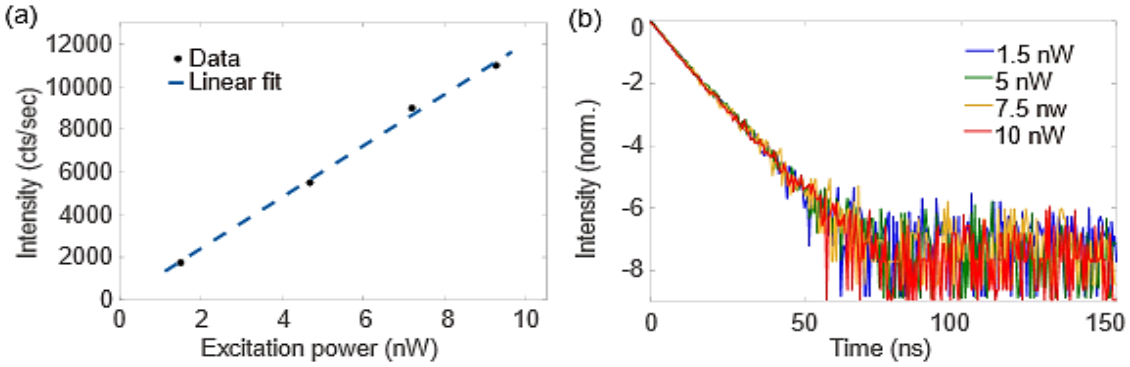

Figure 2-12. Power-dependent intensity curve (a) and decay curves (b) of a same single nanoplatelet (NPL) emitter under different excitation powers.

In addition, we checked, by measuring the number of photons detected and estimating the number of excitons created per laser pulse, that less than one exciton was created per laser pulse in the entire NPLs chain: when we pump the sample in the linear excitation regime, the detected photon number is about 10000 counts per seconds. We calculate, for these emitters on a glass slide imaged with a 1.4 oil objective, a photon collection efficiency around 80 %. Considering the optical transmission efficiency of the homebuilt microscope is about 70% and the detection efficiency of the APDs are 55% at 550 nm, we deduce that about 32500 photons are emitted by our sample per second. The quantum yield of our threads is unknown. According to the literature, a quantum yield of 30 % for single platelets and of 1.4% for stacked NPLs was reported [16]. Since our emitters are very bright and show less defects, we believe the QY is higher than reported values but we can still take the values 1.4% as a very conservative limit. It leads to an estimation that 1.1×10^5 to 2.3×10^6 excitons are generated per second in the chain. During the image measurements, the repetition rate of the laser pulse is set at 2.5 MHz, so that each laser pulse creates 0.04 to 0.9 exciton in the chain. As a result, the contribution of multi-excitonic effects is negligible.

To further exclude the presence of nonlinear effect induced by potential multiexciton, we analysed the power-dependent energy migration length on platelet chains (figure 2-13 (a)): the excitation laser power varies from 0.01-nW to 100-nW to generate very few (~10^3 counts per second) or massive (>10^5 counts per second) photons. As a result, the deconvolved emission profile l_{FRET} show no power dependence and is reproducible at low excitation power.

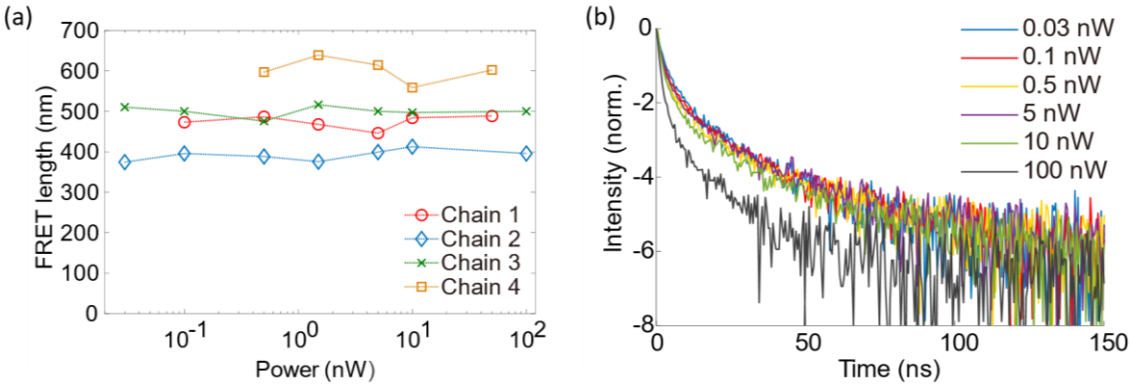

Figure 2-13. (a) Power-dependent FRET length measurements on 4 different chains: excitation powers vary from below 0.1 to 100 nW, generating typically 10^3 – 10^5 photon counts/sec. (b) Decay curves of a same platelet chain under different excitation powers.

We also excite a same platelet chain with different input powers and record its power-dependent decay curves (figure 2-13 (b)). A variable neutral density filter is used to keep a constant photon detection rate (around 10^3 counts per second) in the avalanche photon detector to avoid instrument response induced effects. When the excitation power varies from 0.03 to 5-nW, which covers the typical power range that was used in the platelet chain measurements, the decay dynamics of the chain remain unchanged, confirming the absence of nonlinear effects. At 10 nW (which starts to exceed the power range used in the measurements), the decay rate slightly changes and then it significantly accelerates at 100 nW. The measurements were performed under 5 nW excitation, within the range where the decay shows little power dependence. The faster decay at 100 nW excitation may be due either to multi-excitonic effects such as exciton-exciton Auger annihilation or to quenching mechanisms.

At this point, we verified the long-range energy migration on the NPLs chain over 500 nm corresponding to about 90 NPLs. However, we cannot conclude for the moment that this migration is due to energy transfer mechanism, because the dielectric index of the chain is much higher than the surrounding medium, so waveguiding of the excitation beam or of the emitted light might also explain our observation. Thus, in the next section, we will study the waveguiding effect in our stacked NPLs sample.

2.3 Studies of waveguiding efficiency

Waveguiding effect is a phenomenon by which the electromagnetic waves propagate under the guidance of the dielectric structure with higher dielectric index. Here on the assembled NPLs chains, it is possible that the observed 500 nm energy migration results from the waveguiding effect, since the index of the CdSe NPLs chain is higher than the index of the surrounding medium. The elongated fluorescence shown in the CCD images possibly result from waveguided excitation light or emission light, or both of them. Thus, we need to analyse waveguiding efficiency for laser beam and emission light. To pursue a conclusion on this hypothesis, we performed experimental analysis and FDTD simulation.

2.3.1 Experimental analysis of waveguiding of the excitation beam

A very straightforward measurement, that can characterize the waveguiding effect of excitation beam, is to send the laser beam onto the stacked NPLs and record its image to see if the beam shows any evidence of energy migration.

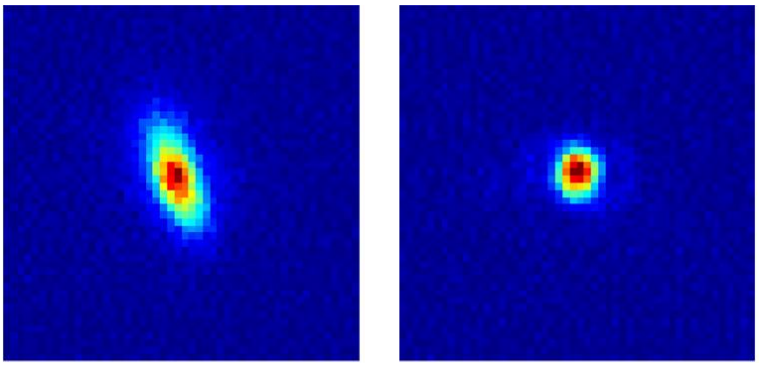

Figure 2-14. Experimental analysis of the waveguiding effect of the excitation beam. Left: imaging the fluorescence of an NPL chain at the wavelength of 550 nm with the laser beam located at its center. Right: imaging the shape of the laser beam under the same condition, but with a different wavelength at 470 nm.

The left panel in figure 2-14 presents the fluorescence elongation on a single thread obtained by focusing the laser spot on the thread and recording the fluorescence, which is same as the images shown in figure 2-5. Then we changed the optical filter to select only the wavelength of laser and cut the emission light from the sample. By doing this, it can be expected for the excitation light that, if the waveguiding is efficient on the stacked NPLs structure, we should be able to observe the laser light propagating along the structure, or the excitation beam is diffracted at the end of the chain. However, in the right panel, we can see that the laser spot remains a round shape and doesn't show

any signature of waveguiding along the stacked structure. This suggests that, in the NPLs chains, there is no efficient waveguiding for the excitation beam.

2.3.2 FDTD simulations of excitation and emission beam

In this subsection, we will perform FDTD simulation on the stacking structure to numerically prove that the waveguiding is negligible on our samples for both excitation and emission light.

Lumerical FDTD Solution is employed to conduct this electromagnetic simulation. We built CdSe NPLs with index of 2.64+0.44i [122] and with a dimension of $20 \times 7 \times 1.5$ nm^3 sandwiched by 2 oleic acid layers which have refractive index = 1.46 and thickness of 2.1 nm. NPLs were co facially stacked with center-to-center separation distance of 5.7 nm (obtained from TEM image analysis in chapter 1) to form a 500 nm chain that starts at $x = 0$ nm and ends at $x = 500$ nm. A 750 nm long 500 nm wide monitor was positioned 30 nm under the stacks to properly collect the near field electromagnetic waves for calculation of the electric field intensity E^2. We also simulated the reference case without the chain structure but only one CdSe NPL located at $x = 0$ nm. We quantify the effect of waveguiding by:

$$\left(\left|\vec{E}\right|^2 - \left|\vec{E}_{ref}\right|^2\right) / \left|\vec{E}_{ref}\right|^2 \tag{2.10}$$

We first simulated the waveguiding of the emitted light. Emission dipoles polarized along either vertical (upper panels) or horizontal (lower panels) directions within the NPL plane were positioned in the centre of the left most NPL with coordinates $x = 0$ nm, $y = 250$ nm. As shown in the right panels of figure 2-15, the waveguiding effect is clearly visible, but its normalized value remains within a few % along the whole chain, so that the waveguiding is negligible for both vertical and horizontal emitting dipoles on the chain.

We then studied the waveguiding efficiency for the excitation beam by simulating the plane waves impinging on one end of the same chain, with polarization either longitudinal or lateral with respect to the chain axis. For both excitation polarizations, the waveguiding effect is clearly visible, but its normalized relative value remains below 2 % along the whole chain. Thus, the waveguiding of excitation beam is also very weak, which is consistent with our experimental observation in figure 2-14.

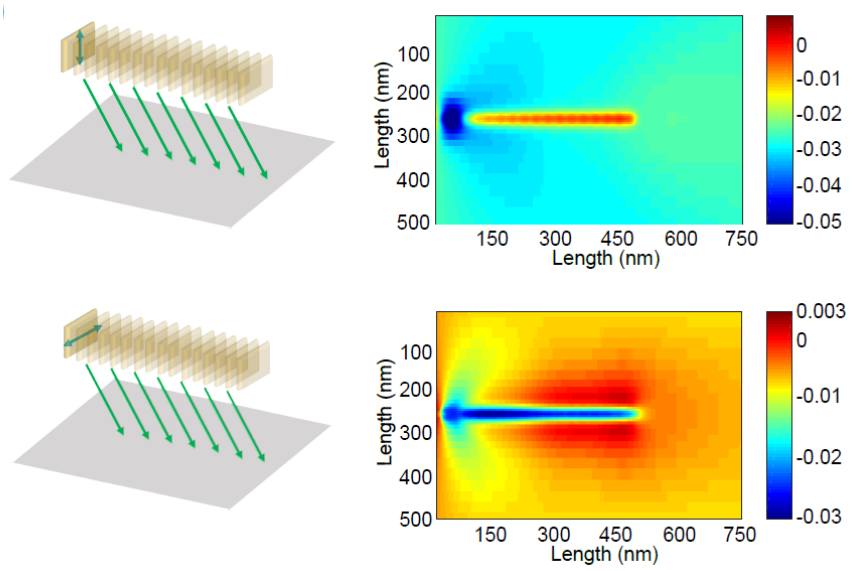

Figure 2-15. FDTD simulations of the waveguiding of the emitted wave, with the dipole source (550 nm) of either orientation along the platelet plan, positioned at the first platelet ($x = 0$) of the chain. Color scale: quantification of the effect of waveguiding by e.q. 2.10.

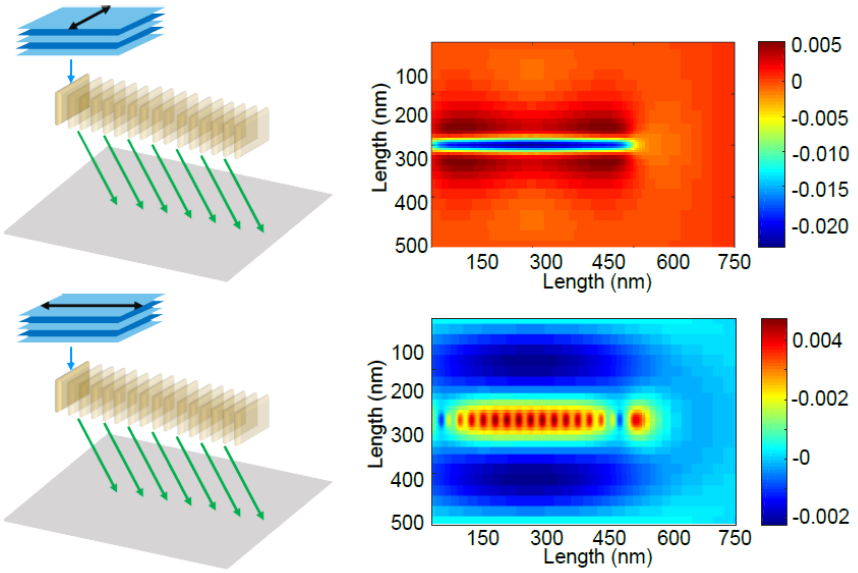

Figure 2-16. (b) FDTD simulations of the waveguiding of the incident beam (plane wave, 470 nm) along the two horizontal polarizations. Color scale: quantification of the effect of waveguiding by e.q. 2.10.

2.3.3 Conclusion

From the above experimental and numerical results, we demonstrated that the energy migration observed in the stacking structures is not due to waveguiding but due to non-radiative energy transfer.

There are two relative non-radiative mechanisms: FRET and Dexter charge transfer. As discussed in the subsection 2.1.3, NPLs are prone to FRET because of their photophysical

characteristics. Dexter transfer is a different mechanism consisting in a simultaneous tunnelling of the electron and hole to a neighbor platelet. Dexter transfer decays exponentially with distance over a typical 1-nm scale [98], while the separation distance of neighbor NPLs in the chain is 5.7 nm, so that we expect it to be negligible here and finally attribute our observation of energy migration to FRET.

Eventually, we conclude that our observation of elongated fluorescence is due to FRET. As illustrated in figure 2-17, we reported a long-range FRET in self-assembled NPLs chains with an energy migration length $l_{FRET} =$ 500 nm, corresponding to energy hopping over about 90 NPLs in the chain.

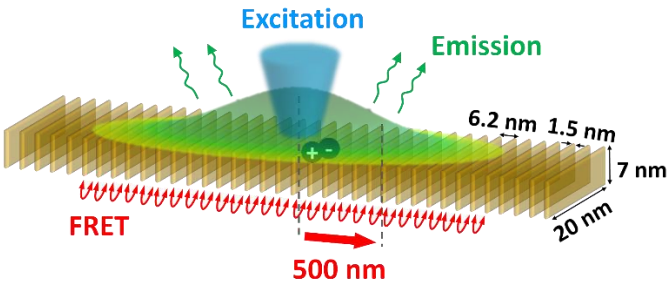

Figure 2-17. Schematic of the proposed FRET migration mechanism.

2.4. Diffusion model for FRET rate deduction

As mentioned in the subsection 2.1.3, the FRET rate, in the case of a film of similar emitters, is difficult to be extracted from decay analysis. Here we propose a diffusion equation model in order to deduce the FRET rate from the experimental energy migration length.

2.4.1 Diffusion model

We assume that the length of NPLs chain is infinite and we introduce a centre-to-centre separation distance between neighbour NPLs δ, a transfer rate between neighbour platelets γ_{tr} and an exciton decay rate γ_0 of single NPL which is a sum of respectively radiative and non-radiative decay rates γ_{rad} and γ_{nr}. The transfer rate γ_{tr} and the decay rate γ_0 are assumed the same for all NPLs in the chain.

If an exciton is created at time $t = 0$, the probability n_i that the i^{th} platelet in the chain is excited obeys:

$$\frac{dn_i}{dt} = -(\gamma_0 + 2\gamma_{tr})n_i + \gamma_{tr}(n_{i-1} + n_{i+1}) \quad (2.11)$$

Considering that the length of the NPLs chain is much larger than δ, one may refer to each NPL by its position x and introduce the exciton probability distribution $n(x,t)$, which is the probability of the NPL located at position x in the linear chain to be excited at time t. We note that:

$$\frac{\partial^2 n}{\partial x^2} \approx \frac{n_{i+1}+n_{i-1}-2\,n_i}{\delta^2} \quad (2.12)$$

so that we obtain the standard diffusion equation with an additional loss term due to exciton recombination γ_0:

$$\left(\frac{\partial n}{\partial t}\right)(x,t) = -\gamma_0\ n(x,t) + D\left(\frac{\partial^2 n}{\partial t^2}\right)(x,t) \quad (2.13)$$

in which $D = \delta^2\gamma_{tr}$ is the diffusion coefficient.

Because this is a linear equation with translational invariance, our discussion can be limited to the case where a single exciton is introduced at $t = 0$ at the position $x = 0$. This corresponds to a Dirac distribution for $n(x, t = 0)$, with the normalization condition $\int_{x=-\infty}^{+\infty} n(x, t = 0)dx = 1$. The solution of this equation is:

$$n(x,t) = \frac{1}{2\sqrt{D\pi t}} e^{-\frac{x^2}{4Dt}} e^{-\gamma_0 t} \quad (2.14)$$

This exciton probability distribution combines a typical diffusive broadening of width $2\sqrt{Dt}$ with a general decrease as $e^{-\gamma_0 t}$ due to the recombination losses. By integrating $n(x,t)$ over x or t, we can obtain theoretical decay curves and FRET images, respectively.

We now calculate the theoretical decay curve:

The photon emission rate of on the whole chain is given by

$$I_{decay}(t) = \int \gamma_{rad} n(x,t)dx \quad (2.15)$$

$n(x,t)$ is a Gaussian function of x, whose integration leads to:

$$I_{decay}(t) = \gamma_{rad} e^{-\gamma_0 t} \quad (2.16)$$

A first consequence of this result is that the luminescence decay curve of the whole chain scales as $e^{-\gamma_0 t}$, same as the decay dynamics of a single NPL. It indicates that FRET is a mechanism of energy diffusion within the chain, but not of energy loss for the overall chain that opens additional decay channel: FRET will not modify exciton's decay characteristics but just redistribute the exciton within the chain. Because of this, the FRET rate cannot be extracted from the decay curves measurements, which is why previous works on the decay of platelet assemblies reported mostly only a theoretical estimation because of this general difficulty in FRET rate extraction, as discussed in subsection 2.1.3.

Our imaging experiment, on the other hand, can provide information on the homo-FRET dynamics within the sample. The original image regardless of the point spread function of the chain is obtained by summing the probabilities of photon emission from a given point x over all times t:

$$I(x) = \int_{t=0}^{+\infty} \gamma_{rad} n(x,t) dt \tag{2.17}$$

One can find $I(x)$ by noting that

$$\frac{dI}{dx} = \frac{\gamma_{rad}}{2\sqrt{D\pi}} \int_{t=0}^{+\infty} \frac{dt}{\sqrt{t}} \frac{(-x)}{2Dt} e^{-\left(\frac{x^2}{4Dt} + \gamma_0 t\right)} \tag{2.18}$$

which, by introducing $u = x^2/4D\gamma_0 t$, rewrites (for $x > 0$)

$$\frac{dI}{dx} = \sqrt{\frac{\gamma_0}{D}} \frac{\gamma_{rad}}{2\sqrt{D\pi}} \int_{u=+\infty}^{0} \frac{du}{\sqrt{u}} e^{-\left(\frac{x^2}{4Du} + \gamma_0 u\right)} \tag{2.19}$$

where we recognize

$$\frac{dI}{dx} = -\sqrt{\frac{\gamma_0}{D}}\, I \tag{2.20}$$

Eventually we find

$$I(x) = \frac{\gamma_{rad}}{2\gamma_0 l_{FRET}}\, e^{-|x|/l_{FRET}} \tag{2.21}$$

by introducing the migration length $l_{FRET} = \sqrt{D/\gamma_0} = \delta\sqrt{\gamma_{tr}/\gamma_0}$. This quantity can be interpreted in diffusion terms: the excitation can migrate during a typical time $1/\gamma_0$ before it decays, so that l_{FRET} is the diffusion length with diffusion coefficient D during a time $1/\gamma_0$.

Within this model, our experimental image profile $I(x)$ should be an exponential convolved by the apparatus Gaussian response function l_{RF}. However, functions of such form could not provide fits as good as the simple Gaussian fit of figure 2-9 (b). It indicates the limits of our simple model and might reveal some degree on diffusion confinement as demonstrated for quantum dot films [101].

The total number of emitted photons can be obtained either by integrating $I_{decay}(t)$ or by integrating $I(x)$. Both summations lead to the same total number of photons emitted (probability for photon emission when one exciton is introduced): γ_{rad}/γ_0. This probability is none other than the quantum yield of single NPLs: even though FRET redistributes the energy along the thread, the radiative decay and total decay of the overall thread are the same as the decay for a single platelet.

2.4.2 FRET rate deduction

In the last subsection, we deduced the relation of FRET length l_{FRET} and transfer rate γ_{tr}, so we can calculate the FRET rate by:

$$\gamma_{tr} = \gamma_0 \left(\frac{l_{FRET}}{\delta}\right)^2 \tag{2.22}$$

in which γ_0 is the overall recombination rate of a single platelet and $\delta = 5.7$ nm is the separation distance of the neighbour NPLs. We know from imaging experiments that the FRET length $l_{FRET} =$ 500 nm, thus we need to probe the decay rate (γ_0) of single NPLs for the calculation of FRET rate γ_{tr}.

We analysed the decay curves of 8 different single platelets (more details about decay analysis will be given in chapter 3). As depicted in figure 2-18, we obtain a lifetime distribution with an averaged value of 12 ns, which can be assumed to correspond to the exciton recombination time, and a standard deviation of 2.7 ns. Such an inhomogeneity in decay times distribution is typical with semi-conductor nanoparticles. It may have different causes such as local electric fields or inhomogeneity of the oscillator strength due to the dispersion of lateral dimensions.

Finally, we can use this diffusion equation model to extract the FRET rate from the experimental migration results:

$$\gamma_{tr} = \gamma_0 (l_{FRET}/\delta)^2 \cong (1.5 \text{ ps})^{-1} \tag{2.23}$$

We can also calculate the neighbor-to-neighbor FRET efficiency by $\eta = 1 - \gamma_0/\gamma_{tr}$, which yields a value of 99.99 %.

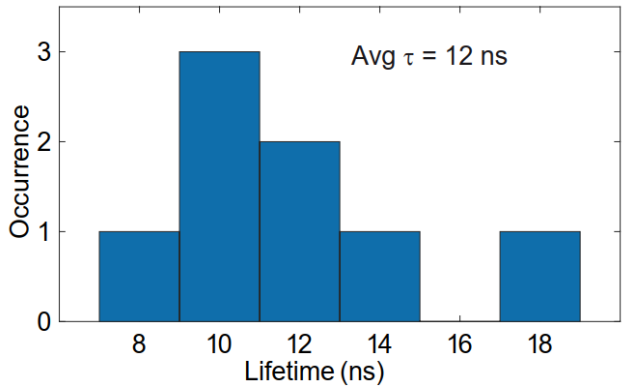

Figure 2-18. Distribution of single-platelet lifetimes.

2.4.3 Theoretical FRET rate calculation from Förster's theory

Now we compare the above deducted FRET rate (1.5 ps)$^{-1}$ to the theoretical value calculated following Förster's theory (as introduced previously in subsection 2.1.1).

Since the transition dipoles in nanoplatelets are along the plane of the platelets [6,29], when co-facially stacked, the second term in the orientation factor κ^2 is equal to 0 (because $\overrightarrow{n_R}.\overrightarrow{n_D} = 0$ and $\overrightarrow{n_R}.\overrightarrow{n_A} = 0$). Thus, considering only the parallel dipoles (as orthogonal dipoles would have no coupling), we obtain $\kappa^2 = 1$.

Then we estimate the Förster radius R_F. To do this, we first calculate the spectral overlap integral J, in which $f_D(\omega)$ is the emission spectrum normalized by $\int f_D(\omega)d\omega = 1$ and σ_A is the absorption cross-section. We can write $\sigma_A(\omega)$ as $\sigma_0 u(\omega)$ where $u(\omega)$ is our measured absorption spectrum normalized by $u = 1$ at the maximum. The absorption cross-section for our CdSe nanoplatelets (with lateral area of ~ 150 nm^2) is estimated to $\sigma_0 = 7.10^{-14}$ cm² according to ref. [28]. We employ our experimental emission spectrum and absorption spectrum in figure 1-4 for the calculation of $f_D(\omega)$ and $u(\omega)$, respectively, which are then normalized and plotted in figure 2-19.

We simplify the Förster's radius equation by considering that the emission line is sufficiently narrow so that the frequency-dependent term $n^4(\omega)\omega^4$ can be considered as constant over the emission spectrum. Then Förster radius can be written as:

$$R_F{}^6 = \frac{9}{8\pi}\left(\frac{\lambda}{2\pi n}\right)^4 \int f_D(\omega)\sigma_A(\omega)d\omega \qquad (2.24)$$

in which we take λ = 550 nm, the homogeneous surrounding medium's index $n = 1.5$ and we calculate the integral $\int f_D(\omega)\sigma_A(\omega)d\omega = 5.1\ \text{nm}^2$ from figure 2-19. Eventually, we obtain $R_F =$ 17 nm, so that we conclude for the theoretical FRET time: $(1/\gamma_{tr})$ = 17 ps.

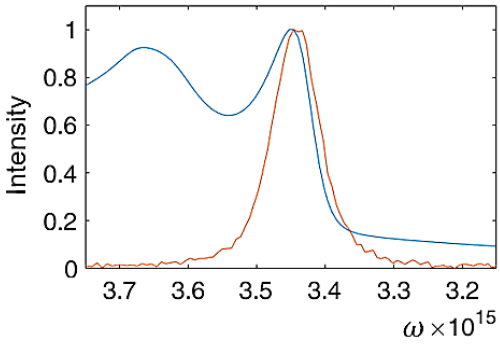

Figure 2-19. Normalized emission spectrum $f_D(\omega)$ (red) and absorption spectrum $u(\omega)$ (blue).

Our estimated experimental FRET time is 1.5 ps, an order of magnitude shorter than this theoretical result. This probably shows that treating the platelets as points in the Förster radius calculation is a crude approximation because two-dimensional emitters show much higher FRET rates [98]. Another group reported a different method to estimate the theoretical FRET rate in assembled NPLs by calculating the energy absorption rate over all the volume of NPL acceptor [15]:

$$\gamma_{tr} = \frac{Im(\varepsilon(\omega))}{h} \iiint_{V_A} \vec{E} \cdot \overrightarrow{E^*} dV \tag{2.25}$$

in which $\vec{E}$ is the electrical field created by the donor dipole, V_A is the acceptor volume and h is Planck's constant. They found a theoretical FRET rate of 10 ps in 4/5 monolayer CdSe NPL binary films, which is still much longer than our experimental observation, although for their NPLs, the lateral size is larger and the separation distance is shorter than our samples.

2.4.4 Discussion

We use a diffusion equation model to relate the energy migration length to FRET rate, from which we calculated an ultrafast FRET rate of $(1.5\ \text{ps})^{-1}$. However, two questions are remaining unsolved in our study of FRET rate.

The first question is the discrepancy between the experimental FRET image and theoretical diffusion images deduced from diffusion model: we expect the profile to decay exponentially on the images, but the results obey Gaussian functions. Possibly, this results from a lack of consideration of

other effects like random distribution of recombination rate and the presence of quenching sites. The resolution of our imaging system might also be a little insufficient to analyse the profile shape adequately.

The second question is the difference between theoretical FRET rate and our result deduced from experiments. The theoretical transfer time for neighbour NPLs is more than 10 picoseconds, while the experimental results lead us to a rate as fast as 1.5 ps. Thus, our experimental demonstration of long-range FRET reveals a transfer rate faster than the theory. This probably indicate that treating the platelets as points is a crude approximation in the current models and more theoretical work is necessary to describe Förster transfer between non-localized emitters involving the electron-hole pair wave functions. The diffusion model used to extract the experimental FRET rate might also be a little over-simplified. To further study this question, one can perform similar imaging experiments and see the FRET length/rate as a function of temperature, or as a function of the separation distance between NPLs in the chain.

2.5 Conclusion and perspectives

To conclude this chapter, we reported a FRET migration length of 500 nm (corresponding to energy hopping over 90 NPLs) in self-assembled NPLs chains by imaging analysis. This migration distance is 20 times longer than other reported values with nanoparticles, as mentioned in subsection 2.1.3.

A diffusion model is developed to relate this migration length to the transfer rate, which leads us to an estimation of the time of FRET transfer between neighbour NPLs of 1.5 ps. This rate is faster than all excitonic mechanisms known to occur in fluorescent semiconductor nanoparticles, such as radiative recombination (typical radiative rates of $(12\ ns)^{-1}$), Auger recombination (typical time of 150-500 ps for CdSe/CdS NPLs [15]) as well as fast non-radiative quenching effect by trap sites (rate estimated to be 35 ps [16]).

Consequently, the behavior of collective assembled emitters is expected to present totally new photophysical behaviour other than simply an averaging effect on an ensemble of single emitters. For instance, a single quencher in clusters of 2 to 10 quantum dots may induce synchronized blinking of an ensemble of emitters, acting as an exciton sink due to fast energy transfer between the emitters [103]; in clusters of 4-5 quantum dots, two excitons from two separate emitters may recombine by FRET-

assisted Auger effect rather than emit two photons simultaneously, leading to single-photon emission by an ensemble of emitters [123].

Moreover, a faster FRET rate could be expected, because, in our samples, FRET is possibly limited by the twisting (induced by strain during stacking) and trapping sites (defected NPLs) on chains. Therefore, we predict that new FRET rate records, possibly faster than picosecond scale, could be achieved in future reports.

Besides, as perspectives, a longer-range energy migration length can be realized in self-assembled NPLs chains through different strategies: a) since the FRET rate will strongly modified by the inter-NPL distance with $1/d^4$ dependence, we could shorten the distance between NPLs by using different ligands with different alkyl chains to replace the native oleic acid; b) NPLs with longer decay lifetime, such as core-crown CdSe/CdTe platelets [55], would help to obtain longer energy transfer length.

Chapter 3. Blinking, decay and single photon emission

Introduction

The objective of this chapter is to investigate the general characteristics of the fluorescent behaviour, including blinking, decay and antibunching of CdSe NPLs in various structures, from single NPLs, clusters to assembled NPLs chains. We will study how assembly modifies the fluorescent behaviour, and will conclude respectively on the typical behaviours of non-assembled and assembled emitters. This knowledge is not only important for the study of effects of the self-assembly, but also a powerful tool to distinguish the cases of single NPLs and clusters, which cannot be resolved by optical microscopy.

We use a time-correlated single-photon counting (TCSPC) system to record the intensity time trace and decay curves, and use a Hanbury-Brown and Twiss (HBT) configuration to obtain the second order photon correlation function $g^{(2)}$. On single NPLs, we find typically the binary blinking and mono-exponential decay dynamics, while more off-state events in blinking traces and the multi-exponential characteristics in decay curves can rise in the NPLs with the presence of more trapping sites (defects). For clusters, in intensity trajectories, their off-states are averaged out by fast switches between on- and off-state, forming flickering intermediate grey-state. For NPL chains, they have less blinking as compared to the former two cases because of a stronger averaging effect. The decay curves of clusters and chains are multi-exponential, with a striking acceleration in the fast decay components and with an appearance of significant slow decay components. The acceleration in fast decay components may result from radiative trion recombination and nonradiative Auger quenching. The slow decay components in both non-stacked and stacked NPLs are attributed to the trapping/de-trapping retardation. In assemblies the trapping effect seems more involved because homo-FRET can funnel the exciton to the trapping sites and, as a result, their slow decay components are more significant.

In the first section, we will give a general introduction on fundamentals of the blinking, the decay and the antibunching and their relevant characterization methods or tools. We will also review the literature and introduce briefly the state of the art.

In the second section, we focus on single NPLs to study their blinking and decay behaviours. They usually present clear binary blinking switching between on- and off-state. Their decay curve is

quasi mono-exponential while the multi-exponential decay, with more significant slow decay components, arises in the NPLs with many defects.

We will study the blinking and the decay of assembled NPLs, i.e., clusters and chains in the 3rd section, and then compare the decay and blinking behaviours between single and assembled NPL samples in the 4th section. We propose a model of FRET-assisted processes, which helps to modify the collective decay characteristics of the assemblies.

In section five, we will study the antibunching in single NPLs and clusters. We demonstrate for the first time a strong antibunching in core-only CdSe NPLs without post-processing, indicating that they can be promising single photon source. We also demonstrate the partial antibunching in CdSe clusters, in which we can apply the time gating method to distinguish clusters from the case of single NPLs with multiexciton radiation.

Finally, we finish this chapter by an overall conclusion and perspectives in section six.

3.1 Introduction: blinking, decay and antibunching

In this section we will introduce the basics of blinking, decay and antibunching as well as their characterization methods/tools, some of which will be employed in our study in this chapter. We will also review some of the related literature and present briefly the state of the art.

3.1.1 Exponential decay and principles of TCSPC

Exponential decay

The term "exponential decay" refers to the process in which the quantity of excited emitters decreases with a rate proportional to the remaining population. This can be expressed by the following equation:

$$\frac{dn(t)}{dt} = -\gamma \cdot n(t) \tag{3.1}$$

from which we can write:

$$n(t) = n_0 \cdot e^{-\gamma \cdot t} \tag{3.2}$$

where n_0 is the initial number of excited emitters (or probability to be excited for a single emitter) and γ refers to the decay rate, which is the inverse of the excited-state lifetime τ. Thus, the exponential decay can also be expressed in terms of lifetimes:

$$n(t) = n_0 \cdot e^{-t/\tau} \tag{3.3}$$

When nano-emitters are excited, their emission intensity will be proportional to the population of the excited emitters, thus their number will decay exponentially, because the rate of photon emission is the product of radiative recombination rate and the number of excited emitters, $\gamma_{rad} \cdot n(t)$.

Multiple decay channels

In many cases, the decay processes are contributed by two or more recombination channels, in which the total decay rate is the sum of the rates of all channels:

$$\frac{dn(t)}{dt} = -(\gamma_1 + \gamma_2 + \cdots) \cdot n(t) \tag{3.4}$$

which gives

$$n(t) = n_0 \cdot e^{-(\gamma_1+\gamma_2+\cdots)\cdot t} \tag{3.5}$$

The overall average lifetime of the emitter can be calculated as:

$$\tau = \frac{1}{(\gamma_1+\gamma_2+\cdots)} \tag{3.6}$$

Multiple decay channels are often expected in nano emitters, including radiative recombination (γ_{rad}) and non-radiative recombination (γ_{nr}). In this case, we can write:

$$n(t) = n_0 \cdot e^{-(\gamma_{rad}+\gamma_{nr})\cdot t} \tag{3.7}$$

The quantum yield Q of an excited state of the nano emitter represents the probability of emitting a photon, which in the case of an exponential decay can be written as the ratio between the radiative recombination rate γ_{rad} and the sum of the radiative and non-radiative rates γ_{nr}:

$$Q = \frac{\gamma_{rad}}{\gamma_{rad}+\gamma_{nr}} \tag{3.8}$$

Thus, the measured emission intensity of a nanocrystal under pulsed excitation will depend on the ratio between γ_{rad} and γ_{nr}:

$$I \propto Q = \frac{\gamma_{rad}}{\gamma_{rad}+\gamma_{nr}} = \frac{1}{1+\frac{\gamma_{nr}}{\gamma_{rad}}} \tag{3.9}$$

Other mechanisms can occur in the case of several electron-hole pairs excited simultaneously (multi-excitons). In figure 3-1, the process (a) and (b) represent the competition between nonradiative Auger recombination and radiative biexciton recombination in the system with 2 excitons.

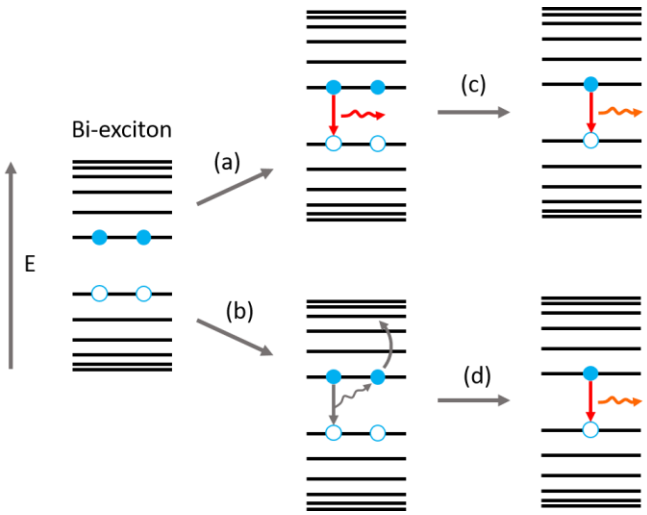

Figure 3-1. Schematic representations of (a) radiative biexciton recombination, (b) Auger recombination and (c) and (d) mono-exciton recombination.

Besides, in nanocrystals, one may have biexcitons emission (process (a) and (c)), i.e., the cascading emission of two successive photons. The first photon is emitted by the biexciton decay and then the second photon is from the mono-exciton decay. This process can be expressed by a multi-exponential function. In the later sections, we will deal with the decay curves of NPLs emitters using the multi-exponential decay model.

Time-correlated single-photon counting (TCSPC) measurements

Time-correlated single-photon counting (TCSPC) is a widely employed technique used to analyse the fluorescence lifetime of different emitting systems, such as molecular fluorophores and semiconductors quantum dots. This technique can help to construct decay curves which give access to the dynamics of exciton recombination process and to the information on radiative or non-radiative recombination rates.

Figure 3-2 shows the basic principle of TCSPC measurements. We use a pulsed laser to excite the emitter and record the time difference between excitation and photon detection. Then these photon counts with coded time tags are sorted into a histogram consisting of a range of time bins as shown in figure 3-2. Since in our study we use weak excitation power to excite single emitters, we normally generate less than one photon in each repetition period, as discussed in chapter 2. Low excitation regime is important to conduct a reliable lifetime analysis, because, if more than one photon is emitted in a pulse duration, the detector will register the first photon but miss the following ones. This would lead to an over-representation of early photons in the histogram, called as "pile-up" effect. This happens because of: 1) the deadtime of the avalanche photodiode: before detecting a subsequent photon, the sensor needs to be de-charged and the bias should be reset (this recovering takes time in the scale of tens of nanoseconds); 2) the manner of working of the acquisition card: the laser pulse starts a voltage ramp and the first photon count stops it.

In our measurements, the laser was set at 2.5 MHz repetition rate (400 ns period) with an input power of 10 nW. A fast TCSPC module combined with PicoHarp acquisition card was used for decay curve measurements with 500 ps characteristic time of the total system response function.

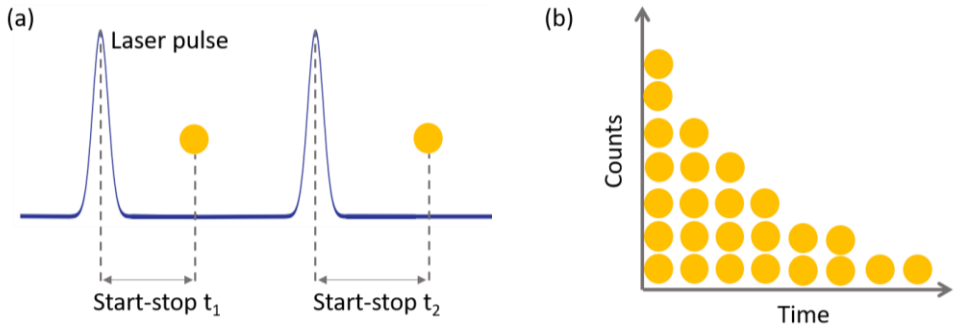

Figure 3-2. (a) The measurement of start-stop times in TCSPC. (b) The simplified histogram of start-stop times in time-resolved fluorescence measurement with TCSPC.

Decay lifetime analysis

The decay curves are plotted in semi-log scale and the time binning interval is set to equal to the temporal resolution of the Picoharp card (512 ps). Self-luminescence of the substrate is also recorded as noise that needs to be subtracted to obtain the noise-corrected decay curve. To fit the experimental data, we use either mono- or multi-exponential decay models, depending on the decay characteristics of different NPLs samples (single or stacked NPLs). We then calculate the intensity-averaged lifetime from the fitting results as shown in the following.

The intensity decay curve can be expressed by:

$$I(t) = \frac{dn}{dt} = \sum_{i=1}^{n} A_i \cdot e^{-t/\tau_i} \tag{3.10}$$

where i represents the i^{th} exponential component, A_i represents the amplitude of the i^{th} component and τ_i means the corresponding lifetime of the i^{th} component.

We integrate time t from 0 to the infinity and get the overall photon number N, which represents the area under the decay curves:

$$N = \sum_{i=1}^{n} \cdot A_i \cdot \int_0^{\infty} e^{-t/\tau_i} \cdot dt = \sum_{i=1}^{n} \tau_i \cdot A_i \tag{3.11}$$

Note that here the underlying assumption is that all the τ_i are shorter than the period of the pulsed laser (e.g. 400 ns).

The overall average lifetime τ of all the i components is defined by the following formula:

$$\tau = \frac{\int_0^{\infty} t \cdot n(t) \cdot dt}{\int_0^{\infty} n(t) \cdot dt} \tag{3.12}$$

By inserting the expression of $n(t)$ (eq. 3.3) into eq. 3.13, we end up with the following result:

$$\tau = \frac{\sum_{i=1}^{n} {\tau_i}^2 \cdot A_i}{\sum_{i=1}^{n} \tau_i \cdot A_i} \tag{3.13}$$

However, it is noteworthy that, in the literature on FRET in nanoplatelets, a substantial number of papers estimated average lifetime of emitters by calculating "amplitude-average lifetime" as shown below:

$$\tau = \frac{\sum_{i=1}^{n} \tau_i \cdot A_i}{\sum_{i=1}^{n} A_i} \tag{3.14}$$

Although the variation of this value reflects the trend of shortening or lengthening in the lifetime, this is not the correct way to calculate the average lifetime.

3.1.2 Blinking: mechanisms and analytical methods

Emission intermittency, also widely known as blinking, is a random fluctuation in the intensity of photoluminescence, in some typical cases being a binary switch between bright ("on") and dark ("off" or "grey") states. This phenomenon has been reported on different emitting systems such as dyes [124], polymers [125], nanocrystals [126] and nanowires [127].

Blinking mechanisms

Many efforts have been made in the literature to study the mechanism of blinking. However, the origin of fluorescence blinking is still not fully understood [128]. One of the widely acknowledged theories was related to Auger mechanism [129]. In Auger blinking (figure 3-3 (a)), the different intensity ranges in the intensity time trace correspond to different emission mechanisms: for the on-state emission, it is mainly contributed by radiative recombination of neutral excitons [130,131] while for the off-state, it is correlated to charged excitons, i.e. trions, and thus experiences a fast non-radiative Auger process which is competing efficiently with the radiative recombination [132]. Therefore, in Auger blinking model, the emitter is "off" when it is ionized, resulting in the off-state in the intensity time trace (figure 3-3 (a)), and the lifetime of the off-state emission is shorter than that of the on-state (figure 3-3 (b)).

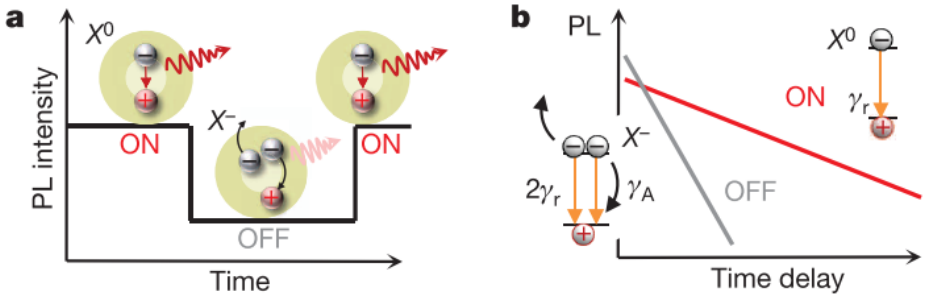

Figure 3-3. Auger (type A) blinking mechanisms (a) and its decay dynamics (b). (a) and (b) are adapted from ref. [132]

However, in addition to Auger blinking, massive work has been devoted to exploring other blinking mechanisms on various emitting systems. Different theories and models have been proposed, such as:

1) Hot-carrier (HC) blinking. C. Galland et al reported hot-carrier blinking [132], in which the emission is intercepted by surface electrons trapping sites before cooling down to the band edge (figure 3-4 (a)), because the trapping rate γ_T is much faster than the relaxation rate γ_R.

2) BC-blinking (figure 3-4 (b)): G. Yuan et al. reported on BC-blinking induced by band-edge carrier traps, in which the activation and inactivation of short-lived shallow traps opens/closes nonradiative channels [133].

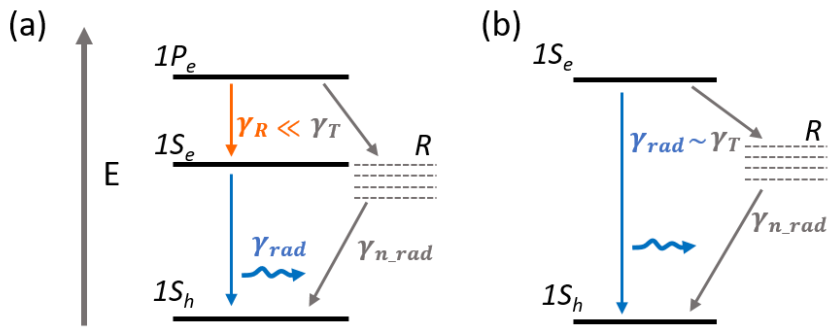

Figure 3-4. (a) Hot-carrier blinking. When recombination centres (R) is active, hot electrons (e.g. at state $1P_e$) will be trapped at a rate γ_T which is much faster than the relaxation rate γ_R. (b) Band-edge carrier blinking. In this case the rate of nonradiative channel (γ_T and γ_{n_rad}) is similar to that of the radiative channel (γ_{rad}).

From a point of view of decay dynamics, Auger blinking, HC-blinking and BC-blinking have different characteristics:

1) In Auger blinking, both radiative and nonradiative rates change when the nanocrystal switches between the neutral (on) and charged (off) states: the overall decay rate of the on-state is dominated by the radiative decay rate of the neutral exciton, and the off-state decay rate is dominated by non-radiative Auger recombination.

2) In HC blinking, large changes in the emission intensity are not accompanied by significant changes in emission decay time (because the electron is intercepted before cooling down to the band edge) [132].

3) For BC blinking, the radiative rate is unchanged while the nonradiative rate fluctuates due to the opening and closing of band-edge traps, whose trapping and nonradiative recombination lifetimes are comparable to the radiating lifetime. As a result, the on-state corresponds to the closing of the band-edge traps, with an overall decay rate dominated by the radiative decay rate of the exciton, while the off-state corresponds to the opening of the trapping state, with the radiative and the non-radiative decay channels competing with each other. This mechanism leads to a linear correlation between the lifetime and the fluorescence intensity [133,134].

Characterization of blinking

A powerful tool to distinguish the blinking mechanisms in emitters is the fluorescence lifetime-intensity distribution (FLID) diagram [135], which can reveal the correlation between decay lifetime and fluorescence intensity, with the horizontal axis the lifetime and the vertical axis the emission intensity, as depicted in figure 3-5.

Figure 3-5 (a) shows the "type A" blinking: the higher intensity corresponds to longer lifetime and the lower intensity corresponds to shorter lifetime. This observation may be explained by an Auger mechanism [132], in which the reduced emission is caused by new non-radiative decay channels. Figure 3-5 (b) shows the "type B" blinking: the lifetime of higher and lower intensities are similar, which seems correlated with the hot-carrier mechanism. Figure 3-5 (c) shows characteristics similar to type A blinking, but with the specificity that the decay lifetime and fluorescence intensity are linearly correlated (we will call this case in this thesis "type A′ blinking"), as explained by the BC blinking model.

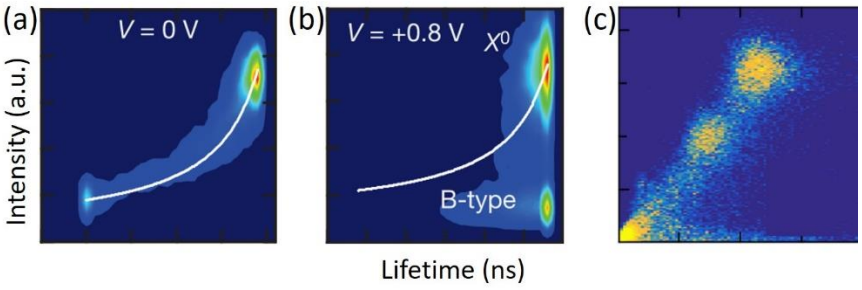

Figure 3-5. Fluorescence lifetime–intensity distributions (FLID) characteristic of (a) Auger blinking, (b) HC blinking and (c) BC blinking. (a) and (b) are adapted from ref. [132] and (c) is adapted from ref. [133]

Besides, since many of the blinking mechanisms are related to charged states, an approach of electrochemical control of emission intensity from individual nanocrystals can be employed to study the effect of charging [132,136].

In addition, to study blinking dynamics of on- and off-state, one can set threshold value in intensity to define on- and off-state emission (e.g. red line in figure 3-6 (b)). Once this is done, each time bin in the time trajectory can be assigned to either on- or off-state categories and their corresponding durations can be sorted into a histogram. The result obtained typically obeys either a power law [137,138] function (e.g. figure 3-6 (c), which is the case for Auger blinking) or exponential function [139] (which can be described simply by a trapping and a de-trapping rate).

However, there is not always a clear boundary between on and off state emission. For instance, figure 3-6 (b) displays also fast passage (flickering) through a continuum of intermediate states. The study of such fast dynamics is difficult as compared to on and off states of longer durations because, in order to properly plot the intensity trajectory, a time bin in the scale of typically 10 ms is desired, which is enough to study long-duration (in the second scale) on- and off-state but not enough for the fast intermediate state. Recently, F. Rabouw et al. reported on an analysis method to study the

microsecond blinking dynamics of individual QDs based on photon correlation, and revealed that the sub-millisecond blinking events are more common than one might expect [140].

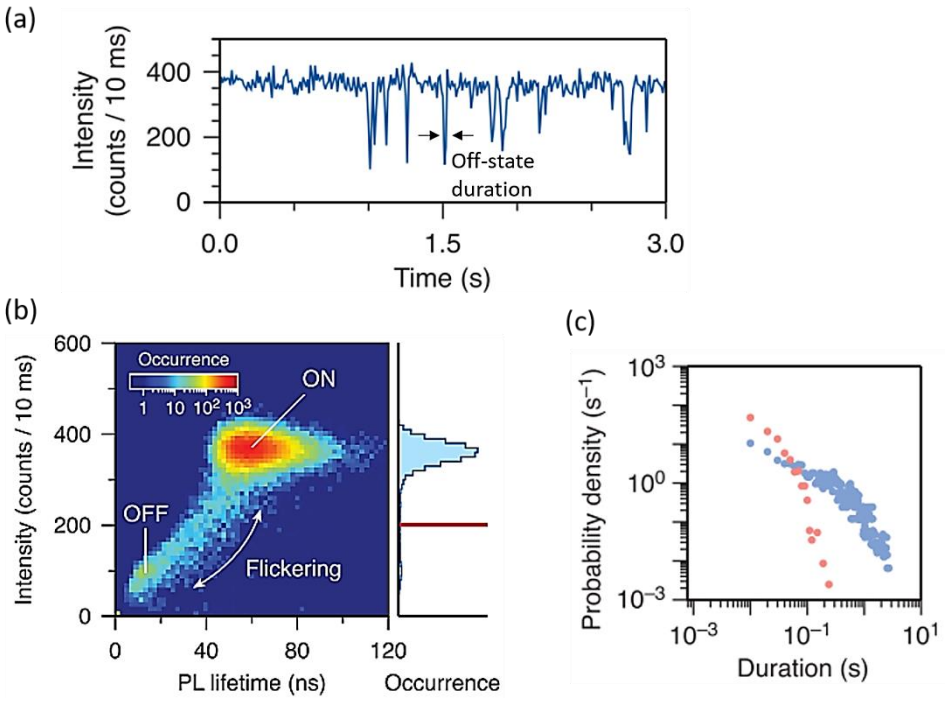

Figure 3-6. (a) Intensity time trace of an individual nanocrystal. Binning time 10 ms. (b) FLID of the same emitter, with the red line in the corresponding intensity histogram defining the threshold of on- and off-state. (c) Blinking statistics for the on periods (blue) and off periods (red), which obey the power law. Adapted from ref. [140].

In applications, stable emission is desired especially for optoelectronic devices. Thus, to suppress blinking, different strategies have been reported, such as passivating the trapping state [141], growing core-multishell structure [142,143] and modify its morphology [144]. Non-blinking emitters have also been reported by tuning the thickness of shells [145].

3.1.3 Antibunching and HBT measurements

Single photon emitter is a central building block of quantum information technologies. An ideal single photon source should have excellent performances in three aspects: single photon purity, indistinguishability and brightness [93]. Our study involves an analysis of single photon purity, or antibunching, which means that no more than one photon is emitted in a given time interval (laser pulse). Antibunching can be characterized by the second order correlation function $g^{(2)}$ measured under the Hanbury Brown and Twiss configuration [146].

Typically, photon antibunching results from Auger recombination, a non-radiative recombination mechanism as introduced in chapter 1. Antibunching has been demonstrated on

various systems, such as atoms [147], molecules [148], quantum dots [149], NV centers [150] and even quantum dot clusters [123]. A single CdSe NPL is also able to emit anti-bunched photons. For example, Ma et al. reported that core/shell CdSe/CdS NPLs with different lateral sizes show size-dependent behaviour: antibunching is not observed for NPLs larger than 150-200 nm² but is observed for smaller NPLs due to enhanced Auger interactions [151].

The second order correlation function

For classical fields, the correlation between the electromagnetic field are given by the second order correlation function $g^{(2)}(t,\tau)$, which is defined as

$$g^{(2)}(t,\tau) = \frac{\langle E^*(t)E^*(t+\tau)E(t)E(t+\tau)\rangle}{\langle E^*(t)E(t)\rangle\langle E^*(t+\tau)E(t+\tau)\rangle} = \frac{\langle I(t)I(t+\tau)\rangle}{\langle I(t)\rangle\langle I(t+\tau)\rangle} \tag{3.15}$$

where $I(t) \propto |E(t)|^2$ and $I(t+\tau)$ are the averaged intensities of the mode at a given time. The bracket $\langle \cdots \rangle$ denotes a statistical time average computed by integrating over a time period. It can be shown, for purely mathematical reasons, that a classical electromagnetic field always verifies $g^{(2)}(t,0) \geq 1$: the classical emission is "bunched".

Using the transformation formalism from classical field quantities into equivalent quantum mechanical operators, we can rewrite the electric field $E(t)$ of a mode k with the help of annihilation $\hat{a}$ and $\hat{a}^\dagger$ creation operators [152]:

$$\hat{E}_k(t) = \hat{E}_k^{(+)}(t) + \hat{E}_k^{(-)}(t) \tag{3.16}$$

with

$$\hat{E}_k^{(+)}(t) \propto \hat{a}_k \cdot e^{-i(\omega_k - \vec{k}\vec{r})} \tag{3.17}$$

$$\hat{E}_k^{(-)}(t) \propto (\hat{a}_k)^\dagger \cdot e^{-i(\omega_k - \vec{k}\vec{r})} \tag{3.18}$$

representing the "positive" and "negative" ω_k frequency parts of the mode. For a single mode we can rewrite the $g^{(2)}$ function :

$$g^{(2)}(t,\tau=0) = \frac{\left\langle \hat{E}_k^{(-)}(t)\hat{E}_k^{(-)}(t+\tau)\hat{E}_k^{(+)}(t)\hat{E}_k^{(+)}(t+\tau)\right\rangle}{\left\langle \hat{E}_k^{(-)}(t)\hat{E}_k^{(+)}(t)\right\rangle\left\langle \hat{E}_k^{(-)}(t+\tau)\hat{E}_k^{(+)}(t+\tau)\right\rangle} = \frac{\langle \hat{a}^\dagger\hat{a}^\dagger\hat{a}\hat{a}\rangle}{\langle \hat{a}^\dagger\hat{a}\rangle^2} = \frac{\langle \hat{n}(\hat{n}-1)\rangle}{\langle \hat{n}\rangle^2} \tag{3.19}$$

where $\hat{n} = \hat{a}^{\dagger}\hat{a}$ is the number operator of photons and $\langle \hat{n} \rangle$ is average number of photons in the mode. Thus, we have $g^{(2)}(0) = 0$ for a single photon source.

The $g^{(2)}$ function is proportional to the conditional probability of detecting a photon at time $t_0 + \tau$ given that one photon has already been detected at time t_0. The result $g^{(2)}(t_0, 0) = 0$ indicates that no more than one photon is emitted in each excitation pulse in ideal cases, while $0 < g^{(2)}(t_0, 0) < 1$ corresponds to a partially anti-bunched single photon emission and reveals a purely quantum state of light, and $g^{(2)}(t_0, 0) > 1$ corresponds to bunched photon emission. The case $g^{(2)}(t_0, 0) = 1$ relates to the coherent light.

Reduced antibunching can be used to characterize the biexciton emission: the ratio, here labelled g_0, between the **area** of the zero-delay peak ($\tau = 0$) and the average **area** of the other peaks is reported to represent the quantum yield ratio between mono-exciton and biexciton under the assumptions that 1) both biexciton and exciton emissions are exponential, 2) the excitation is linear (much less than one photon per pulse) and 3) there is no contribution from higher order (> 3) excitons. The intensity correlation function then gives access to the value of the biexciton's quantum yield [153,154].

In addition, B. D. Mangum et al. demonstrated in a post-processing approach that the application of a proper time-gating filter to the $g^{(2)}$ function analysis can help to distinguish the following two cases [155]: 1) biexciton emission from a single emitter; 2) a cluster of several single photon emitters. This approach exploits the fact that the biexciton decay rate is faster than the mono-exciton: by applying a time-gating filter, slow-arriving photons can be selectively analysed, void of the fast-arriving photons that more likely to correspond to the biexciton emission. Thus, one can expect full antibunching ($g^{(2)} \sim 0$) (resp. partial antibunching ($0 < g^{(2)} < 1$)) for single emitters (resp. clusters) from the $g^{(2)}$ function constructed by the post-selected photons.

In practice, we will assign the emitters with $g^{(2)}(t_0, 0) < 0.5$ to single emitters (not ideally equal to zero because of the contribution of minor multi-excitonic recombination and substrate self-luminescence) and emitters with $0.5 < g^{(2)}(t_0, 0) < 1$ to clusters consisted of N emitters which are calculated by [156]:

$$N = \frac{1}{(1 - g_0)} \tag{3.20}$$

under the assumption that all the emitters are identical single-photon emitters.

The Hanbury-Brown and Twiss (HBT) configuration

The $g^{(2)}$ function can be reconstructed from single photon measurements under the Hanbury-Brown and Twiss (HBT) start-stop configuration, which is a powerful tool to reveal the temporal coherence of the emitter based on photon statistical properties.

The Hanbury-Brown and Twiss configuration was first demonstrated in 1956 [146], then it has become a widely used powerful tool for many aspects of scientific research. Generally, in HBT measurements, light is sent to a beam splitter, separated into two paths and measured by two detectors (figure 3-7). The detection results are sent to a correlation card that records the delay times between one photon on one photodiode and the next photon on the other photodiode, from which a second order correlation function can be established.

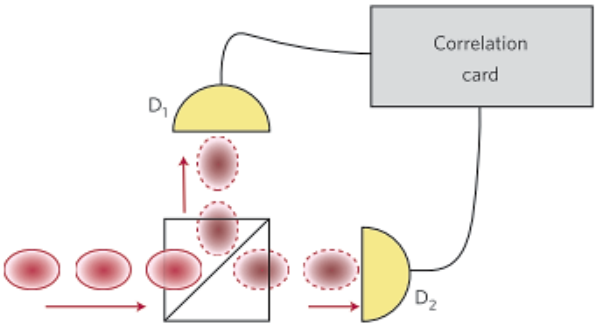

Figure 3-7. HBT configuration. Adapted from ref. [93].

In our experiments, we measured photon correlation functions of both isolated single NPLs and clusters under HBT configuration. We used the 470-nm pulsed laser (70ps pulse width) with 2.5MHz repetition rate to excite the emitter and used the polarizing beam splitter cube (50:50) to separate the emitted photon flux into either reflection or transmission paths to be detected by 2 avalanche photodiodes (APD). The fields E_1 and E_2 measured on the two APDs are proportional to the emitted field, from which we can reconstruct their second-order correlation.

Note that here the use of a polarizing cube is not strictly allowed for a HBT configuration, but it should not induce any parasitic effect.

3.2 Blinking and decay in single NPLs

In this section, we will analyse the blinking behaviour of single CdSe NPLs and compare the radiative rate of on-state and off-state events to preliminarily investigate the involved blinking

mechanism. In the literature, the blinking behaviour of NPLs is actually not much reported [144,157], especially for the core-only CdSe NPLs.

Besides, we will also analyse the decay dynamics of single NPLs. It has been reported that the surface defects, poorly passivated surface states and crystal defect (e.g., cadmium vacancies) are related to charge trapping mechanisms [158], resulting in non-emissive emitters or modified decay dynamics [16]. The trap-induced fast non radiative recombination is reported to have a decay rate on the order of 10 ps [159]. However, in the literature, most decay analyses are focused on the fast component (transient portion) of the decay curve, while the slow decay tails are normally neglected. In this section, we will study the decay dynamics of single NPLs both on the transient fast portion and the slow decay component.

3.2.1 Blinking in single NPLs

Typical blinking behaviour of single NPLs

In single CdSe NPLs, their typical blinking curves consist of major on-state events and minor off-state events, as shown in figure 3-8 (a). To obtain information on the blinking mechanism, we can calculate the ratio of radiative recombination rates between different emission states as color-coded in figure 3-8 (b).

The emission intensity from NPLs under pulsed excitation is proportional to their quantum yield, which can be related to the radiative and non-radiative recombination lifetimes, as:

$$I \propto \frac{\gamma_{rad}}{\gamma_{rad}+\gamma_{nr}} = \frac{\tau}{\tau_{rad}} \tag{3.21}$$

in which γ_{rad} and γ_{nr} are respectively the radiative or non-radiative recombination rate, τ is the overall lifetime and τ_{rad} represents the radiative recombination lifetime. We can estimate the ratio of radiative recombination lifetime τ_{rad} between different states by:

$$\frac{\tau_{rad1}}{\tau_{rad2}} = \frac{\tau_1}{\tau_2} \cdot \frac{I_2}{I_1} \tag{3.22}$$

We use this equation in order to extract the radiative lifetime fluctuations of our single platelet (even though this equation relies on an exponential decay model which is not perfectly verified here). In figure 3-8 (c) we list the average intensities of different color-coded states and their corresponding decay lifetimes (defined as the time of decay by a factor of 10). We take the on-state emission (purple

area in figure 3-8 (b)) as a reference and plot the normalized radiative lifetime of all states in figure 3-8 (d). It is found that the radiative recombination rate does not change significantly as the emission intensity varies, remaining in the range of 0.85 - 1.3 while the total decay rate changes significantly (figure 3-8 (c)).

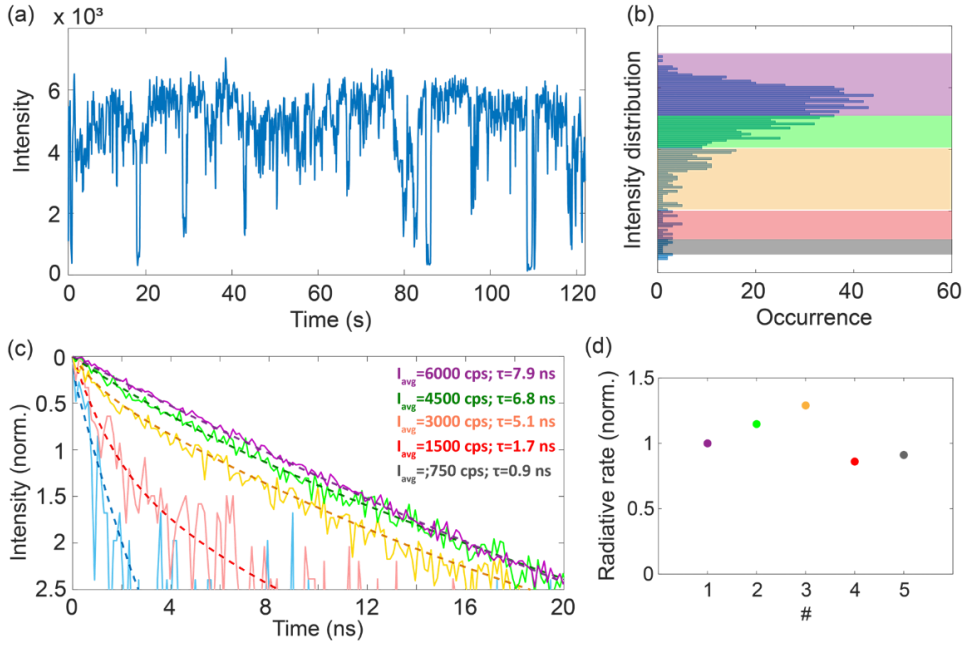

Figure 3-8. (a) Typical blinking behaviour of a single CdSe NPL. Excitation power: 7 nW. Binning time 100 ms. (b) Intensity distribution of (a). Different intensity ranges are coded by colors. (c) Decay curves of different color-coded intensity ranges. (d) Normalized radiative recombination rates of different intensity ranges as color-coded in (b) and (c).

The overall lifetime of the low-intensity portion is much faster than that of the high-intensity portion, suggesting the absence of type B blinking. Thus, our samples clearly possess type A blinking, and more precisely the trend of figure 3-8 (d) indicates type A′ blinking. The decay curve of the highest intensity portion (purple) is quasi mono-exponential, which can be attributed mostly to the radiative recombination of the neutral exciton. In the grey and red portions in figure 3-8, the emission intensity is quenched by fast non-radiative decay channels, either by Auger process or by band-edge trapping channels, or by a combination of them.

In the literature, mostly people found Auger blinking together with other blinking mechanisms in quantum dots [132,133]. Here in our preliminary measurements, the result suggests the BC-blinking and excludes the HC blinking. This result is in consistence with another report on the BC-blinking in CdSe NPLs sample [144]. To determine the physicochemical mechanism of the blinking in our single NPLs, further studies would be necessary, such as electrochemical analysis (which is beyond the scope of this thesis).

Power dependent blinking behaviour of single NPLs

To understand more about the origin of the blinking in single NPLs, we performed power dependent analysis, with excitation power varying between 1.5 nW and 10 nW. Note that it is delicate to use neither lower excitation powers, because the detected photon counts are not enough to construct intensity time traces with decent signal-to-noise ratio, nor higher excitation powers, because pure CdSe NPLs, unlike the core shell NPLs that widely reported in the literature, are less light-resistant and will be bleached quickly at higher power.

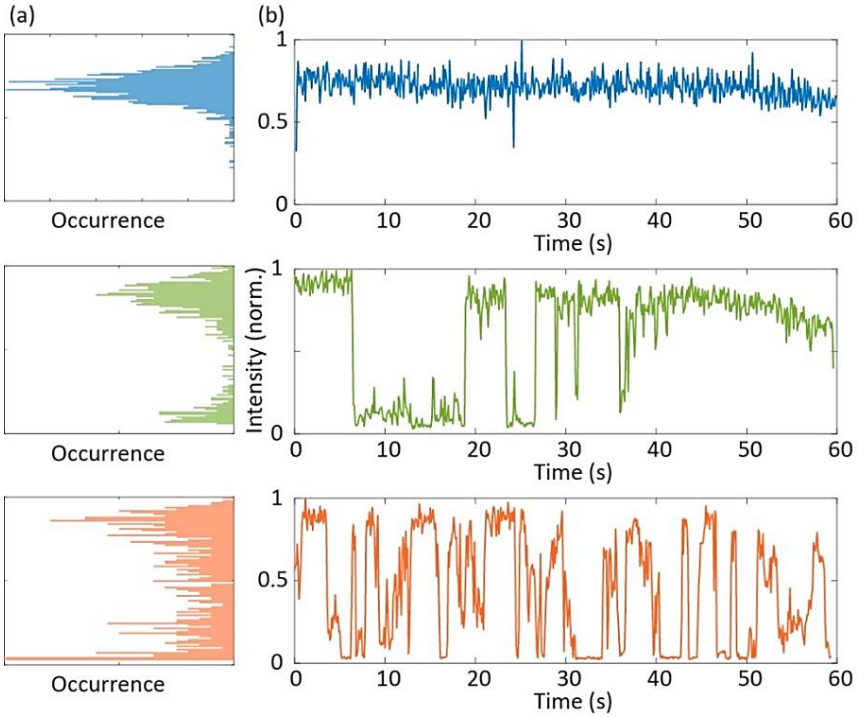

Figure 3-9.(a) Intensity distribution of time trajectory (b) (binning time 100 ms) of the same single nanoplatelet under (top) 1.5 nW, (middle) 5 nW and (bottom) 10 nW excitation.

We show in figure 3-9 the curves of a same single NPL at three different excitation powers: 1.5 nW, 5 nW and 10 nW. The blinking becomes more frequent as the power is increased: at 1.5 nW, the emitter is mostly in on-state with barely any contribution from off-state or intermediate grey-state in the emission. When the power is increased to 5 nW, we start to see quasi binary blinking between on- and off-state with few intermediate "grey-state" appearing. Then at 10 nW, we have much more frequent blinking, with a significant grey-state contribution. It indicates that, with higher excitation power, more non-radiative channels are generated in NPLs and consequently the switch between on-state and off-state become more frequent, resulting in the flickering grey state. We also analysed for these power-dependent experiments the decay rates of different emission states. Again, we found that

the high intensity portion has longer lifetime while the low intensity portion are much faster in decay, due to non-radiative decay channels.

3.2.2 Decay in single NPLS

Multi- and mono-exponential decay in single NPLs

We statistically studied numerous single NPLs, revealing two kinds of typical decay dynamics as shown in figure 3-10 (a): the green curve has a major mono-exponential fast component (0-50 ns), followed by minor slow components (50-100 ns), while the blue curve shows another typical decay behaviour that is more multiexponential, consisted of a faster transient decay component (0-10 ns) and a more significant decay tail (slow components).

It is important to explore the origins of these different decay behaviours and to understand if either one of them represents the intrinsic behaviour of single NPLs while the other one is modified by some effects of defects, or both of them are intrinsic behaviour of good-quality NPLs differing in lateral sizes, etc.

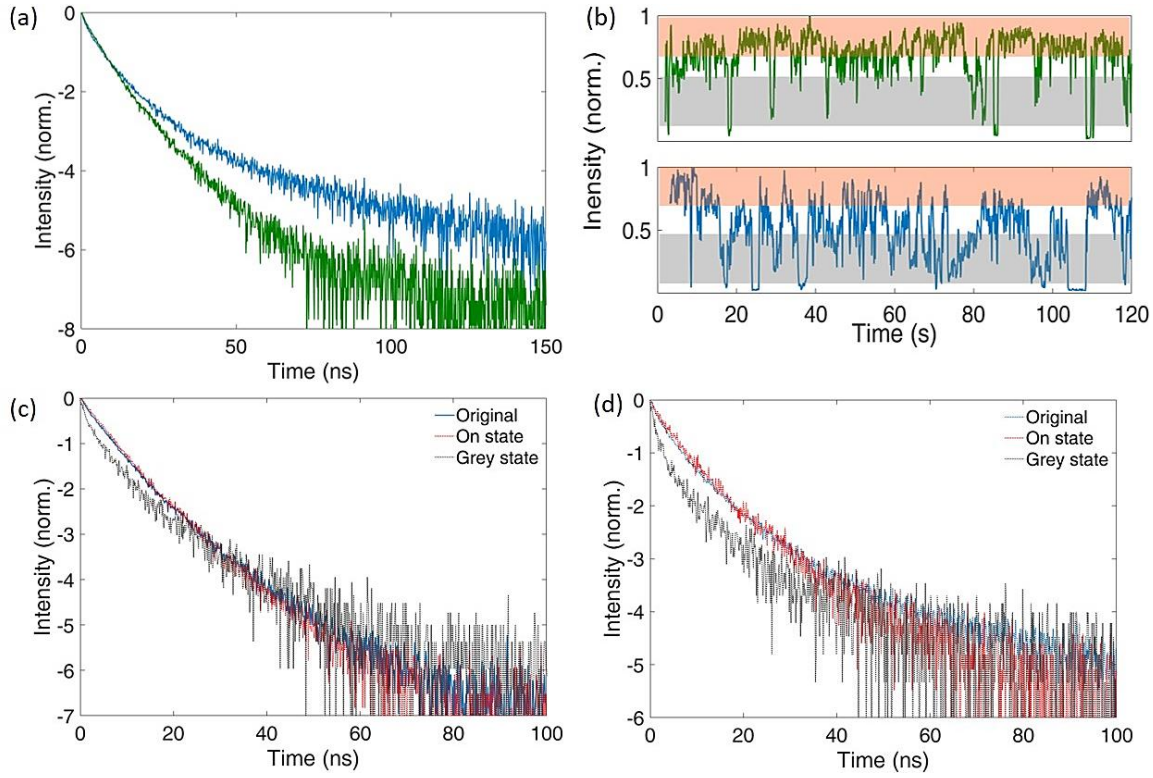

Figure 3-10. (a) Decay curves of two types of NPLs: mono-exponential type (green) and multi-exponential type (blue). Excitation power: 7 nW. (b) Blinking behaviour of these two NPLs, one is mostly in on-state (green) while the other one blinks more frequently (blue). (c) and (d) compare respectively the less-blinking and more-blinking NPL's decay dynamics of their on-state (red shaded area in (a)) and off-state (grey shaded area in (a)) emissions.

To this end, we first compare their blinking behaviours in figure 3-10 (b). The multi-exponential-decay NPL possesses more frequent blinking, with significant contributions from intermediate grey-state while the on-state intensity is very unstable. On the contrary, the mono-exponential NPL shows more stable on-state emission with less blinking events, which is a signature of the single nano-emitters with good quality (or to say with fewer defects). Thus, we assign the mono-exponential decay to the intrinsic decay characteristic of a good-quality NPL. It also implies that there is a correlation between the off-state in blinking trajectory and the slow components in multi-exponential decay curves.

Origin of the multi-exponential characteristic in decay

To further investigate the correlation between the off-state and the slow components, we respectively analyse the decay curves of the on-state events (red shadow in figure 3-10 (b)) or grey-state events (grey shadow in figure 3-10 (b)). It manifests that, for both of the less-blinking NPL (figure 3-10 (c)) and the more-blinking NPL (figure 3-10 (d)), their on- and grey-state events decay in very different manners: the on-state's decay stays quasi mono-exponential (red lines) with slow components (tails) becoming less obvious, while the off-state's decay (in grey) trends to become more multiexponential, with a notable acceleration in the fast component (transient part) and more significant slow components in the tail of the decay curve. It indicates that the multi-exponential type of decay dynamics is more related to off-state that originates from defects in NPLs, while the quasi mono-exponential type of decay is more related to the on-state emission, which is a signature of neutral exciton' recombination in good-quality emitters.

Origin of slow decay components in multiexponential decay

Now we characterize the power dependent decay dynamics on a same NPL. As presented in figure 3-11, different excitation powers result in different decay characteristics, changing from quasi mono-exponential to multi-exponential. As power increases, the fast component (0-20 ns) remains almost the same (with a tiny acceleration) while the slow component (40-100 ns) becomes more significant. This suggests that the slow component is related to photo-induced defects which are boosted by higher excitation power. This power-dependent measurement is within the linear excitation regime as demonstrated in chapter 2. Figure 3-11 (b) depicts the corresponding antibunching curves of the same measurement, from which we further confirm that the experiments remain in single exciton regime.

Thus, power dependent measurement suggests that the emerging slow component in decay curve is not due to non-linear effects of multiexciton, but can be generated from photo-induced defects, which is consistent with our conclusion that the multi-exponential decay characteristic originates from defects in NPLs. Here we interpret the slow components in decay curves of single NPLs by **trapping/de-trapping retardation:** some charges may be trapped in deeper defected states for some delay time, before de-trapping and sequent radiative/non-radiative recombination.

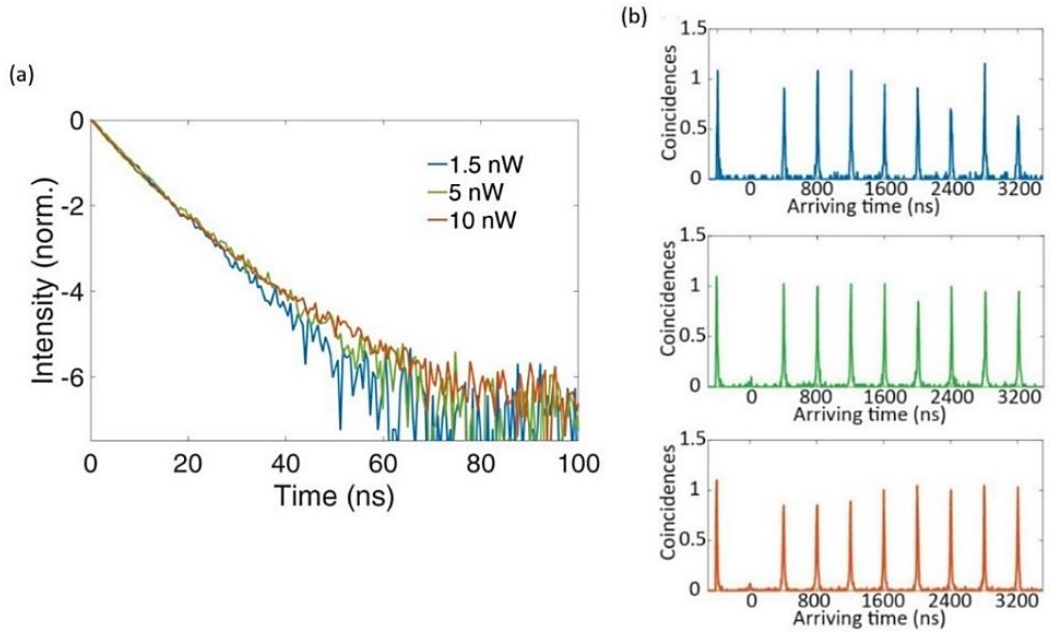

Figure 3-11. (a) Power-dependent decay curves of a same NPL and (b) the corresponding photon correlation functions under (top) 1.5 nW, (middle) 5 nW and (bottom) 10 nW excitation.

3.2.3 Conclusion

In this section we studied the blinking and decay behaviours of single CdSe NPLs. By analysing the decay curves of on- and off-state events, we excluded the type B blinking mechanism in our sample and found that the type A blinking mechanism may correspond to Auger and BC blinking. We also found that the good-quality NPLs have stable on-state emission with less blinking as compared to the NPLs with more defects. For the decay dynamics, we observed a correlation between the off-state events in blinking and the presence of a well-known additional fast component but also an additional slow component in the multi-exponential decay. Our blinking and decay analysis suggests that the defects in NPLs modify the decay curves of single NPLs from mono-exponential to multi-exponential, and the slow component in decay curves may be attributed to the traps in the defected sites of the NPLs.

3.3 Blinking and decay in clusters and chains

In the literature, photophysical characteristics of assembled emitters have been studied a lot on various systems, including quantum dot molecules [160], cluster of core/shell quantum dots [103], cluster of nano rods [161], etc. For assembled NPLs, there are many studies involving photophysical properties as well. For examples, B. Guzelturk et al. demonstrated that in stacked CdSe NPLs, photoluminescence quantum yield and lifetime are decreased by an order of magnitude, resulting from FRET-assisted strong quenching [16]; Y. Gao et al. controlled the orientation of CdSe NPLs layer, either face-down or edge-up, using liquid−liquid interfacial assembly, and showed that the face-down assembly has a longer lifetime, which is attributed to suppressed exciton diffusion to quenching sites [12]; C. Rowland et al. reported on the picosecond FRET in CdSe NPLs solids consisted of 4 or 5 mono-layer emitters [15].

However, time- and ensemble-averaging may obscure these effects, as shown by the previous section, and systematic studies on blinking or decay mechanisms of NPL assembly is still lacking. In this section we will analyse the decay and the blinking behaviour of assembled CdSe NPLs, including clusters and self-assembled chains.

3.3.1 Blinking and decay in clusters

The typical blinking mechanism in NPL clusters

Similar to analyses of single NPLs demonstrated in the last section, figure 3-12 (a) and (b) show the blinking time trace of a typical NPL cluster together with its intensity distribution. Unlike the single NPLs, in clusters we have multiple NPLs being excited at the same time, leading to an average effect that the off-state is averaged out, forming the intermediate “grey-portion”. In the study of clusters, we will use the terms “bright events” and ‘grey events’ to denote the different portions in intensity time traces.

Figure 3-12 (c) shows that the decay of both bright and grey events are very multi-exponential, and the brighter events have longer lifetime as compared to the darker events.

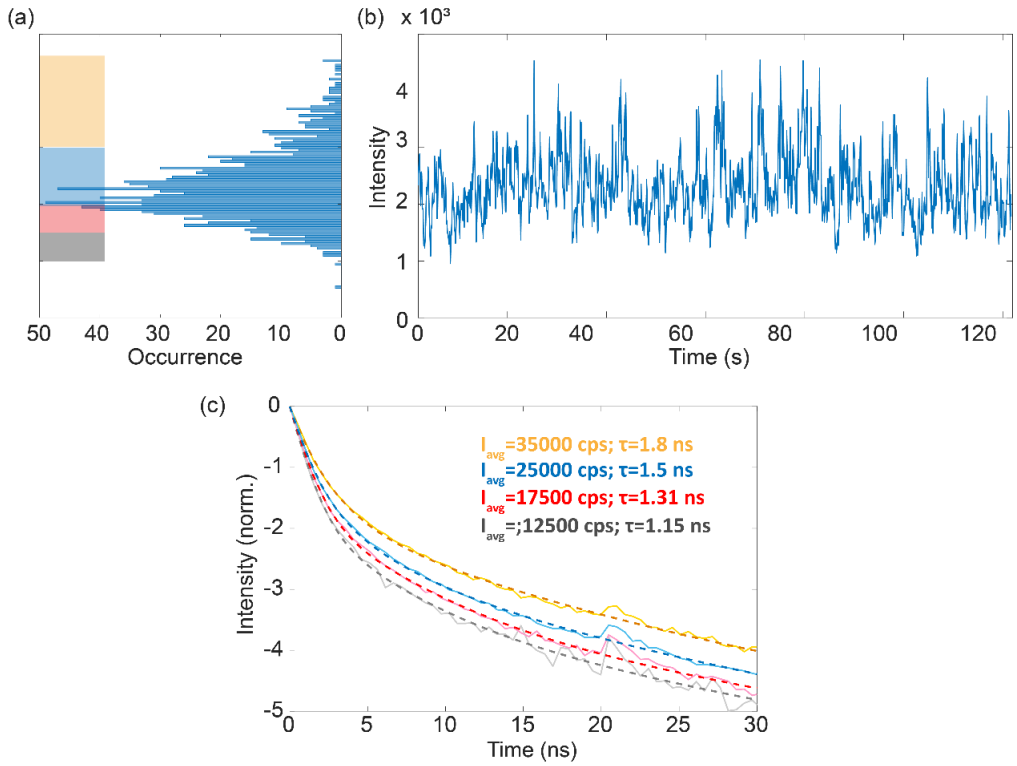

Figure 3-12. Intensity distribution (a) of the intensity time trace (b) of a typical CdSe NPL cluster. Excitation power: 7 nW. Binning time 100 ms. (c) Decay curves of different intensity ranges as color-coded in (a).

Collective blinking in clusters

In addition to the typical chaotic blinking in clusters as shown above, in some special cases, we also observed in intensity time traces a collective binary switch between two distinct emission states: "brighter state" (red-coded area) and "darker state" (grey-coded area) as shown in figure 3-13 (a).

As a complementary measurement, figure 3-13 (c) presents the antibunching curve of this cluster. We have $g^{(2)}(0)\sim0.8$ for the brighter events (coded by red in figure 3-13 (c)) and $g^{(2)}(0)\sim0.6$ for the darker state emission (coded by black), which indicates that we have 2~3 NPLs contributing to the emission of the darker events and ~5 NPLs contributing to the brighter events (the estimation of the number of NPLs in a cluster will be given later in section 3.5). Thus, this observation can be interpreted by two emitting groups: the darker state corresponds to the case in which only one emitting group contributes to the emission while in the brighter states, both of the two emitting groups are active and contribute to the emission simultaneously. Figure 3-13 (c) shows that the darker state has a faster decay, which may be due to the activation of more efficient non-radiative decay channels.

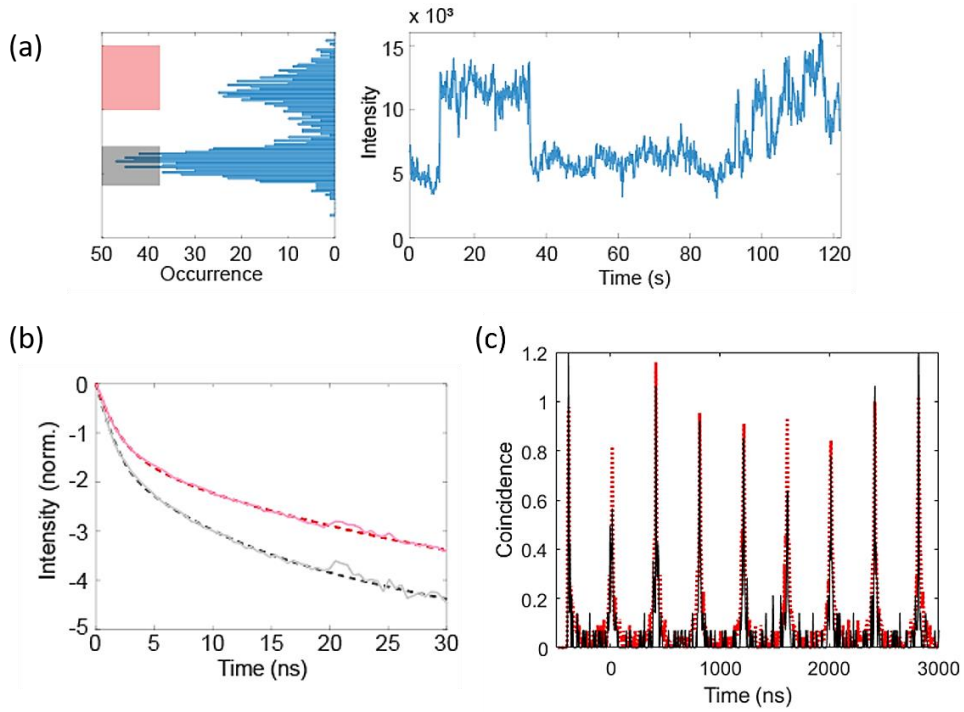

Figure 3-13. (a) The intensity distribution and the intensity time trace of a special CdSe NPL cluster. Excitation power: 7 nW. Binning time 100 ms. (b) Decay curves of different emission states as color-coded in (a). (c) Antibunching curve of different emission states as color-coded in (a).

3.3.2 Blinking and decay in chains

Blinking behaviours in chains

NPLs chains generally have less blinking than single NPLs and NPL clusters, because more NPLs (~50) are simultaneously excited by the laser beam and thus the off-state is averaged out. However, we still find interesting collective blinking behaviours on different samples.

As introduced in chapter 1, we have two batches of chain samples with different lengths: the shorter chains are typically 100-500 nm and the longer chains are normally over 1000 nm. We compared the collective blinking behaviours of short and long chains and we found that, generally, long chains have less obvious collective blinking as compared to short chains. In figure 3-14 (d), the intensity fluctuations correspond to 20 to 50 % of the maximum intensity: since a short chain contains 20 to 90 NPLs, these fluctuations would correspond to simultaneous on/off switching ("collective blinking") of 4 to 45 NPLs.

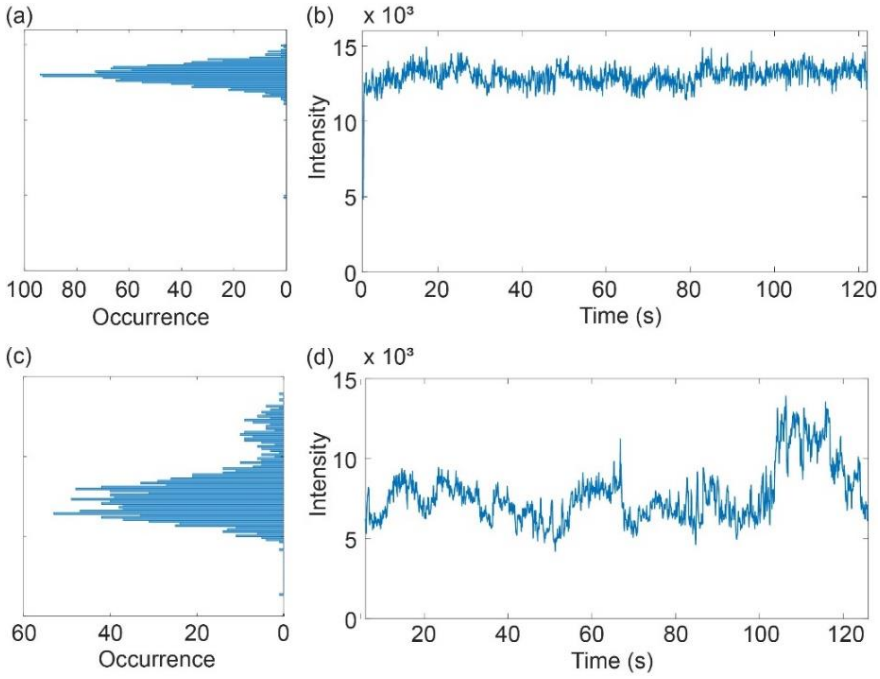

Figure 3-14. Typical blinking behaviours of (a) and (b) long or (c) and (d) short NPLs chains.

To investigate the origin of the brighter events in emission, we sonicated the non-blinking long chains to increase the number of defects on them and then compared their blinking trajectory to the same kind of long chain samples without sonication. As shown in figure 3-15, the sonicated long chains start to display frequent blinking, similar to the blinking behaviour of short chains (figure 3-14 (b)). Comparing figure 3-15 (b) and (d), we obtained similar photon counts per second, but under different excitation power (within the linear excitation regime of the chain as discussed in chapter 2): the former one is under lower excitation (~3 nW) while the later one is at higher power (~7 nW). This can be explained by defect-induced effect: in sonicated chains (which have more defects), excitons are more likely to decay through fast non-radiative channels, resulting in a lower quantum yield. Thus, the blinking behaviour in a chain may be dominated by "super quenchers", i.e. very efficient non-radiative decay channels.

In addition, the fact that the short chains have more collective blinking than long chains may indicate that the defects participated more in the short chain than the long chain. This might occur because: 1) there are intrinsically more defects in the non-twisted chains (short chains), as compared to the long chains which are twisted; in other words, the twists can help to release the inter-NPL strain and consequently to reduce the defects in chains; 2) in shorter chains, excitons can be transferred by FRET over the whole NPLs, increasing their chance to meet with the fast decay channels.

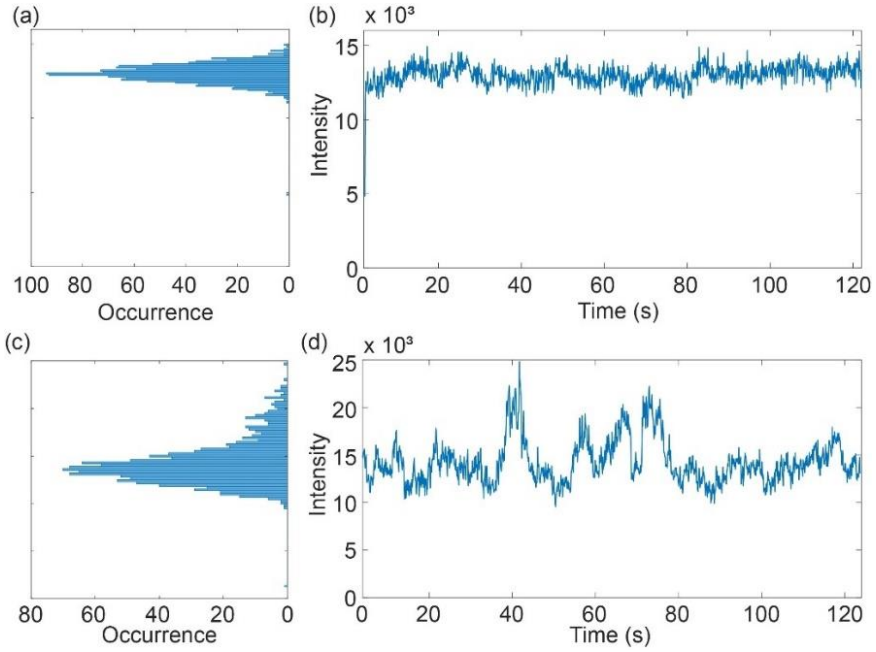

Figure 3-15. Typical blinking behaviour of a chain without ((a) and (b)) and with ((c) and (d)) sonication. Excitation power: 3 nW for (a) and (b), 7 nW for (c) and (d).

3.4 Assembly-induced effects and interpretations

In the last two sections, we have analysed the blinking and decay behaviours of different NPLs emitters, including single NPLs, clusters and chains. In this section we will compare the blinking and the decay of these different emitters and reveal the influence of self-assembly on the fluorescence properties of CdSe NPLs.

Emerging blinking/decay features induced by self-assembly

Figure 3-16 (a) presents the typical blinking behaviours of three kinds of NPL emitters: single NPLs (blue), clusters (orange) and chains (green). All emitters show intensity fluctuations, however the single NPLs usually present clear binary blinking switching between on- and off-state, while the clusters present a more chaotic intensity time trace as might be expected from a sum of several independently blinking emitters. For the NPL chains, the intensity fluctuation is very low, which can be attributed to an averaging of the blinking of more emitters.

We can roughly quantify the extent of blinking by a blinking factor (standard deviation), which is defined as:

$$S = \sqrt{\frac{1}{N-1}\sum_{i=1}^{N}|I_i - \bar{I}|^2} \tag{3.23}$$

in which N is the number of time binning in the intensity time trace and I represents the intensity value of the i^{th} time bin. It appears that the blinking factor is generally lower for the clusters than for the single platelets (figure 3-16 (d)). As for the chains (which are not plotted in the figure), their blinking factors are typically 0.05-0.1.

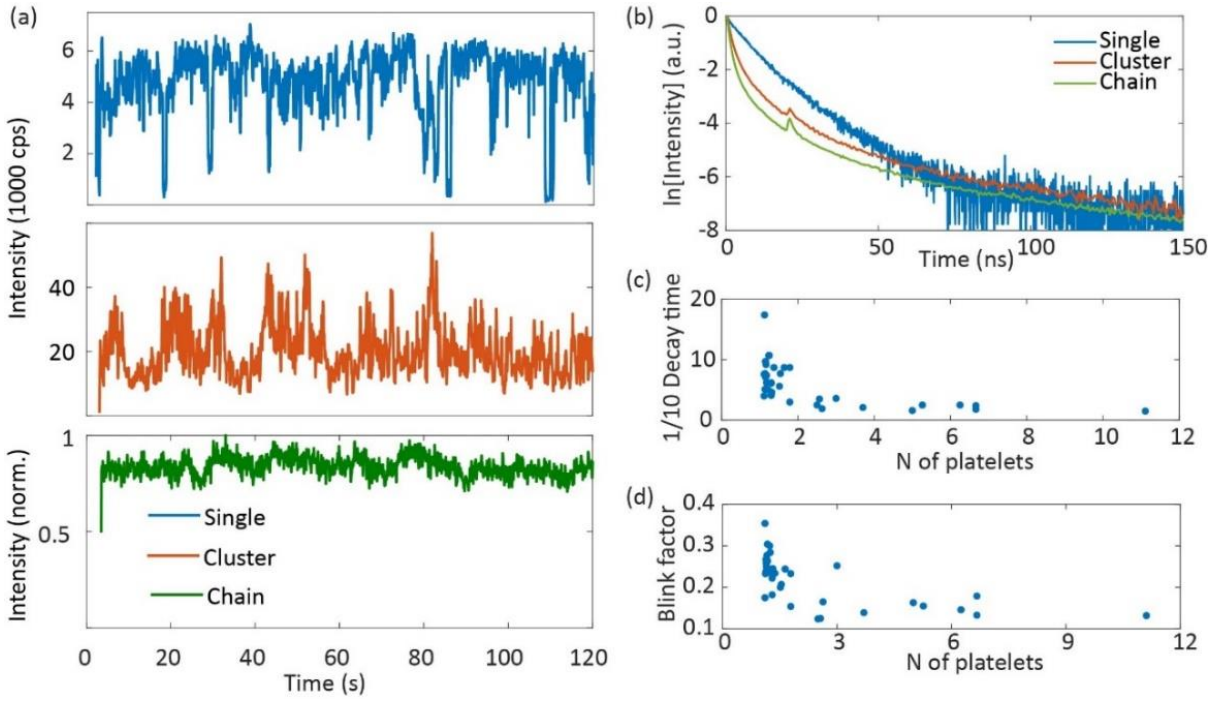

Figure 3-16. Intensity time traces (a) of typical single platelet (blue), NPL cluster (orange) and long NPL chain (green). And their corresponding decay curves (b). (c) Decay lifetimes (defined as the time of decay by a factor 10) as a function of the number N of NPLs in NPL emitters. (d) Blinking factors as a function of the number N of NPLs in NPL emitters.

The typical decay curves for single NPLs, clusters and chains are shown in figure 3-16 (b). The single NPL's decay is quasi mono-exponential with negligible slow components (a noise tail), which is typical behaviour for exciton recombination in a semiconductor nano-emitter. For the clusters and the chains, on the other hand, their decay curves are multi-exponential: the transient component is much faster than the single NPLs while the slow component becomes significant.

Thus, the first assembly-induced effect that can be concluded is that, **self-assemblies can significantly accelerate emitter's fast decay component as compared to the non-assembled emitters**. We can interpret it by the **FRET assisted exacerbation of trion recombination**.

<u>Modulations of assembly's collective behaviour by defected NPL</u>

Although we keep the excitation power within the linear regime of CdSe NPLs, we can still efficiently achieve trion recombination thanks to the ultrafast homo-FRET between NPLs in the

assembly, whose transfer lifetime (estimated to be 1.5 ps [31]) is much shorter than any other recombination mechanisms in the system, as discussed in chapter 2. Thus, excitons can be funnelled to the fast decay sites by FRET, resulting in an acceleration in decay.

For the slow decay components of assembled emitters, similar to single NPLs, we expect them to be induced by trapping/de-trapping retardation: charges stay in the trapping states for some time before de-trapping and sequent radiative/non-radiative recombination. However, in assemblies the slow decay components are more significant than that in single NPLs, because excitons have more chance to be trapped by the retardation sites in the chain with the help of FRET.

To sum up, the defected NPLs in the assembly can be regarded as a modulator, controlling the decay dynamics of the whole chain with the help of FRET.

Model: FRET induced trion decay in assembly

Now we propose a trion decay model to represent the process of obtaining trion under linear excitation regime, as shown in figure 3-17.

The first row shows that the first laser pulse generates an exciton in "NPL1". One charge of the exciton, e.g. the hole, is trapped by the defected sites on the chain, either on the same NPL ("NPL1") or on another NPL transferred by FRET. In the second row, another exciton is generated on "NPL 2" by the sequent laser pulse. With the help of the FRET (the third row), the later generated exciton can be transferred (funnelled) to the sites with trapped charge (i.e. "NPL1"). At this point, we have trions on the same NPL.

Then, with multi-ion on the same site, we can expect the trion radiative (resp. non-radiative) recombination as shown in the left (resp. right) panel in the fourth row on figure 3-17. Both of these decay channels are faster than the recombination rate of a neutral exciton, resulting in the acceleration in the fast decay component. The fast non-radiative recombination process, i.e. FRET assisted quenching, has already been reported by many other groups [9,11,12,16]. However, the presence of the radiative trion recombination is still not clear, which remains to be investigated in future work.

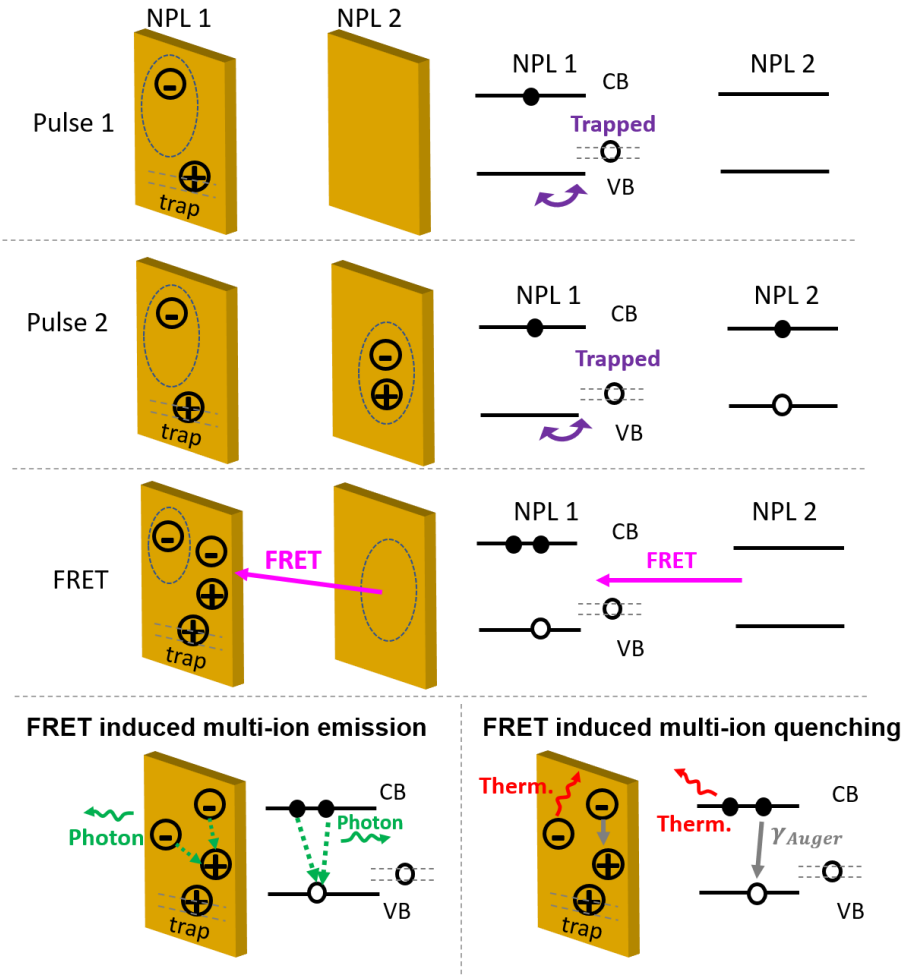

Figure 3-17. Model of FRET induced trion decay.

3.5 Antibunching in CdSe NPLs

Antibunching in CdSe single NPLs

In the literature, antibunching in CdSe NPLs has been reported by a few groups [144,151]. Nevertheless, most of the studies focus on NPLs with core-shell structure while core-only CdSe single NPLs as well as their clusters have never been considered.

Here we report for the first time, to the best of our knowledge, on antibunching in pure CdSe single NPLs. In figure 3-18 (b), the second-order photon correlation function $g^{(2)}$ of a representative single NPL shows clear antibunching, with g_0 factor (we will label here g_0 the ratio between the area of the zero-delay peak and the averaging area of the successive peaks) as low as ~0.1, indicating that single CdSe NPLs can be promising candidates for single-photon sources. For most of the single NPLs, the factor g_0 is in the range of 0~0.2, which can be mainly attributed to the substrate self-luminescence with minor multi-exciton recombination. For some other single NPLs, the g_0 is in

range of 0.2~0.4. In this case, we believe there is more contribution from multi-exciton recombination, which may result from the less efficient Auger effect in large-area NPLs [151].

Identification between single NPL and clusters

One can use $g^{(2)}$ functions combined with a photon post-selection, as demonstrated in figure 3-18 (a), to distinguish between single and clustered CdSe NPLs, which are all looks like point emitters from the microscope.

The post-processing, i.e. time gating, can be used to eliminate the contributions both from multi-excitonic recombination and substrate self-luminescence, as these contributions correspond to faster (a few ns) decay. We set the gating time to be 2 ns so that only the photons detected more than 2 ns after the excitation laser pulse contribute to the $g^{(2)}$ function. Figure 3-18 (b) and (c) show the photon correlation functions $g^{(2)}(\tau)$ for a single NPL and a cluster, respectively. The blue solid lines show the original antibunching curves while the red dashed lines show the temporal filter selected curve, in order to remove the multi-excitonic contribution.

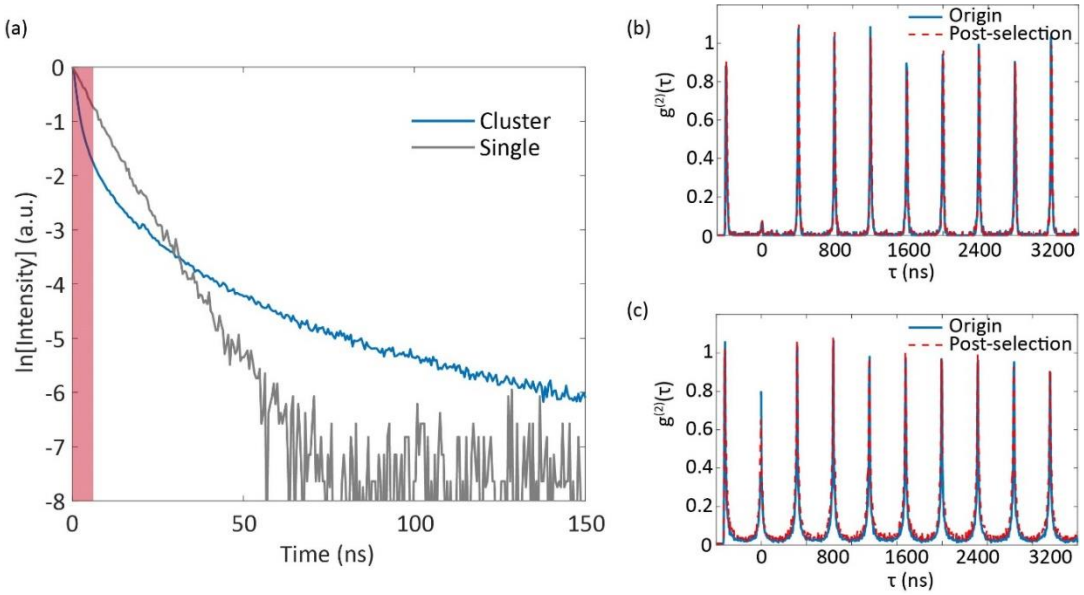

Figure 3-18. (a) Decay curves from two emitters, one attributed to a single NPL and the other to a cluster. Photon correlation curves of (b) the single NPL and (c) the cluster: as compared to the original curve (full line), the post-selected curves (dotted line) are obtained by selecting only photons after 2 ns in the decay curve (excluding the red interval in (a)). The post-selected curve improves partially the antibunching for the cluster, however not to a full single-photon emission.

As introduced in section 3.1, we assign the emitters with $g^{(2)}(t_0, 0) < 0.5$ to single emitters and emitters with $0.5 < g^{(2)}(t_0, 0) < 1$ to be clusters consisted of N emitters which are be calculated by:

$$N = \frac{1}{(1-g_0)} \tag{3.24}$$

For the NPL cluster, after post-selection, we still find only incomplete antibunching with $g_0 \approx 0.68$. Thus, we attribute this case to be a cluster consisted of 3-4 NPLs. Meanwhile, blinking and decay characteristics of the emitter (as demonstrated in figure 3-16) can also help to corroborate the identification of a single NPL emitter: single NPLs have a binary blinking and quasi mono-exponential decay dynamics, while the assembled NPLs have averaged blinking behaviour and multi-exponential decay profiles.

3.6 Conclusion and perspectives

In this chapter, we investigated the general characteristics of the fluorescence behaviours, including blinking, decay and antibunching of CdSe NPLs in various structures, from single NPLs, clusters to assembled NPLs chains.

For single NPLs, they usually present clear binary blinking switching between on- and off-state, with type A and/or type A' characteristics induced probably by Auger effect and/or band-edge non-radiative channel. Their decay curve is quasi mono-exponential while the multi-exponential decay, with more significant slow decay components, arises in the NPLs with many defects, which may be attributed to retardation induced by trapping sites.

For assembled NPLs, i.e. clusters and chains, their decay and blinking behaviours are very different as compared to single NPLs: in intensity time traces, their off-state emission is averaged out, resulting in the flickering intermediate grey states; their decay profiles become highly multi-exponential, consisting of a fast decay component followed by significant slow components.

The acceleration in the fast decay component originates from the FRET assisted effect, involving nonradiative Auger quenching and possibly radiative trion recombination (which remains to be confirmed). Meanwhile, the slow decay components are attributed to the trapping/de-trapping retardation in the defected site in the emitter. In assembled NPLs, the trapping states are more involved with the help of homo-FRET funnelling to the traps, as a result, their slow decay components are more significant compared with single NPLs,

Nevertheless, the interpretations appearing in this chapter are based on preliminary experiments. More work is necessary to confirm the results on larger statistical collections of acquisitions and to have a good view of defect-related effects.

Additionally, for the blinking analysis, we can record blinking videos for the chains to have access to spatially-resolved information, such as the variation in the position of the emitting center (or quenching center) and the variation in their emission intensity. This method can be combined with intensity time trace analysis, which is expected to be able to extract underlying information on blinking mechanisms in the assembled systems.

Chapter 4. Analyses of transition dipole components

Introduction

In this chapter we will investigate the dimensionality and orientation of dipoles in CdSe NPLs emitters, from single isolated NPL to linearly assembled NPL chains. A combination of polarimetry and Fourier plane image analysis will be employed to probe the proportions of dipole components in single emitters, with a record precision reaching ± 0.03 by a careful design of the experimental configurations. For single NPLs, we will study their dipole components, which can work as a reference for the measurements on NPLs chains. Then we will analyse the assembled NPLs (clusters and chains) and compare the result to single NPLs. Thanks to the precision of our micro-photoluminescence analysis protocol, here we will report for the first time the out-of-plane dipole component in self-assembled stacks of CdSe NPLs, and several hypotheses of its origin will be discussed.

In the first section of this chapter, we will first introduce the principle of polarization analysis as well as its experimental implementation. Then we will introduce Fourier plane and show the theoretical calculation of radiation patterns obtained under different experimental configurations. After that, we will explain the protocol of Fourier plane imaging with intuitive examples and demonstrate the influence of experimental configurations on the results of both polarization analysis and Fourier plane imaging, pointing out the necessity of a careful design of experimental configurations for optimizing the measurement resolution. We will finish this section by a state of the art of dipole analyses for single and ensembled NPLs as well as other fluorescent systems.

In the second section, we will apply the dipole analysis protocol on single isolated CdSe NPLs to confirm the absence of the out-of-plane dipoles. We will also estimate the resolution of our protocol. These results will work as a reference for the measurements on NPLs chains in the next sections.

In section three, we will apply the dipole analysis protocol on NPLs chains. The goals are 1) to verify the presence of the vertical dipole in the chain since NPLs stand on their edge, and 2) to check again the presence/absence of the out of plane dipole component in the chain. Then in section four we will study NPLs clusters with different sizes as intermediate cases and summarize in section five how the out-of-plane dipole evolves as the number of assembled NPLs is increased. By comparing the results of single NPLs, clusters and chains, we study effects of the stacking dielectric shape on

the dipole property, which will improve our understanding on photo-physics in self-assembled nanostructures.

Then we seek for the explanation for the emerging out-of-plane dipole component. In the sixth section, we will perform FDTD simulation to estimate the efficiency of dielectric enhancement for the dipole in chains and exclude the hypothesis that the emerging dipole component solely results from an antenna effect.

In the last section, we will study and discuss possible explanations and suggest that the added out-of-plane dipole can be induced by strain-induced nanoplatelet deformations due to assembly.

4.1 Protocols of dipoles analysis

Typically, the radiation of a single photoluminescent emitter may be described by a single linear dipole, or by an incoherent sum of several orthogonal dipoles. Considering optical selection rules, one can deduce the number (figure 4-1) and the polarization orientation of optically allowed transitions from the different degenerated state (as shown in chapter 1), which is the origin of the dimensionality and the orientation of dipoles in an emitting system.

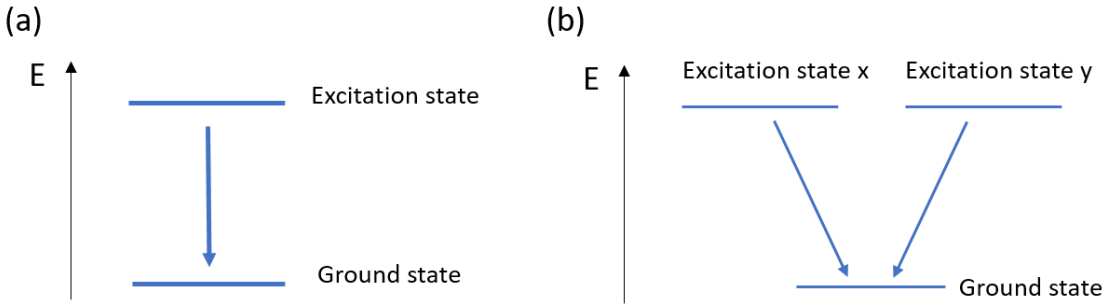

Figure 4-1. Schematic of 1 dipole (a) or 2 dipoles (b) transition.

In the literature, there are many reports on both 1-dipole emitters (such as CdSe/CdS nanorod [162], molecules [163,164]) and 2-dipole emitters (molecules [165], NV centers [166], colloidal quantum dots [167]). Accordingly, a 3-dipole emitter corresponds to the incoherent sum of three linear dipoles (which can be achieved experimentally for instance with fluorescent nanospheres containing a large number of fluorescent dye molecules). In our case of CdSe NPLs, their emission has been experimentally and theoretically shown to consist in 2 orthogonal linear dipoles [6,29,77] parallel to the NPL plane.

Knowing the number of contributing dipoles is not the end of the story. We also need to learn about the orientations of all the dipole components in emitters, for a purpose of optimizing the light matter interaction in plasmonic or photonic systems for instance.

Figure 4-2 demonstrates the definition of the orientation in 1-dipole or 2-dipole models. For the 1 linear dipole model (left), its orientation $\vec{d}$ is along the oscillation direction while in the case of 2-dipole model (right), the dipole orientation $\vec{d}$ is defined as the normal to the plane formed by the two orthogonal dipoles. We use an azimuthal (in-plane) angle Φ and a polar (out-of-plane) angle Θ to described the orientation of the dipole and, in the same time, we denote the orientation of the emission from either 1 dipole or 2 dipoles by the angle (θ, φ).

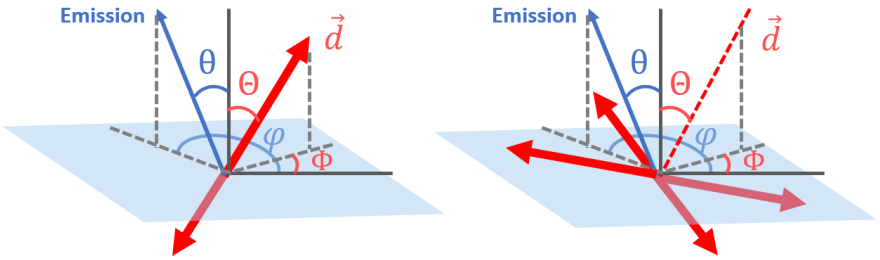

Figure 4-2. Illustration of dipole orientation in 1-dipole (left) and 2-dipole (right) models. The orientation of emission is defined by the angle (θ, φ) and of dipole is defined by the angle (Θ, Φ).

The dimensionality and the orientation of oscillating dipoles in a single emitter is critical for studies in nano-optics and plasmonics, because the dipole properties of an emitter has a strong influence on its coupling to the environment [168,169]. With this in mind, various methods have been suggested to probe the information on emitting dipoles. Early study using polarizing spectroscopy[170,171] has been working well to probes the in-plane angle Φ, but it has limitation in probing the polar angle Θ. Then, another widely employed method to measure the polar angle Θ is the defocused imaging, which is very convenient to implement [172,173]. However, this method is limited by the detection efficiency of the sensor and the emission intensity of the emitters, especially in the case of single emitters with very weak emission, because the resolution is constructed by dispersing the detected photons on many pixels.

Previously in our group, Clotilde Lethiec has demonstrated during her thesis (advisors A. Maître and L. Coolen) a protocol to probe the three dimensional orientation, i.e., both Φ and Θ, of a 1-dipole or 2-dipole emitter by polarimetry [174]. Then in the works of Fu Feng and Loan Thu Nguyen (advisors A. Maître and L. Coolen), they have combined the polarimetry with Fourier plane imaging,

which gives not only the qualitative information on dipole dimensionality and dipole orientation, but also allows quantitative analysis of the proportions of different dipole components [6,29].

In this chapter, we further develop the protocol of polarization and Fourier plane image analysis, paving a way to achieve precisely quantitative probes on single emitters with different dimensionalities (i.e. isolated NPLs, clusters or self-assembled chains). The optimal experimental configurations are carefully designed to maximize the sensitivity of the protocol to probe dipole components in single emitters, with a record precision reaching ±0.03 for the probing of the specific dipole component that is of our interest.

4.1.1 Polarization analysis

A glance at radiation diagrams

We first show the theoretical radiation diagrams of 1-dipole (left) or 2-dipole (right) emitters in an infinite homogenous medium (vacuum). These diagrams are three-dimensional surfaces showing the angular distribution of the emission: the distance from the origin to the surface along a certain direction is proportional to the power emitted into this direction. As we can see from figure 4-3, emission from one dipole is in a toroidal shape, with maximal intensity propagating perpendicular to the dipole orientation (black arrow) and no radiation along the dipole orientation. For the emissions from two orthogonal dipoles, their overall emission is an incoherent sum of two emitting dipoles. As a result, their emission is a peanut shape with maximal emission intensity along the direction normal to the plane formed by the two dipoles (note that the two dipoles contribute incoherently so that we sum their intensities and not their electric fields: they do not interfere). Accordingly, the emission from three orthogonal dipoles is isotropic, because of the identical contribution along all the three (x, y and z) dimensions.

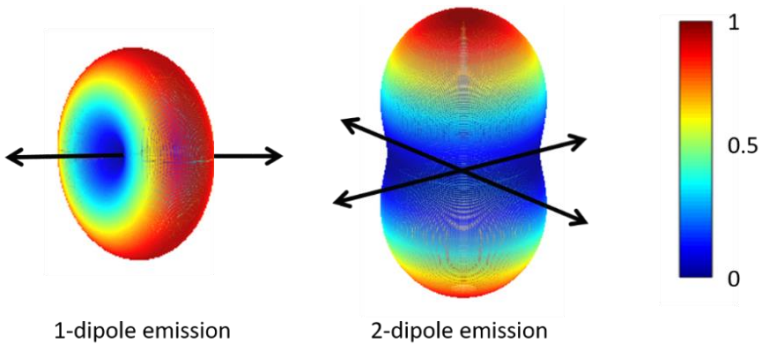

Figure 4-3. Radiation diagram of 1 dipole (left) or 2 orthogonal dipoles (right) in a homogenous medium. Color scale: normalized emission intensity.

When dipoles are located in the vicinity of an optical interface (with a distance denoted as z_0), their emission diagrams will be significantly modified (and so will the polarization of their emission) because the collected electric field is a sum of the direct emission and the emission reflected by the interface formed by the lower index medium and higher index medium. As an example, we simulate the situation in figure 4-4 (a): we put 1 or 2 emitting dipoles with orientations either vertical or horizontal to the reflection interface (i.e. PMMA-air interface) with a distance z_0 =30 nm. The radiation diagrams observed by the objective are shown in figure 4-4 (b).

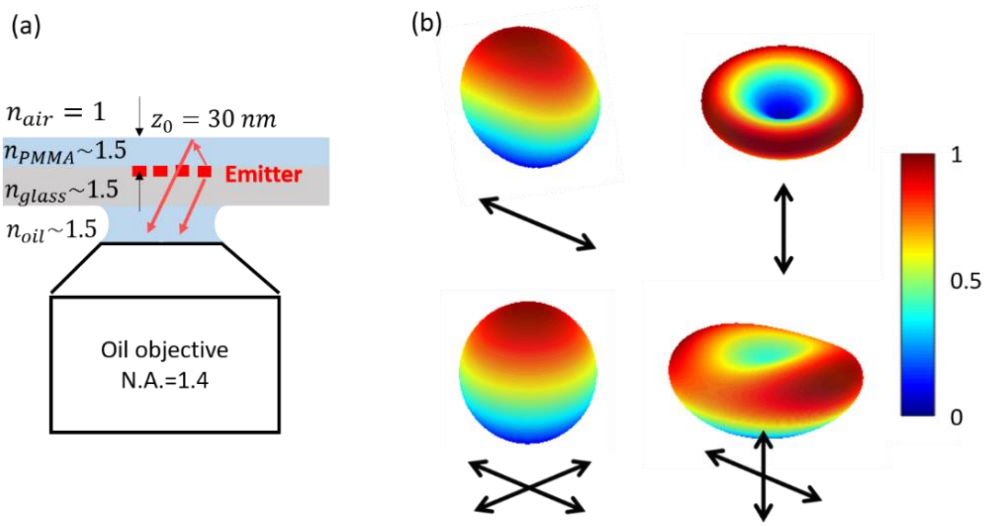

Figure 4-4. (a) A representative configuration, with emitter located 30 nm below the reflection interface: the emitter is deposited on a glass slide and covered by a PMMA layer with glass and PMMA indices of 1.5. The sample is imaged by an immersion objective. (b) Radiation diagrams of 1 or 2 dipoles with directions either horizontal or vertical to the reflection interface located 30 nm below. Color scale: normalized emission intensity.

Polarization dependence

The degree of polarization measured from the emission of a single emitter may vary significantly depending on many issues:

1) As seen in figure 4-4, the orientation and the number of dipoles contributing to the emission are the principal dominants for the polarization. For example, the emission of a horizontal dipole (normal to the optical axis) is remarkably polarized, while the emission from either one dipole vertical to the substrate or from two horizontal dipoles (with same dipole moment) are completely unpolarized.

2) By comparing the emissions measured under different optical environments in figure 4-3 and figure 4-4 , one can see that emissions from the same dipole components may still result in very different radiation patterns depending on their environment, and thus degrees of polarization.

3) The numerical aperture of the objective will also play an important role in the polarization measurement. Larger numerical aperture will collect emitted light from a larger angle range, while the emitted field has a different polarization depending on the direction of emission and we detect a sum of all emission directions within the numerical aperture. Therefore, a larger numerical aperture results in lower degree of polarization.

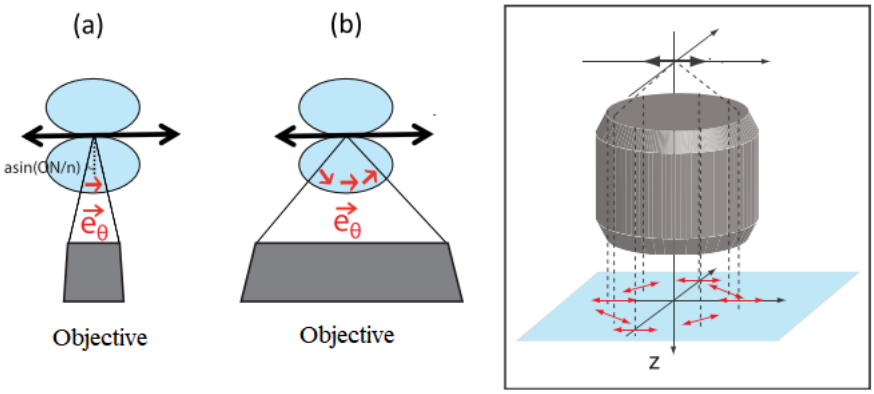

Figure 4-5. Influence of numerical aperture of the objective on polarization measurements. The smaller (resp. larger) numerical aperture (a) (resp. (b)) will give higher (resp. lower) degree of polarization. Inset: In the case (b) of a large numerical aperture, several polarization directions are collected. Adapted from ref. [175].

Experimental polarization measurements

A simplified schematic of the polarization analysis setup is shown in figure 4-6. Samples are excited by a 470 nm diode laser, which is then filtered by the high-pass filter. The emission light is collected by an oil objective (N.A.=1.4) and passes through a rotating system consisted of a half wave plate and a polarizing beam splitter cube (50:50). The half wave plate rotates in front of the polarizing beam splitter cube, working equivalently to a continuously rotating polarizer. The equivalent polarizer orientation α is twice the orientation of the half wave plate eigenaxes with respect to the axes of the cube. The emission is then separated by the cube into reflection/transmission paths and detected by 2 avalanche photodiodes (PerkinElmer SPCM), respectively. We plot the normalized intensity I_{exp} on one photodiode as:

$$I_{exp}(\alpha) = \frac{I_{APD1}}{I_{APD1}+m\cdot I_{APD2}} \tag{4.1}$$

in which I_{APD1} and I_{APD2} are the measured intensities on the two photodiodes and m is the factor to center the normalised curve at 0.5. We use a $cos^2(\alpha)$ function to fit $I_{exp}(\alpha)$ as:

$$I_{fit}(\alpha) = k_1 + k_2 \cdot cos^2(\Phi - \alpha) \tag{4.2}$$

from which we can extract the polarization orientation Φ (in-plane angle of the dipole) and calculate the **experimental degree of polarization** δ_{exp} by:

$$\delta_{exp} = \frac{I_{max}-I_{min}}{I_{max}+I_{min}} = \frac{k_2}{k_1+2k_2} \tag{4.3}$$

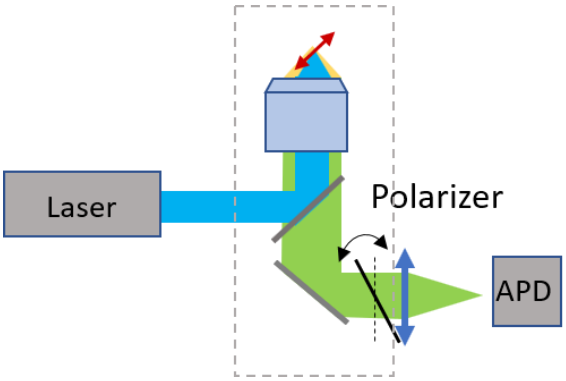

Figure 4-6. Simplified schematic of the polarization analysis set up.

Model for theoretical polarization calculations

To determine the orientation of a single emitter, one can obtain rich information by relating the experimental degree of polarization δ_{exp}, obtained by the polarization analysis, to the theoretical model of δ-Θ dependence.

For 1-dipole or 2-dipole emissions, the measured intensity I as a function of the rotating angle α of the polarizer is expressed respectively by [174]:

$$I_{1D}(\alpha) = I_{min} + (I_{max} - I_{min}) \cdot cos^2(\Phi - \alpha) \tag{4.4}$$

$$I_{2D}(\alpha) = I_{min} - (I_{max} - I_{min}) \cdot cos^2(\Phi - \alpha) \tag{4.5}$$

Note that:

1) the difference in the sign between I_{1D} and I_{2D} expression is from the different definitions of dipole orientation in the 1-dipole case and the 2-dipole case, as introduced in figure 4-2. The orientation of a 1-dipole model is **parallel to** the orientation (Θ, Φ) so we obtain **maximal** intensity when $\alpha = \Phi$, while in the 2-dipole model, the dipoles are **normal** to the orientation (Θ, Φ), so the intensity is **minimal** when $\alpha = \Phi$.

2) the theory here for 2-dipole emission involves 2 radiating dipoles which have dipole moments of equal norms and oriented orthogonal to each other. The case of different dipole norms will be considered later in the chapter in order to fit the experimental data.

We can calculate, for 1-dipole emission, I_{max} and I_{min} respectively by:

$$I_{min} = A \cdot sin^2\Theta + B \cdot cos^2\Theta \tag{4.6}$$

$$I_{max} - I_{min} = C \cdot sin^2\Theta \tag{4.7}$$

Here, the constants A, B and C are expressed analytically in ref. [174] depending on 1) the numerical aperture of the objective; 2) the refractive index of the medium in which the emitter is embedded and 3) the interface configuration between the sample and the objective (as will be elaborated later in figure 4-19).

Similarly, for 2-dipole emission case, we can write:

$$I_{min} = A + B + (A - B + C) \cdot cos^2\Theta \tag{4.8}$$

$$I_{max} - I_{min} = C \cdot sin^2\Theta \tag{4.9}$$

As for 3-dipole emission, we will obtain $I_{min} = I_{max}$ since the emission is isotropic from 3 dipoles orthogonal to each other with equal dipole moments.

Next, we can calculate respectively the theoretical degree of polarization δ_{theo} for 1-dipole and 2-dipole emission by:

$$\delta(\Theta)_{theo,1D} = \frac{C \cdot sin^2\Theta}{(2A-2B+C) \cdot sin^2\Theta + 2B} \tag{4.10}$$

$$\delta(\Theta)_{theo,2D} = \frac{C \cdot sin^2\Theta}{-(2A-2B+C) \cdot sin^2\Theta + 4A + 2C} \tag{4.11}$$

Again, in the case of 3-dipole emission, $\delta(\Theta)_{theo,3D} = 0$.

Figure 4-7 shows examples of the theoretical degree of polarization for 1-dipole or 2-dipole emission as a function of the dipole out-of-plane orientation Θ. When $\Theta = 0°$, the emission is unpolarized ($\delta = 0$) because the radiation diagrams in these cases have revolution symmetry around the optical axis (figure 4-4). As Θ increases, the 1-dipole emission becomes more and more

polarized, reaching nearly 100% when the dipole is horizontal ($\Theta = 90°$) on the substrate; the 2-dipole emission also becomes increasingly polarized, with maximum value close to 80%.

Note here that, for both 1-dipole and 2-dipole cases, the theoretical degree of emission polarization will not reach 100%, because the emitted field has a different polarization depending on the direction of emission and we detect a sum of the emissions within the numerical aperture.

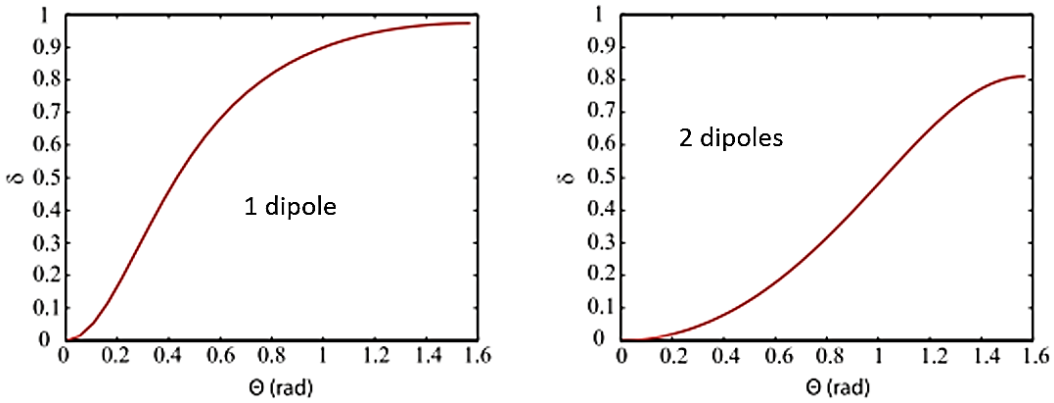

Figure 4-7. Theoretical degree of polarization of 1-dipole or 2-dipole emission in the case of an emitter near a planar gold/glass interface measured by an immersion objective. Adapted from ref. [176].

3-dipole model towards quantitative probing

The above calculation involves dipoles with same relative strengths (we will call this case "symmetric dipoles"). Starting from here, we can further develop the theory by considering "asymmetric" 3-dipole emission, i.e., emission from dipoles along x, y, z orientation with different strengths (proportional to the square of the dipole moment) denoted as η_x, η_y and η_z respectively. We consider as main axes of the emitter the optical axis z and two orthogonal axes x and y along the geometric axes of the emitter (i.e. the short- and long-axes of a NPL). We normalize their proportion by:

$$\eta_x + \eta_y + \eta_z = 1 \tag{4.12}$$

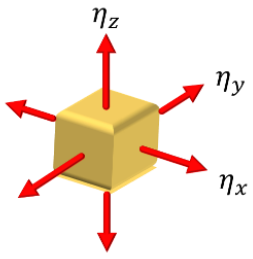

Figure 4-8. Schematic of 3-dipole model.

We build up a polar coordinate system assigning the x axis along the direction $\Phi = 0$ and $\Theta = \frac{\pi}{2}$. Accordingly, we obtain y axis along direction of $(\Phi = \frac{\pi}{2},\ \Theta = \frac{\pi}{2})$ and z axis of $(\Phi = 0,\ \Theta = 0)$. Then, one can calculate the emission intensities $I(\alpha)$ from the x, y and z dipoles, respectively, as a function of the rotating angle α of the polarizer by:

$$I_x(\alpha) = \eta_x \cdot (A + C \cdot cos^2(\Phi - \alpha)) \tag{4.13}$$

$$I_y(\alpha) = \eta_y \cdot (A + C \cdot cos^2\left(\Phi + \frac{\pi}{2} - \alpha\right)) \tag{4.14}$$

$$I_z(\alpha) = \eta_z \cdot B \tag{4.15}$$

Because the three dipole contributions are incoherent, their intensities can be summed and no interference terms needs to the included. The theoretical degree of polarization δ_{theo} for an incoherent sum of the three dipoles is then:

$$\delta_{theo} = \frac{I_{max} - I_{min}}{I_{max} + I_{min}} \tag{4.16}$$

in which

$$I_{max} = \eta_x \cdot (A + B) + \eta_y \cdot A + B \tag{4.17}$$

$$I_{min} = \eta_x \cdot A + \eta_y \cdot (A + C) + B \tag{4.18}$$

Eventually we obtain the theoretical degree of polarization:

$$\delta_{theo} = \left|\frac{C \cdot (\eta_x - \eta_y)}{2A + C + \eta_z \cdot (2B - 2A - C)}\right| \tag{4.19}$$

In figure 4-9, we present values of δ_{theo} as functions of proportions η_x, η_y and η_z, ranging from 0 to 1, under transmission experimental configuration (more details for experimental configurations will be introduced later). From this map, we can see some specific features:

(a) When $\eta_x = 0$, $\eta_y = 0$ and $\eta_z = 1$ (only one dipole orthogonal to the substrate), $\delta_{theo} = 0$;

(b) Whenever $\eta_x = \eta_y$ (two symmetric in-plane dipoles plus an out-of-plane dipole), $\delta_{theo} = 0$;

(c) When $\eta_x = 1$, $\eta_y = 0$ and $\eta_z = 0$ (one horizontal dipole), $\delta_{theo} = 0.93$, which is the maximum degree of polarization, very close to $\delta = 1$, indicating that this is a sensitive configuration for polarization analysis.

This 3-dipole model can relate the proportion values η_x, η_y and η_z to the theoretical degree of polarization δ_{theo}, which gives access to a precisely quantitative probing of multi-dipole contributions in single emitters. However, one cannot obtain full information on η_x, η_y and η_z from experimental polarization analysis, because it is now an under-constrained problem, as opposed to the situations considered by C. Lethiec et. al involving only 1-dipole and symmetric 2-dipole so that there were only 2 unknown quantities (the dipole orientation Φ and Θ) for 2 measured quantities (the polarization maximal angle and degree of polarization).

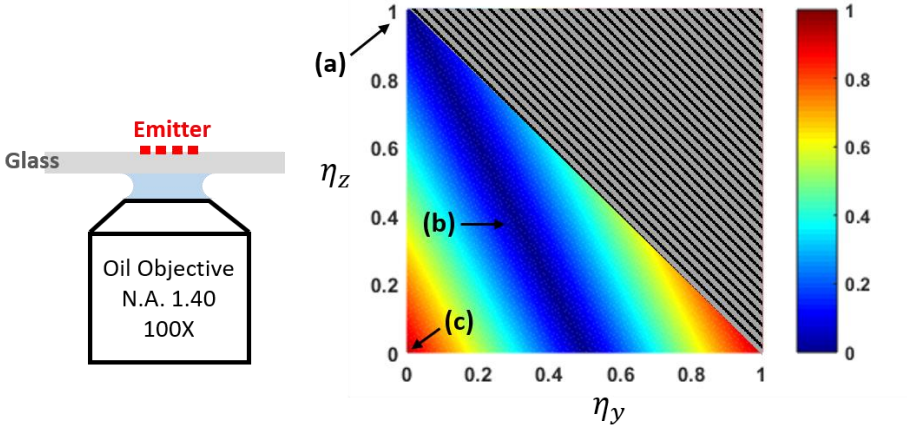

Figure 4-9. Theoretical map (right) of degree of polarization δ_{theo} under the illustrated configuration (left).

To solve this problem and quantitatively probe multi-dipole components in single emitters, we need to utilize another powerful tool: Fourier plane imaging.

4.1.2 Fourier plane analysis

Fourier plane is the back focal plane of the objective. Fourier plane imaging has emerged as a powerful tool, widely used in many aspects of research, involving single emitter analysis [172], nano antennas [169,177], Raman scattering [178], etc. Fourier plane imaging provides information on radiating dipoles in a nano object, thanks to their angular dependent distribution of light in the far field (radiation pattern), where different points in the Fourier plane image corresponds to different emission angles.

Fourier plane description

We consider an electric field in the x-y plane propagating towards z direction (figure 4-10). According to the principles of Fourier optics, the field emitted at a given wavevector $\hat{\vec{E}}(k_x, k_y)$ is deduced from the Fourier transform of the electrical field in the front focal plane $\vec{E}(x, y)$:

$$\vec{E}(x,y) = \iint_{-\infty}^{+\infty} \hat{\vec{E}}(k_x, k_y) \cdot e^{i(k_x \cdot x + k_y \cdot y)} dk_x dk_y \tag{4.20}$$

This equation is known as the angular spectrum representation [97], where x, y are the Cartesian transverse coordinates and k_x, k_y the corresponding spatial frequencies or reciprocal coordinates.

Each position $(x_F,\ y_F)$ in the Fourier plane image corresponds to the emission along different directions coded by the in-plane angle ϕ and the polar angle θ. We can find the correspondence between these two coordinates systems as:

$$x_F = r \cdot cos\phi = f \cdot sin\theta \cdot cos\phi \tag{4.21}$$

$$y_F = r \cdot sin\phi = f \cdot sin\theta \cdot sin\phi \tag{4.22}$$

in which f is the focal of the objective and $r = f \cdot sin\theta$ is the radial coordinate from the optical axis on the back focal plane, according to Abbe's sine condition.

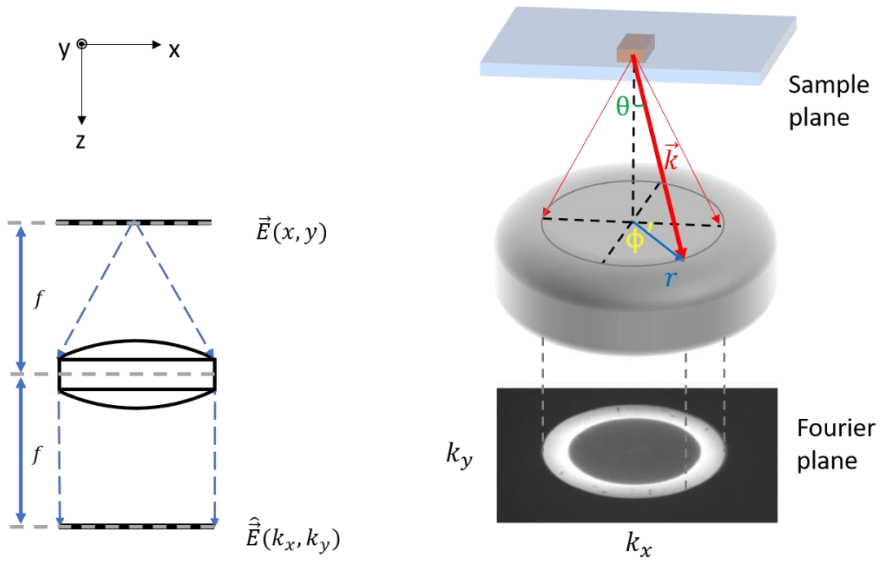

Figure 4-10. Schematic of the front and back focal planes of an objective, in which $\vec{k}$ is the wavevector, θ is the polar angle (out-of-plane angle) and ϕ is the azimuthal angle (in-plane angle).

Theoretical calculation of light distribution on Fourier plane

To analyse the experimental radiation patterns of our emitters, it is imperative to study the theoretical angular distribution of emitted light from dipoles embedded in the actual experimental environments. Here we recount the theoretical angular dependent distributions of light from emitting dipoles under both reflection (figure 4-11 (a)) and transmission (figure 4-11 (b)) experimental configurations, following the pioneering theoretical works of Walter Lukosz [179,180,181,182] and also the ingenious works of Lukas Novotny [97,172].

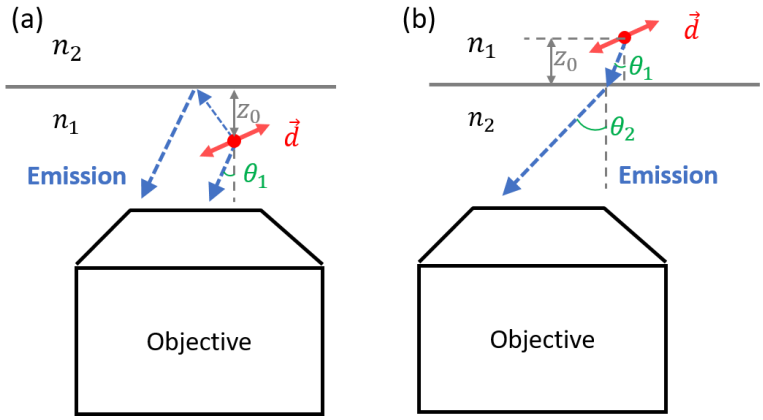

Figure 4-11. Schematic of the reflection (resp. transmission) configuration in (a) (resp. (b)); an emitter (represented by a dipole $\vec{d}$) located in a medium with a refractive index n_1, below (resp. above) the interface by a distance of z_0. Another medium has a refractive index $n_2 < n_1$.

Considering a dipole oriented along a polar angle Θ and an azimuthal angle Φ, the resulting intensity distribution in Fourier plane can be expressed as:

$$P = P_s + P_p \propto (E_p E_p^* + E_s E_s^*) \tag{4.23}$$

in which E_p and E_s are the p- and s-polarized components of the electric fields. We calculate the theoretical radiation pattern for different experimental configurations:

1) Reflection case

For the samples with a PMMA cover layer (reflection configuration), the collected fields consist of direct emission and reflected emission (figure 4-11 (a)). They can be calculated by:

$$E_p = c_1(\theta) \cdot cos\Theta \cdot sin\theta + c_2(\theta) \cdot sin\Theta \cdot \cos\theta \cdot \cos(\phi - \Phi) \tag{4.24}$$

$$E_s = c_3(\theta) \cdot sin\Theta \cdot \sin(\phi - \Phi) \tag{4.25}$$

with $c_1(\theta)$, $c_2(\theta)$ and $c_3(\theta)$ given by:

$$c_1(\theta) = e^{-ikn_2 \cdot \cos\theta \cdot z_0} + r_p \cdot e^{ikn_2 \cdot \cos\theta \cdot z_0} \tag{4.26}$$

$$c_2(\theta) = e^{-ikn_2 \cdot \cos\theta \cdot z_0} - r_p \cdot e^{ikn_2 \cdot \cos\theta \cdot z_0} \tag{4.27}$$

$$c_3(\theta) = e^{-ikn_2 \cdot \cos\theta \cdot z_0} + r_s \cdot e^{ikn_2 \cdot \cos\theta \cdot z_0} \tag{4.28}$$

where n_2 is the refractive index of the medium below the interface and z_0 is the distance between the dipole and the interface. r_p and r_s are the Fresnel reflection coefficients for p- and s-polarized light, respectively:

$$r_s = \frac{n_1 cos\theta_1 - n_2 cos\theta_2}{n_1 cos\theta_1 + n_2 cos\theta_2} \tag{4.29}$$

$$r_p = \frac{n_2 cos\theta_1 - n_1 cos\theta_2}{n_1 cos\theta_2 + n_2 cos\theta_1} \tag{4.30}$$

with n_1 (resp. n_2) the refractive indices of the medium above (resp. below) the interface and θ_1 and θ_2 to be the propagation angle in the corresponding medium.

Thus, in the reflection configuration, we can calculate the light distribution on Fourier plane by a simplified expression:

$$P_p = \frac{3}{8\pi} |cos\Theta \cdot sin\theta_1 \cdot \left(1 + r_p \cdot e^{2ikn_2 \cdot \cos\theta_1 \cdot z_0}\right) - sin\Theta \cdot \cos\theta_1 \cdot \cos(\phi - \Phi) \cdot \left(1 - r_p \cdot e^{2ikn_2 \cdot \cos\theta_1 \cdot z_0}\right)|^2 \tag{4.31}$$

$$P_s = \frac{3}{8\pi} |sin\theta_1 \cdot \sin(\phi - \Phi) \cdot \left(1 + r_s \cdot e^{ikn_2 \cdot \cos\theta_1 \cdot z_0}\right)|^2 \tag{4.32}$$

In our 3-dipole model, we have dipoles components with a fraction of η_x long direction of $\Phi = 0$ and $\Theta = \frac{\pi}{2}$, η_y along ($\Phi = \frac{\pi}{2}$, $\Theta = \frac{\pi}{2}$) and η_z along ($\Phi = 0$, $\Theta = 0$). We can write the theoretical radiation diagram of 3 dipoles with η proportions (again the intensities are summed without any interference term as the 3 dipoles are incoherent) as:

$$P_{theo} = \eta_x \cdot \left(P_{px} + P_{sx}\right) + \eta_y \cdot \left(P_{py} + P_{sy}\right) + \eta_z \cdot \left(P_{pz} + P_{sz}\right) \tag{4.33}$$

2) Transmission cases

When samples are deposited on the substrate without cover layer, i.e. the transmission condition (figure 4-11 (b)), there are two possible cases:

2.1) If the emitter is located in a medium with refractive index greater than the transmission medium, i.e. $n_1 > n_2$, we can calculate the radiation power of s- and p-polarized field by:

$$P_p = \frac{3}{8\pi}|-cos\theta_2 \cdot sin\theta_1 \cdot t_p + sin\theta_2 \cdot \cos\theta_1 \cdot \cos(\phi - \Phi) \cdot t_p|^2 \tag{4.34}$$

$$P_s = \frac{3}{8\pi}|sin\theta_2 \cdot \sin(\phi - \Phi) \cdot t_s|^2 \tag{4.35}$$

in which t_p and t_s are the Fresnel transmission coefficients for p- and s-polarized light, respectively:

$$t_p = \frac{2n_1 cos\theta_1}{n_1 cos\theta_2 + n_2 cos\theta_1} \tag{4.36}$$

$$t_s = \frac{2n_1 cos\theta_1}{n_1 cos\theta_1 + n_2 cos\theta_2} \tag{4.37}$$

As a result, in our model of 3 dipoles with components η_x long direction ($\Phi = 0,\ \Theta = \frac{\pi}{2}$), η_y along ($\Phi = \frac{\pi}{2},\ \Theta = \frac{\pi}{2}$) and η_z along ($\Phi = 0,\ \Theta = 0$), we can write the theoretical radiation diagram for this case as:

$$P_{theo} = \eta_x \cdot \left(P_{px} + P_{sx}\right) + \eta_y \cdot \left(P_{py} + P_{sy}\right) + \eta_z \cdot \left(P_{pz} + P_{sz}\right) \tag{4.38}$$

2.2) In the case of $n_1 < n_2$, the propagating waves in the first medium will be deflected on the transmission interface, resulting an angle $0 < \theta_2 < \theta_c$, in which θ_c is the critical angle:

$$\theta_c = \arcsin\left(\frac{n_1}{n_2}\right) \tag{4.39}$$

For this component, the expression of its theoretical radiation diagram is the same as the last case.

Additionally, if the distance of the dipole from the surface of the top-most layer is less than one wavelength, the evanescent field can be transformed into propagating waves [97] in the denser medium along the direction $\theta_c < \theta_2 < \frac{\pi}{2}$. In this case, we will have another component:

$$P_{p\_ev} = f_p[\left(\frac{n_2}{n_1}\right)^2 \cdot cos^2\Theta \cdot sin^2\theta_2 + sin^2\Theta \cdot \cos^2(\Phi - \phi) \cdot (\left(\frac{n_2}{n_1}\right)^2 \cdot sin^2\theta_2 - 1)] \quad (4.40)$$

$$P_{s\_ev} = f_s \cdot (sin\Theta)^2 \cdot (\sin(\Phi - \phi))^2 \quad (4.41)$$

where f_s is given by:

$$f_s = \frac{3}{2\pi} \cdot \frac{\left(\frac{n_2}{n_1}\right)^3}{\left(\frac{n_2}{n_1}\right)^2 - 1} \cdot \cos^2(\phi) \cdot e^{\frac{-2z_0}{\delta}} \quad (4,42)$$

with

$$\delta = \frac{\lambda}{2\pi} \cdot \frac{1}{\sqrt{\left(\frac{n_2}{n_1}\right)^2 \cdot sin^2\theta_2 - 1}} \quad (4.43)$$

and f_p is given by:

$$f_p = \frac{f_s}{(\left(\frac{n_2}{n_1}\right)^2 + 1) \cdot sin^2\theta_2 - 1} \quad (4.44)$$

Eventually, in this transmission case of $n_1 < n_2$, the theoretical radiation diagram of our 3-dipole model becomes:

$$P_{theo} = \begin{cases} \eta_x \cdot (P_{px} + P_{sx}) + \eta_y \cdot (P_{py} + P_{sy}) + \eta_z \cdot (P_{pz} + P_{sz}) & when\ 0 \le \Theta \le \Theta_c \\ \eta_x \cdot (P_{px\_ev} + P_{sx\_ev}) + \eta_y \cdot (P_{py\_ev} + P_{sy\_ev}) + \eta_z \cdot (P_{pz\_ev} + P_{sz\_ev}) & when\ \Theta_c < \Theta \le \frac{\pi}{2} \end{cases} \quad (4.45)$$

The apodization factor

From the above calculations, we know the theoretical radiation diagram of emitting dipoles under different experimental configurations. To fit the experimental Fourier plane image, additionally, we need to take the apodization factor into consideration for the purpose of energy conservation.

On a camera, the detected power can be expressed by:

$$dP_{cam} = I_{cam}(pixel) \cdot dS_{pixel} \quad (4.46)$$

in which dS_{pixel} is the area of a pixel of the camera and I_{cam} is the intensity of different pixels, i.e. the Fourier image.

This power should be equal to the power on the reference spherical as shown in figure 4-12:

$$dP_{cam} = dP_{sph}(\theta, \phi) \tag{4.47}$$

with

$$dP_{sph}(\theta, \phi) = R_{sph}(\theta, \phi) \cdot \mathrm{d}\Omega \tag{4.48}$$

in which R_{sph} is the emission pattern on the reference spherical and $\mathrm{d}\Omega$ the solid angle element. Since $dS_{pixel} = dA_2 = dA_1 \cdot cos\theta$ and $dA_1 = f^2 \cdot \mathrm{d}\Omega$, we have:

$$R_{sph}(\theta, \phi) \propto I_{cam}(pixel) \cdot cos\theta \tag{4.49}$$

with $cos\theta$ the apodization factor.

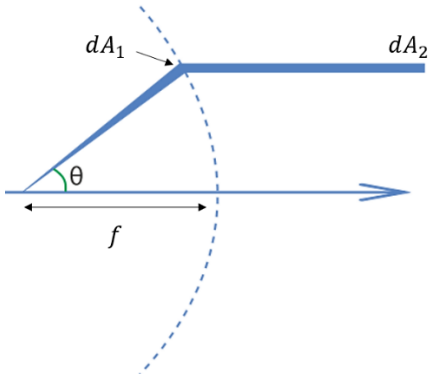

Figure 4-12. The apodization factor due to energy conservation. Adapted from ref. [176].

Ray transfer matrix (ABCD matrix) calculation

In order to practically obtain a Fourier plane image, we need to conjugate the back focal plane of the objective onto a detector by a proper choice of a lens with a suitable focal length and by properly positioning this lens and the detector. This implementation must be compatible with preserving the rest of the measurement functionalities in the setup. To achieve this goal, we introduce Ray transfer matrix (ABCD matrix) calculation.

As shown in figure 4-13, two reference planes are defined, one as an input plane and the other one as an output plane, both of which are normal to the optical axis of the system. The light propagates through the input plane into the system at position x_1 with incident angle θ_1, and arrive at the position x_2 at an angle θ_2 with respect to the optical axis.

We can relate the orientation and position of input and output lights by:

$$\begin{pmatrix} x_2 \\ \theta_2 \end{pmatrix} = \begin{pmatrix} A & B \\ C & D \end{pmatrix} \cdot \begin{pmatrix} x_1 \\ \theta_1 \end{pmatrix} \tag{4.50}$$

in which the ABCD matrix represents the system that the light propagates through and can be calculated by multiplying the transfer matrices of all the optical components included in this system.

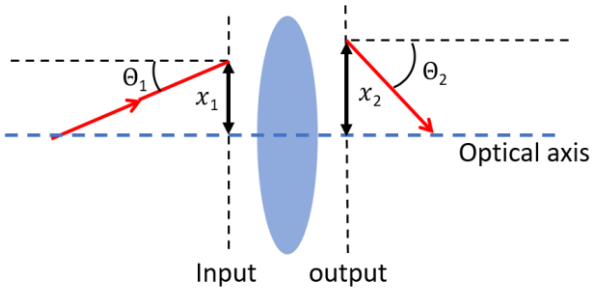

Figure 4-13. Principle of the ABCD matrix.

By calculating the matrix equation, one can get:

$$\begin{cases} x_2 = Ax_1 + B\theta_1 \\ \theta_2 = Cx_1 + D\theta_2 \end{cases} \tag{4.51}$$

In the case of B =0, the position where the outcoming light crosses the output plane is calculated by $x_2 = Ax_1$, independent to the angle of the incident beam. At this position, the output plane is actually conjugated to the input plane image, with a magnification of A.

Experimental implementation

As shown in figure 4-14, we establish a system to conjugate the back focal plane of the objective onto an EMCCD. In this system, light propagates through several lenses (with focal lengths denoted as f) and free spaces between focal planes (with lengths denoted as L_1, L_2, and L_3). Lens 2 is the tube lens of the microscope; lens 3 is used to re-collimate the beam and send it to the different measurement units in the setup; lens 4 is added specifically for the Fourier plane imaging, and its position is what we must design adequately.

One can find the ray transfer matrices for a thin lens with a focal length f as:

$$\begin{pmatrix} 1 & 0 \\ -\frac{1}{f} & 1 \end{pmatrix} \tag{4.52}$$

and for propagations in free space over a distance L as:

$$\begin{pmatrix} 1 & L \\ 0 & 1 \end{pmatrix} \tag{4.53}$$

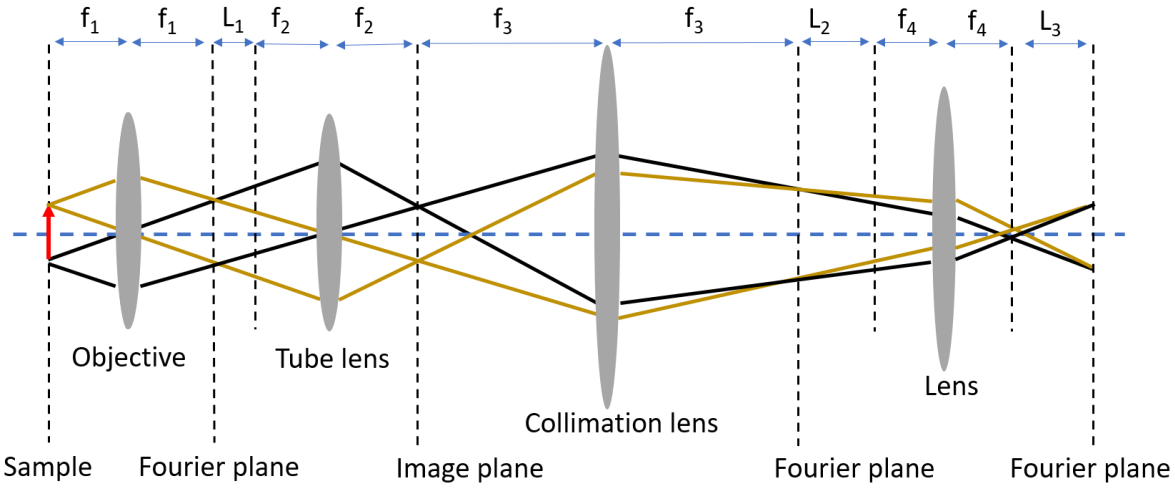

Figure 4-14. Schematic of the Fourier-plane setup

We calculate the product of the matrices of all the optical components and eventually we write the transfer matrix from the objective Fourier plane to the final Fourier plane where the detection will occur:

$$\begin{pmatrix} A & B \\ C & D \end{pmatrix} = \begin{pmatrix} -\frac{f_3 L_3}{f_2 f_4} & \frac{(f_2{}^2 L_2 + f_3{}^2 L_1) L_3 - f_2{}^2 f_4{}^2}{f_2 f_3 f_4} \\ \frac{f_3}{f_2 f_4} & \frac{(4L_2 + f_3{}^2 L_1)}{f_2 f_3 f_4} \end{pmatrix} \tag{4.54}$$

In our homebuilt setup, the focal length of the oil objective (Olympus) is: f_1 =1.8 mm. We used a tube lens with focal length f_2 =18 cm to match the Olympus objective and it locates 9 cm behind the objective (L_1 =9 cm). For the collimation lens, we have f_3 =10 cm. We then chose a Fourier lens with focal length (f_4) of 15 cm, and accordingly, we designed that L_2 =3 cm and L_3 =27 cm. Under this configuration, according to the ABCD matrix calculation, we expect that the Fourier plane image is conjugated on the EMCCD with a magnification of 1.0 X.

We installed the Fourier lens and an EMCCD (Andor iXon Ultra 897, pixel size 16 μm) according to the calculated distances and then characterized the performance of this Fourier imaging system. We took commercial molecular fluorophores (ThermoFisher Scientific, 200 nm in diameter) as reference emitters as their emission (wavelength at 600 nm) is isotropic. We spin-coated it on a glass substrate and collected the emission from a single fluorophore using an oil objective ($N.A.=$ 1.4).

The theoretical size of the collected emission pattern on the first Fourier plane image can be calculated by:

$$d = 2f \cdot N.A. \tag{4.55}$$

which yields a diameter of 5 mm. In figure 4-15, the outer radius of the image spreads over about 335 pixels on the CCD sensor, corresponding to a diameter of 5.3 mm (given the pixel size of 16 μm). Thus, we can calculate that the actual magnification of the Fourier imaging system is of 1.06X, which is close to the designed value. The inner circle is related to the critical angle of the experimental configuration. We find on the EMCCD that the diameter of the inner circle is 3.7 mm, corresponding to a critical angle of 43°, in consistent with the theoretical value calculated by

$$\theta_c = \sin^{-1}\left(1/n_{glass}\right) = 42° \tag{4.56}$$

in which the refractive index of the glass substrate is close to 1.5.

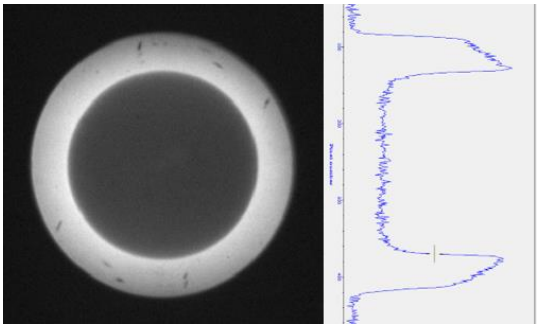

Figure 4-15. Fourier plane image on the EMCCD camera of a point-like emitter

Thus, we installed the EMCCD working in great accordance with our expectation, with a magnification of the conjugated image on camera of 1.06X. The angular resolution in the Fourier image is estimated to range between 0.3° and 0.8° depending on value of θ, which ranges from 0° to 69° ($\theta_{max} = \sin^{-1}\left(N.A./n_{glass}\right) = 69°$).

Protocol of Fourier plane image analysis

Now we take an experimental measurement as an example to explain the protocol of Fourier plane image analysis.

The Fourier plane image obtained by EMCCD is shown in figure 4-16 (b). This is a representative Fourier plane image of a single CdSe NPL emitter measured using an oil objective

(N.A.=1.4) while the emitter is deposited on a glass substrate, covered by a PMMA layer of 130 nm in thickness.

We analysed the Fourier plane image by investigating the cross-section profiles along two specific cutting lines oriented at angle Φ (red dashed line, which is obtained from polarization analysis) and at angle $\Phi + \frac{\pi}{2}$ (green dashed line), respectively. We plotted the cutting line profiles in figure 4-16 (c) and then changed the coordinate into polar angles, as shown in figure 4-16 (d), which is fitted by the theoretical radiation diagrams calculated following the introduction in subsection 4.2.1.

Different experimental optical configurations will provide different Fourier plane images theoretically. Here in this case, we have some characteristic features: 1) a lobe at normal 0° angle ; 2) sharp peaks at the critical angle $\theta_c = \sin^{-1}(1/n_{glass}) = 42°$; 3) lobes at $\theta > \theta_c$ corresponding to total internal reflection of the emission. The radiation diagram is cut by the maximal collected angle, as determined by numerical aperture $\theta_{coll} = \sin^{-1}(N.A./n_{glass}) = 69°$.

Figure 4-16 (a) shows the theoretical 3-dimensional radiation diagram of this emitter under the depicted configuration. The analytical radiation diagram shown in figure 4-16 (d) is actually the longitudinal and transversal cross-section profiles of that.

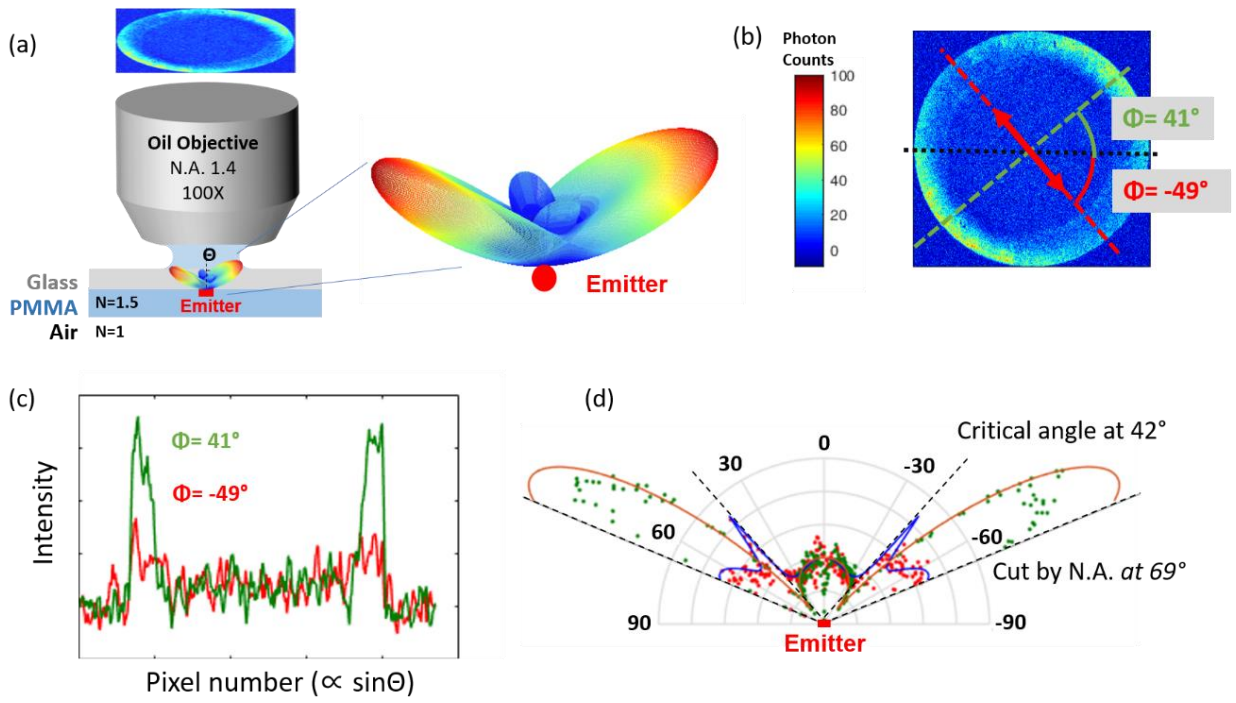

Figure 4-16. (a) Experimental configuration and 3D radiation diagram of an arbitrary single emitter. (b) Experimental raw Fourier plane image. (c) Cross-section profiles along red and green cutting lines. (d) Radiation pattern plotted in polar coordinates.

We have shown in figure 4-3 and figure 4-4 that one can obtain diverse theoretical radiation diagrams when an emitter is put in different environments. This suggests the opportunity to design the optimal experimental configurations depending on the objectives of experiments. In the next sections, we will show that, in our case of probing the out-of-plane dipoles in NPLs, a properly designed experimental configuration can help to resolve a small proportion of a contributing dipole component, by fitting the experimental radiation diagram to the theory.

Figure 4-17 shows the radiation patterns of a 3-dipole model (with arbitrarily chosen proportions for horizontal dipoles $\eta_x = 0.6$, $\eta_y = 0.1$ and for vertical dipoles $\eta_z = 0.3$) calculated under 3 representative experimental configurations:

1) Emitters are deposited on a gold substrate (with a 30 nm SiO_2 spacer to avoid quenching) covered by a layer of PMMA. In this configuration, the radiation pattern has only one lobe centered at 0°.

2) Emitters are deposited on a glass substrate. In this case, the radiation pattern has one more feature: lobes along around critical angle.

3) Emitters are deposited on a glass substrate with a PMMA cover layer (130 nm). This time, we have sharp peaks at the critical angle θ_c and lobes at $\theta > \theta_c$ corresponding to total internal reflection of the emission.

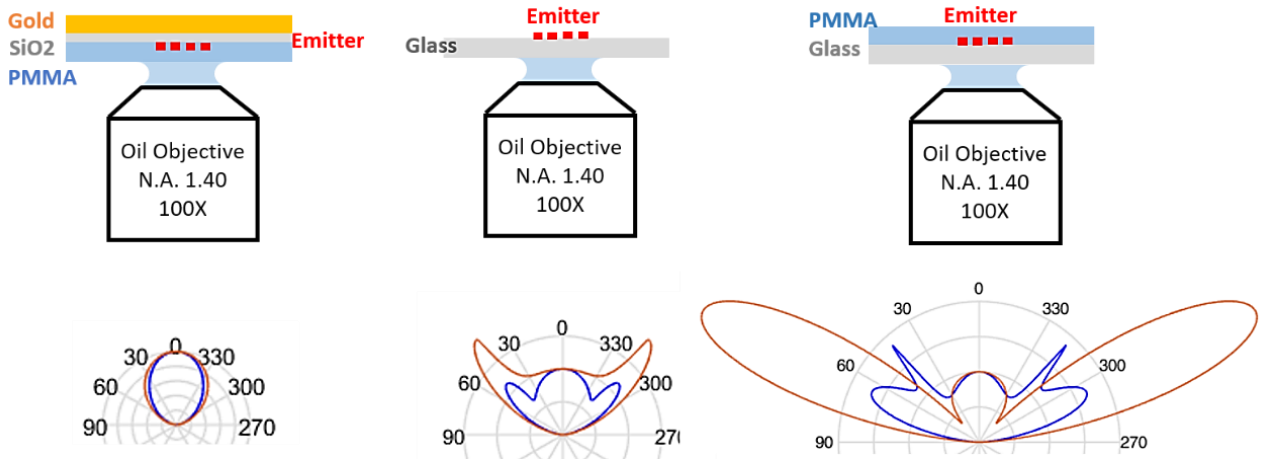

Figure 4-17. Theoretical radiation pattern of an arbitrary emitter under different experimental configuration with dipole proportion η_x=0.6, $\eta_y = 0.1$ and $\eta_z = 0.3$. Blue and orange curves are the cut lines along two symmetric axes in Fourier image (e.g. figure 4-16 (b)).

Under a same configuration, if we change the dipole proportions (η_x, η_y and η_z), the radiation pattern will change accordingly. In figure 4-18 (a), we plot the reference case (here we take the third

case in figure 4-17 as our reference), then we increase the proportion of η_z (or η_y) and keep the same value for η_y (or η_z) as plotted in figure 4-18 (b) (or (c)), while always keeping $\eta_x = 1 - \eta_y - \eta_z$.

Comparing the radiation patterns in figure 4-18, one can find general rules relating the η values to the modifications in radiation patterns:

1) When changing η_y (i.e. a horizontal dipole component), we change the ratio between the 2 horizontal dipoles x and y, which will significantly influence the anisotropy of the radiation diagram (while the z dipole has no contribution to the revolution anisotropy of it). As a result, we change the ratio between the two major lobes (lobes at Θ~70° in the example) along Φ and $\Phi + \frac{\pi}{2}$ (blue and green curves)

2) When changing η_z (i.e. the vertical dipole), the ratio between the horizontal dipoles (x and y) and vertical dipole (z) will change accordingly. Since the z dipole has no emission at $\Theta = 0°$, the ratio between the major lobe (at 70°) and the minor lobe in the center (Θ~0°) will be changed consequently.

In a word, **changing η_y will modify the ratio between the blue and the green major lobes at Θ~70°, while changing η_z will modify the ratio between the lobe at Θ~70° and the emission at Θ~0° for both of the blue and green curves**: these rules can work as a guidance when we fit the experimental data to theoretical calculations.

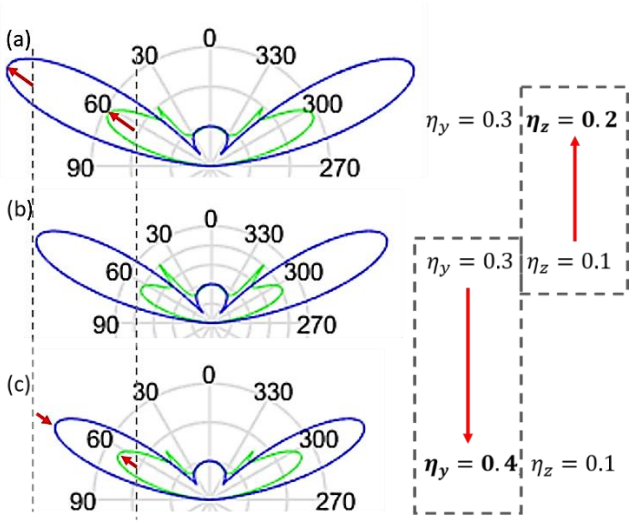

Figure 4-18. Comparison on radiation patterns of 3-dipole models with different dipole proportions. When increasing η_z from fig. (b) to (a), the major lobes at Θ~70° increase as indicated by red arrows. When

changing η_y from fig. (b) to (c), the ratio between blue and green major lobes at Θ~70° change accordingly as indicated by red arrows. Blue and green curves are the cut lines along two symmetric axes in Fourier image.

4.1.3 Choice of experimental configurations

Our objectives of single NPL measurements are to probe their anisotropic proportions of in-plane dipole components and also to check the presence/absence of their out of plane dipole component. This goal is hard to achieve because the emission of a single CdSe NPL is very weak, and in the meantime, we have to use a very low excitation power (less than 7.5 nW) to avoid quenching the emitter. On the one hand, we need to optimize the detection efficiency of the setup to obtain good signal/noise ratio out of a small amount of detected photons; on the other hand, we need to characterize different experimental configurations to find the optimal design which is 1) highly sensitive in resolving emission's degree of polarization and Fourier plane patterns, and 2) efficient in emission collection, especially for the cases of single emitters with low QY.

As summarized by C. Lethiec et. al. [174], 5 different sample-objective experimental configurations (figure 4-19) can be employed in standard microscopy measurements. Among them, the cases using air objective (case 3 and 4) have much lower emission collection efficiency than the configurations using oil objective (case 2 and 5): in the former case, the collection efficiency ranges normally from 10% to less than 50%, depending on the refractive index contrast in the medium above and below the emitters; for the latter situation, the photon collection efficiency can, for example, reach ~80 % in the case of emitters deposited on a glass slide imaged by an oil objective with a numerical aperture of 1.4. Hence, in the single NPLs measurements, the oil objective is much more efficient than air objective. Consequently, among five conditions in figure 4-19, we choose case 2 (reflection configuration) and case 5 (transmission configuration) as appropriate candidates.

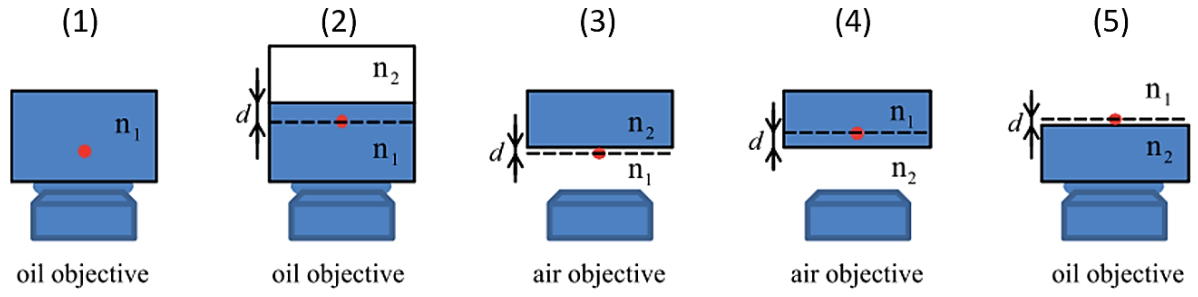

Figure 4-19. Schematic of the five cases corresponding to different experimental configurations between the sample and the objective.

We then choose materials for the substrates depending on their refractive indices. Figure 4-20 shows some practical reflection and transmission configurations with oil objectives: a) emitters are

deposited on a gold substrate (with a SiO_2 spacer to avoid quenching) covered by PMMA layer; b) emitters are deposited on a silicon wafer covered by PMMA layer; or using glass substrate with (d) or without (c) PMMA cover layer.

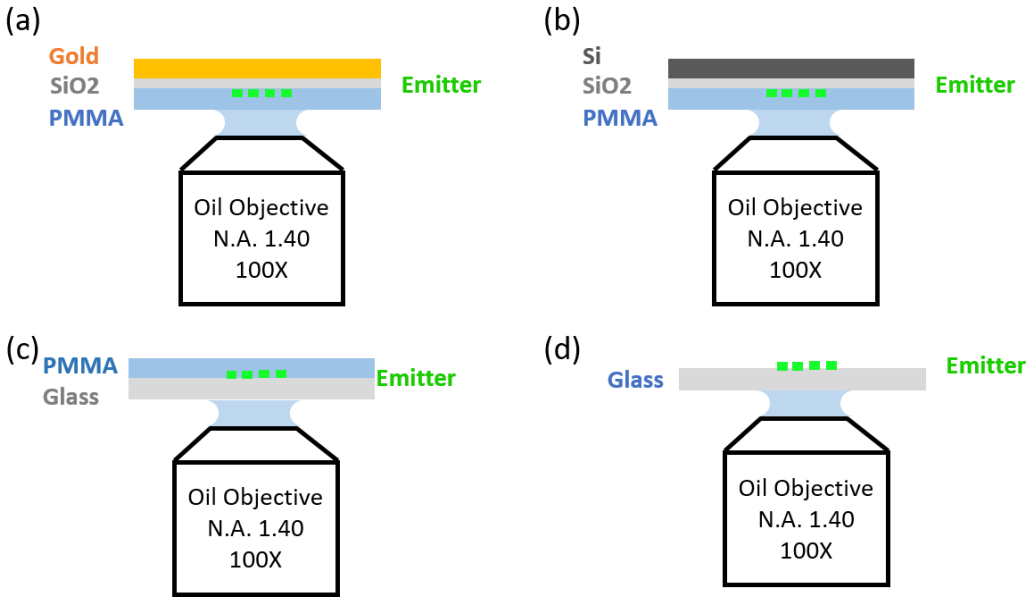

Figure 4-20. NPLs are deposited on (a) gold or (b) Si substrate with a SiO_2 spacer; or on glass substrate (c) with or (d) without PMMA cover layer.

We now consider the emission collection efficiency. For case (a), it suffers from an effect of quenching related to the short-range nonradiative energy transfer from emitters to the gold surface; case (b) experiences the similar problem that lots of light are emitted into silicon because of the high refractive index of Si. Thus, we exclude these two lossy configurations and focus on cases (c) and (d), referred to as reflection configuration and transmission configuration, respectively.

Next, we estimate the sensitivity when probing the theoretical radiation pattern using reflection and transmission configuration:

First step, we calculate the theoretical radiation patterns (e.g. figure 4-18), under the two configurations, with 2 variables η_y and η_z ranging respectively from 0 to 1. We take the value of the major lobe (at Θ~70°) of each configuration into consideration, and plot these values into a 2D map as functions of η_y and η_z, i.e. $I_r(\eta_y, \eta_z)$ for the reflection configuration and $I_t(\eta_y, \eta_z)$ for the transmission configuration. Second step, we calculate the gradients of the map, $G^y_{r/t}(\eta_y, \eta_z) = \frac{\partial I_{r/t}(\eta_y, \eta_z)}{\partial \eta_y}$ and $G^z_{r/t}(\eta_y, \eta_z) = \frac{\partial I_{r/t}(\eta_y, \eta_z)}{\partial \eta_z}$ (with the subscript r/t indicating the reflection or transmission case), which can be regarded as indicators of the sensitivity of the corresponding

configuration. In other words, if the gradient is larger, the radiation pattern will be modified more significantly when changing the fitting coefficient η_y or η_z. Then, we compare the sensitivity of the reflection and the transmission configurations by calculating the difference of their gradients: $G_r^y(\eta_y,\eta_z) - G_t^y(\eta_y,\eta_z)$ for the analysis of the y dipole and $G_r^z(\eta_y,\eta_z) - G_t^z(\eta_y,\eta_z)$ for the analysis of the z dipole.

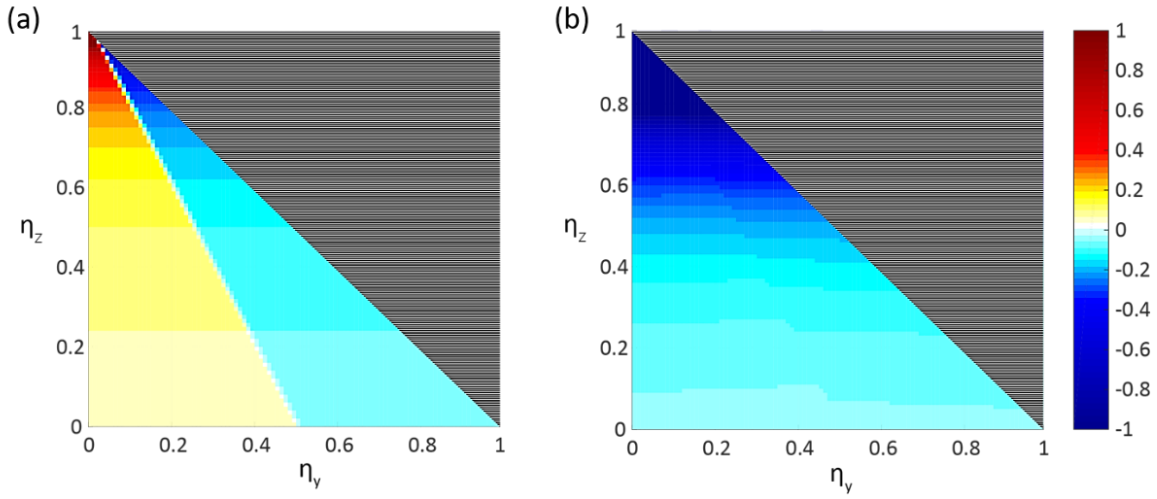

Figure 4-21. Theoretical comparison of sensitivity between the two reflection and transmission configurations when probing (a) η_y or (b) η_z. Color scale: the calculated difference of the gradients between reflection and transmission configuration.

The result of $G_r^y(\eta_y,\eta_z) - G_t^y(\eta_y,\eta_z)$ (respectively $G_r^z(\eta_y,\eta_z) - G_t^z(\eta_y,\eta_z)$) is plotted in figure 4-21(a) (respectively (b)). The left map shows the case when probing η_y (in plane dipole), and the right one is of the case when study η_z (out-of-plane dipole). In the red-yellow area, the reflection configuration is more sensitive than transmission configuration, while in blue area, it is the opposite situation. Therefore, it is now known that the reflection configuration is more sensitive in probing the in-plane dipole component, while the transmission configuration is optimal for the measurement of the out-of-plane dipole (out-of-plane with respect to the sample plane).

Based on the above estimations, **we choose the reflection configuration to measure stacked NPLs chains and the transmission case for single NPLs,** as will be elaborated in the next sections.

4.1.4 State of the art of dipole analysis

Many important processes, such as light-matter coupling [168,169], energy transfer [14,31], directional emission and light extraction [17] etc, depend critically on the dimensionality and

orientation of optical transition dipoles in emitters. With this in mind, many groups have investigated the information of transition dipoles in single or ensembled NPLs as well as other fluorescent systems.

In ref. [84], X. Ma and co-authors investigated single NPLs by higher-order laser scanning microscopy and found that the absorption dipoles in NPLs are isotropic in three dimensions. The emissions are polarized depending on the aspect ratio of the lateral dimensions, which is explained by isotropic radiating dipoles modified by the dielectric structure ("electric field renormalization effect"). In ref. [77], R. Scott et al. performed Fourier plane study on a monolayer of NPLs film prepared by Langmuir technique. They experimentally demonstrated that emission from NPLs are exclusively from in-plane dipoles with an uncertainty of 5%, and theoretically explain it by the anisotropy of the electronic Bloch states governing the dipole moment, which is further enhanced by the optical local density of states and local fields. Another group in Korea investigated the polarized emission of NPLs with different lateral aspect ratios controlled by varying the amount of acetate salts, and they also attributed the shape-dependent fluorescence polarization to the local field effect [87].

During previous studies in our group, F. Feng and L.T. Nguyen have characterized, as part of their PhD (resp. advisors L. Coolen and A. Maître), single nanoplatelets with different geometries [6,29]: 1) Square or 2) rectangular thin CdSe nanoplatelet core sandwiched in **thin** CdS shells and 3) quasi square thin CdSe core sandwiched in **thick** CdS shells (to form a cubic shape). All these NPL emitters behave with excellent precision as a sum of 2 orthogonal incoherent dipoles lying parallel to the CdSe NPL plane, in good agreement with the theoretical calculation as introduced in chapter 1, and also with the experimental results of other groups. By comparing the results of 1) and 2), the rectangular NPL's emission is partially polarized and the emission pattern is anisotropic, whereas they remain unpolarized and isotropic for the square NPL. They explained this result by dielectric antenna effect induced by the elongated shape of rectangular platelets.

One may notice that, to explain the anisotropic emission of NPLs, different groups mention different terms, such as "electric field renormalization effect", "optical local density of states", "dielectric antenna effect" etc., which are actually the same effect. Here we denote all of them as "dielectric antenna effect", which is caused by the dielectric contrast between the dielectric structure and the surrounding medium. In the case of elongated shape, the dielectric structure could induce a field distribution along the elongation axis, thus enhance the corresponding emission intensities. This effect is particularly strong if the contrast between the dielectric constants and the environment outside is large, as introduced in section 1.2 in chapter 1.

There are also reports analysing the transition dipoles in assembled NPL samples in the literature. B. Abécassis et al. synthesized the self-assembled NPL needles, which emits linearly polarized light [69]. Y. Gao and co-authors manage to control the orientation (standing on edge or lying face down) of self-assembled NPL monolayer film [12]. They pointed out that the face-down NPL film exhibited in-plane dipoles within the plane of the film, which could improve the external efficiency of NPL-based optoelectronics, such as LEDs, laser etc, while the edge-up NPL films could be more efficient in FRET, in consistence with the report by Demir's group [14].

In addition to NPLs, dipole analyses are also performed on other emitting systems, such as nanorods (to study the fine-structure of the band-edge exciton) [183], layered InSe flakes (to demonstrate an out-of-plane dipole in a two-dimensional semiconductor) [184], Ga_2Se_2 crystals (to show a shift of dipole orientation induced by quantum confinements) [185], etc.

4.2 Reference: dipole analysis on single nanoplatelets

In this section we will work on individual CdSe NPLs, the building blocks of stacked NPLs chains, as a reference for the dipole analysis on self-assembled NPLs chains in the later sections. Note that, as compared to the widely studied core-shell NPLs (e.g. CdSe/CdS NPLs), the analysis of naked CdSe NPLs here is more difficult, as they are prone to photobleaching and photodegradation because they have no protective shell.

We deposited samples on glass substrates for optical study. Here we mainly used transmission configuration for the single NPLs, following the description in section 4.1. Besides, we also performed measurements under reflection configuration, as a further corroboration of our measurements.

The glass substrates were first cleaned by UV-Ozone cleaner for 20 min and then washed by ethanol. The dispersion solution of single NPLs was diluted 10000 times in hexane and spin-coated on a glass slide at 4000 rpm for 40 s to result in well-separated single emitters. At this point, the deposited sample is ready for measurements using transmission configuration. For the experiments under reflection configuration, the sample was then covered by a spin-coated layer of polymethylmetacrylate (PMMA) with thickness of 30 nm as determined by profilometry.

The refractive indices of immersion oil, glass substrate and PMMA are all close to 1.5. Thus, we consider our emitters to be located in a dielectric semi-infinite medium with $n = 1.5$.

4.2.1 Polarization analysis

We use the three-dipole model to describe the behaviour of single NPLs with proportions denoted as $\eta_{\parallel,1}$, $\eta_{\parallel,2}$ and $\eta_{\perp}$, as shown in figure 4-22. $\eta_{\parallel,1}$ and $\eta_{\parallel,2}$ correspond to proportions of the in-plane dipoles and $\eta_{\perp}$ corresponds to that of the out-of-plane dipole in NPL, with the assumption that the NPL deposits horizontally on the substrate.

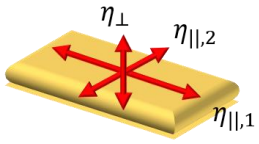

Figure 4-22. 3-dipole model

Following the deduction in section 4.1, here these dipoles will respectively result in emissions as:

$$I_{\parallel,1}(\alpha) = A + C \cdot cos^2(\Phi - \alpha) \tag{4.57}$$

$$I_{\parallel,2}(\alpha) = A + C \cdot cos^2(\Phi + \frac{\pi}{2} - \alpha) \tag{4.58}$$

$$I_{\perp}(\alpha) = B \tag{4.59}$$

where α is the orientation of the polarizer and ABC coefficients are defined in ref. [174].

Thus, the total emission intensity I_{tot} of the three-dipole model with coefficient $\eta_{\parallel,1}$, $\eta_{\parallel,2}$ and $\eta_{\perp}$ will be:

$$I_{tot}(\alpha) = A \cdot (\eta_{\parallel,1} + \eta_{\parallel,2}) + B \cdot \eta_{\perp} + C \cdot \eta_{\parallel,2} + C(\eta_{\parallel,1} - \eta_{\parallel,2})\cos^2(\Phi - \alpha) \tag{4.60}$$

The theoretical degree of polarization for an incoherent sum of the three dipoles is thus:

$$\delta = \frac{I_{max} - I_{min}}{I_{max} + I_{min}} \tag{4.61}$$

in which

$$I_{max} = \eta_{\parallel,1} \cdot (A + C) + \eta_{\parallel,2} \cdot A + B \cdot \eta_{\perp} \tag{4.62}$$

$$I_{min} = \eta_{\parallel,1} \cdot A + \eta_{\parallel,2} \cdot (A + C) + B \cdot \eta_{\perp} \tag{4.63}$$

eventually we can write:

$$\delta = \frac{C\cdot(\eta_{\parallel,1}-\eta_{\parallel,2})}{2A+C+\eta_{\perp}\cdot(2B-2A-C)} \tag{4.64}$$

To implement the experimental measurement on single NPLs, we scanned the laser spot on the sample substrate to locate the emitters and we identified the single isolated ones from their optical characteristics (blinking, decay and antibunching) as described in chapter 3.

Figure 4-23 (a) shows an emission intensity time trace of a typical single CdSe NPL. Its normalized polarization curve (blue dots in figure 4-23 (b)) is well fitted by a $\cos^2(\Phi-\alpha)$ function with $\Phi = 44°$ and deduced degree of polarization $\delta = 0.40$. These δ and Φ values indicates that 1) the emission from our single NPL is partially polarized (as we expect for the anisotropic 2 dipoles model) and 2) the orientation of the stronger in plane dipole, which is enhanced by dielectric antenna effect [6] along the direction of the long axis of the emitter, is at 44° with respect to the chosen axis of the optical setup.

Note that, in the polarization curve, there are some dots deviating from the fitting curve, which are actually related to the off-state emissions as shown in the intensity time trace. For example, the dots at the angle of ~100° in figure 4-23 (b) corresponds to the emission at t=25 s in figure 4-23 (a).

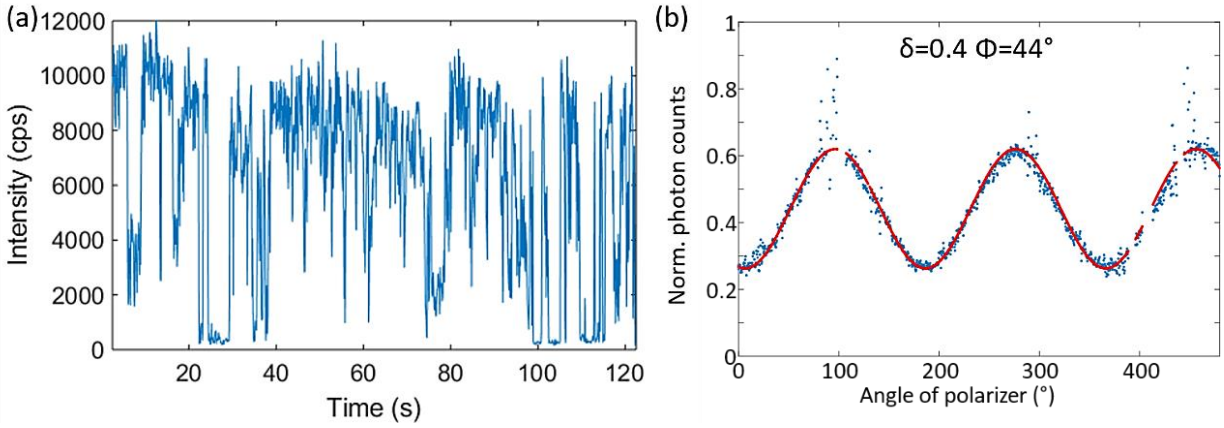

Figure 4-23. (a) Intensity time trance of a representative single NPL and (b) its polarization curve (blue dots: raw data; red line: fitting).

4.2.2 Fourier plane image analysis.

Figure 4-24 (a) shows the Fourier plane image measured for the same single NPL as in figure 4-23. We plotted respectively the cross-section profiles of cutting lines parallel (blue dots) and perpendicular (yellow dots) to the orientation of the major in-plane dipole, i.e., the dipole along $\Phi =$

44° as known from the polarization analysis (figure 4-23 (b)). The theoretical radiation pattern (calculated in section 4.1) is plotted by solid lines in figure 4-24 (b). We fitted the radiation pattern by trying different combinations of values for $\eta_{\parallel,1}$, $\eta_{\parallel,2}$ and $\eta_{\perp}$ and ended up with an excellent fitting when the proportions of dipole components are:

$$\eta_{\parallel,1} = 0.72; \quad \eta_{\parallel,2} = 0.28; \quad \eta_{\perp} = 0$$

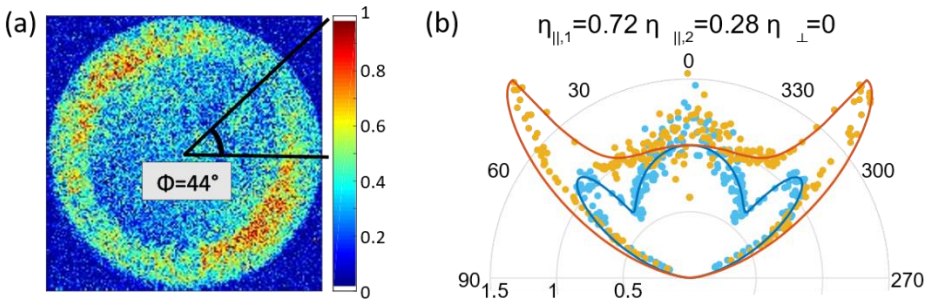

Figure 4-24. (a) Experimental Fourier plane image. (b) raw data of cutting lines along 44° (blue dots) and 134° (yellow dots) and theoretical fitting (full lines). Color scale: normalized emission intensity.

In order to evaluate the fitting precision, we slightly decreased/increased the values for $\eta_{\parallel,2}$ and $\eta_{\perp}$ to see the changes in fitting results. Here we used a transmission experimental configuration, which is sensitive in probing the vertical dipole component. As we can see from figure 4-25, we obtained poor fittings (pointed out by red arrows) when changing the in-plane (resp. out-of-plane) dipole proportions $\eta_{\parallel,2}$ (resp. $\eta_{\perp}$) by ± 0.03 (resp. ± 0.05). Thus, we conclude here that the fitting precision of our Fourier plane image analysis can reach ± 0.03.

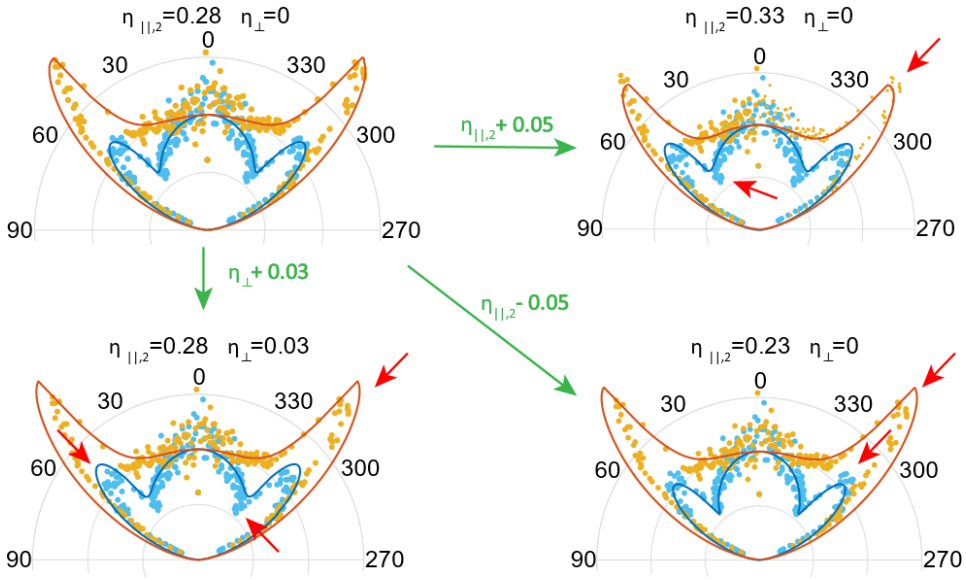

Figure 4-25. Fitting precision of single NPL's radiation pattern. Poor fitting areas are pointed out by the red arrows.

Knowing the proportions of $\eta_{\parallel,1}$, $\eta_{\parallel,2}$ and $\eta_{\perp}$, we can calculate the theoretical degree of polarization δ_{theo} of the emission from this NPL, as deduced in subsection 4.2.1. We then compare δ_{theo} to the experimental values δ_{exp} obtained from polarization analysis, in order to corroborate our results.

Figure 4-26 shows the theoretical map of δ_{theo}, from which we obtained $\delta_{theo} = 0.41$ when $\eta_{\parallel,1} = 0.72$, $\eta_{\parallel,2} = 0.28$ and $\eta_{\perp} = 0$. This theoretical result is in great consistence with our experimental result ($\delta_{exp} = 0.40$), strongly confirming the accuracy of our probing on the three dipole components.

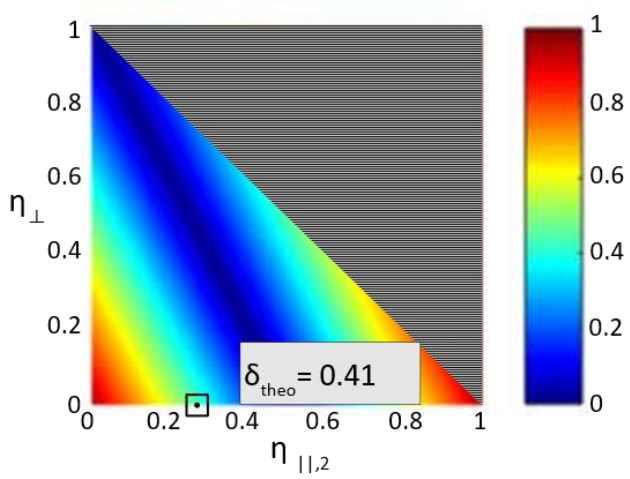

Figure 4-26. Theoretical δ (degree of polarization) for a single NPL with $\eta_{\parallel,1} = 0.72$, $\eta_{\parallel,2} = 0.28$ and $\eta_{\perp} = 0$.

To statistically extract the dipole proportions for our single NPLs sample, we measured 13 single NPLs following the same analysis protocol. A summary on different values of proportions η is shown in a histogram (figure 4-27), from which we can extract the average proportions for the dipole components as:

$$\eta_{\parallel,1} = 0.70,\ \eta_{\parallel,2} = 0.30,\ \eta_{\perp} = 0$$

Therefore, we found no out-of-plane dipole ($\eta_{\perp} = 0$) for all the considered single NPL emitters, in agreement with the previous reports [6, 12,29,77] by our group and other groups. The distribution of $\eta_{\parallel,1}$ and $\eta_{\parallel,2}$ are quite concentrated with respectively an average value of 0.70 and 0.30, and a standard deviation of 0.04.

Besides, one can calculate the ratio between the two in-plane dipoles as an anisotropy factor:

$$A_{NPL} = \frac{\eta_{\parallel,2}}{\eta_{\parallel,1}} = 0.43$$

It is probably caused by the dielectric shape of the rectangles, which enhance the dipole along the NPL's elongation direction [6, 84,85].

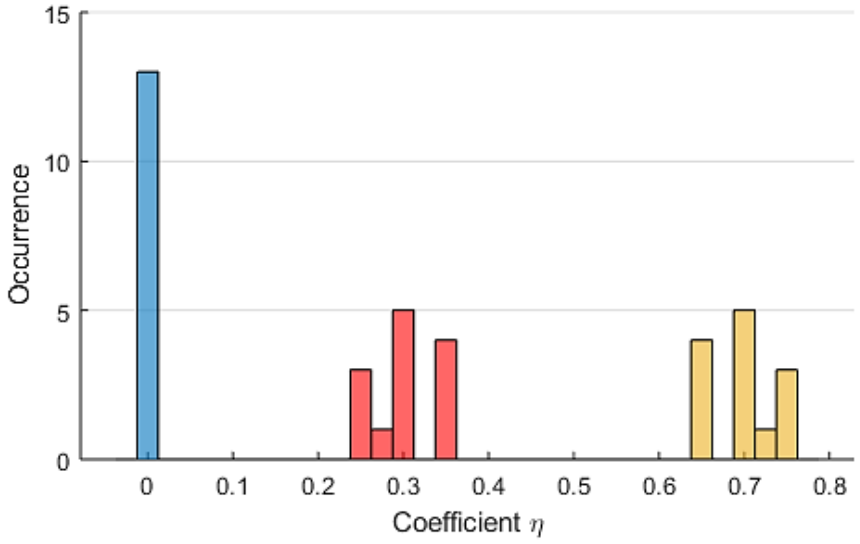

Figure 4-27. Histogram of the measured coefficients $\eta_{\parallel,1}$ (yellow), $\eta_{\parallel,2}$ (red) and $\eta_{\perp}$ (blue) for 13 single NPLs (transmission case).

4.2.3 Dipole analysis under reflection configuration

In subsection 4.2.1 and 4.2.2, it has already been demonstrated under **transmission** experimental configuration that there are two in-plane emitting dipoles in NPLs, while no out-of-plane dipole is detected. In this subsection, we use a different configuration, the **reflection** case, to repeat all the experiments. The aims of that are: 1) to further confirm the accuracy of our probing on in-plane dipole components and, 2) to corroborate the absence of the out-plane dipole in single NPL, considering the limitation of our experimental resolution.

Figure 4-28 shows polarization analysis and Fourier plane imaging of a same representative single NPL under reflection configuration. The distance z_0 between emitter and reflection interface is 30nm. Comparing figure 4-28 (a) and (c), we find a good accordance on the orientation of the stronger in-plane dipole ($\Phi = 81°$). Likewise, the experimental degree of polarization δ_{exp}, extracted from polarization curve, is 0.28, similar to the theoretical value (δ_{exp} =0.31) calculated for emitting dipoles with the same proportions ($\eta_{\parallel,1} = 0.71$, $\eta_{\parallel,2} = 0.29$ and $\eta_{\perp} = 0$) as extracted from the decent fitting in figure 4-28 (b).

We now compare the values of emitting dipoles' proportions $\eta_{\parallel,1}$, $\eta_{\parallel,2}$ and $\eta_{\perp}$ measured under different configuration (in figure 4-24 and figure 4-28). First, the in-plane dipoles proportions are very consistent, i.e., $\eta_{\parallel,1} = 0.7$ (or 0.71) and $\eta_{\parallel,1} = 0.30$ (or 0.29) for transmission measurements (or reflection case). Second, in all the measurements, we always find $\eta_{\perp} = 0$, confirming the inexistence of the out-of-plane dipole in the single NPL (with fitting precision ± 0.03).

One may notice that, the degree of polarization, δ, is much lower here in figure 4-28 (c) than the value shown in the measurement using transmission configuration in figure 4-23 (b), although with very similar contributing dipoles components. It is because, as briefly demonstrated in section 4.1, different experimental configurations will result in quite different degree of polarization. In addition, the deviation in the lateral anisotropy of the single NPLs can be a minor reason.

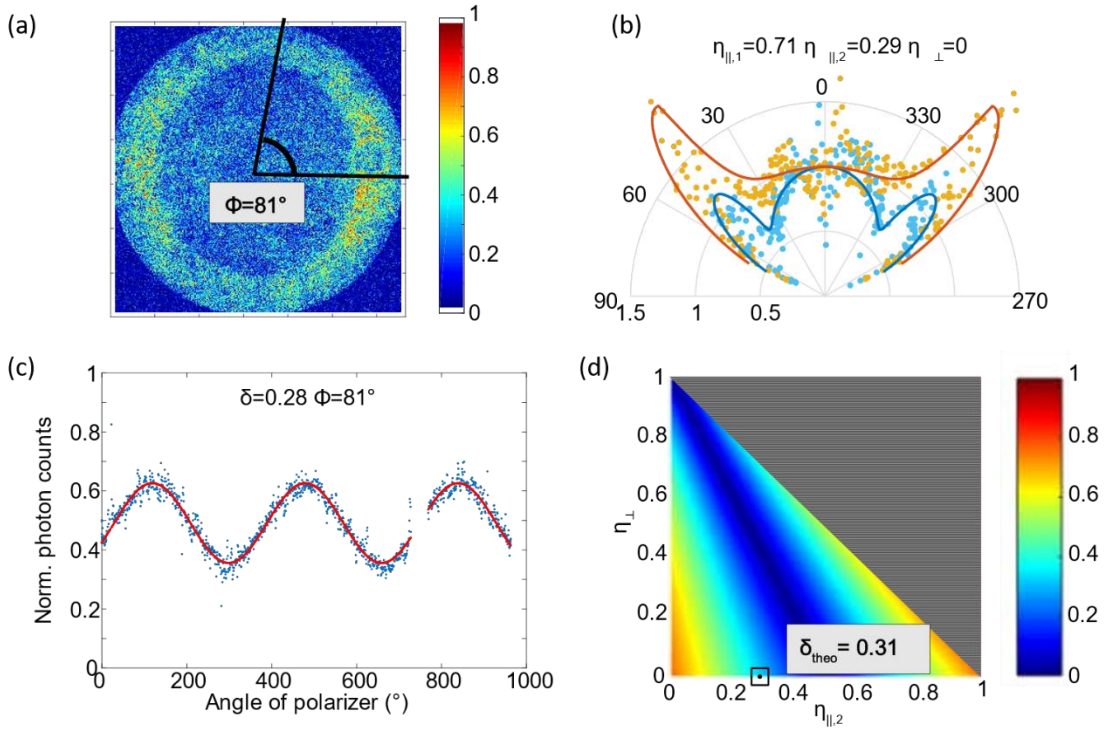

Figure 4-28. Measurements of a representative single NPL under reflection configuration (z_0 = 30nm). (a) Experimental Fourier plane image; Color scale: normalized emission intensity. (b) radiation pattern of cutting lines along 81° (blue dots) and 171° (yellow dots) and theoretical fittings (full lines); (c) experimental polarization curve; (d) theoretical degree of polarization with dipole proportions as extracted in (b).

4.2.4 Summary and discussion

In this section, we probed the proportions of emitting dipoles in the single NPLs using different experimental configurations and statistically we found that $\eta_{\parallel,1} = 0.70, \eta_{\parallel,2} = 0.30$, and $\eta_{\perp} = 0$. This result is in great consistence with the previous reports by our group and also by other groups, which indicates:

1) Two in-plane dipoles contribute to the emission of NPLs. The overall emission from them is partially polarized, because of the anisotropic efficiency of dielectric enhancement (dielectric antenna effect).

2) No out-of-plane dipole is observed. It can been explained that, at room temperature, the emission of CdSe NPLs originates only from ± 1 transitions [44], which is equivalent to an incoherent sum of two orthogonal in-plane dipoles. For CdSe nanocrystals, A.L. Efros et al. have calculated that a third dipole component can present [79], but not for the case of CdSe NPLs.

However, it is necessary to point out that, a tiny portion (less than 0.03, beyond the resolution of our measurements) of an out-of-plane dipole is possible to exist in single NPLs, due to reasons irrelevant to novel transition state, such as the deformation of NPLs, or inner local electrical fields induced by loss of ligand.

4.3 Dipole analysis of self-assembled NPLs chains

In this section, we will apply our dipole analysis protocol to self-assembled NPLs chains.

We prepared samples using the same protocol as for single NPLs (but with a different dilution concentration of 500X). When isolated NPLs chains are deposited on the glass substrate, all the NPLs in the chain should stand on their edges, instead of lying face down as in the case of single NPLs. We then spin-coated a PMMA layer with specific thickness. According to the introduction in section 4.1, the reflection experimental configuration is more sensitive to probe dipoles lying horizontal to the substrate. Thus, in order to probe the out-of-plane dipole component in the case of assembled NPLs chains, we choose the reflection experimental configuration in this section.

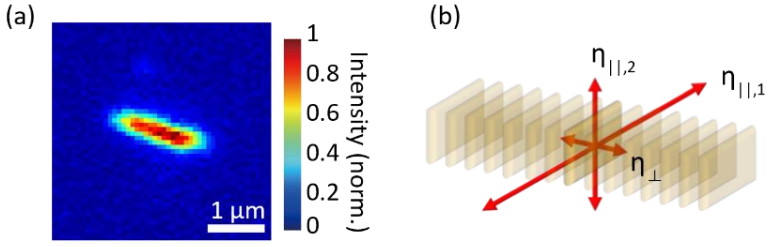

Figure 4-29. (a) CCD image of a long NPL chain under wide-field mercury lamp illumination. (b) Schematic of the three-dipole emission model. Color scale: normalized emission intensity.

When optically characterizing the NPLs chains, we use the same protocol as for single NPLs measurements, but a slightly lower excitation laser power, ranging from 3 to 5 nW, in order to keep the laser power within the linear excitation regime as discussed in chapter 2. A CCD image of a single

chain is shown in figure 4-29 (a), and again we use a 3-dipole model to describe the behaviour of this chain, with dipoles proportions of $\eta_{\parallel,1}$, $\eta_{\parallel,2}$ and $\eta_{\perp}$ (as shown in figure 4-29(b)). Note that now the out-of-plane dipole (out of the NPL planes) is the horizontal dipole parallel to the NPL chain. Thanks to the piezo electric system, we can scan and locate the chains, or position the laser spot precisely on different positions of the chains to perform the polarization and Fourier plane image analysis.

4.3.1 Polarization analysis of single chains

Figure 4-30 shows a representative laser scanning image of a NPLs chain, which is linearly aligned and is about 2 μm in length. We measured emission from different portions of the chain by positioning the excitation laser spot at different positions as represented by red circles. From the polarization curves we can see that both the degree of polarization δ and the orientation of the stronger in-plane dipole Φ are very similar, despite the positions of the probe: it suggests that the stacked NPLs in this chain are highly ordered with similar orientation. Besides, by comparing the angle Φ obtained from polarization curve to the orientation of the chain shown on the laser scanning image, we find that the stronger dipole in the chain is oriented along the direction of the elongated axis of each NPL (orthogonal to the stacking direction of the chain), which is in great accordance with the observation on single NPLs in section 4.2, and also with the reports on NPL needles (bundles of NPL chains) [69].

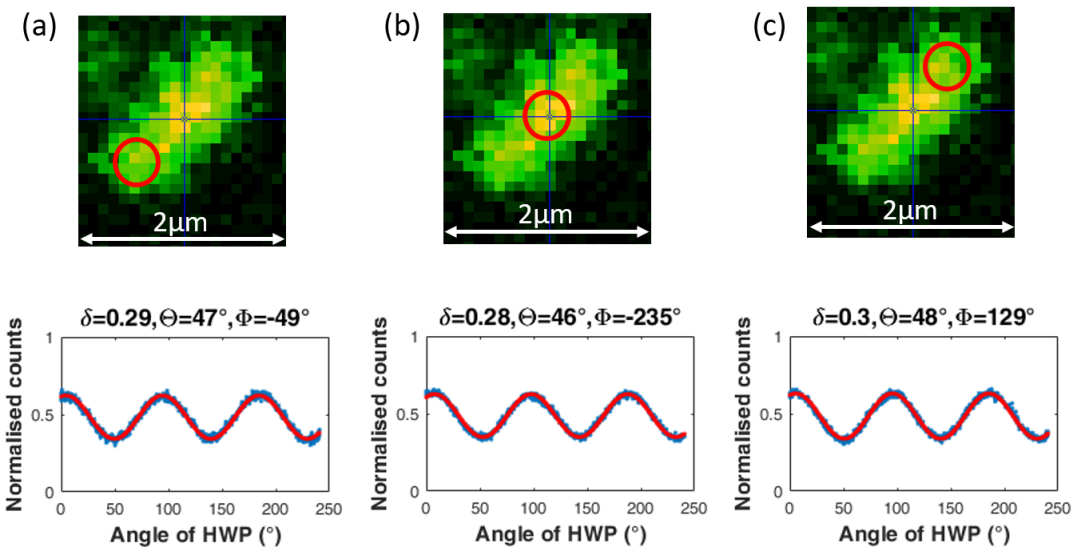

Figure 4-30. Polarization analysis of a same NPLs chain with excitation on different position: (a) head; (b) middle and (c) tail.

However, there are still a bit of deviations in the values of δ and Φ, which can be attributed to: 1) different behaviours of different portions of the chain, some being twisted; 2) slight tilting of NPLs in the chain because of a slight disorder, as well as 3) the experimental uncertainty.

4.3.2 Fourier plane image analysis of single chains

We then analyse the Fourier plane image (figure 4-31(a)) of the same chain (as in figure 4-30) to investigate their dipole components. Satisfyingly, we obtained again a great consistence on the dipole orientations between angle Φ (obtained by the polarization analysis) and Fourier plane image.

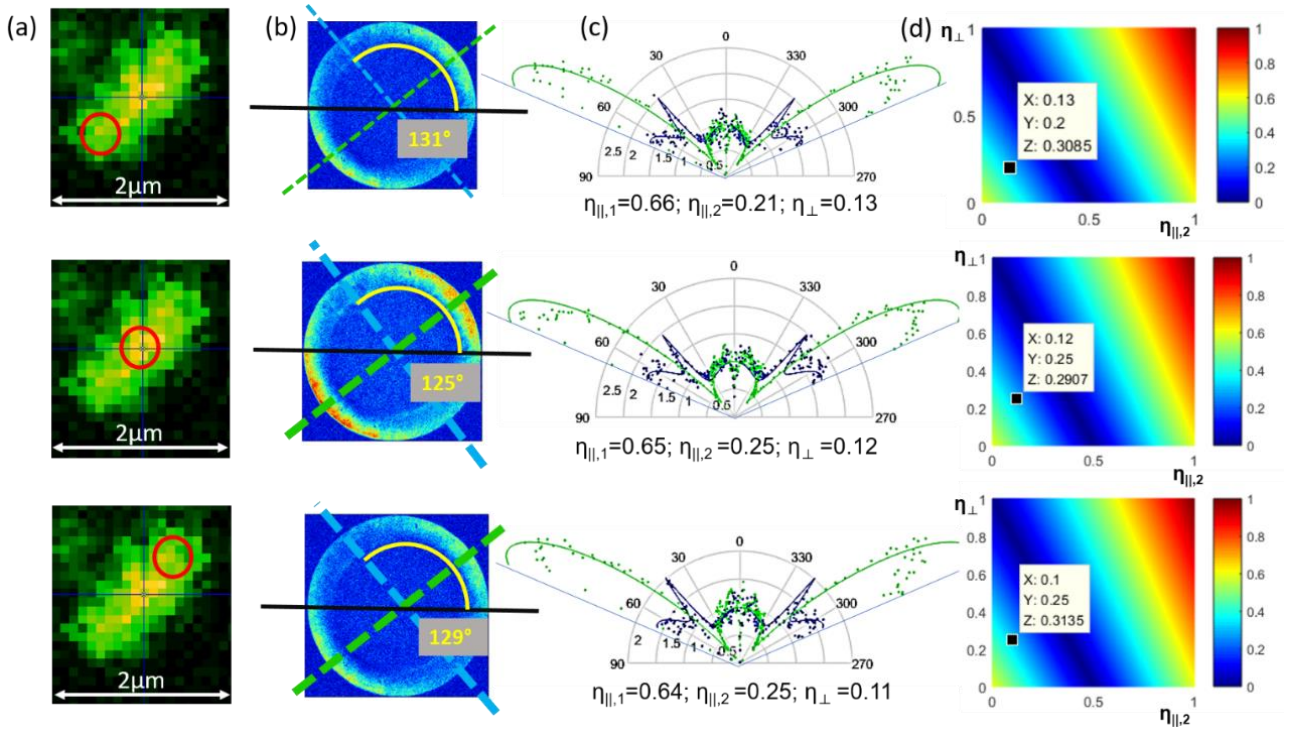

Figure 4-31. Fourier plane image of the same chain. (a) Probe of different portion in the chain. (b) Raw data of Fourier plane image. (c) Fitting (solid lines) of profiles of cutting lines (dots) along two orientations indicated by blue/green dashed lines in Fourier image (c). (d) theoretical degree of polarization $\delta_{theo}$with dipole portion as extracted in (c).

Same as before, we plot the cross-section profiles along two cutting lines (dashed line in figure 4-31 (b)) into blue and green dots in figure 4-31 (c) and fit them by solid lines. As shown in figure 4-31 (c), for different portions of the chain, one can always achieve decent fittings with consistent dipole components η, confirming the highly ordered assembly in this chain. When looking closely at the fitting, some deviations can be noticed in the small angle portion ($\theta \sim 0°$) and high angle portion ($\theta > 60°$) as well. The former deviation is subject to very strong noise because they are inferred from just a few pixels on the Fourier image, while the latter deviation can be caused by objective aberrations [186].

Next, we calculate the theoretical degree of polarization δ_{theo} and plot in figure 4-31 (d) and compare it to the experimental results δ_{exp} by polarimetry. As a result, we find one more time an excellent consistence, confirming the accuracy of our probing on the three dipole components in NPLs chains.

Now we discuss the result of η. As expected, on different positions of a same NPLs chain, we extracted similar in-plane dipole components ($\eta_{\parallel,1}$ and $\eta_{\parallel,2}$) from Fourier plane image analysis. However, surprisingly, we also found a contribution from an out-of-plane dipole component ($\eta_{\perp}$~0.12) in the chain's emission. We evaluated the fitting precision of our experimental configuration by slightly tuning the dipole portions $\eta_{\parallel,1}$, $\eta_{\parallel,2}$ and $\eta_{\perp}$. As it is shown in figure 4-32, the fitting becomes poor when changing $\eta_{\parallel,2}$ by ± 0.05 or changing $\eta_{\perp}$, the proportion of the novel out-of-plane component, by ± 0.03. Therefore, the extracted proportion of the out-of-plane dipole component $\eta_{\perp}$~0.12 is far above the resolution of our probing.

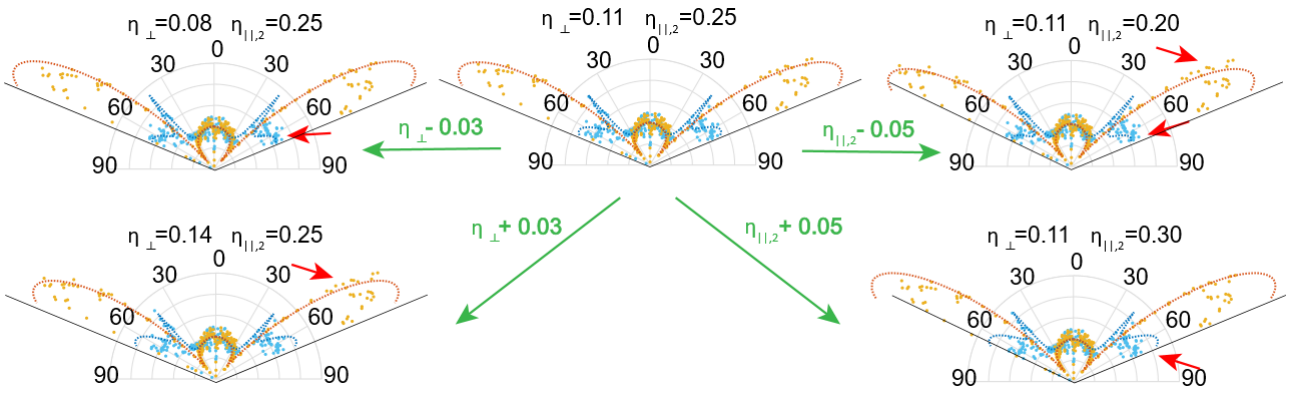

Figure 4-32. Fitting precision of NPLs chain's radiation pattern. Poor fitting areas are pointed out by the red arrows.

4.3.3 Dipole analysis of NPLs chains with different configurations

Although we have demonstrated that, within our resolution, an out-of-plane dipole component is extracted from the emission of self-assembled NPLs chains, we seek for further support to corroborate our observation. Thanks to the reflection experimental configuration, by tuning the thickness of PMMA cover layer, we can obtain a set of different theoretical radiation patterns for Fourier plane image analysis, because the collected electric field is a sum of direct emission and emission reflected by the glass-air interface, which is modified when tuning the distance between NPLs and PMMA-air interface. As shown in figure 4-33, if we create three dipoles with the same fractions ($\eta_{\parallel,1} = 0.62$, $\eta_{\parallel,2} = 0.26$ and $\eta_{\perp} = 12$), three different radiation pattern can be obtained in figure 4-33.

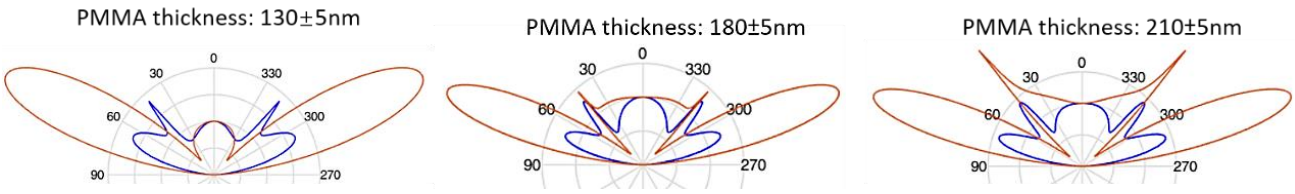

Figure 4-33. Designs of 3 different radiation pattern by tuning the thickness of PMMA layer.

We analysed the polarization curve and Fourier plane image for different NPLs chains using these different configurations as shown in figure 4-34 (a). We recorded polarization curves and Fourier plane images in figure 4-34 (b) and (c) respectively, from which we obtain consistence in the orientation of the major dipole in the NPLs chains.

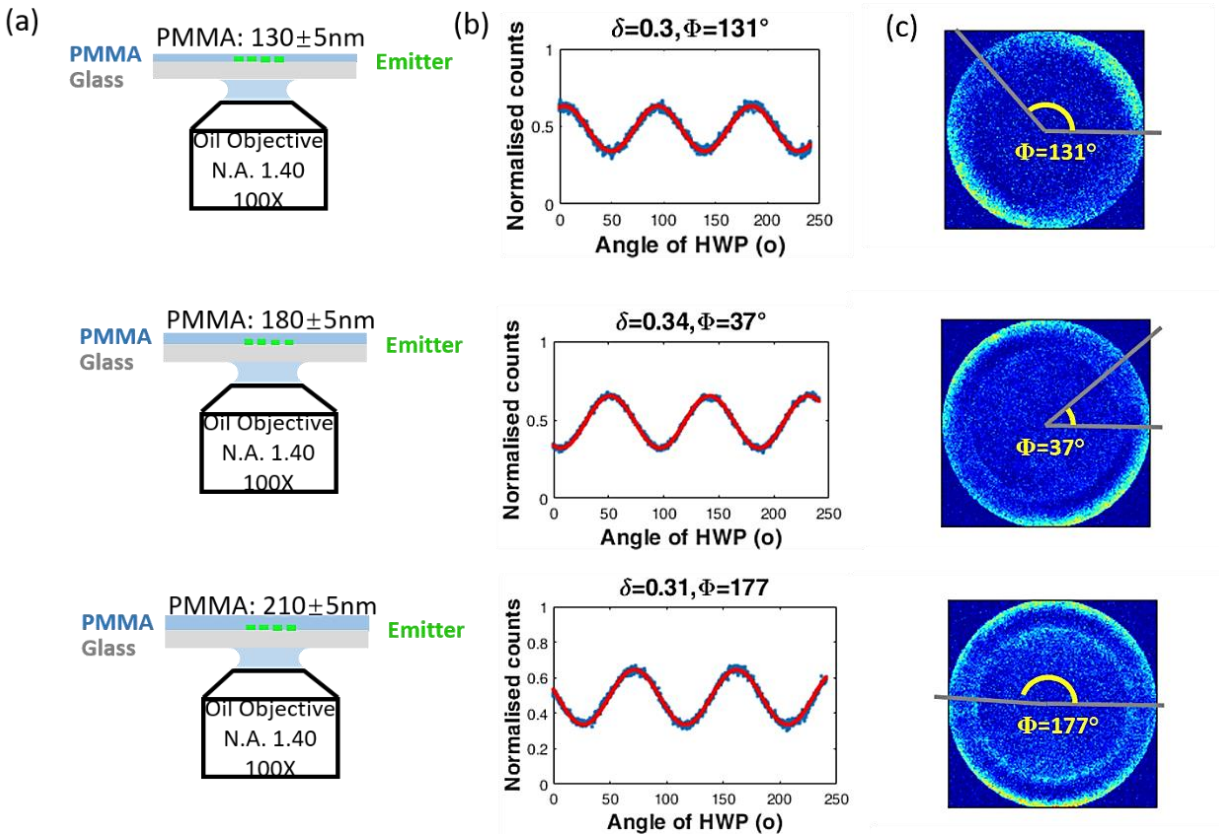

Figure 4-34. Polarization (b) and Fourier plane image analysis (c) using different configuration (a).

We then analyse the radiation pattern. As shown in figure 4-35, the overall agreement between the experimental and fitted curves is excellent, under these different configurations, with very similar dipole proportions: $\eta_{\parallel,1} =$ 0.61-0.64, $\eta_{\parallel,2} =$ 0.25-0.27, and $\eta_{\perp} =$ 0.11-0.14.

To confirm the fitting accuracy, we calculated theoretical degree of polarization δ_{theo} and compare it to δ_{exp}. Again, we find a very good agreement, with δ_{theo} (resp. δ_{exp}) values of 0.3

(resp. 0.3), 0.34 (resp. 0.34), 0.33 (resp. 0.31) for different configurations. The agreement between δ_{theo} and δ_{exp} is excellent.

Thus, although the radiation patterns are significantly different when the PMMA thickness changes, all the Fourier plane images can be well fitted by very consistent η values: this is a striking confirmation on the accuracy of our probing on the three-dimensional dipole components.

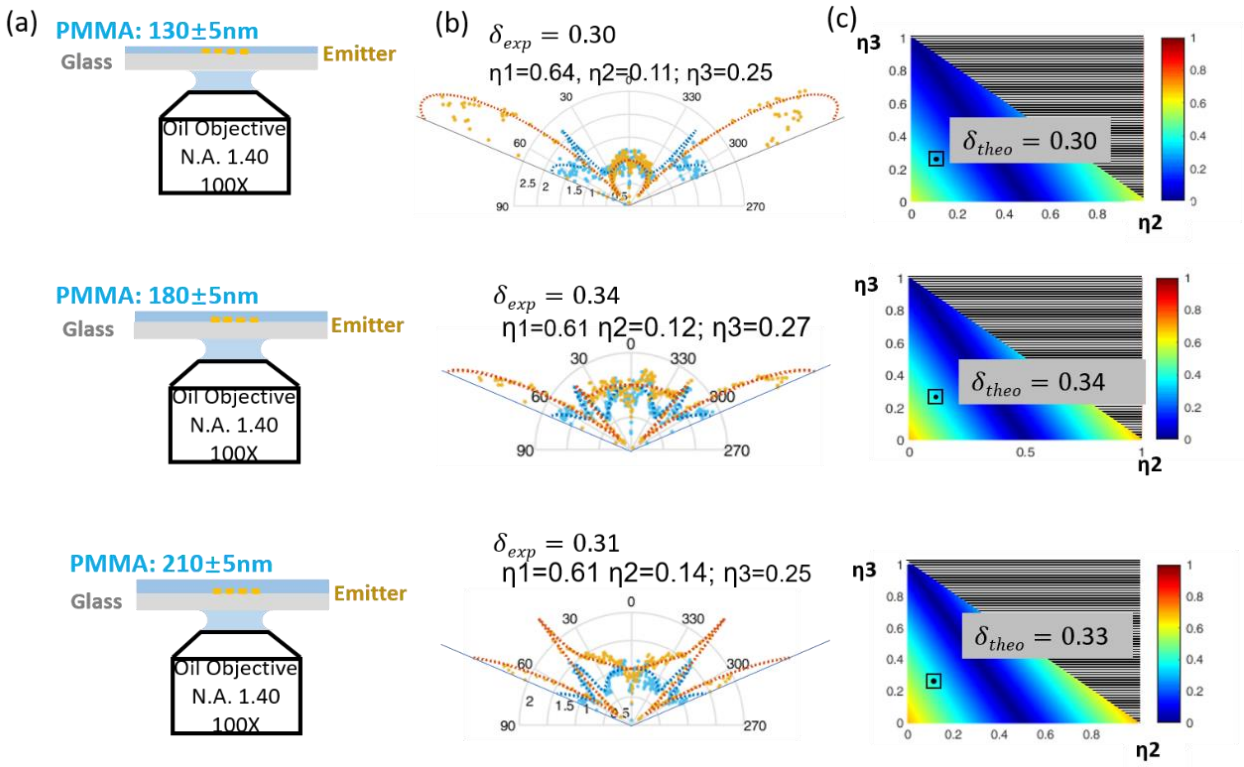

Figure 4-35. Fitting the Fourier images (b) under different configuration (a). Calculated theatrical degree of polarization δ_{theo}.

4.3.4 Summary and discussion

To sum up this section, we plot a histogram of 27 chains measured under different experimental configuration. As it can be seen in figure 4-36, the distribution of extracted proportions η are very monodisperse, with average values:

$$\eta_{\parallel,1} = 0.62,\ \eta_{\parallel,2} = 0.26,\ \eta_{\perp} = 0.12$$

and with standard deviations of 0.03, 0.02 and 0.03 respectively. The slight deviation could be attributed to twisted or tilted NPLs in the chain due to the imperfect stacking, or experimental uncertainty of our protocol.

One can now calculate the anisotropy factor of the two in-plane dipoles in the chain by

$$A_{chain} = \frac{\eta_{\parallel,2}}{\eta_{\parallel,1}} = 0.42$$

which is very close to the anisotropy factor of the single NPLs (A_{NPL} =0.43). This indicates that the two in-plane dipoles are not strongly modified by the self-assembly, or to say the overall orientation of the NPLs are almost perfectly aligned in the whole chain, regardless of the presence of twisting as shown in TEM image (figure 1-10 in chapter 1). Consequently, it raises a new question in the same time: what is the origin of the novel out-of-plane dipole?

To try to find more information on the assembly-induced effect, in the next section, we turn to analyse NPL clusters consisting of different numbers of NPLs.

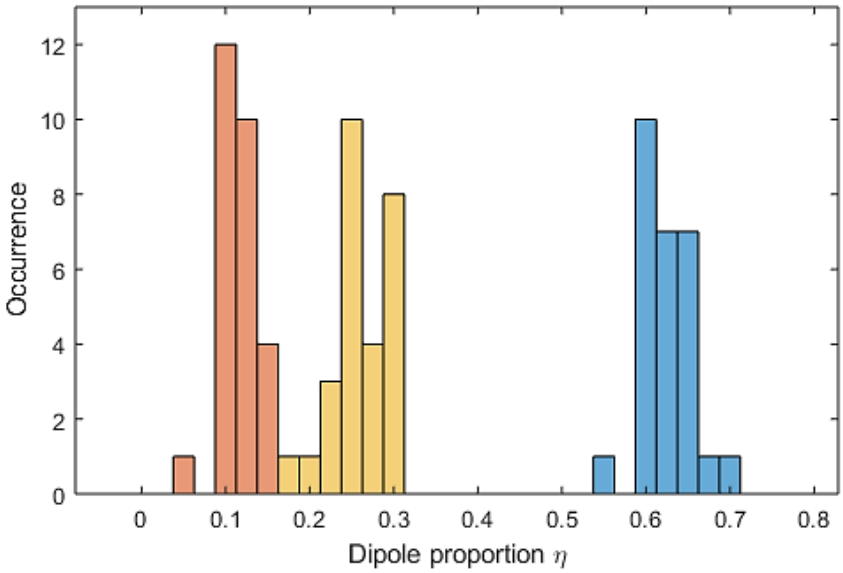

Figure 4-36. Histogram of the measured coefficients $\eta_{\parallel,1}$ (blue), $\eta_{\parallel,2}$ (yellow) and $\eta_{\perp}$ (orange) for 27 different NPLs chains.

4.4 Dipole analysis on clusters as intermediate cases

We use the transmission experimental configuration, same as used for single NPLs measurements. Here we did not choose the reflection case because the distance z_0 between the emitter and the PMMA-air reflection interface will be significantly affected by the size and orientation (vertical or horizontal to the substrate) of the clusters, inducing a new source of error in the probing (which is not a problem for single NPLs because they all lie face down on the substrate with very thin and well controlled thickness).

We prepared the samples using the dispersion solution of single NPLs, from which we can obtain clusters by reducing the dilution concentration. In the TEM image (figure 1-8), we can see that some of the clusters are horizontal and some are vertical. However, during our optical measurements, we find mostly the face down cases together with very few edge-up clusters. These two deposition cases can be well distinguished by polarization and Fourier plane image analysis. In this section, our study is based on the horizontally deposited clusters measured under transmission experimental configuration (the analysis under reflection condition is not reliable, because the size of the cluster is uncertain and so is the fitting result of the Fourier imaging). For the face-down clusters, the out-of-plane dipole is thus the vertical dipole.

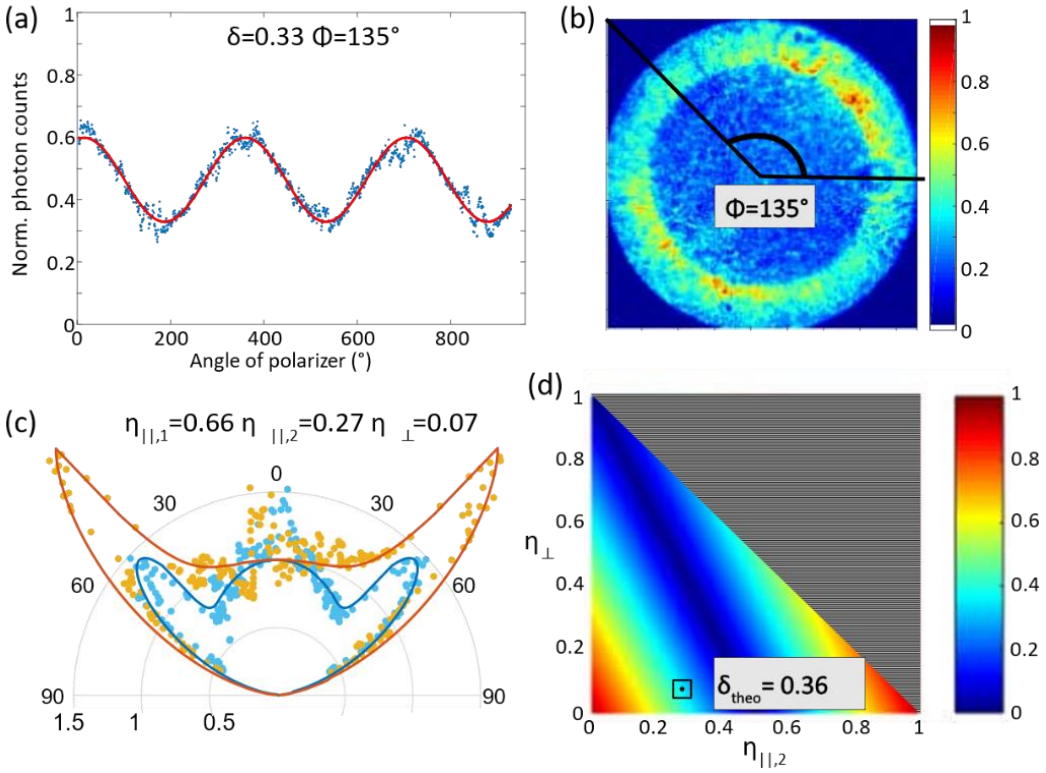

Figure 4-37. Measurements of a representative NPL cluster under transmission configuration. (a) Experimental polarization curve; (b) Fourier plane image; Color scale: normalized emission intensity. (c) radiation pattern of cutting lines along 135° (blue dots) and 45° (yellow dots) and theoretical fittings (full lines); (d) theoretical degree of polarization with dipole portion as extracted in (b).

We analysed the polarization curve and Fourier plane image for clusters following the same protocol. The results of a representative cluster are shown in figure 4-37 (a) and (b). We plot in figure 4-37 (c) the cross section profiles of the two cutting lines along $\Phi = 45°$ and $\Phi = 135°$, as determined by polarization curve fitting in figure 4-37 (a). The radiation pattern of this cluster is very similar to that of the single NPLs measured also under transmission configuration (figure 4-24 (b)), indicating that this cluster is lying horizontally on the substrate. The result of fitting to the radiation

pattern is $\eta_{\parallel,1} = 0.66$, $\eta_{\parallel,2} = 0.27$, $\eta_{\perp} = 0.07$. Thus, we detected again an out-of-plane dipole in clusters, which is also seen in NPLs chains but not in single NPLs.

Once more, we evaluated the fitting precision of dipole probing under transmission experimental configuration by slightly tuning the dipole portions $\eta_{\parallel,1}$, $\eta_{\parallel,2}$ and $\eta_{\perp}$. As it is shown in figure 4-38, we observed poor fitting portions when changing $\eta_{\parallel,2}$ by ± 0.05 or changing $\eta_{\perp}$, the out-of-plane dipole component, by ± 0.03. Thus, we demonstrate that the observed result $\eta_{\perp} = 0.07$ is significantly different from zero.

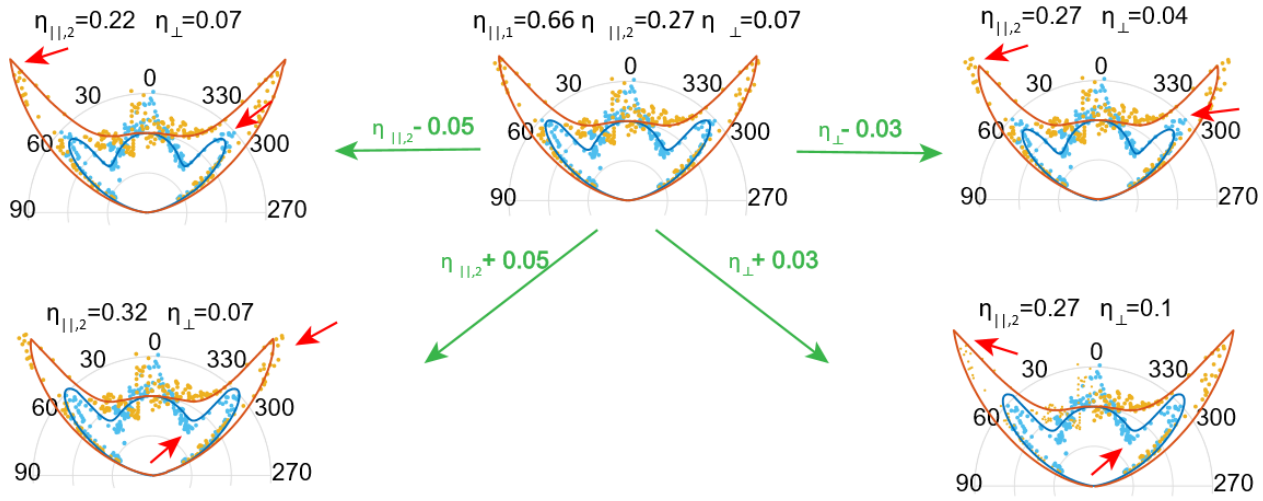

Figure 4-38. Fitting precision of NPLs chain's radiation pattern. Poor fitting areas are pointed out by the red arrows.

We statistically analysed 10 different clusters. Their dipole components distributions are shown in figure 4-39, with the values in averages of:

$$\eta_{\parallel,1} = 0.59,\ \eta_{\parallel,2} = 0.35,\ \eta_{\perp} = 0.06$$

This time, if we calculate the anisotropy factor of the two in-plane dipoles in the cluster, we can find:

$$A_{clus} = \frac{\eta_{\parallel,2}}{\eta_{\parallel,1}} = 0.59$$

Compared to that factors for single NPLs ($A_{NPL} = 0.42$) and NPLs chains ($A_{chain} = 0.43$), this value is a bit different but still in a general agreement. This deviation may be because, in clusters, the NPLs are not parallelly aligned, as shown in chapter 1 on figure 1-8.

Most importantly, in all of the considered clusters, we always find the out-of-plane dipole component, of which the average value is $\eta_\perp$~0.06 with a dispersion ranging from 0.03 to 0.10: these results are in the intermediate stages between single NPLs ($\eta_\perp = 0$) and NPLs chains ($\eta_\perp$~ 0.12).

The observations on NPLs clusters may imply that the novel out-of-plane dipole is attributed to an effect related to self- assembly. In the next subsection, we will investigate the evolution trend of $\eta_\perp$ as the degree of assembly increases.

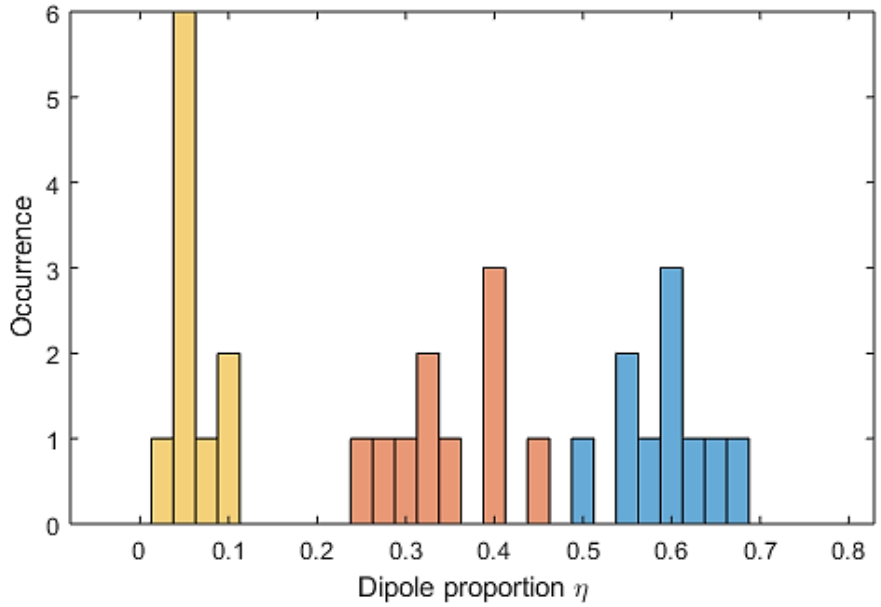

Figure 4-39. Histogram of the measured coefficients $\eta_{\parallel,1}$ (blue), $\eta_{\parallel,2}$ (red) and $\eta_\perp$ (yellow) for 10 different NPLs clusters.

4.5 Evolution of the novel dipole as a function of the number of NPLs

At this point, we finished the dipole analysis on different NPLs emitters, with an increasing degree of assembly from isolated single NPLs, to clusters and eventually to highly ordered NPLs chains.

All the measured proportions η of dipole components, on single NPLs, clusters and chains, are summarized in figure 4-40. For the NPLs chains, we have two batches of samples referred as 'short' or 'long' chain (as introduced in chapter 1), because their lengths are shorter than 500 nm (without twist) or longer than 1 μm (with twist), respectively. The obtained values are similar for both the short and the long chain samples, showing no influence of either the chain length or its twist. This may be because, as introduced in chapter 1, the NPL rotation occurs in limited portions of the chains and most NPLs form straight stacks [71].

The major contributions to the emission of all kinds of NPLs emitters are from the two in-plane dipoles horizontal to the NPL's plane, in consistence with the previous measurements by our group [6,29] and by other groups [77,84]. The anisotropy factor ($A = \eta_{\parallel,2}/\eta_{\parallel,1}$) of these two in-plane dipoles are also in good agreement (0.43 for single NPLs and 0.42 for NPLs chains). This indicates that the polarization in emission results mostly from the antenna enhancement effect by the elongated dielectric shape of each NPL [6,84,85], while the stacking in the other dimension (perpendicular to the NPL plane) doesn't modify the ratio between the in-plane dipoles.

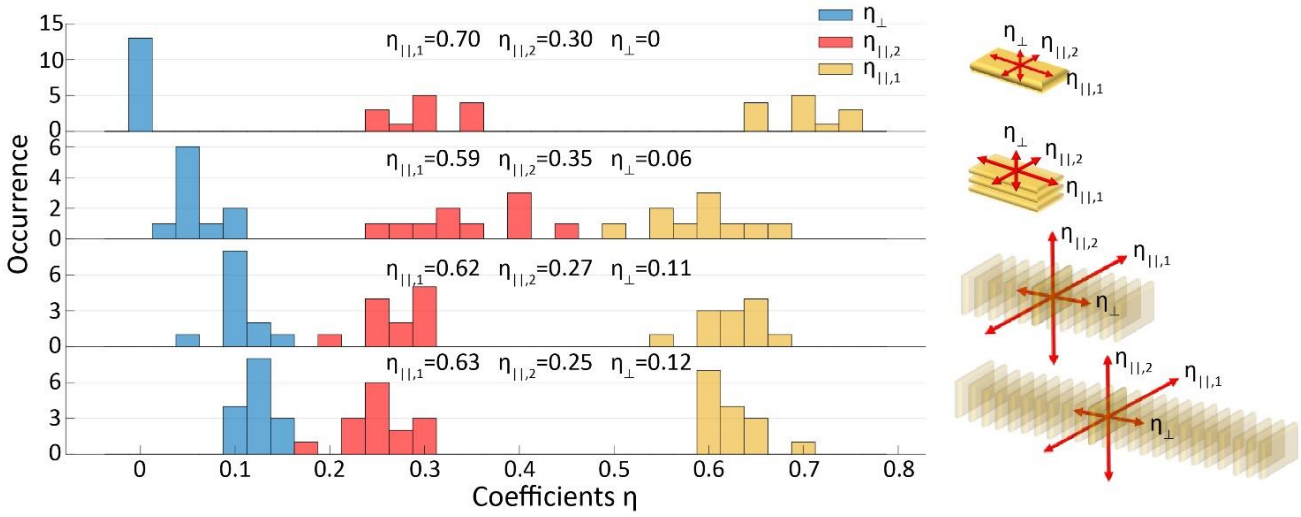

Figure 4-40. Summary of the measured coefficients $\eta_{\parallel,1}$, $\eta_{\parallel,2}$ and $\eta_{\perp}$ for the different NPL samples: single NPLs, clusters, short chains and long chains.

As for the out-of-plane dipole component $\eta_{\perp}$, it increases as the number of platelets increases, from $\eta_{\perp} = 0$ for single NPLs, to an averaged value of 0.06 for clusters, then $\eta_{\perp} = 0.11$ for short chains and $\eta_{\perp} = 0.12$ for long chains.

To further study the influence of the assembly degree (i.e. the number of NPLs in the assembly) on the values of $\eta_{\perp}$, we reconstruct the evolution of $\eta_{\perp}$ as a function of N in NPLs assemblies. This number N is of the order of 35 for the 100-500 nm 'short' chains and 250 for the 1-2 µm 'long' chains. For clusters, we estimate the number N, from their partial antibunching curves measured under Hanbury-Brown and Twiss configuration, as explained in chapter 3.

Eventually, figure 4-41 presents the evolution of the out-of-plane dipole proportion $\eta_{\perp}$ as a function of number N: firstly $\eta_{\perp}$ increases relatively fast, when N is between 1 and 3 (small clusters); then this increase slows down in the cases of bigger clusters when N ranges between 3 and 10, followed by a quick saturation when $N > 10$, in the cases of big clusters as well as short or long chains.

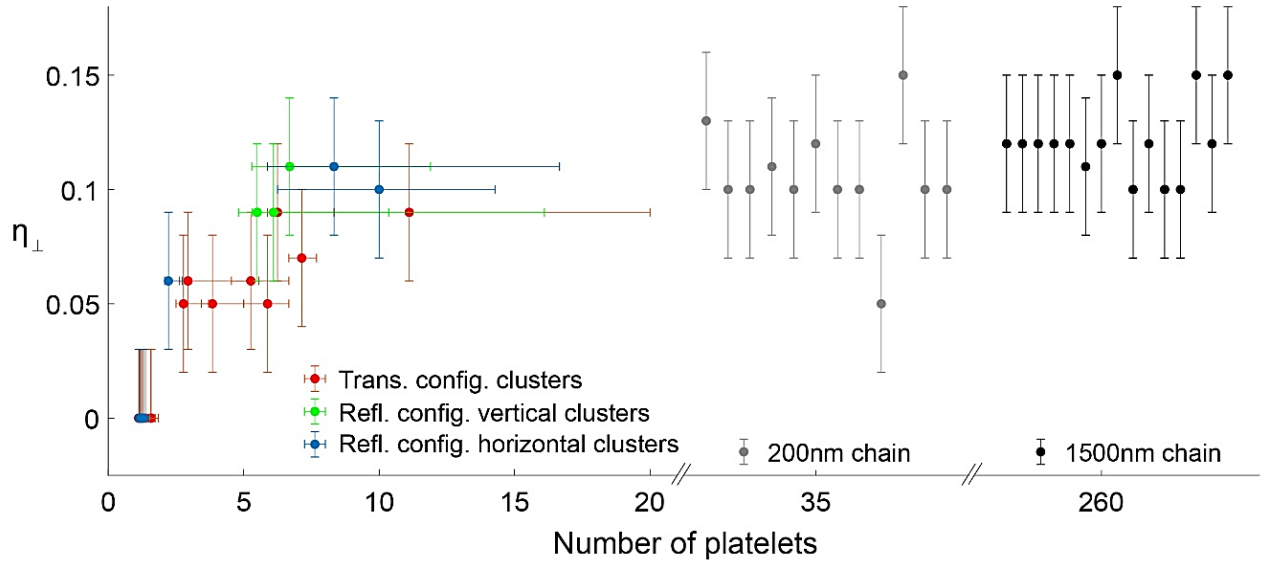

Figure 4-41. Out-of-plane dipole components plotted as a function of the number of platelets for different NPL emitters: single NPLs or clusters measured in reflection/transmission configurations, or chains measured by reflection configurations with difference PMMA thickness.

In addition, in figure 4-42, we summarize the values of experimental polarization degree δ_{exp} and the theoretical values δ_{theo} calculated from η proportions extracted from Fourier plane imaging, for all the NPLs emitters.

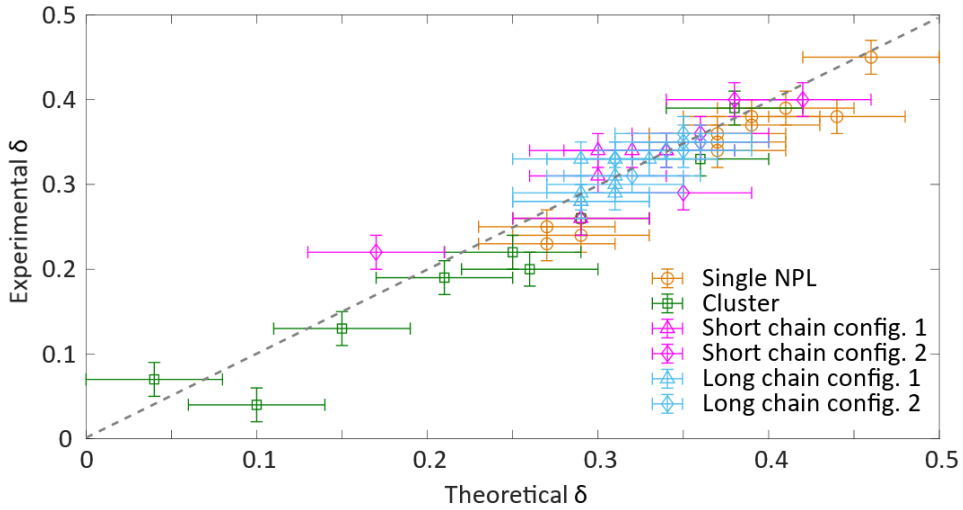

Figure 4-42. Relation between the experimental degree of polarization and its theoretical value (calculated with the η coefficients from Fourier imaging) for isolated NPLs, clusters and chains measured with PMMA layers of either 130 nm (denoted as config.1) or 180 nm (config.2) in thickness.

As we can see, the distribution of delta values of single NPLs and long/short chains are very concentrated, suggesting the homogeneity in the elongated shape of single NPLs and the well-controlled linear stacking of NPLs in chains. While for the polarization degree of clusters, values are

very deviated from close to 0 up to about 0.4. This is because, in the clusters, the NPLs are not parallelly stacked.

The uncertainty of the experimental polarization degree δ_{exp} is ± 0.02 as estimated from the fitting precision of the polarization curves, while the theoretical values δ_{theo} have also a deviation resulting from the fitting precision of the Fourier plane image analysis: for transmission configuration (cases of single NPL and cluster), uncertainty is ± 0.055; for reflection conditions with 130 nm (denoted as config.1 for chains) or 180 nm (config.2) PMMA layer, the uncertainty is ± 0.03 or ± 0.04, respectively.

Remarkably, an excellent agreement is always found between δ_{exp} and δ_{theo}, again corroborating the accuracy of our probing on proportions of dipole components η for all the NPLs emitters considered in this chapter.

To conclude this section, we emphasize that it is the precision of our dipole analysis protocol that allowed us to reveal this new dipole component, which was hidden in previous reports [12,69].

It is of widespread interest to well understand the dipole components in single emitters, as the overall performance of optoelectronic or plasmonic systems depends critically on the interaction between emitters and the adjacent structures, which is then dominated by the dipole conditions. During our dipole analyses, we concluded the nonexistence of out-of-plane dipoles component in single NPLs, in agreement with previous reports and with the theoretical estimations. On the contrary, for assembled NPLs (clusters and chains), we confirmed the presence of an out-of-plane dipole component, whose proportion increases as the number of stacked NPLs in the assembly increases. This striking result is, to the best of our knowledge, the first experimental observation on an out-of-plane emitting dipole in CdSe NPLs. The origin of this out-of-plane component will be discussed in the next sections.

4.6 FDTD simulations: antenna effect

It is well understood that the two in-plane dipoles in single NPLs become asymmetric because one of the dipoles is enhanced more along the long axis of the dielectric structure by antenna effect (as introduced in section 4.1.4). Given this, one may suspect that the out-of-plane dipole component emerging in the NPLs chains also originates from the dielectric stacking along the direction normal to the NPL's plane by the same optical mechanism (antenna enhancement). To study this hypothesis,

in this section, we employ Lumerical FDTD Solution to examine how the elongated shape of the dielectric structure enhances its own radiation and calculate the enhancement factor, k, in our system.

4.6.1 Numerical calculation of antenna effects.

We built up models with different structures as shown in figure 4-43: a symmetric 10 x 10 x 10nm^3 cube (a), a single CdSe NPL (b), a stacked NPLs chain (c) and a continuous CdSe block (d). The size of a single NPL is 20 x 7 x 1.5 nm^3, same as our samples. The length of the chain and the block is 1500 nm. Here we set the refractive index of all the dielectric structures as 2.64+0.44i [187], which is the refractive index of bulk zinc-blende CdSe at 550 nm wavelength. The index of the surrounding medium is 1.5, a typical value for glass substrate and PMMA cover layer. We positioned a monitor 30 nm below the structure with a large enough lateral expansion (15x15 μm^2) to properly collect all the near field electromagnetic waves. We then numerically integrated the projected electrical field intensity E^2 in the far field.

In the simulation, we define the coefficients η of three incoherent electrical dipoles in dielectric structures along x, y and z axis as η_x, η_y and η_z, which are proportional to the square of the dipole moments, so they are also proportional to the emitted intensities. We normalize these coefficients by:

$$\eta_x + \eta_y + \eta_z = 1 \tag{4.65}$$

We also define I_x, I_y and I_z as the intensities detected respectively from a dipole along the x, y and z dipoles.

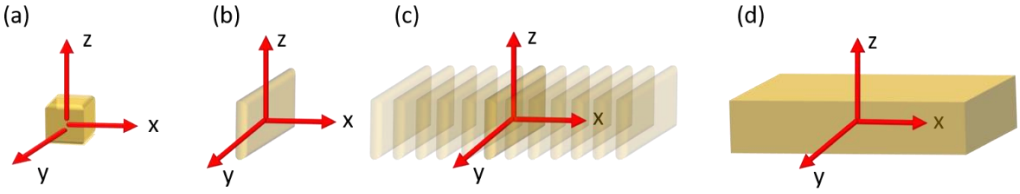

Figure 4-43. Different models of (a) a symmetric 10x10x10 nm^3 cube, (b) a single 20x7x1.5 nm^3 NPL, (c) a stacked 20x7x1500 nm^3 NPLs chain and (d) a 20x7x1500 nm^3 CdSe block.

We started with a symmetric structure, the (10nm)^3 CdSe cube. We added repestively x, y and z dipoles located at the center of the stucture with identical dipole moments $\eta_x : \eta_y : \eta_z = 1:1:1$. As expected for an isotropic structure, we found $I_x : I_y : I_z = 1:1:1$.

We then performed simulation for x, y and z dipoles respectively in the other structures and summarized all the results in table 4-2.

Table 4-2. Emission intensities of dipoles along x, y or z axis in three different configurations.

	I_x (a.u.)	I_y (a.u.)	I_z (a.u.)
Single NPL	7	53	42
NPL chain	9	46	32
CdSe Block	59	28	10

For the single NPL (i.e. the reference for the stacked NPLs chains) as expected in an elongated dielectric antenna, the emission is much stronger for an in-plane dipole (y or z) than for an out-of-plane dipole (x), and it is stronger for the main axis of the platelet (y) than for its shorter axis (z).

This remains true for the NPL chain: the main effect is the effect of each single NPL which enhances the in-plane dipoles (y and z) with respect to the out-of-plane dipole (x). However, the ratio of x with y and z is slightly larger for the chain: there is a slight dielectric antenna effect of the stacking axis x of the chain. But this effect only weakly restores the x dipole contribution which was quenched by the NPL flat shape. This is very different from the case of an elongated CdSe block, where the x axis dipole is strongly enhanced by dielectric antenna effect as compared to the other axes.

These calculations in table 4-2 mean that, if a sum of 3 incoherent dipoles of equal moments ($\eta_x = \eta_y = \eta_z$) is inserted in a platelet inside a chain:

1) For single NPLs, the y dipole will be enhanced 53/7 = 7.6 times with respect to the x dipole, and the z dipole 6 times. A dipole with $\eta_x = \eta_y = \eta_z =$ 0.33 inserted in a NPL should thus behave like a dipole with $\eta'_x = 0.07$, $\eta'_y = 0.52$, $\eta'_z = 0.41$ inside a homogeneous medium.

2) For NPL chains, similarly, the y dipole will be enhanced 46/9 = 5.1 times and the z dipole 3.55 times. Thus a dipole with $\eta_x = \eta_y = \eta_z =$ 0.33 inserted in a chain will behave like a dipole with $\eta'_x = 0.10$, $\eta'_y = 0.53$, $\eta'_z = 0.37$ inside a homogeneous medium.

From 1) and 2), again, we see that the y and z dipoles are enhanced with respect to the x dipole, because of the anisotropy of the NPL's dielectric shape. We name this effect as dielectric **anisotropy effect**. Additionally, if we compare the η_x values between single and stacked NPLs, we see an

enhancement in x direction by a factor of 0.10/0.07 = 1.43, which results from a antenna enhancement due to the stacking. Here we name this effect as **stacking effect** and we define **enhancement factors of the stacking effect, κ,** and calculate them for the x, y and z dipoles:

$$\kappa_x = 1.43;\ \kappa_y = 1.02;\ \kappa_z = 0.90$$

These results mean that, as compared to single NPLs, the stacked dielectric structure of the chain will enhance the x dipole by a factor of 1.43, while slightly modifying the coefficients of y and z dipoles by factors of 1.02 and 0.90, respectively.

4.6.2 Comparisons: analytical calculation vs numerical simulation

In the last subsection we numerically calcualted the enhancement effect in our samples. To check the accuracy of the FDTD simulation, in this subsection, we will compare the results of FDTD simulation with the analytical calculations by MATLAB using the same models and configurations.

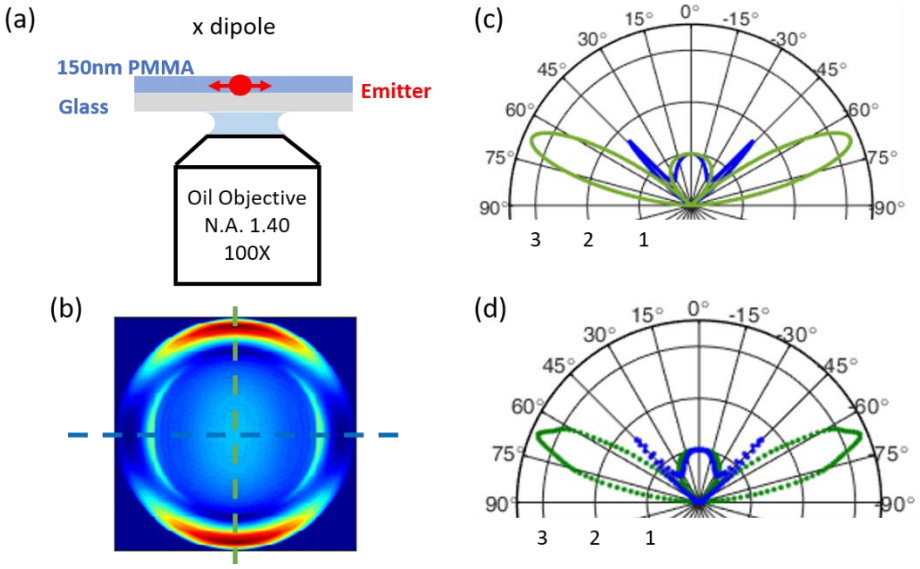

Figure 4-44. Theoretical analysis of the x dipole in the configuration illustrated in (a). (b) Theoretical far field emission map from FDTD simulation. (c) Analytical calculation and (d) numerical simulation of radiation patterns.

As shown in figure 4-44 (a), we put a dipole along x axis in a 1.5 μm chain on the glass substrate coverd by a layer of PMMA. The refractive index of the CdSe NPLs in the chain is 2.6+0.44i while the indices of PMMA and the substrate are close to 1.5. We put the same monitor as introduced previously to collect the electromagnetic waves from which we obtain the projected light distribution in the far field as shown in figure 4-44 (b). Then we plot the radiation pattern along two cutting lines

for comparisons. As a result, the analytically calculated radiation pattern (figure 4-44 (c)) and the numerically simulated pattern (figure 4-44 (d)) are in excellent agreement.

We also analysed the results for y and z dipoles as shown in figure 4-45 and figure 4-46, respectively. Note that, for the z dipole, we analysed it together with a y dipole in order to make a proper normalization, because, when plotting the radiation pattern, we normalize it by the values at $\Theta \sim 0°$ where for a solely z dipole the emission power is close to 0.

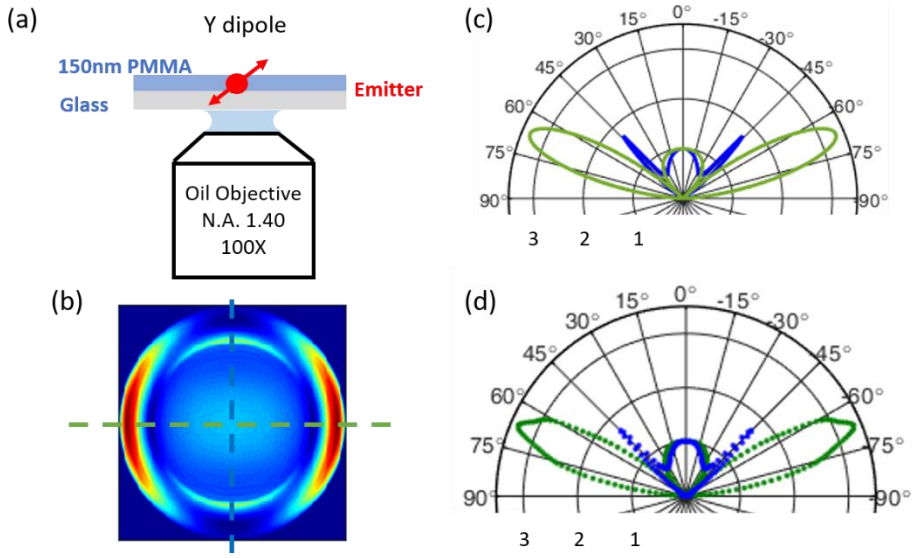

Figure 4-45. Theoretical analysis of the y dipole in the configuration illustrated in (a). (b) Theoretical far field emission map from FDTD simulation. (c) Analytical calculation and (d) numerical simulation of radiation patterns.

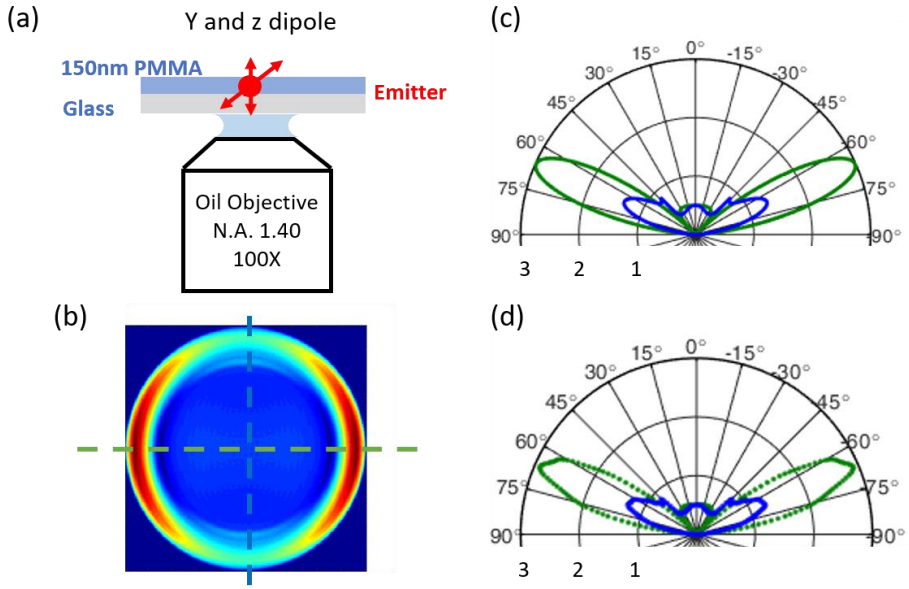

Figure 4-46. Theoretical analysis of the y and z dipole in the configuration illustrated in (a). (b) Theoretical far field emission map from FDTD simulation. (c) Analytical calculation and (d) numerical simulation of radiation patterns.

As we can see, for all of the x, y, z dipoles, the accordance between the analytical calculation and numerical simulation is excellent. Thus, we can consider the enhancement factor ($\kappa_x = 1.43$, $\kappa_y = 1.02$, $\kappa_z = 0.90$) extracted from FDTD simulation as a reliable estimation of antenna enhancement efficiency of the stacked NPLs chains. Hereafter, we are able to quantitatively deduce original dipole component in the NPLs based on the enhancement factors.

4.6.3 Dielectric effects in single NPLs and NPLs chains

Given the numerical calculation of the antenna enhancement effect, in this subsection we will work backward, from the resulted dipole coefficients η'_x, η'_y and η'_z obtained in the measurements in section 4.3 and 4.4 for single NPLs and chains, to deduce the intrinsic dipole components η_x, η_y and η_z in an imaginary homogeneous medium ***without*** *the modification by the dielectric antenna effects.*

Original dipoles in NPLs chains without dielectric anisotropy effect

We assume that the dipole-in-NPL behaves like a dipole that can be enhanced by the dielectric structure by a factor of κ. According to the FDTD simulation in subsection 4.6.1, to account for the experimental observation that the NPL chain behaves as a sum of dipole contributions $\eta'_x = 0.12$, $\eta'_y = 0.62$, $\eta'_z = 0.26$, we need to place a sum of dipoles $\eta_x = 0.385$, $\eta_y = 0.385$, $\eta_z = 0.23$ inside the NPL chain, so that the antenna effect modifies the latter dipole sum into the former.

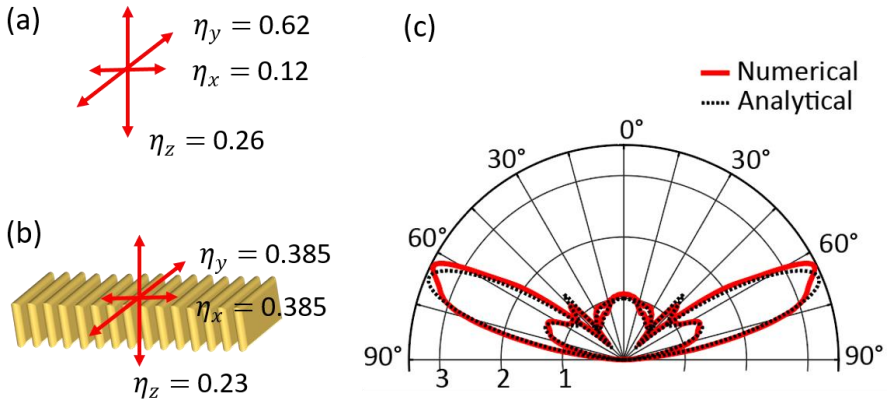

Figure 4-47. (a): Three dipoles in ratio of $\eta'_x:\eta'_y:\eta'_z = 0.62:0.26:0.12$ in a homogeneous medium. (b): Three dipoles in ratio of $\eta_x:\eta_y:\eta_z = 0.385:0.385:0.23$ with antenna enhancement. (c): Radiation patterns of analytical calculation (black dotted line) corresponding to model (a) and of numerical calculation corresponding to model (b).

We can verify that such a dipole would indeed match with our measurements by conducting the following two theoretical calculations:

1) 3 dipoles with coefficients of $\eta'_x = 0.12$, $\eta'_y = 0.62$, $\eta'_z = 0.26$ in a homogeneous medium analytically calculated by the equations introduced in section 4.1.2 (figure 4-47 (a)).

2) 3 dipoles with proportion of $\eta_x = 0.385$, $\eta_y = 0.385$, $\eta_z = 0.23$ in the dielectric NPLs chain (with antenna effect) calculated by FDTD simulation (figure 4-47 (b)).

The radiation patterns of the case 1) and 2) are plotted in figure 4-47 (c), in which we find excellent agreement between them, confirming the accuracy of our deduction.

Deduction of the dipoles in single NPLs

Now we can move on to study another question: what kind of dipole coefficients are needed for the single NPLs (the building blocks of the NPL chains), to result in the dipoles measured in the chain (i.e. $\eta'_x = 0.12$, $\eta'_y = 0.62$, $\eta'_z = 0.26$) in consideration of the dielectric antenna effect?

To this end, we put the dipoles with deduced coefficients $\eta_x = 0.385$, $\eta_y = 0.385$, $\eta_z = 0.23$ into the single NPLs and calculate the corresponding dipole coefficients in a homogeneous medium. As a result, for single NPLs, we obtain:

$$\eta_x = 0.08,\ \eta_y = 0.63,\ \eta_z = 0.29$$

In other words, to explain the experimental observation of a 0.12 out-of-plane dipole component for the NPL chain radiation purely by a dielectric antenna effect, theoretically we would need to have a 0.08 out-of-plane dipole in a single NPL. In section 4.2, we confirmed the absence of the out-of-plane dipole component in single NPLs, by statically analysing several samples and corroborating out results by using different experimental configurations. Thus, dielectric antenna effect solely cannot explain the emerging out-of-plane dipole in our experiments.

One may also wonder whether, modified by the dielectric antenna effect, two in-plane dipoles solely may also be able to explain the emerging out of plane dipole. As additional verification, we plot in figure 4-48 the experimental radiation pattern of a NPL chain and compare it with the simulated radiation patterns of a NPL chain. In the first 4 cases, we insert various dipoles with no out-of-plane component and none of these theoretical cases is able to describe the experimental data: when $\eta_z = 0.25$ (blue curve), the bigger lobes (along Φ~65°) are reasonably fit but not the small lobes (as indicated by red arrows). As the value of η_z increases, the big and small lobes will enlarge

simultaneously. One can fit the small lobes well when $\eta_z = 0.47$ (yellow curve), but at the same time the fit to the big lobes is lost.

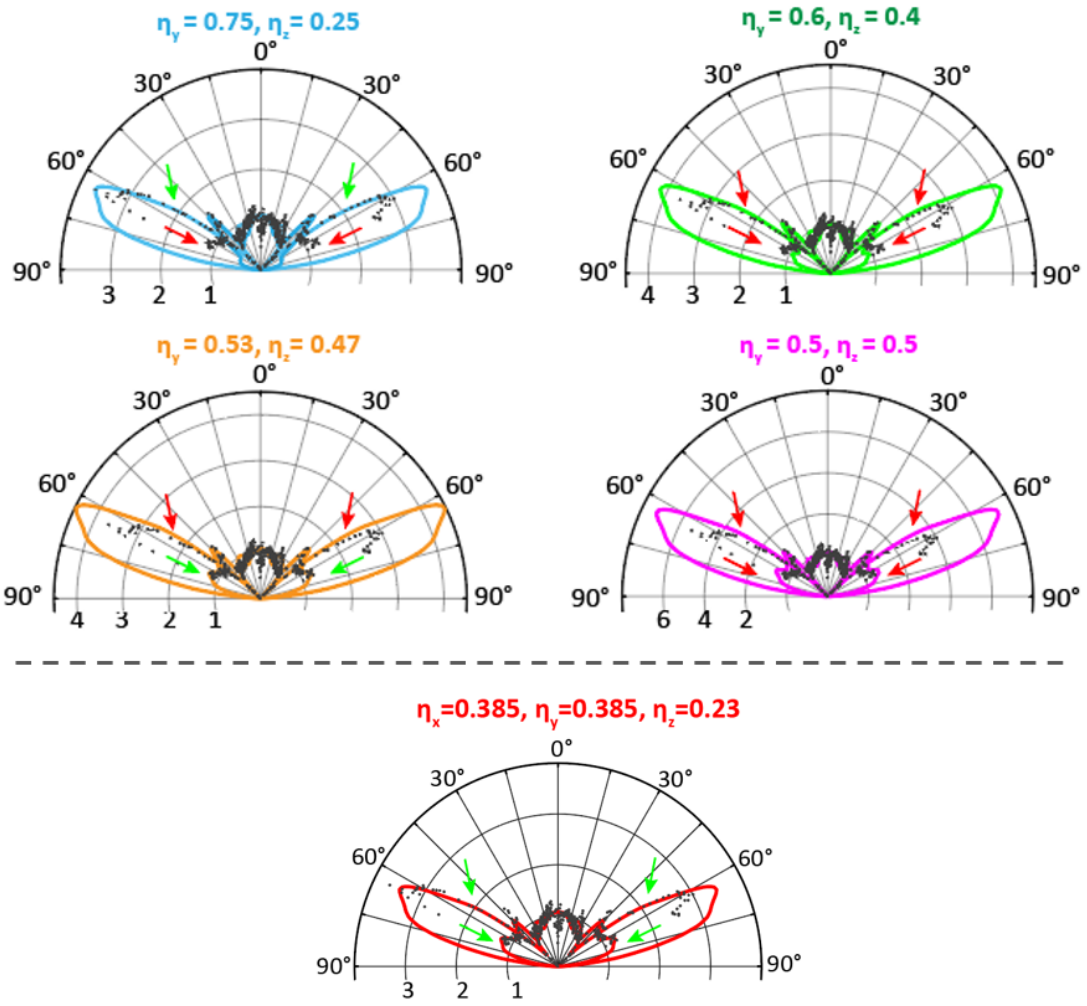

Figure 4-48. Comparison of the experimental radiation pattern (black dots) of a NPL chain with the theoretical radiation patterns (colored lines) of several dipole components inserted inside a NPL chain. The first 4 curves being with no out of-plane dipole, and the 5th curve with 3 dipoles providing the best fit. The green and red arrows show respectively where the agreement and disagreement between experiment and theory are the most noteworthy (keeping in mind that the highest angles may be affected by aberrations)

4.6.4 Summary and Discussion

Figure 4-49 shows all the results of simulated antenna enhancement efficient as a function of the number of NPLs in chains, from N=1 to N=200. We calculate the enhancement factor by integrating the emission intensity over all the semi-sphere in the far field, and normalize this value by the reference case, i.e., a single NPL (N=1).

For the out-of-plana dipole (blue curve), it is indeed enhanced as the number of NPLs increases in the stacked chain. However, its enhancement factor quickly saturated with a maximum value of

only 1.26, which is not enough to originate the out-of-plane dipole componnet ($\eta_x \sim 0.12$) observed in the NPL chain.

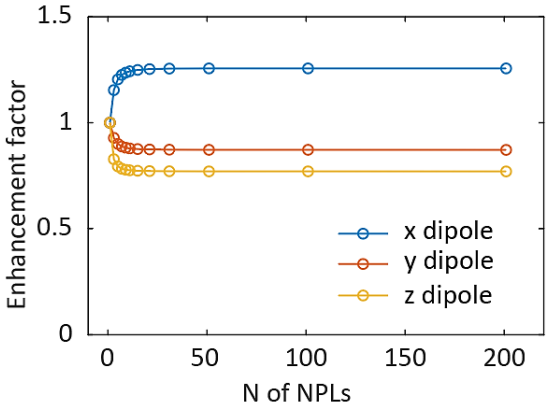

Figure 4-49. FDTD simulation results of antenna enhancement factor.

4.7 Hypothesis on the origin of the out-of-plane dipole in NPLs

In the previous sections, we confirmed the presence of an out-of-plane dipole component in the assembled NPLs emitter, which is surprising since this component is absent in the non-assembled single NPLs and is also theoretically forbidden by the selection rules. To explain the origin of the out-of-plane dipole component, antenna enhancement effect is the first thought, but one cannot generate a non-existent dipole by antenna enhancement, and in the last section of FDTD simulation, it was shown that the antenna enhancement on the out-of-plane dipole is not sufficient in our sample.

Other hypotheses can be raised such as the following:

1) Effect of disorders in assembly

2) New emission states

3) Local electric field induced by trapped ions/charges in defected sites

4) Strain-induced effects

In this section, we will discuss these hypotheses in sequence.

4.7.1 Effects of disorder in assembly: TEM image study

Now we study the possibility that the out-of-plane dipole $\eta_\perp = 0.12$ in the chain may be generated by disorders, i.e. tilted NPLs. We assume that the $\eta_{||,1}$ dipole is tilted by angle β_1 and the $\eta_{||,2}$ dipole is tilted by angle β_2, as depicted in figure 4-50.

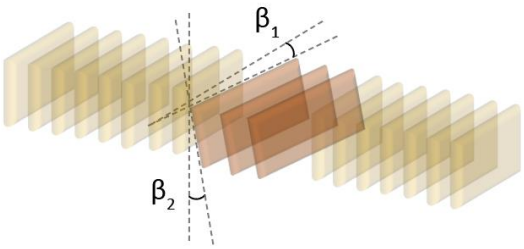

Figure 4-50. Tilted NPLs in a chain. Yellow: well-aligned NPLs. Red: disordered NPLs.

The effect of the tilt angle on the dipole contributions can be estimated by simple geometrical arguments. Let us first consider the in-plane angle β_1 (and keep β_2 = 0). If the platelet possesses two in-plane dipole components $\eta_{||,1}$ (horizontal) and $\eta_{||,2}$ (vertical) with no out-of-plane dipole ($\eta_\perp$= 0), the effect of the tilt is to create effective dipole contributions:

$$\eta'_{||,1} = cos^2\beta_1 \cdot \eta_{||,1} \tag{4.66}$$

$$\eta'_{||,2} = \eta_{||,2} \tag{4.67}$$

$$\eta'_{\perp} = sin^2\beta_1 \cdot \eta_{||,1} \tag{4.68}$$

In order to account for an experimentally-measured ratio $\frac{\eta'_\perp}{\eta'_{||,1}} = \frac{0.12}{0.62} = 0.19$, we would need a tilted angle $tan^2\beta_1 = 0.19$ so that $\beta_1 = 23°$.

On the other hand, if the assume that there is a tilt angle β_2 (and keep β_1 = 0), then we write:

$$\eta'_{||,1} = \eta_{||,1} \tag{4.69}$$

$$\eta'_{||,2} = cos^2\beta_2 \cdot \eta_{||,2} \tag{4.70}$$

$$\eta'_{\perp} = sin^2\beta_2 \cdot \eta_{||,2} \tag{4.71}$$

so that an experimental ratio $\frac{\eta'_\perp}{\eta'_{||,2}} = \frac{0.12}{0.26} = 0.46$ would be accounted for by a tilt angle $\beta_2 = 34°$.

However, if we take into account the dielectric antenna effect, as explained in section 4.6, we would only need to account for a NPL of dipole parameters η'_x = 0.08, η'_y = 0.63, η'_z = 0.29. This would require a tilt angle $\beta_1 = 20°$ or $\beta_2 = 28°$.

We then analyse a TEM image of NPL chains (figure 4-51 (a)) in order to evaluate the angle by which the NPLs may be tilted with respect to the stacking axis due to the slight stacking disorder. Note that at the tilt angle β_2 is difficult to estimate here, so we analyse only the in-plane angle β_1.

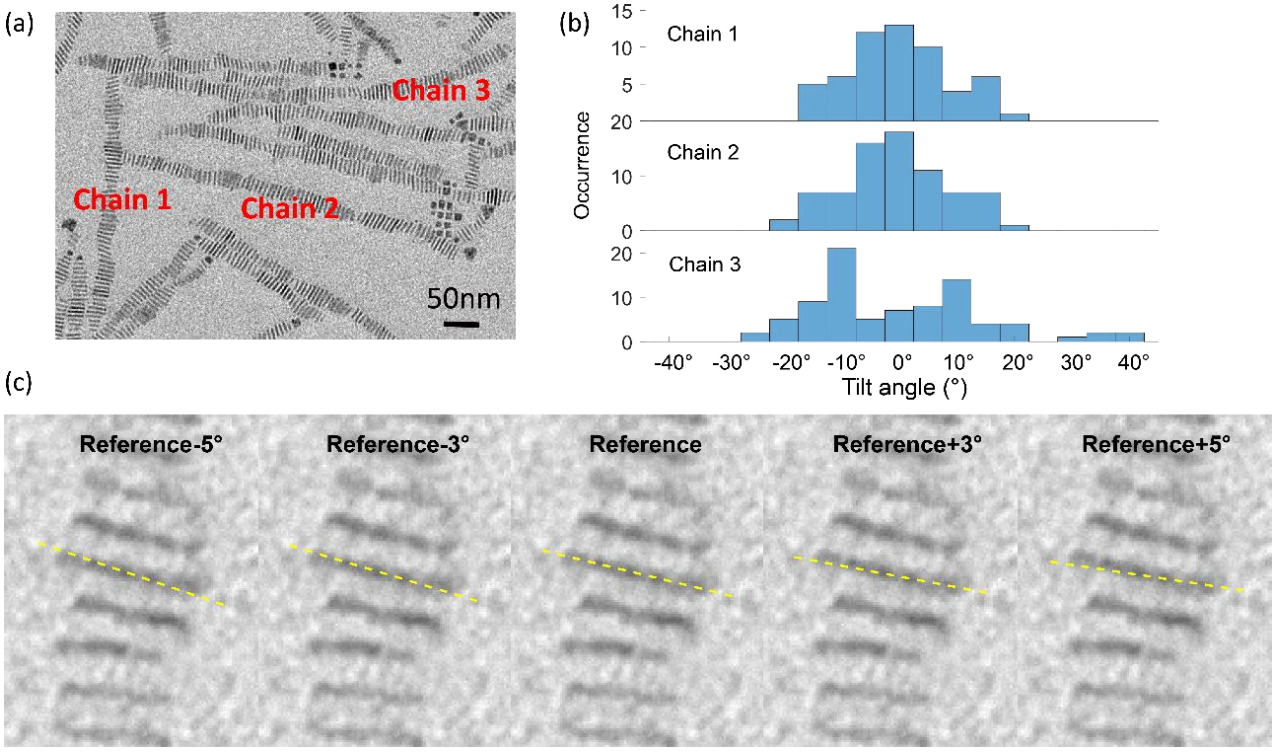

Figure 4-51. (a) TEM image analysis of tilted NPLs in chains. (b) Distributions of tilt angles of NPLs in three chains. (c) Estimation of the resolution on the tilt angle β_1. The yellow dashed line in the reference case (middle image) indicates the estimated orientation of the platelet. It shows clear deviations if we rotate the reference line by more than ±3°

ImageJ software is employed to analyse the β_1 angles of each NPL in the chain, with a resolution of 3° as estimated in (figure 4-51 (c)). Distributions of NPLs' tilt angles in three randomly chosen chains are shown in (figure 4-51 (b)). For the normal linear chains (e.g. the first two chains), the mean of $|\beta_1|$ is 7°. Although in our optical measurements we considered only chains deposited linearly, here we still choose a bent chain (chain 3) on purpose as a limit case, of which the angles are more broadly distributed with a mean value of $|\beta_1|$ of 12°. All of these values are significantly smaller than 20° and, because the apparent out-of-plane dipole caused by the tilt scales as $tan^2(\beta)$, the measured tilt angles would create much smaller out-of-plane dipoles.

As a conclusion, the tilt angle estimated here seems rather insufficient to induce the observed 0.12 out-of-plane dipole.

4.7.2 Analysis of new transition states

The emerging out-of-plane dipole also may originate from a new state generated by the mixture of wavefunctions of neighbour emitters. An evidence for this hypothesis is that, in the literature, many groups reported an additional redshifted emission peak observed on stacked NPLs chains at low temperature. However, its origin is, up to now, still in a heated debate with various explanations proposed such as: phonon coupling [7], p-state emission [188], excimers [18], surface states [72], energy splitting by different dielectric confinements [189], polaron [190] and most recently trion emission [73], the latter hypothesis being valid in fact also for isolated NPLs [191].

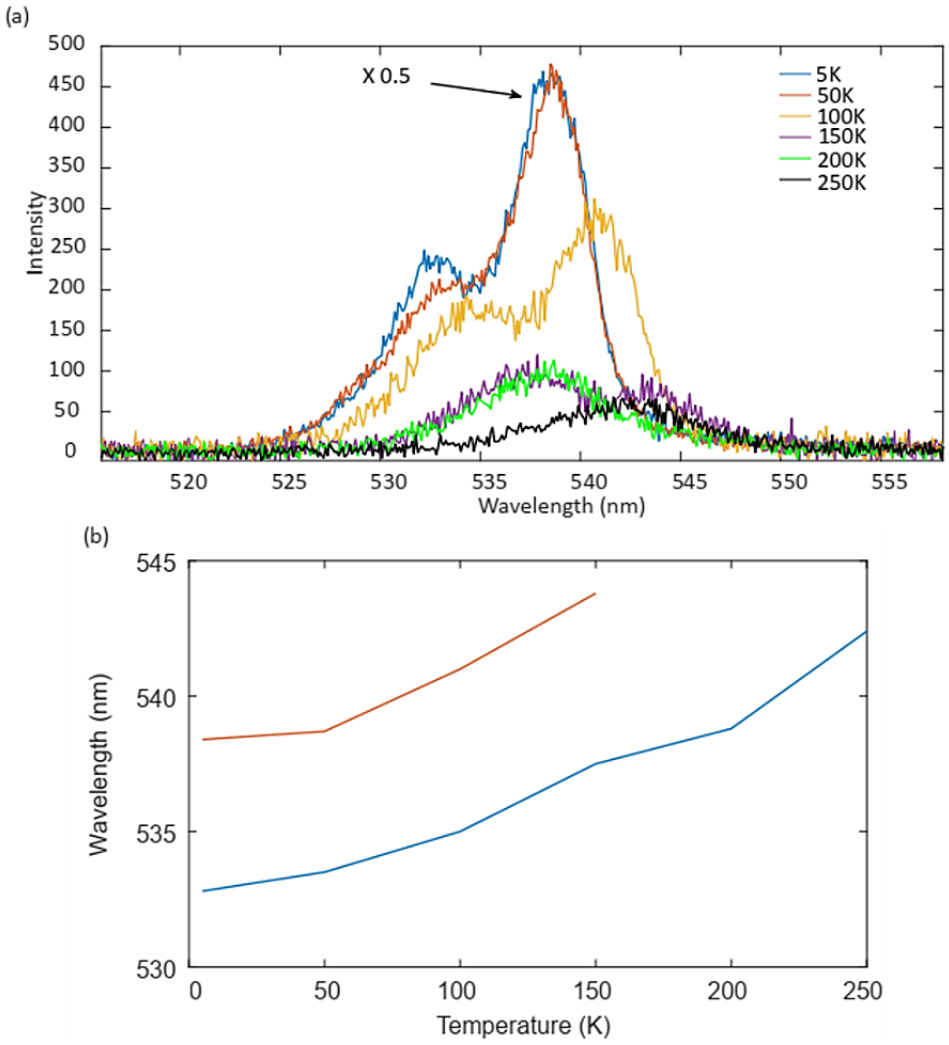

Figure 4-52. (a) NPL chain emission spectra at various temperatures from 5K up to 250K. (b) Center positions of the two peaks as a function of temperature.

We measured the NPL chain emission spectra at various temperatures from 5K up to 250K and found a similar redshifted peak as shown in figure 4-52. When the temperature is between 5K and 100K, the redshifted peak is stronger than the original emission peak, while its intensity reduces faster as the temperature increases. At 150K, the redshifted peak becomes weaker than the blue one and then it completely disappears at temperatures above 200 K while only the original blue emission peak remains.

Note that, as the temperature decreases, the intensities of both emission peaks increase, which has been attributed to the GOST effect [5]. The excitonic peak shifts as a function of temperature due to a change in the bulk band gap energy.

Since the additional red peak clearly disappears at 200 K, this new transition does not contribute to our room-temperature measurements. We can thus exclude the connection between the novel transition and the out-of-plane dipole.

In addition to the temperature measurements, we also performed polarization-resolved analysis. We put a polarizer oriented either parallel or perpendicular to the chain's stacking axis to select the emission corresponding to the out-of-plane or in-plane dipole transition, respectively. We measured their decay curves (figure 4-53, left) and the emission spectra (figure 4-53, right) and observed no polarization dependence. This indicates that the different dipole contributions 1) do not originate from different emitter populations with different dynamics and 2) do not originate from states of different energies (within the spectral resolution of room-temperature spectroscopy).

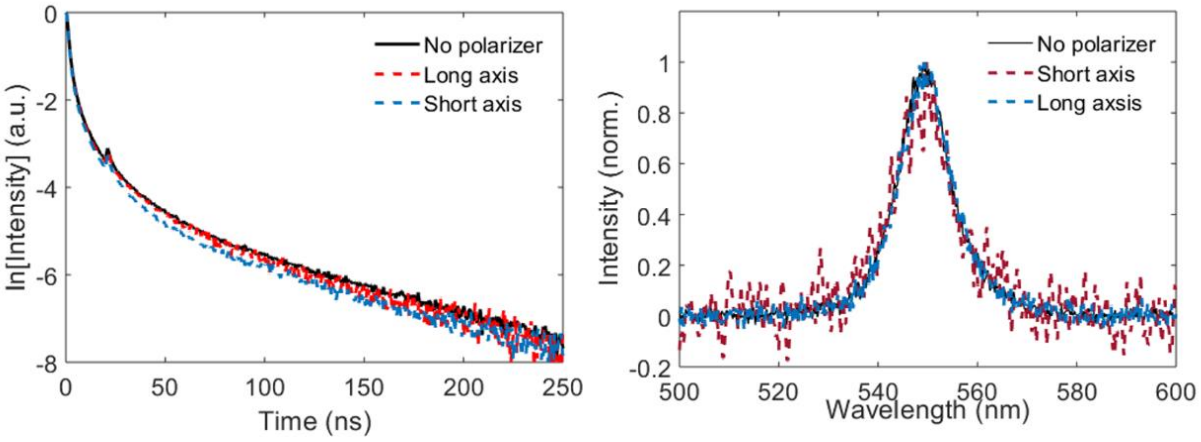

Figure 4-53. Decay curve and emission spectrum of a NPL chain analysed with a polarizer either parallel or perpendicular to the chain's long axis

4.7.3 Local electric field induced by trapped ions/charges in defected sites

In chapter 3, we demonstrated that, in an assembly of CdSe NPLs, the trapped ions/charges in defect sites will modify their blinking and decay dynamics. The 'grey-state' emission originates from the charged excitons, which are greatly affected by defects and recombine more probably by fast non-radiative mechanism. On the contrary, the 'bright-state' emission of the assembly happens in the sites where the neutral excitons are more likely to radiatively recombine, not significantly affected by quenching defects. Consequently, one may relate the novel out-of-plane dipole observed in chains to an effect of local electrical field induced by trapped charge.

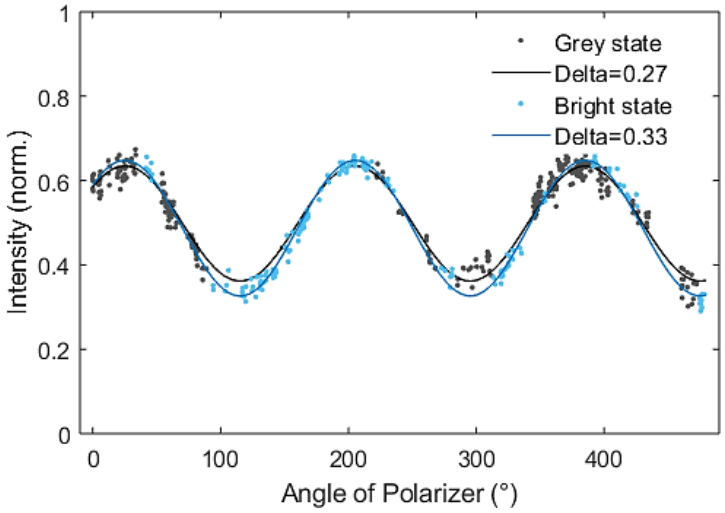

Figure 4-54. Polarization analysis of bright- and grey-state emission.

To study this hypothesis, we analysed the polarization degree of bright- and grey-state emission (e.g. figure 4-54) by post-selection of corresponding signals on intensity time trace (shaded areas in figure 4-55), for single NPLs, clusters and chains respectively. We extracted respectively for bright- and grey-state emission the degree of polarization δ and calculate their difference by:

$$\delta_{diff} = \delta_{bright} - \delta_{grey}$$

In single NPLs, δ_{diff} distributes with a center close to 0.01 and a deviation of ± 0.02 (which is the precision of our polarization measurement). Here δ_{diff} doesn't change much because most single NPLs mainly carry out on-state emission, less affected from trapped ions. Compared to single NPLs, δ_{diff} in clusters and chains is larger, consistent with the intuition that trapping sites are more involved in stacked NPLs assisted by ultra-fast FRET effect. Note that, for chains, the reduction is

considered only on blinking chains, not on non-blinking ones in which we cannot properly select their on- and grey-state component for analysis.

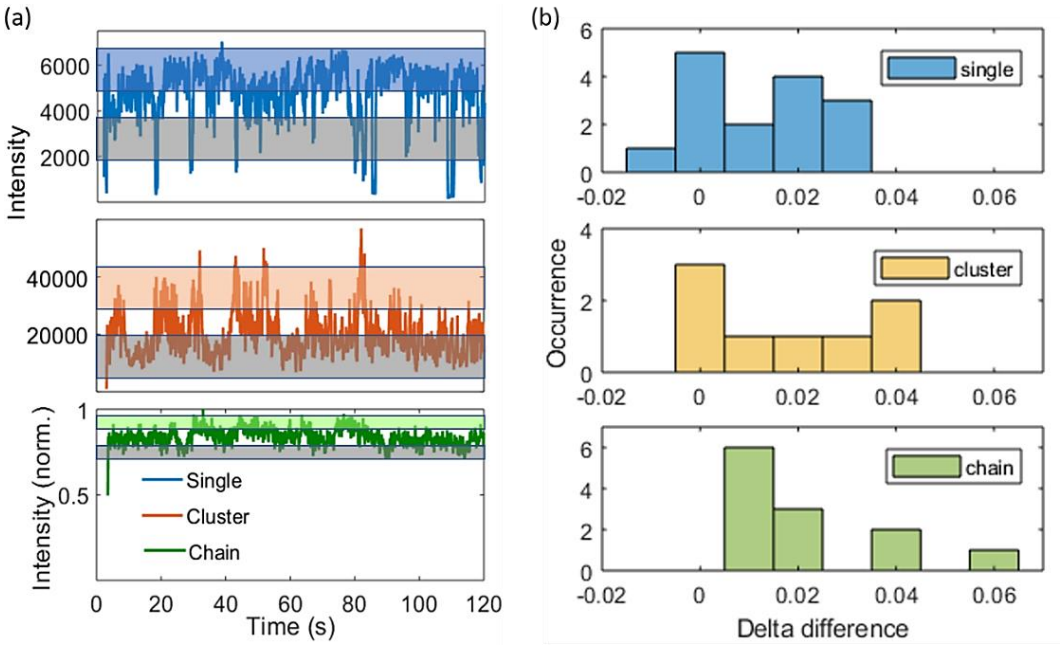

Figure 4-55. (a) Fluorescence intensity time traces of a single NPL (blue), a cluster (orange) or a chain (green). Colored shades: bright-state emission. Grey shades: grey-state emission. (b) Calculated difference in delta (δ_{diff}).

We then compared the experimental results to theoretical values. If we assume that the bright-state emission relates to 2 transition dipoles ($\eta_{\parallel,1}$ =0.7, $\eta_{\parallel,2}$ =0.3) and the grey state emission relates to 3 transition dipoles ($\eta_{\parallel,1}$ = 0.62, $\eta_{\parallel,2}$ = 0.26, $\eta_{\perp}$ =0.12), we can obtain the theoretical δ_{diff} as shown in Figure 4-56: δ_{theo} changes from 0.25 to 0.27 for the single NPL, from 0.3 to 0.42 for the cluster, or 0.33 to 0.37 for the chains. Thus, δ_{diff} are 0.02, 0.12 and 0.04 for the single NPL, the cluster and the chain, respectively.

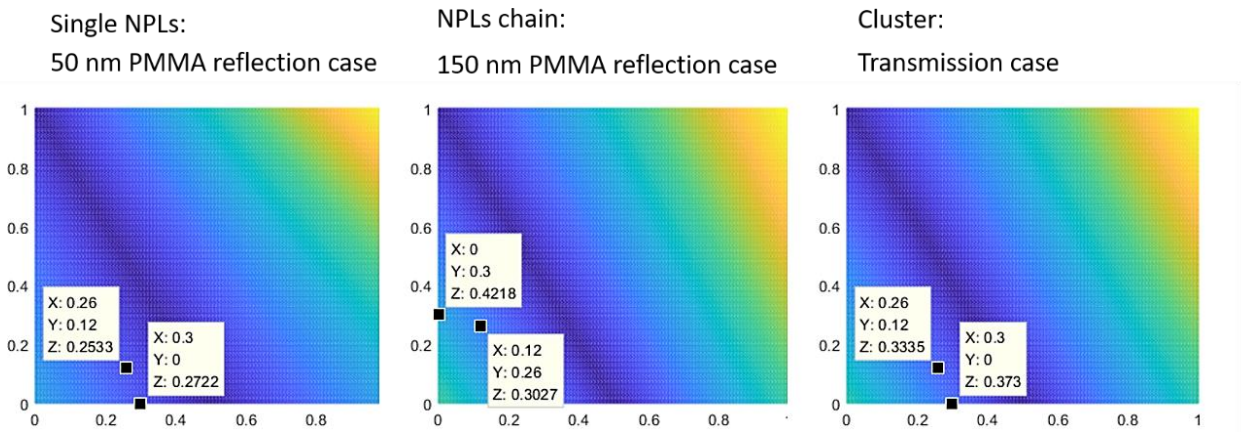

Figure 4-56. Theoretical delta difference (δ_{diff}) in the single NPL, the cluster, or the chain.

Comparing the experimental and theoretical values of δ_{diff}, we find a good consistence between them in the case of single NPLs and clusters; for chains, the theoretical δ_{diff} should be ~ 0.12, but the maximal value we observed is 0.06, while for all the non-blinking chains, we obtained $\delta_{diff} = 0$.

To sum up, although we can well select on/grey state emission for single NPLs and clusters, their results of δ_{diff} aren't resolvable/convincing in consideration of our experiments uncertainty. For chains, we have a problem to properly select their on- and grey-state emission. Thus, unfortunately, we cannot draw conclusion that the trapped charges/ions will modify emission's polarization.

However, there is another approach to indirectly estimate the relation between the emission's degree of polarization and the number of trapped charges/ions. We used different laser powers, varying from very low (0.1 nW) to very high values (50 nW), to excite NPLs chains and measured their power-dependent degree of polarization. The idea of this experiment is that, by using different input power, different amount of trapping sites will be generated accordingly and result in modifications in emission's polarization degree.

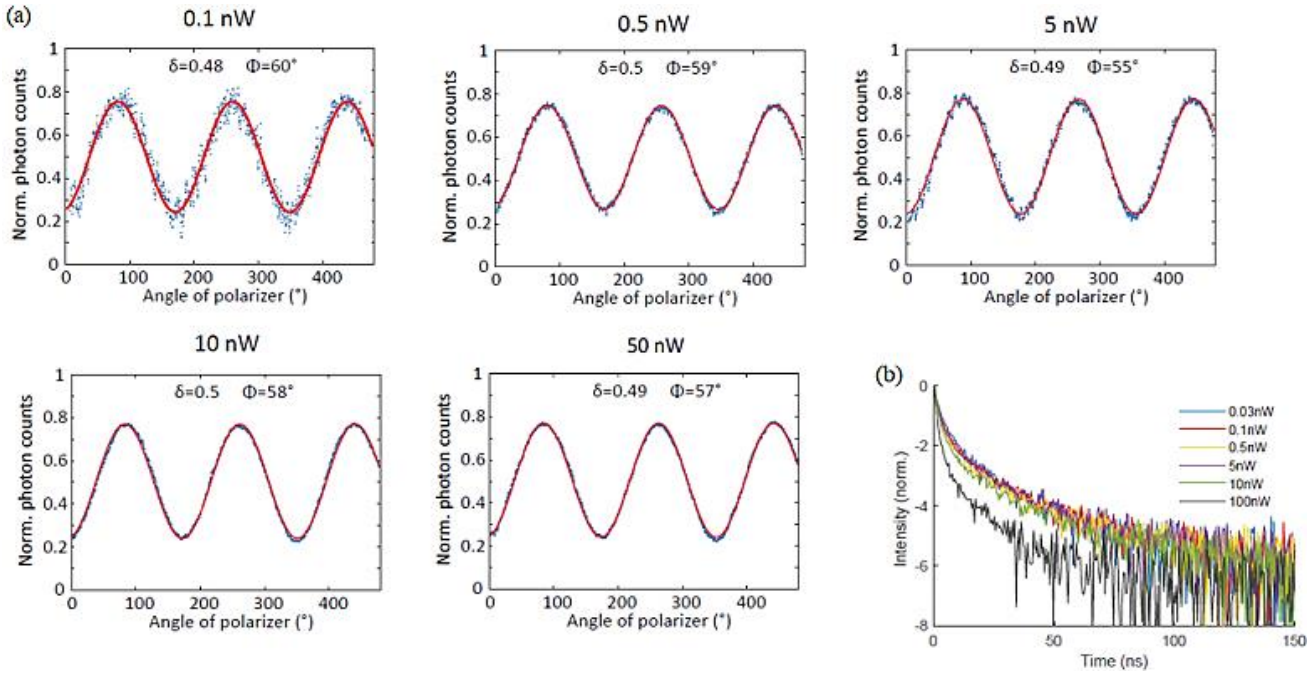

Figure 4-57. (a) Polarization analysis curves and fitted δ and Φ parameters. Blue dots: experimental data; red lines: fitting. (b) Decay curves of a given NPL chain under different excitation powers

As a result, from figure 4-57, we find no power dependence, which suggests that the emerging out-of-plane dipole is not a photo-induced effect.

Therefore, as a conclusion, we found no evidence supporting the hypothesis that the out-of-plane dipole originates from a trapped-charges-induced effect.

4.7.4 Strain-induced effects

Recently, I. Dozov et al. analysed solutions of chains of 23 to 92 NPLs by transient electric birefringence [192] and demonstrated a permanent out-of-plane dipole (dipole parallel to the chain axis) with dipole moments of 350 to 6900 Debyes, increasing with the number of NPLs in the chain. This permanent dipole was attributed to the strain-induced shape deformation, which is responsible for the helicoidal assembly of the NPL chains as shown in figure 1-10 (b). Our observations of the out of plane dipoles in assembled NPLs may also originate from the strain-induced effect and be related to a deformation (and not just a tilt as we considered in section 4.7.1) of the NPLs.

4.8 Conclusion

In this chapter we investigated the dimensionality and orientation of dipoles in CdSe NPL emitters, from single isolated NPLs to linearly assembled NPL chains. A combination of polarimetry and Fourier plane image analysis was employed to probe the proportions of dipole components in single emitters, with a record precision reaching ± 0.03 by a careful design of the experimental configurations.

On single NPLs, we found no out-of-plane dipoles, in agreement with previous reports and with the theoretical estimations. However, on assembled NPLs (clusters and chains), we confirmed the presence of an out-of-plane dipole component, whose proportion increases from 0.03 up to 0.12 as a function of the number of NPLs increasing in the assembly [193]. We discussed various mechanisms for the presence of this dipole and suggest that it might be related to a strain-induced NPL deformation within the NPL assembly, with an enhancement by a dielectric antenna effect. A better understanding of the role of self-assembly on the emission dipole could be obtained by further high-resolution electron imaging and a comparison with numerical models of the NPL crystalline structure and internal strain.

Thanks to the precision of our micro-photoluminescence analysis protocol, we report for the first time the out-of-plane dipole component in self-assembled stacks of CdSe NPLs, which was hidden

in previous reports. The method demonstrated in this chapter can have a wide range of applications in fundamental study of optical and electrical properties of semiconducting single emitters or two-dimensional materials, such as perovskite quantum dots and transition metal dichalcogenide semiconductors.

Chapter 5. Conclusion and perspectives

Colloidal semiconducting nanoplatelets have drawn massive attention because of their unique optical characteristics. Many potential applications can only be realized once the fluorescence properties of single and packed NPLs are understood. In this thesis, we employed various techniques of micro-photoluminescence, including time-correlated single photon counting, polarimetry and Fourier plane imaging, to study the fluorescence properties of different CdSe samples, from isolated single NPLs, NPL clusters to highly-ordered self-assembled chains of NPLs. Our study involved analyses of excitonic energy transfers, decay, blinking, transition dipole components etc. We revealed emerging collective effects: the excitonic properties of isolated single emitters are drastically modified by the self-assembly.

The first research topic is about the non-radiative excitonic energy transfer in stacked chains of NPLs.

We demonstrated the excitonic energy transfer in self-assembled NPLs with a length of 500 nm (corresponding to exciton hopping over 90 NPLs) by a method of imaging analyses. This migration distance is 20 times longer than other reported exciton diffusion lengths in semiconducting nanoparticle systems. A diffusion model is developed to relate this migration length to the transfer rate, which leads us to an estimate of the FRET rate between neighbor NPLs to be $(1.5\ ps)^{-1}$. This rate is faster than any other excitonic mechanisms known to occur in fluorescent semiconductor nanoparticles, such as radiative recombination, Auger recombination as well as fast non-radiative quenching effects induced by trapping defects. Therefore, FRET effect is fast enough to modify the excitonic property of assembled emitters as compared to isolated ones, which is expected to lead to emerging FRET-mediated collective photophysical effects.

In the near future, a longer-range energy migration length can be expected in self-assembled NPLs chains by different strategies, such as shortening the distance between NPLs by using different ligands, or using core-crown NPLs with longer decay lifetimes. Besides, in our samples, exciton migration is possibly limited by the twisting (induced by strain during stacking) and trapping sites (defected NPLs) in chains. Therefore, we predict that new FRET rate records, possibly faster than the picosecond scale, could be achieved on the chains with fewer defects in the future reports.

The second research topic is about the general characteristics of the fluorescence behaviour, including the blinking, the decay and the antibunching, of CdSe NPLs in various structures, from single NPLs, clusters to assembled NPLs chains.

We find typical binary blinking behaviours in NPLs, while in clusters and chains, blinking is suppressed by an averaging effect. The decay curves of single NPLs are generally mono-exponential, while multi-exponential characteristics can rise in the presence of trapping defects. The decay curves of clusters and chains are multi-exponential, with a striking acceleration in the fast decay components and with an arising of slow decay components.

The acceleration in the fast decay component should result from the homo-FRET assisted effect, involving radiative trion recombination channels and nonradiative Auger quenching, while the slow decay components are attributed to the trapping/de-trapping retardation. Compared to single NPLs, in assemblies the trapping effect is much more involved because homo-FRET can funnel the exciton to the trapping sites. As a result, the slow decay components become more significant.

For the blinking analysis, the on-going work is to record blinking videos for the micron-scale chains, which will give us spatially-resolved information, such as the variation in the position of the emitting center (or quenching center) and the variation in their emission intensity. Combining the blinking videos analysis with the intensity time trace analysis, the underlying information on blinking mechanisms and defect-related effects in the assembled systems is expected.

Besides, we demonstrated on single NPLs strong antibunching, and as a perspective, we can try to achieve antibunching on assembled NPL chains by a more localized excitation of only a few NPLs in a chain, if FRET diffusion favors Auger quenching of multi-excitons. This may be achieved by using shorter ligands to reduce the NPL centre-to-centre distance and enhance FRET transfer.

The third research topic is to investigate the dimensionality and orientation of transition dipoles in single and assembled NPLs emitters.

We developed a protocol combining polarimetry and Fourier plane imaging to probe the proportions of dipole components in single emitters, with a record precision reaching ± 0.03 by careful design of the experimental configurations. On single NPLs, we confirmed the absence of out-of-plane dipoles, in agreement with previous reports and with the theoretical estimations. However, on assembled NPLs (clusters and chains), we observed an out-of-plane dipole component, whose proportion increases from 0.03 up to 0.12 as the number of platelets is increased in the assembly. We

discussed various mechanisms for the presence of this dipole and suggested that it might be related to a strain-induced NPL deformation within the NPL assembly, with an enhancement by a dielectric antenna effect. A better understanding of the role of self-assembly on the emission dipole could be obtained by further high-resolution electron imaging and comparison with numerical models of the NPL crystalline structure and internal strain.

Thanks to the precision of our micro-photoluminescence analysis protocol, we report for the first time the out-of-plane dipole component in self-assembled stacks of CdSe NPLs, which was hidden in previous reports. This protocol can probe the information on transition dipoles in nano objects, which is important knowledge to control and optimize photonic and optical processes, such as light-matter coupling, energy transfer, directional emission and light extraction. This protocol can also have a wide range of applications in fundamental studies of optical and electrical properties of semiconducting single emitters or two-dimensional materials, such as perovskite quantum dots and transition metal dichalcogenide semiconductors.

Appendix A. Compensation of polarizing effects of the setup

To perform polarization analyses of single emitters by a microscope, it is imperative to characterize and minimize the polarizing effects induced by the setup. If we deposit emitters on a sample state (defined as x-y plane) and define the electrical field observed by the objective as $\begin{pmatrix} E_x \\ E_y \end{pmatrix}$, then, after passing all the optical elements, the field reaching the detectors will become:

$$\begin{pmatrix} E_x \cdot t_x \\ E_y \cdot t_y \cdot e^{i\psi} \end{pmatrix}$$

in which t_x and t_y denoting the transmittance of the setup for the light polarized along x and y, the polarization eigen-axes of the microscope (assuming that the microscope does possess such eigen-axes, which will not be the case if optical elements are misaligned), and ψ is the angle of phase retardation between x and y direction.

In order to perform adequate polarization analysis, it is necessary to have $t_x = t_y$ and $\psi = 0$. However, it is a priori not the case because of the reflections and transmissions at non-normal incidence (45° beam-splitter and mirrors) which affect differently the s- and p-polarizations. We find $t_x \neq t_y$, which is called **diattenuation** and $\psi \neq 0$, which is called **retardation**. Following the protocol developed by Thu-Loan Nguyen during her thesis in the group under A. Maître's supervision [94], we systematically analysed the polarization effects introduced by the setup, and we found that the major source of diattenuation is the beam splitter under the objective ("Beam splitter 1" in figure a-1) while the retardation mainly results from the prism ("Prism 1" in figure a-1).

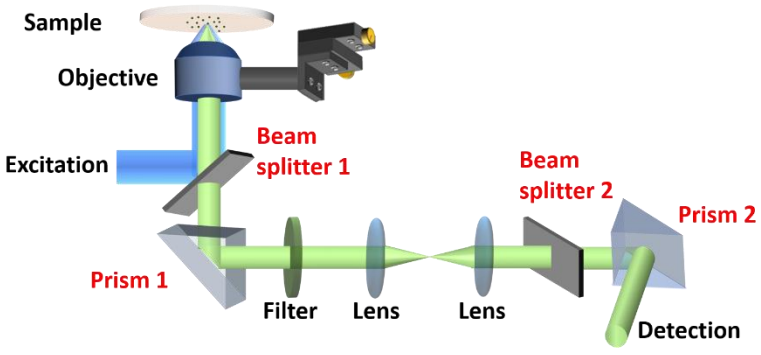

Figure A-1. Schematics of the setup with compensators.

We inserted an additional beam splitter ("Beam splitter 2") and prism ("Prism 2") oriented approximately 90° with respect to the beam splitter 1 and prism 1, and used fluorescent polymer spheres (Thermo Fisher, 200nm, 580-605 nm emission) as reference for the setup polarization calibration. By a fine tuning of the orientation of the compensators, the polarizing effect of the setup can be effectively suppressed.

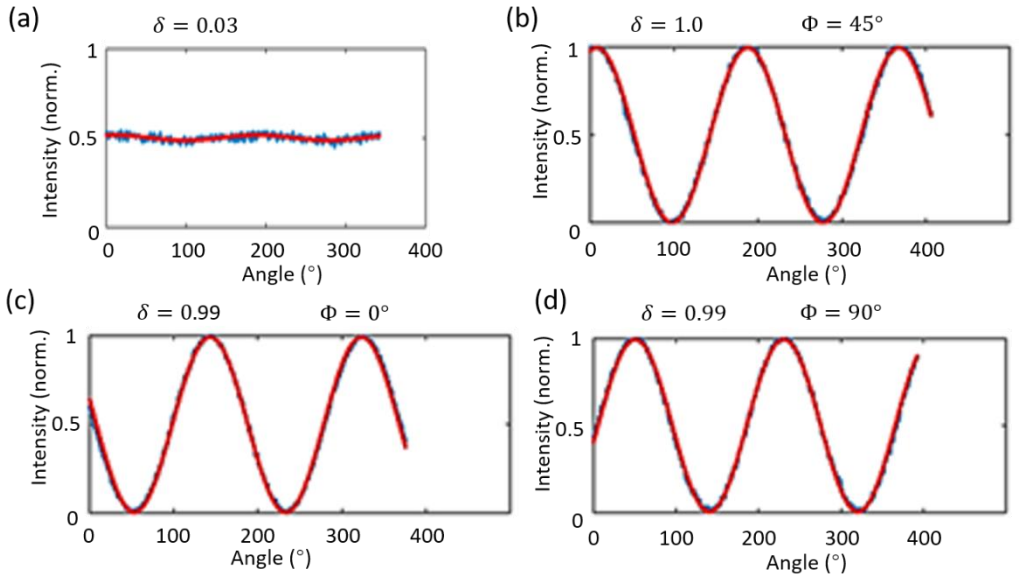

Figure A-2. Linear polarization analysis of the emission from a microsphere (a) without any polarizer, or with a polarizer positioned after the objective at an orientation (b) $\Phi = 45°$, (c) $\Phi = 0°$ and (d) $\Phi = 90°$.

As shown in figure a-2, when we sent the non-polarized light from a single fluorescent sphere for the linear polarization analysis, we measured a degree of linear polarization $\delta = 0.03$. When introducing a polarizer along orientation $\Phi = 0°$, 45° or 90° below the objective to polarize the emission, a 0.99 degree of linear polarization was obtained.

For the circular polarization analysis, we analysed it by introducing a polarizer before the spectrometer entrance and comparing the +45° and -45° positions of a quarter-wave plate before the polarizer. As shown in figure a-3, an average degree of circular polarization of 0 was measured, with fluctuation in the range of ±0.02. It can be noted that adequate polarization correction is obtained over a broad spectral range.

We thus conclude that the emission polarization was preserved by the setup with 1-3 % precision.

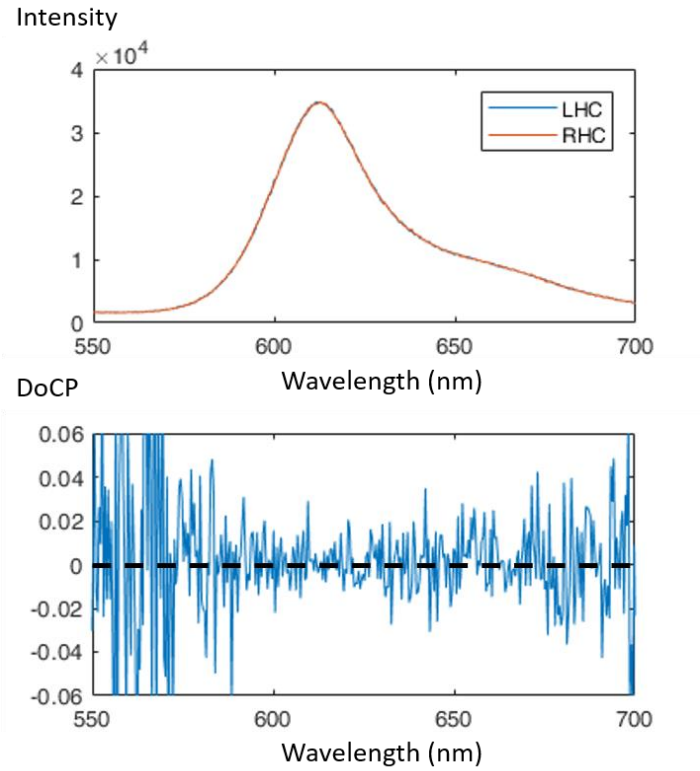

Figure A-3. Circular polarization analysis of the emission from a microsphere. (a) emission spectra of left-handed luminescence (blue) and right-handed luminescence (orange) (the two curves overlap completely). (b) Degree of circular polarization calculated by $\frac{I_L - I_R}{\frac{1}{2}(I_L + I_R)}$, with I_L and I_R the intensity of the left- and right-handed emission.

Appendix B. Circular polarization measurements of chiral Dy crystals

Introduction

The luminescence of Lanthanide (III) ions attracted interests of researchers throughout the world with optical characteristic of narrow spectral bands, large Stokes shift and long excited state lifetime, which lead to versatile utilization and potential application such as electroluminescent devices [194], medical imaging [195] and telecommunication [196]. When lanthanide complexes are engineered to possess chiral structure, they are reported to emit circularly polarized light with different left-handed and right-handed intensities depending on the ligand enantiomer. This is an important optical phenomenon called circularly polarized luminescence (CPL), which is usually quantified by the luminescence dissymmetry factor: $g_{lum} = \frac{I_L - I_R}{\frac{1}{2}(I_L + I_R)}$, where I_L and I_R are the left- and right-hand polarized emission intensities, respectively.

Circularly polarized luminescence has been studied a lot based on diverse chiral samples and many potential analytical applications have been developed taking advantage of the sensitivities to anions [197,198], cations [199] and pH [200]. However, in the literatures, most of the chiral samples are made of organic molecules, polymers, or biochemical systems. Few CPL study performed on lanthanide complexes is reported, although they are much more circularly-polarized than widely researched pure organic molecules: for lanthanide complexes, g_{lum} values are typically in a range from 0.1 to 1.19 [201] with maximum record that has been reported, to the best of our knowledge, to be 1.38 measured on Eu(III) complex [202]; while it is only on the order of 10^{-2} to 10^{-3} for the molecules, etc.[203]. Moreover, among the few CPL study on lanthanide complexes, most measurements have been performed in solution, with few reports of solid-state doped crystals, especially for dysprosium.

During this thesis, we collaborated with Jean-Pascal Sutter and Virginie Béreau from Laboratoire de Chimie de Coordination and Université Toulouse-III-Paul-Sabatier, who synthesized crystals of a chiral-at-metal Dy(III) single-molecule magnet (figure b-1) and demonstrated some magnetization effects at low temperature. In our work, we modified our setup for the purpose of circular polarization analysis of the chiral Dy(III) compounds at low temperature by photoluminescence microscopy. We analyzed the circular polarized emission and interpreted the mechanics behind their optical properties.

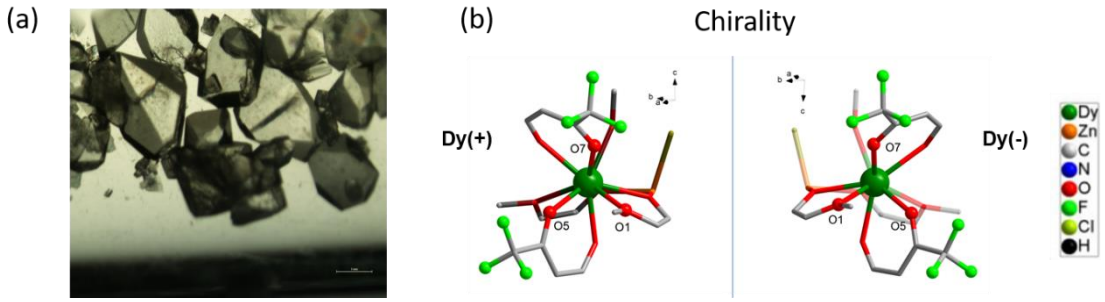

Figure B-1. (a) Microphotograph of Dy crystals. (b) Structure of Dy(+) and Dy(-) enantiomers.

Method

The luminescence properties of the rare-earth doped crystals were analyzed by low temperature micro-photoluminescence: crystals of size 300-800 µm were attached by silver lacquer to the cold finger of a helium-flux cryostat (Oxford, HiRes II) and observed by a homemade microscope (0.7 numerical aperture objective, x60 magnification). The sample was illuminated through the objective by the light from a mercury lamp filtered over a 330-480 nm pass band. The fluorescence emission was collected by the same objective, filtered by 500nm long-pass filter and analysed by an imaging spectrometer (Horiba Jobin-Yvon, Triax-190). Linear and circular polarization analyses were performed by introducing a polarizer before the spectrometer entrance and respectively rotating a half-wave plate or comparing the +45° and -45° positions of a quarter-wave plate before the polarizer.

Circular polarization

The emission of single rare-earth-doped crystals was analysed at low temperature by photoluminescence microscopy. Figure B-2 (a) shows the emission spectra for a Dy(+) crystal along left-handed and right-handed polarizations. Two groups of emission peaks appear at 573 and 663 nm and are attributed respectively to the $^4F_{9/2}$-$^6H_{13/2}$ and $^4F_{9/2}$-$^6H_{11/2}$ transitions of Dy^{3+} [204,205]. The emission intensity decreases as a function of temperature, barely no emission being observed above 30 K. For both transitions, the left-handed circularly-polarized emission is slightly stronger than the right-handed. This observation was repeated over all observed Dy(+) crystals. On the other hand, for the Dy(-) crystals (figure b-2 (b)), the right-handed emission was consistently stronger than the left-handed emission.

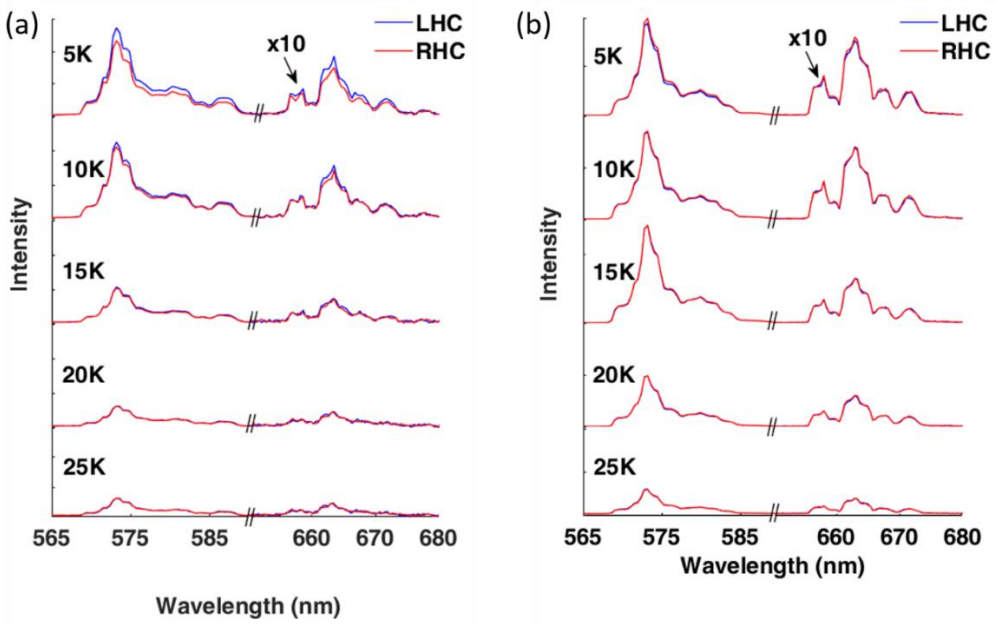

Figure B-2. Temperature dependent emission of (a) Dy(+) crystal and (b) Dy(-) crystal. Blue lines: left-handed circular (LHC) polarization; red lines: right-handed circular (RHL) polarization.

We extract the degree of circular polarization of each transition by integrating the emission respectively over the 569-585 and 656-673-nm intervals for the left-handed and right-handed polarizations and using equation $g_{lum} = \frac{I_L - I_R}{\frac{1}{2}(I_L + I_R)}$. The resulting values of g_{lum} is reported in figure b-3.

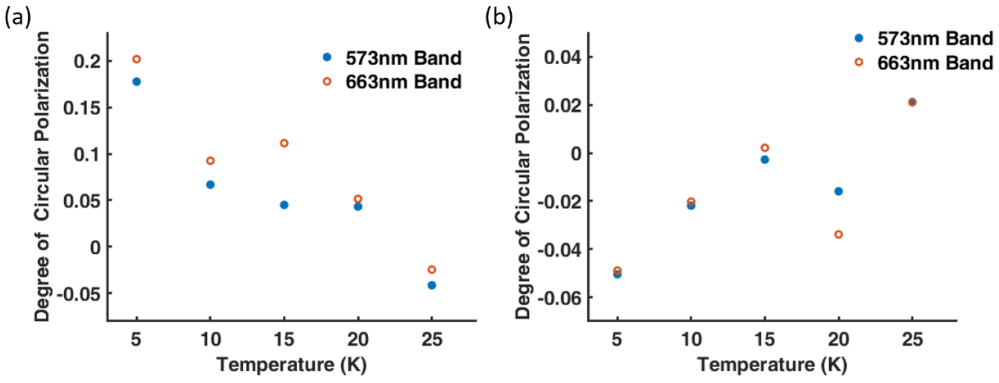

Figure B-3 Temperature-dependent variation of degree of circular polarization for a) Dy(+) and b) Dy(-) crystals.

In spite of some significant uncertainty on g_{lum} values, possibly caused for instance by slight fluctuations of the excitation lamp between the left-handed and right-handed measurements, a general trend is observed: the degree of circular polarization decreases with temperature and vanishes around

25 K. These observations were repeated for several crystals, with a distribution of g_{lum} values ranging between 0.04 and 0.18 for Dy(+) and between -0.04 and -0.16 for Dy(-) at 5 K.

As a comparison, figure b-4 plots the left-handed and right-handed circularly-polarized emission spectra for isostructural Eu^{3+}-doped crystals. Groups of emission bands at 580, 587-600, 610-624, 648-656 and 683-704 nm and are attributed respectively to the $^5D_0$–$^7F_0$, $^5D_0$-$^7F_1$, $^5D_0$–$^7F_2$ transitions [206]. Europium photo-luminescence is detected at much higher temperatures than for dysprosium (up to 250 K). For all these peaks, the emission is exactly the same for the two circular polarizations. As shown in figure b-5, the degree of circular polarization was calculated for each peak at each temperature and g_{lum} was always close to 0, fluctuating between ±0.02.

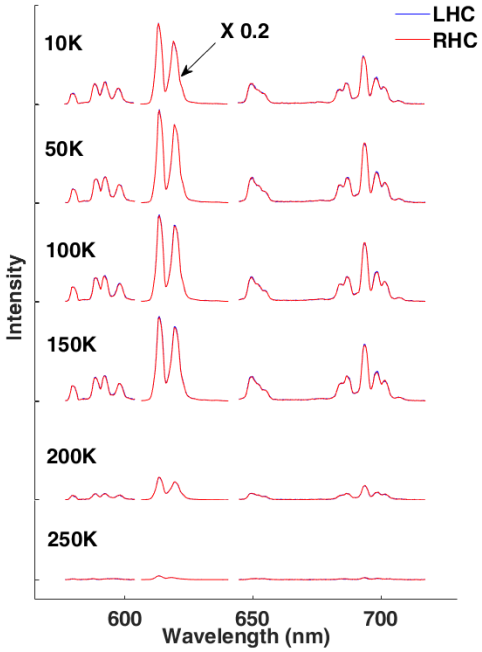

Figure B-4 temperature dependent emission of Eu(III) crystal. Blue lines: left-handed circular (LHC) polarization; red lines: right-handed circular (RHL) polarization.

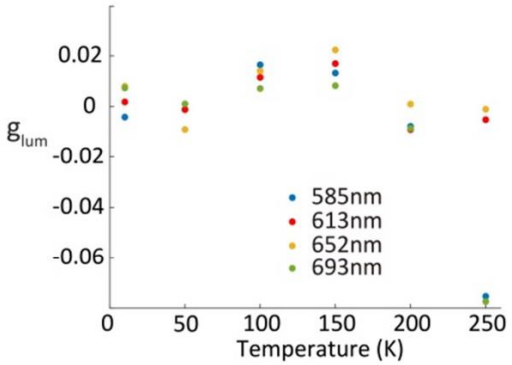

Figure B-5 Degree of circular polarization of Eu(III) doped crystal for different emission bands at different temperature.

Figure B-6 shows the left-handed and right-handed emission of the two transitions as a function of the emission direction for a Dy(+) and a Dy(-) crystal. In spite of some significant noise, the resulting curves show that the degree of circular polarization has little dependence on the emission angle.

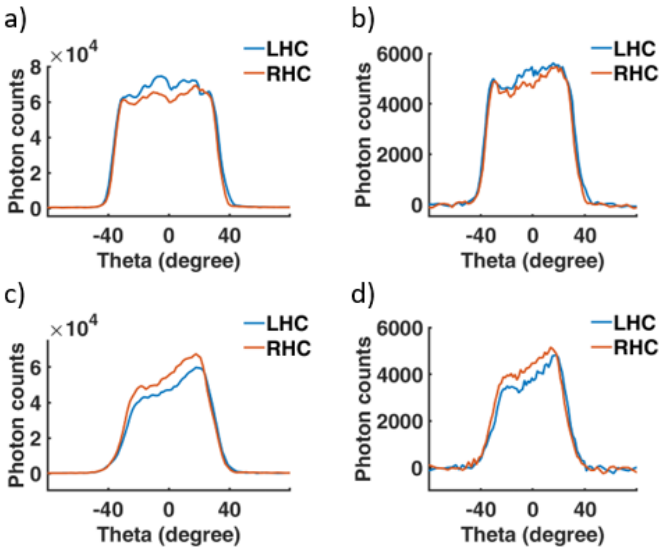

Figure B-6 Angular distribution of emission for the a) 573-nm band and b) 663-nm band of Dy(+) crystal, and c) first band, d) second band of Dy(-) crystal.

As a conclusion, we demonstrated circularly polarized luminescence (CPL) on chiral Dy crystals, a rare-earth element whose CPL has been relatively little analysed, especially in solid crystalline matrices. The observed luminescence dissymmetry factor was as large as ~0.18 and its sign depended on the ligand chirality [207]. The origin of the circularly polarized emission needs further investigation, but it is noteworthy that the observation of CPL coincides with the observation by J.-P. Sutter and V. Béreau of slow relaxation of magnetization (paper presently under submission): both effects are observed only below 25 K and both occur for the Dy crystals but not the Eu(III) crystals. More experimental work, such as CPL measurement under an applied magnetic field, would be necessary to confirm the link between luminescence and magnetic chirality effects.

Reference

1. Ekimov, A. & Onushchenko, A. Quantum size effect in three-dimensional microscopic semiconductor crystals. *Sov. J. Exp. Theor. Phys. Lett.* (1981).
2. Murray, C. B., Norris, D. J. & Bawendi, M. G. Synthesis and Characterization of Nearly Monodisperse CdE (E = S, Se, Te) Semiconductor Nanocrystallites. *J. Am. Chem. Soc.* (1993). doi:10.1021/ja00072a025
3. Peng, X. *et al.* Shape control of CdSe nanocrystals. *Nature* (2000). doi:10.1038/35003535
4. Ithurria, S. & Dubertret, B. Quasi 2D colloidal CdSe platelets with thicknesses controlled at the atomic level. *J. Am. Chem. Soc.* (2008). doi:10.1021/ja807724e
5. Ithurria, S. *et al.* Colloidal nanoplatelets with two-dimensional electronic structure. *Nat. Mater.* **10**, 936–941 (2011).
6. Feng, F. *et al.* Consequence of shape elongation on emission asymmetry for colloidal CdSe/CdS nanoplatelets. *Nano Res.* **11**, 3593–3602 (2018).
7. Tessier, M. D. *et al.* Phonon line emission revealed by self-assembly of colloidal nanoplatelets. *ACS Nano* **7**, 3332–3340 (2013).
8. Jana, S., Davidson, P. & Abécassis, B. CdSe Nanoplatelets: Living Polymers. *Angew. Chemie - Int. Ed.* **55**, 9371–9374 (2016).
9. Antanovich, A., Prudnikau, A., Matsukovich, A., Achtstein, A. & Artemyev, M. Self-Assembly of CdSe Nanoplatelets into Stacks of Controlled Size Induced by Ligand Exchange. *J. Phys. Chem. C* **120**, 5764–5775 (2016).
10. Miethe, J. F., Schlosser, A., Eckert, J. G., Lübkemann, F. & Bigall, N. C. Electronic transport in CdSe nanoplatelet based polymer fibres. *J. Mater. Chem. C* (2018). doi:10.1039/c8tc03879a
11. Kim, W. D. *et al.* Stacking of Colloidal CdSe Nanoplatelets into Twisted Ribbon Superstructures: Origin of Twisting and Its Implication in Optical Properties. *J. Phys. Chem. C* **123**, 9445–9453 (2019).
12. Gao, Y., Weidman, M. C. & Tisdale, W. A. CdSe Nanoplatelet Films with Controlled Orientation of their Transition Dipole Moment. *Nano Lett.* **17**, 3837–3843 (2017).
13. Momper, R. *et al.* Kinetic Control over Self-Assembly of Semiconductor Nanoplatelets. *Nano Lett.* (2020). doi:10.1021/acs.nanolett.9b05270
14. Erdem, O. *et al.* Orientation-Controlled Nonradiative Energy Transfer to Colloidal Nanoplatelets: Engineering Dipole Orientation Factor. *Nano Lett.* **19**, 4297–4305 (2019).
15. Rowland, C. E. *et al.* Picosecond energy transfer and multiexciton transfer outpaces Auger recombination in binary CdSe nanoplatelet solids. *Nat. Mater.* **14**, 484–489 (2015).
16. Guzelturk, B., Erdem, O., Olutas, M., Kelestemur, Y. & Demir, H. V. Stacking in colloidal nanoplatelets: Tuning excitonic properties. *ACS Nano* **8**, 12524–12533 (2014).

17. Kim, W. D. *et al.* Pushing the Efficiency Envelope for Semiconductor Nanocrystal-Based Electroluminescence Devices Using Anisotropic Nanocrystals. *Chem. Mater.* **31**, 3066–3082 (2019).

18. Diroll, B. T. *et al.* Semiconductor Nanoplatelet Excimers. *Nano Lett.* **18**, 6948–6953 (2018).

19. Goldstein, L., Glas, F., Marzin, J. Y., Charasse, M. N. & Le Roux, G. Growth by molecular beam epitaxy and characterization of InAs/GaAs strained-layer superlattices. *Appl. Phys. Lett.* (1985). doi:10.1063/1.96342

20. Manna, L., Milliron, D. J., Meisel, A., Scher, E. C. & Alivisatos, A. P. Controlled growth of tetrapod-branched inorganic nanocrystals. *Nature Materials* (2003). doi:10.1038/nmat902

21. Duan, X. & Lieber, C. M. General Synthesis of Compound Semiconductor Nanowires. *Adv. Mater.* **12**, 298–302 (2000).

22. Joo, J., Son, J. S., Kwon, S. G., Yu, J. H. & Hyeon, T. Low-temperature solution-phase synthesis of quantum well structured CdSe nanoribbons. *J. Am. Chem. Soc.* (2006). doi:10.1021/ja0601686

23. Talapin, D. V. *et al.* CdSe/CdS/ZnS and CdSe/ZnSe/ZnS core-shell-shell nanocrystals. *J. Phys. Chem. B* **108**, 18826–18831 (2004).

24. Jin, S. & Lian, T. Electron transfer dynamics from single CdSe/ZnS quantum dots to TiO 2 nanoparticles. *Nano Lett.* (2009). doi:10.1021/nl9011744

25. Tan, C., Chen, J., Wu, X. J. & Zhang, H. Epitaxial growth of hybrid nanostructures. *Nat. Rev. Mater.* **3**, 17089 (2018).

26. Bertrand, G. H. V., Polovitsyn, A., Christodoulou, S., Khan, A. H. & Moreels, I. Shape control of zincblende CdSe nanoplatelets. *Chem. Commun.* **52**, 11975–11978 (2016).

27. Naeem, A. *et al.* Giant exciton oscillator strength and radiatively limited dephasing in two-dimensional platelets. *Phys. Rev. B - Condens. Matter Mater. Phys.* **91**, (2015).

28. Yeltik, A. *et al.* Experimental Determination of the Absorption Cross-Section and Molar Extinction Coefficient of Colloidal CdSe Nanoplatelets. *J. Phys. Chem. C* **119**, 26768–26775 (2015).

29. Feng, F. *et al.* Probing the Fluorescence Dipoles of Single Cubic CdSe/CdS Nanoplatelets with Vertical or Horizontal Orientations. *ACS Photonics* **5**, 1994–1999 (2018).

30. Tessier, M. D., Javaux, C., Maksimovic, I., Loriette, V. & Dubertret, B. Spectroscopy of Single CdSe Nanoplatelets. *ACS Nano* **6**, 6751–6758 (2012).

31. Liu, J., Guillemeney, L., Abécassis, B. & Coolen, L. Long Range Energy Transfer in Self-Assembled Stacks of Semiconducting Nanoplatelets. *Nano Lett.* acs.nanolett.0c00376 (2020). doi:x

32. Guzelturk, B., Kelestemur, Y., Olutas, M., Delikanli, S. & Demir, H. V. Amplified spontaneous emission and lasing in colloidal nanoplatelets. *ACS Nano* **8**, 6599–6605 (2014).

33. Li, M. *et al.* Ultralow-threshold multiphoton-pumped lasing from colloidal nanoplatelets in solution. *Nat. Commun.* (2015). doi:10.1038/ncomms9513

34. She, C. *et al.* Red, Yellow, Green, and Blue Amplified Spontaneous Emission and Lasing Using Colloidal CdSe Nanoplatelets. *ACS Nano* (2015). doi:10.1021/acsnano.5b02509

35. Grim, J. Q. *et al.* Continuous-wave biexciton lasing at room temperature using solution-processed quantum wells. *Nat. Nanotechnol.* **9**, 891–895 (2014).

36. Altintas, Y. *et al.* Giant Alloyed Hot Injection Shells Enable Ultralow Optical Gain Threshold in Colloidal Quantum Wells. *ACS Nano* (2019). doi:10.1021/acsnano.9b04967

37. Dai, X., Deng, Y., Peng, X. & Jin, Y. Quantum-Dot Light-Emitting Diodes for Large-Area Displays: Towards the Dawn of Commercialization. *Advanced Materials* (2017). doi:10.1002/adma.201607022

38. Chen, Z., Nadal, B., Mahler, B., Aubin, H. & Dubertret, B. Quasi-2D colloidal semiconductor nanoplatelets for narrow electroluminescence. *Adv. Funct. Mater.* (2014). doi:10.1002/adfm.201301711

39. Liu, B. *et al.* Nanocrystal light-emitting diodes based on type II nanoplatelets. *Nano Energy* **47**, 115–122 (2018).

40. Aharonovich, I., Englund, D. & Toth, M. Solid-state single-photon emitters. *Nature Photonics* **10**, 631–641 (2016).

41. Lhuillier, E. *et al.* Electrolyte-gated field effect transistor to probe the surface defects and morphology in films of thick CdSe colloidal nanoplatelets. *ACS Nano* (2014). doi:10.1021/nn500538n

42. Gromova, Y. A. *et al.* Magnetic Circular Dichroism in 2D Colloidal Semiconductor Nanocrystals. *Opt. Spectrosc. (English Transl. Opt. i Spektrosk.* **125**, 698–702 (2018).

43. Li, Q. *et al.* Size-Independent Exciton Localization Efficiency in Colloidal CdSe/CdS Core/Crown Nanosheet Type-I Heterostructures. *ACS Nano* **10**, 3843–3851 (2016).

44. Biadala, L. *et al.* Recombination dynamics of band edge excitons in quasi-two-dimensional cdse nanoplatelets. *Nano Lett.* **14**, 1134–1139 (2014).

45. Cho, W. *et al.* Direct Synthesis of Six-Monolayer (1.9 nm) Thick Zinc-Blende CdSe Nanoplatelets Emitting at 585 nm. *Chem. Mater.* **30**, 6957–6960 (2018).

46. Delikanli, S. *et al.* Ultrathin Highly Luminescent Two-Monolayer Colloidal CdSe Nanoplatelets. *Adv. Funct. Mater.* **29**, 1901028 (2019).

47. Bowers, M. J., McBride, J. R. & Rosenthal, S. J. White-light emission from magic-sized cadmium selenide nanocrystals. *J. Am. Chem. Soc.* (2005). doi:10.1021/ja055470d

48. Schliehe, C. *et al.* Ultrathin PbS sheets by two-dimensional oriented attachment. *Science (80-.).* (2010). doi:10.1126/science.1188035

49. Koh, W. *et al.* Thickness-Controlled Quasi-Two-Dimensional Colloidal PbSe Nanoplatelets. *J. Am. Chem. Soc.* **139**, 2152–2155 (2017).

50. Son, J. S. *et al.* Large-scale soft colloidal template synthesis of 1.4 nm thick cdse nanosheets. *Angew. Chemie - Int. Ed.* (2009). doi:10.1002/anie.200902791

51. Nasilowski, M., Mahler, B., Lhuillier, E., Ithurria, S. & Dubertret, B. Two-Dimensional

Colloidal Nanocrystals. *Chemical Reviews* **116**, 10934–10982 (2016).

52. Prudnikau, A., Chuvilin, A. & Artemyev, M. CdSe-CdS nanoheteroplatelets with efficient photoexcitation of central CdSe region through epitaxially grown CdS wings. *J. Am. Chem. Soc.* **135**, 14476–14479 (2013).

53. Tessier, M. D. *et al.* Efficient exciton concentrators built from colloidal core/crown CdSe/CdS semiconductor nanoplatelets. *Nano Lett.* **14**, 207–213 (2014).

54. Delikanli, S. *et al.* Continuously Tunable Emission in Inverted Type-I CdS/CdSe Core/Crown Semiconductor Nanoplatelets. *Adv. Funct. Mater.* **25**, 4282–4289 (2015).

55. Pedetti, S., Ithurria, S., Heuclin, H., Patriarche, G. & Dubertret, B. Type-II CdSe/CdTe core/crown semiconductor nanoplatelets. *J. Am. Chem. Soc.* **136**, 16430–16438 (2014).

56. Wu, K. *et al.* Efficient and ultrafast formation of long-lived charge-transfer exciton state in atomically thin cadmium selenide/cadmium telluride type-II heteronanosheets. *ACS Nano* **9**, 961–968 (2015).

57. Antanovich, A. V. *et al.* Colloidal synthesis and optical properties of type-II CdSe-CdTe and inverted CdTe-CdSe core-wing heteronanoplatelets. *Nanoscale* **7**, 8084–8092 (2015).

58. Yadav, S., Singh, A. & Sapra, S. Long-Lived Emission in Type-II CdS/ZnSe Core/Crown Nanoplatelet Heterostructures. *J. Phys. Chem. C* **121**, 27241–27246 (2017).

59. Kelestemur, Y. *et al.* CdSe/CdSe1-xTex Core/Crown Heteronanoplatelets: Tuning the Excitonic Properties without Changing the Thickness. *J. Phys. Chem. C* **121**, 4650–4658 (2017).

60. Mahler, B., Nadal, B., Bouet, C., Patriarche, G. & Dubertret, B. Core/shell colloidal semiconductor nanoplatelets. *J. Am. Chem. Soc.* **134**, 18591–18598 (2012).

61. Polovitsyn, A. *et al.* Synthesis of Air-Stable CdSe/ZnS Core-Shell Nanoplatelets with Tunable Emission Wavelength. *Chem. Mater.* **29**, 5671–5680 (2017).

62. Kunneman, L. T. *et al.* Bimolecular auger recombination of electron-hole pairs in two-dimensional CdSe and CdSe/CdZnS core/shell nanoplatelets. *J. Phys. Chem. Lett.* **4**, 3574–3578 (2013).

63. Kelestemur, Y. *et al.* Platelet-in-Box Colloidal Quantum Wells: CdSe/CdS@CdS Core/Crown@Shell Heteronanoplatelets. *Adv. Funct. Mater.* **26**, 3570–3579 (2016).

64. Sharma, M., Delikanli, S. & Demir, H. V. Two-Dimensional CdSe-Based Nanoplatelets: Their Heterostructures, Doping, Photophysical Properties, and Applications. *Proc. IEEE* **108**, 655–675 (2020).

65. Yu, J. H. *et al.* Giant Zeeman splitting in nucleation-controlled doped CdSe:Mn2+ quantum nanoribbons. *Nat. Mater.* **9**, 47–53 (2010).

66. Muckel, F. *et al.* sp–d Exchange Interactions in Wave Function Engineered Colloidal CdSe/Mn:CdS Hetero-Nanoplatelets. *Nano Lett.* **18**, 2047–2053 (2018).

67. Sharma, M. *et al.* Understanding the Journey of Dopant Copper Ions in Atomically Flat Colloidal Nanocrystals of CdSe Nanoplatelets Using Partial Cation Exchange Reactions.

Chem. Mater. **30**, 3265–3275 (2018).

68. Khan, A. H. *et al.* Tunable and Efficient Red to Near-Infrared Photoluminescence by Synergistic Exploitation of Core and Surface Silver Doping of CdSe Nanoplatelets. *Chem. Mater.* (2019). doi:10.1021/acs.chemmater.8b05334

69. Abécassis, B., Tessier, M. D., Davidson, P. & Dubertret, B. Self-assembly of CdSe nanoplatelets into giant micrometer-scale needles emitting polarized light. *Nano Lett.* **14**, 710–715 (2014).

70. Jana, S. *et al.* Stacking and Colloidal Stability of CdSe Nanoplatelets. *Langmuir* **31**, 10532–10539 (2015).

71. Jana, S., de Frutos, M., Davidson, P. & Abécassis, B. Ligand-induced twisting of nanoplatelets and their self-assembly into chiral ribbons. *Sci. Adv.* **3**, e1701483 (2017).

72. Yu, J., Zhang, C., Pang, G., Sun, X. W. & Chen, R. Effect of Lateral Size and Surface Passivation on the Near-Band-Edge Excitonic Emission from Quasi-Two-Dimensional CdSe Nanoplatelets. *ACS Appl. Mater. Interfaces* **11**, 41821–41827 (2019).

73. Shornikova, E. V. *et al.* Negatively Charged Excitons in CdSe Nanoplatelets. *Nano Lett.* **20**, 1370–1377 (2020).

74. Erdem, O. *Orientation-Controlled Construction of Superstructures of Atomically-Flat Nanocrystals: Pushing the Limits of Ultra-Thin Colloidal Gain Media*. *arxiv.org/abs/2005.10724* **115**, (2020).

75. Woggon, U. & Gaponenko, S. V. Excitons in Quantum Dots. *Phys. status solidi* **189**, 285–343 (1995).

76. Klimov, V. I. *Nanocrystal Quntum Dots*. (CRC Press, 2010).

77. Scott, R. *et al.* Directed emission of CdSe nanoplatelets originating from strongly anisotropic 2D electronic structure. *Nat. Nanotechnol.* **12**, 1155–1160 (2017).

78. Htoon, H., Furis, M., Crooker, S. A., Jeong, S. & Klimov, V. I. Linearly polarized ‘fine structure’ of the bright exciton state in individual CdSe nanocrystal quantum dots. *Phys. Rev. B* **77**, 035328 (2008).

79. Efros, A. L. *et al. Band-edge exciton in quantum dots of semiconductors with a degenerate valence band: Dark and bright exciton states*. *Physical Review B - Condensed Matter and Materials Physics* **54**, (1996).

80. Norris, D., Efros, A. L. & Rosen, M. *Size dependence of exciton fine structure in CdSe quantum dots*. *Physical Review B - Condensed Matter and Materials Physics* **53**, (1996).

81. Nirmal, M. *et al.* Observation of the ‘dark exciton’ in CdSe quantum dots. *Phys. Rev. Lett.* **75**, 3728–3731 (1995).

82. Oron, D. *et al.* Universal role of discrete acoustic phonons in the low-temperature optical emission of colloidal quantum dots. *Phys. Rev. Lett.* (2009). doi:10.1103/PhysRevLett.102.177402

83. Gu, B., Kwong, N. H. & Binder, R. Relation between the interband dipole and momentum

matrix elements in semiconductors. *Phys. Rev. B - Condens. Matter Mater. Phys.* **87**, 125301 (2013).

84. Ma, X. *et al.* Anisotropic Photoluminescence from Isotropic Optical Transition Dipoles in Semiconductor Nanoplatelets. *Nano Lett.* **18**, 4647–4652 (2018).

85. Rodina, A. V. & Efros, A. L. Effect of dielectric confinement on optical properties of colloidal nanostructures. *J. Exp. Theor. Phys.* **122**, 554–566 (2016).

86. LANDAU, L. D. & LIFSHITZ, E. M. Electrostatics of Conductors. in *Electrodynamics of Continuous Media* 1–33 (1984). doi:10.1016/b978-0-08-030275-1.50007-2

87. Yoon, D. E. *et al.* Origin of shape-dependent fluorescence polarization from CdSe nanoplatelets. *J. Phys. Chem. C* **121**, 24837–24844 (2017).

88. Robel, I., Gresback, R., Kortshagen, U., Schaller, R. D. & Klimov, V. I. Universal size-dependent trend in auger recombination in direct-gap and indirect-gap semiconductor nanocrystals. *Phys. Rev. Lett.* **102**, (2009).

89. Klimov, V. I. *et al.* Optical gain and stimulated emission in nanocrystal quantum dots. *Science (80-.).* (2000). doi:10.1126/science.290.5490.314

90. Kazes, M., Oron, D., Shweky, I. & Banin, U. Temperature dependence of optical gain in CdSe/ZnS quantum rods. *J. Phys. Chem. C* (2007). doi:10.1021/jp070075q

91. Nozik, A. J. Quantum dot solar cells. in *Physica E: Low-Dimensional Systems and Nanostructures* (2002). doi:10.1016/S1386-9477(02)00374-0

92. Bae, W. K. *et al.* Controlling the influence of Auger recombination on the performance of quantum-dot light-emitting diodes. *Nat. Commun.* (2013). doi:10.1038/ncomms3661

93. Senellart, P., Solomon, G. & White, A. High-performance semiconductor quantum-dot single-photon sources. *Nature Nanotechnology* **12**, 1026–1039 (2017).

94. Loan, N. T. Development of polarimetric and emission pattern analysis : applied to determine a single nanoplatelet To cite this version : HAL Id : tel-01701761 Thu-Loan Nguyen Development of polarimetric and emission pattern analysis : Applied to determine a single n. (2018).

95. Coolen, L. Coherence temporelle des photons uniquesemis par un nanocristal individuel de CdSe / ZnS. (2007).

96. Forster, T. Energiewanderung und Fluoreszenz. *Naturwissenschaften* **33**, 166–175 (1946).

97. Novotny, L. & Hecht, B. *Principles of nano-optics*. *Principles of Nano-Optics* **9781107005**, (2009).

98. Guzelturk, B. & Demir, H. V. Near-Field Energy Transfer Using Nanoemitters For Optoelectronics. *Adv. Funct. Mater.* **26**, 8158–8177 (2016).

99. van der Meer, B. W., van der Meer, D. M. & Vogel, S. S. Optimizing the Orientation Factor Kappa-Squared for More Accurate FRET Measurements. in *FRET - Förster Resonance Energy Transfer: From Theory to Applications* (2013). doi:10.1002/9783527656028.ch04

100. Kholmicheva, N., Moroz, P., Eckard, H., Jensen, G. & Zamkov, M. Energy transfer in

quantum dot solids. *ACS Energy Lett.* (2017). doi:10.1021/acsenergylett.6b00569

101. Akselrod, G. M. *et al.* Subdiffusive Exciton Transport in Quantum Dot Solids. *Nano Lett.* **14**, 3556–3562 (2014).

102. Lee, E. M. Y. & Tisdale, W. A. Determination of exciton diffusion length by transient photoluminescence quenching and its application to quantum dot films. *J. Phys. Chem. C* (2015). doi:10.1021/jp512634c

103. Ryan, D. P. *et al.* Mapping Emission from Clusters of CdSe/ZnS Nanoparticles. *J. Phys. Chem. C* **122**, 4046–4053 (2018).

104. Mikhnenko, O. V., Blom, P. W. M. & Nguyen, T. Q. Exciton diffusion in organic semiconductors. *Energy and Environmental Science* (2015). doi:10.1039/c5ee00925a

105. Fennel, F. & Lochbrunner, S. Long distance energy transfer in a polymer matrix doped with a perylene dye. *Phys. Chem. Chem. Phys.* **13**, 3527–3533 (2011).

106. Menke, S. M., Luhman, W. A. & Holmes, R. J. Tailored exciton diffusion in organic photovoltaic cells for enhanced power conversion efficiency. *Nat. Mater.* **12**, 152–157 (2013).

107. Akselrod, G. M. *et al.* Visualization of exciton transport in ordered and disordered molecular solids. *Nat. Commun.* **5**, (2014).

108. Dubin, F. *et al.* Macroscopic coherence of a single exciton state in an organic quantum wire. *Nat. Phys.* **2**, 32–35 (2006).

109. Haedler, A. T. *et al.* Long-range energy transport in single supramolecular nanofibres at room temperature. *Nature* **523**, 196–199 (2015).

110. Lin, H. *et al.* Collective fluorescence blinking in linear J-aggregates assisted by long-distance exciton migration. *Nano Lett.* (2010). doi:10.1021/nl9036559

111. Bouchet, D. *et al.* Correlated blinking of fluorescent emitters mediated by single plasmons. *Phys. Rev. A* **95**, 33828 (2017).

112. De Torres, J., Ferrand, P., Colas Des Francs, G. & Wenger, J. Coupling Emitters and Silver Nanowires to Achieve Long-Range Plasmon-Mediated Fluorescence Energy Transfer. *ACS Nano* **10**, 3968–3976 (2016).

113. Kholmicheva, N. *et al.* Mapping the exciton diffusion in semiconductor nanocrystal solids. *ACS Nano* (2015). doi:10.1021/nn507322y

114. Gilmore, R. H., Lee, E. M. Y., Weidman, M. C., Willard, A. P. & Tisdale, W. A. Charge Carrier Hopping Dynamics in Homogeneously Broadened PbS Quantum Dot Solids. *Nano Lett.* (2017). doi:10.1021/acs.nanolett.6b04201

115. Erdem, O., Olutas, M., Guzelturk, B., Kelestemur, Y. & Demir, H. V. Temperature-Dependent Emission Kinetics of Colloidal Semiconductor Nanoplatelets Strongly Modified by Stacking. *J. Phys. Chem. Lett.* **7**, 548–554 (2016).

116. Taghipour, N. *et al.* Near-Unity Efficiency Energy Transfer from Colloidal Semiconductor Quantum Wells of CdSe/CdS Nanoplatelets to a Monolayer of MoS2. *ACS Nano* **12**, 8547–

8554 (2018).

117. Hernández-Martínez, P. L., Govorov, A. O. & Demir, H. V. Generalized theory of Förster-type nonradiative energy transfer in nanostructures with mixed dimensionality. *J. Phys. Chem. C* **117**, 10203–10212 (2013).

118. Olutas, M., Guzelturk, B., Kelestemur, Y., Gungor, K. & Demir, H. V. Highly Efficient Nonradiative Energy Transfer from Colloidal Semiconductor Quantum Dots to Wells for Sensitive Noncontact Temperature Probing. *Adv. Funct. Mater.* **26**, 2891–2899 (2016).

119. She, C. *et al.* Low-threshold stimulated emission using colloidal quantum wells. *Nano Lett.* **14**, 2772–2777 (2014).

120. Moreels, I. Colloidal nanoplatelets: Energy transfer is speeded up in 2D. *Nature Materials* **14**, 464–465 (2015).

121. Feng, F. *et al.* Active control of radiation beaming from Tamm nanostructures by optical microscopy Engineering metallic nanostructures for plasmonics and nanophotonics Active control of radiation beaming from Tamm nanostructures by optical microscopy. *New J. Phys* **20**, (2018).

122. Favero, P. P., De Souza-Parise, M., Fernandez, J. L. R., Miotto, R. & Ferraz, A. C. Surface properties of CdS nanoparticles. in *Brazilian Journal of Physics* (2006). doi:10.1590/S0103-97332006000600062

123. Lv, B. *et al.* Photon antibunching in a cluster of giant CdSe/CdS nanocrystals. *Nat. Commun.* **9**, 1536 (2018).

124. Hoogenboom, J. P., Hernando, J., Van Dijk, E. M. H. P., Van Hulst, N. F. & García-Parajó, M. F. Power-law blinking in the fluorescence of single organic molecules. *ChemPhysChem* (2007). doi:10.1002/cphc.200600783

125. Vanden Bout, D. A. *et al.* Discrete intensity jumps and intramolecular electronic energy transfer in the spectroscopy of single conjugated polymer molecules. *Science (80-.).* (1997). doi:10.1126/science.277.5329.1074

126. Nirmal, M. *et al.* Fluorescence intermittency in single cadmium selenide nanocrystals. *Nature* **383**, 802–804 (1996).

127. Frantsuzov, P., Kuno, M., Jankó, B. & Marcus, R. A. Universal emission intermittency in quantum dots, nanorods and nanowires. *Nat. Phys.* (2008). doi:10.1038/nphys1001

128. Efros, A. L. & Nesbitt, D. J. Origin and control of blinking in quantum dots. *Nat. Nanotechnol.* **11**, 661–671 (2016).

129. Klimov, V. I., Mikhailovsky, A. A., McBranch, D. W., Leatherdale, C. A. & Bawendi, M. G. Quantization of multiparticle Auger rates in semiconductor quantum dots. *Science (80-.).* (2000). doi:10.1126/science.287.5455.1011

130. Fisher, B. R., Eisler, H. J., Stott, N. E. & Bawendi, M. G. Emission intensity dependence and single-exponential behavior in single colloidal quantum dot fluorescence lifetimes. *J. Phys. Chem. B* **108**, 143–148 (2004).

131. García-Santamaría, F. *et al.* Breakdown of volume scaling in auger recombination in CdSe/CdS heteronanocrystals: The role of the core-shell interface. *Nano Lett.* **11**, 687–693 (2011).

132. Galland, C. *et al.* Two types of luminescence blinking revealed by spectroelectrochemistry of single quantum dots. *Nature* **479**, 203–207 (2011).

133. Yuan, G., Gómez, D. E., Kirkwood, N., Boldt, K. & Mulvaney, P. Two Mechanisms Determine Quantum Dot Blinking. *ACS Nano* **12**, 3397–3405 (2018).

134. Tyagi, P. & Kambhampati, P. False multiple exciton recombination and multiple exciton generation signals in semiconductor quantum dots arise from surface charge trapping. *J. Chem. Phys.* (2011). doi:10.1063/1.3561063

135. Zhang, K., Chang, H., Fu, A., Alivisatos, A. P. & Yang, H. Continuous distribution of emission states from single CdSe/ZnS quantum dots. *Nano Lett.* (2006). doi:10.1021/nl060483q

136. Jha, P. P. & Guyot-Sionnest, P. Electrochemical switching of the photoluminescence of single quantum dots. *J. Phys. Chem. C* (2010). doi:10.1021/jp1074626

137. Efros, A. L. & Rosen, M. Random telegraph signal in the photoluminescence intensity of a single quantum dot. *Phys. Rev. Lett.* (1997). doi:10.1103/PhysRevLett.78.1110

138. Peterson, J. J. & Nesbitt, D. J. Modified power law behavior in quantum dot blinking: A novel role for biexcitons and auger ionization. *Nano Lett.* (2009). doi:10.1021/nl803108p

139. Kuno, M., Fromm, D. P., Hamann, H. F., Gallagher, A. & Nesbitt, D. J. Nonexponential "blinking" kinetics of single CdSe quantum dots: A universal power law behavior. *J. Chem. Phys.* **112**, 3117–3120 (2000).

140. Rabouw, F. T., Antolinez, F. V., Brechbühler, R. & Norris, D. J. Microsecond Blinking Events in the Fluorescence of Colloidal Quantum Dots Revealed by Correlation Analysis on Preselected Photons. *J. Phys. Chem. Lett.* **10**, 3732–3738 (2019).

141. Cragg, G. E. & Efros, A. L. Suppression of auger processes in confined structures. *Nano Lett.* **10**, 313–317 (2010).

142. Chen, Y. *et al.* 'Giant' multishell CdSe nanocrystal quantum dots with suppressed blinking. *J. Am. Chem. Soc.* **130**, 5026–5027 (2008).

143. Omogo, B., Gao, F., Bajwa, P., Kaneko, M. & Heyes, C. D. Reducing Blinking in Small Core-Multishell Quantum Dots by Carefully Balancing Confinement Potential and Induced Lattice Strain: The 'goldilocks' Effect. *ACS Nano* (2016). doi:10.1021/acsnano.5b06994

144. Hu, Z., Singh, A., Goupalov, S. V., Hollingsworth, J. A. & Htoon, H. Influence of morphology on the blinking mechanisms and the excitonic fine structure of single colloidal nanoplatelets. *Nanoscale* **10**, 22861–22870 (2018).

145. Mahler, B. *et al.* Towards non-blinking colloidal quantum dots. *Nat. Mater.* **7**, 659–664 (2008).

146. BROWN, R. H. & TWISS, R. Q. Correlation between Photons in two Coherent Beams of

Light. *Nature* **177**, 27–29 (1956).

147. Kimble, H. J., Dagenais, M. & Mandel, L. Photon antibunching in resonance fluorescence. *Phys. Rev. Lett.* (1977). doi:10.1103/PhysRevLett.39.691

148. Lounis, B. & Moerner, W. E. Single photons on demand from a single molecule at room temperature. *Nature* (2000). doi:10.1038/35035032

149. Santori, C., Pelton, M., Solomon, G., Dale, Y. & Yamamoto, Y. Triggered single photons from a quantum dot. *Phys. Rev. Lett.* (2001). doi:10.1103/PhysRevLett.86.1502

150. Kurtsiefer, C., Mayer, S., Zarda, P. & Weinfurter, H. Stable solid-state source of single photons. *Phys. Rev. Lett.* (2000). doi:10.1103/PhysRevLett.85.290

151. Ma, X. *et al.* Size-Dependent Biexciton Quantum Yields and Carrier Dynamics of Quasi-Two-Dimensional Core/Shell Nanoplatelets. *ACS Nano* **11**, 9119–9127 (2017).

152. Loudon, R. *The Quantum Theory of Light*. (Oxford Science Publications, 2000).

153. Shulenberger, K. E. *et al.* Multiexciton Lifetimes Reveal Triexciton Emission Pathway in CdSe Nanocrystals. *Nano Lett.* **18**, 5153–5158 (2018).

154. Nair, G., Zhao, J. & Bawendi, M. G. Biexciton quantum yield of single semiconductor nanocrystals from photon statistics. *Nano Lett.* **11**, 1136–1140 (2011).

155. Mangum, B. D., Ghosh, Y., Hollingsworth, J. A. & Htoon, H. Disentangling the effects of clustering and multi-exciton emission in second-order photon correlation experiments. *Opt. Express* **21**, 7419 (2013).

156. Paul, H. Photon antibunching. *Rev. Mod. Phys.* **54**, 1061–1102 (1982).

157. Tessier, M. D. *et al.* Spectroscopy of colloidal semiconductor core/shell nanoplatelets with high quantum yield. *Nano Lett.* **13**, 3321–3328 (2013).

158. Hines, D. A. & Kamat, P. V. Quantum dot surface chemistry: Ligand effects and electron transfer reactions. *J. Phys. Chem. C* (2013). doi:10.1021/jp404031s

159. Knowles, K. E., McArthur, E. A. & Weiss, E. A. A multi-timescale map of radiative and nonradiative decay pathways for excitons in CdSe quantum dots. *ACS Nano* **5**, 2026–2035 (2011).

160. Cui, J. *et al.* Colloidal quantum dot molecules manifesting quantum coupling at room temperature. *Nat. Commun.* **10**, (2019).

161. Wang, S. *et al.* Collective fluorescence enhancement in nanoparticle clusters. *Nat. Commun.* **2**, (2011).

162. Lethiec, C. *et al.* Polarimetry-based analysis of dipolar transitions of single colloidal CdSe/CdS dot-in-rods. *New J. Phys.* **16**, 093014 (2014).

163. Macklin, J. J., Trautman, J. K., Harris, T. D. & Brus, L. E. Imaging and time-resolved spectroscopy of single molecules at an interface. *Science (80-.).* (1996). doi:10.1126/science.272.5259.255

164. Ha, T., Enderle, T., Chemla, D. S., Selvin, P. R. & Weiss, S. Single molecule dynamics

studied by polarization modulation. *Phys. Rev. Lett.* (1996). doi:10.1103/PhysRevLett.77.3979

165. Pariser, R. Theory of the electronic spectra and structure of the polyacenes and of alternant hydrocarbons. *J. Chem. Phys.* (1956). doi:10.1063/1.1742461

166. Epstein, R. J., Mendoza, F. M., Kato, Y. K. & Awschalom, D. D. Anisotropic interactions of a single spin and dark-spin spectroscopy in diamond. *Nature Physics* (2005). doi:10.1038/nphys141

167. Chung, I., Shimizu, K. T. & Bawendi, M. G. Room temperature measurements of the 3D orientation of single CdSe quantum dots using polarization microscopy. *Proc. Natl. Acad. Sci.* **100**, 405–408 (2003).

168. Vion, C. *et al.* Controlled modification of single colloidal CdSe/ZnS nanocrystal fluorescence through interactions with a gold surface. *Opt. Express* (2010). doi:10.1364/oe.18.007440

169. Belacel, C. *et al.* Controlling Spontaneous Emission with Plasmonic Optical Patch Antennas. *Nano Lett.* **13**, 1516–1521 (2013).

170. Ha, T., Laurence, T. A., Chemla, D. S. & Weiss, S. Polarization spectroscopy of single fluorescent molecules. *J. Phys. Chem. B* (1999). doi:10.1021/jp990948j

171. Güttler, F., Croci, M., Renn, A. & Wild, U. P. Single molecule polarization spectroscopy: Pentacene in p-terphenyl. *Chem. Phys.* (1996). doi:10.1016/0301-0104(96)00250-9

172. Lieb, M. A., Zavislan, J. M. & Novotny, L. Single-molecule orientations determined by direct emission pattern imaging. *J. Opt. Soc. Am. B* **21**, 1210 (2004).

173. Brokmann, X., Ehrensperger, M. V., Hermier, J. P., Triller, A. & Dahan, M. Orientational imaging and tracking of single CdSe nanocrystals by defocused microscopy. *Chem. Phys. Lett.* (2005). doi:10.1016/j.cplett.2005.03.007

174. Lethiec, C. *et al.* Measurement of three-dimensional dipole orientation of a single fluorescent nanoemitter by emission polarization analysis. *Phys. Rev. X* **4**, 021037 (2014).

175. Lethiec, C. Emission polarisée de nanoémetteurs; excitation de plasmons sur une surface métallique. (2014).

176. Feng, F. Coupling between optical Tamm states and fluorescent nanocrystals ; determination of the dipole nature of single colloidal nanoplatelets. (2017).

177. Curto, A. G. *et al.* Unidirectional emission of a quantum dot coupled to a nanoantenna. *Science (80-.).* (2010). doi:10.1126/science.1191922

178. Budde, H. *et al.* Raman Radiation Patterns of Graphene. *ACS Nano* (2016). doi:10.1021/acsnano.5b06631

179. Lukosz, W. Light Emission By Multipole Sources in Thin Layers - 1. Radiation Patterns of Electric and Magnetic Dipoles. *J. Opt. Soc. Am.* **71**, 744–754 (1981).

180. Lukosz, W. & Kunz, R. E. Light emission by magnetic and electric dipoles close to a plane interface I Total radiated power. *J. Opt. Soc. Am.* **67**, 1607 (1977).

181. Lukosz, W. & Kunz, R. E. Light emission by magnetic and electric dipoles close to a plane dielectric interface II Radiation patterns of perpendicular oriented dipoles. *J. Opt. Soc. Am.* **67**, 1615 (1977).

182. Lukosz, W. Light emission by magnetic and electric dipoles close to a plane dielectric interface III Radiation patterns of dipoles with arbitrary orientation. *J. Opt. Soc. Am.* **69**, 1495 (1979).

183. Vezzoli, S. *et al.* Exciton Fine Structure of CdSe/CdS Nanocrystals Determined by Polarization Microscopy at Room Temperature. *ACS Nano* **9**, 7992–8003 (2015).

184. Brotons-Gisbert, M. *et al.* Out-of-plane orientation of luminescent excitons in two-dimensional indium selenide. *Nat. Commun.* **10**, 3913 (2019).

185. Xiao, K., Yan, T. & Cui, X. Dipole Orientation Shift of Ga2Se2 by Quantum Confinement. *ACS Nano* **14**, 1027–1032 (2020).

186. Kurvits, J. A., Jiang, M. & Zia, R. Comparative analysis of imaging configurations and objectives for Fourier microscopy. *J. Opt. Soc. Am. A* **32**, 2082 (2015).

187. Ninomiya, S. & Adachi, S. Optical properties of cubic and hexagonal CdSe. *J. Appl. Phys.* (1995). doi:10.1063/1.359815

188. Achtstein, A. W. *et al.* P -State Luminescence in CdSe Nanoplatelets: Role of Lateral Confinement and a Longitudinal Optical Phonon Bottleneck. *Phys. Rev. Lett.* **116**, 116802 (2016).

189. Movilla, J. L., Planelles, J. & Climente, J. I. Dielectric Confinement Enables Molecular Coupling in Stacked Colloidal Nanoplatelets. *J. Phys. Chem. Lett.* **11**, 3294–3300 (2020).

190. Khosla, M., Rao, S. & Gupta, S. Polarons Explain Luminescence Behavior of Colloidal Quantum Dots at Low Temperature. *Sci. Rep.* **8**, 8385 (2018).

191. Antolinez, F. V. *et al.* Trion Emission Dominates the Low-Temperature Photoluminescence of CdSe Nanoplatelets. *Nano Lett.* (2020). doi:10.1021/acs.nanolett.0c01707

192. Dozov, I., Goldmann, C., Davidson, P. & Abécassis, B. Probing permanent dipoles in CdSe nanoplatelets with transient electric birefringence. *Nanoscale* (2020). doi:10.1039/d0nr00884b

193. Liu, J. *et al.* Fourier-Imaging of Single Self-Assembled CdSe Nanoplatelet Chains and Clusters Reveals out-of-Plane Dipole Contribution. *ACS Photonics* **7**, 2825–2833 (2020).

194. Kido, J. & Okamoto, Y. Organo lanthanide metal complexes for electroluminescent materials. *Chem. Rev.* (2002). doi:10.1021/cr010448y

195. Faulkner, S., Pope, S. J. A. & Burton-Pye, B. P. Lanthanide complexes for luminescence imaging applications. *Appl. Spectrosc. Rev.* (2005). doi:10.1081/ASR-200038308

196. Bünzli, J. C. G. & Eliseeva, S. V. Lanthanide NIR luminescence for telecommunications, bioanalyses and solar energy conversion. *J. Rare Earths* (2010). doi:10.1016/S1002-0721(09)60208-8

197. Maeda, H. *et al.* Chemical-stimuli-controllable circularly polarized luminescence from anion-

responsive π-conjugated molecules. *J. Am. Chem. Soc.* (2011). doi:10.1021/ja203206g

198. Maeda, H. & Bando, Y. Recent progress in research on stimuliresponsive circularly polarized luminescence based on π-conjugated molecules. *Pure Appl. Chem.* (2013). doi:10.1351/PAC-CON-12-11-09

199. Isla, H. *et al.* Conformational changes and chiroptical switching of enantiopure bis-helicenic terpyridine upon Zn2+ binding. *Chem. Commun.* (2016). doi:10.1039/c6cc01748g

200. Saleh, N. *et al.* Acid/base-triggered switching of circularly polarized luminescence and electronic circular dichroism in organic and organometallic helicenes. *Chem. - A Eur. J.* (2015). doi:10.1002/chem.201405176

201. Muller, G. Luminescent chiral lanthanide(III) complexes as potential molecular probes. *Dalt. Trans.* (2009). doi:10.1039/b909430j

202. Lunkley, J. L., Shirotani, D., Yamanari, K., Kaizaki, S. & Muller, G. Extraordinary circularly polarized luminescence activity exhibited by cesium tetrakis(3-heptafluoro-butylryl-(+)-camphorato) Eu(III) complexes in EtOH and CHCl3 solutions. *J. Am. Chem. Soc.* **130**, 13814–13815 (2008).

203. Longhi, G., Castiglioni, E., Koshoubu, J., Mazzeo, G. & Abbate, S. Circularly polarized luminescence: A review of experimental and theoretical aspects. *Chirality* **28**, 696–707 (2016).

204. Petoud, S. *et al.* Brilliant Sm, Eu, Tb, and Dy chiral lanthanide complexes with strong circularly polarized luminescence. *J. Am. Chem. Soc.* **129**, 77–83 (2007).

205. Babu, P., Jang, K. H., Kim, E. S., Shi, L. & Seo, H. J. Optical properties and White-light emission in Dy 3+-doped transparent oxyfluoride glass and glass ceramics containing Caf 2 nanocrystals. *J. Korean Phys. Soc.* (2009). doi:10.3938/jkps.54.1488

206. Tsumatori, H., Harada, T., Yuasa, J., Hasegawa, Y. & Kawai, T. Circularly polarized light from chiral lanthanide(lll) complexes in single crystals. *Appl. Phys. Express* **4**, (2011).

207. El Rez, B. *et al.* Concomitant emergence of circularly polarized luminescence and single-molecule magnet behavior in chiral-at-metal Dy complex. *Inorg. Chem. Front.* **7**, 4527–4534 (2020).